

CENTER FOR RADIOLOGICAL RESEARCH  
ANNUAL REPORT 2015  
*CENTENNIAL EDITION*

---



COLUMBIA UNIVERSITY  
*College of Physicians and Surgeons*





Center for Radiological Research – 630 W. 168<sup>th</sup> St., New York, NY 10032 –  
crr.columbia.edu

# CENTER FOR RADIOLOGICAL RESEARCH ANNUAL REPORT 2015

## *CENTENNIAL EDITION*

---



**DAVID J. BRENNER**  
Director

**SALLY A. AMUNDSON**  
Editor

**HOWARD B. LIEBERMAN**  
Co-Editor

---

*On the Cover: Our directors. Upper Left, Gioacchino Failla, our first director, served from 1916-1960. Upper right, Harald H. Rossi, was our second director from 1960-1984. Lower left, Eric Hall was our third director, from 1984 to 2008. Lower right, David J. Brenner, our fourth and current director, assumed the role in 2008.*



**COLUMBIA UNIVERSITY**  
*College of Physicians and Surgeons*





# Table of Contents

CONTENTS.....	1
COLLABORATING DEPARTMENTS AND INSTITUTIONS .....	4
ACKNOWLEDGEMENT OF SUPPORT.....	5
WEBSITES .....	5
DIRECTOR’S INTRODUCTION.....	6
STAFF NEWS .....	7
LABORATORY COLLOQUIA AND SEMINARS .....	8
FACULTY AND STAFF.....	9
FACULTY AND STAFF PHOTO.....	10
TOOLS OF THE TRADE.....	11
THE CRR IN PICTURES .....	16
CRR GROUP PHOTOS .....	26
RESEARCH REPORTS	
<u>MICROBEAM AND SINGLE CELL STUDIES</u>	
<b>The Super Microbeam at RARAF</b>	
Gerhard Randers-Pehrson, Andrew Harken, Guy Garty, Alan Bigelow, Yanping Xu, David Welch, Brian Ponnaiya, Dennis Farrell, Manuela Buonanno, Leah Turner, and David J. Brenner .....	41
<b>AMOEBAs: Unlocking the Potential of Vertical Focused Ion Beams to Examine the Long-term         Effects of Radiation on Cells and the Effects of Hypoxia on Cellular Radiation Response</b>	
Matthew England, Michael Merchant, Alan Bigelow, David Welch, Andrew Harken, Guy Garty, Eirini Velliou, David J. Brenner, and Karen Kirkby .....	44
<b>Development of a Cell System to Investigate the Repair of Telomeres After Targeted         Microbeam Induced Damage</b>	
Brian Ponnaiya, Andrew Harken, Susan Bailey, and David J. Brenner .....	46
<b>A Microfluidic Array for Parallelized Transcriptional Profiling of Single Cells</b>	
Hao Sun, Tim Olsen, Jing Zhu, Jianguo Tao, Brian Ponnaiya, Sally A. Amundson, David J Brenner, and Qiao Lin .....	49
<b>Cytoplasmic Irradiation Induces Metabolic Shift in Small Airway Epithelial Cells via         Activation of PIM1 Kinase</b>	
Jinhua Wu, Qin Zhang, Yen-Ruh Wu, Sirui Zou, and Tom K. Hei .....	52
<b>Live Cell Imaging of Connexin 43: Towards Visualizing Cell-to-cell Communication of         Bystander Responses Following Microbeam Irradiation</b>	
Brian Ponnaiya, David Piston, and David J. Brenner .....	54
<u>CELLULAR AND MOLECULAR STUDIES</u>	
<b>The Impact of MEK5 on Prostate Cancer Cell Survival</b>	
Stephanie Sanchez, Howard B. Lieberman, and Constantinos G. Broustas .....	58
<b>RAD9 Knockdown Represses Metastasis-associated Gene Anterior Gradient 2 in Prostate Cancer</b>	
Constantinos G. Broustas and Howard B. Lieberman .....	60
<b>DNA Damage Repair Protein Rad9 Regulates Abundance of the MRN Complex Proteins         Mre11 and Nbs1</b>	
Li Wang and Howard B. Lieberman.....	62

<b>Mechanistic Modeling of Dose and Dose Rate Dependences of Radiation-Induced DNA Double Strand Break Rejoining Kinetics in <i>Saccharomyces cerevisiae</i></b>	
Igor Shuryak.....	63
<b>Genes Targeted by Therapeutic Drugs and an Antioxidant in a Breast Cancer Model</b>	
Gloria M. Calaf, Richard Ponce-Cusi, and Marcela Gallardo .....	67
<b>Oxygen Level Effects on Gene Expression in Aging IMR-90 Fibroblasts</b>	
Shanaz A. Ghandhi, Xiuquan Luo, David Boothman, and Sally A. Amundson .....	70
<b>Sensitization of Glioblastoma Cells to Apoptosis by Combined Treatment with Cannabidiol, <math>\gamma</math>-Irradiation, and Specific Inhibitors of Signaling Pathways</b>	
Vladimir N. Ivanov and Tom K. Hei .....	72
<b>The Effects of Ionizing Radiation on the Structure and Function of Human Blood Capillaries</b>	
Peter Grabham, Preety Sharma, Burong Hu, Thomas Templin, Alan Bigelow, and Charles R. Geard.....	78
<b>Isolation and Analysis of mRNA from Urinary Exosomes as Potential Markers for Prostate Cancer</b>	
Kevin M. Hopkins and Howard B. Lieberman .....	82
<b><u>TRANSLATIONAL STUDIES</u></b>	
<b>Far-UVC Light: A Promising Tool for Safe Low-cost Reduction of Surgical Site Infections</b>	
Manuela Buonanno, Sheetal Trivedi, Milda Stanislaukas, Brian Ponnaiya, Alan W. Bigelow, Gerhard Randers-Pehrson, Franklin D. Lowy, Henry M. Spotnitz, Scott M. Hammer, David M. Owens, and David J. Brenner .....	85
<b>Targeting Lung Cancer Stem Cell Factor BMI-1 to Sensitize Non-small Cell Lung Cancer to Chemotherapy and Radiation Therapy</b>	
Kunal Chaudhary, Haiying Cheng, Balazs Halmos, Jose Silva, Tom K Hei, and Simon Cheng.....	89
<b>The Effect of High LET Radiation on a Human Hematopoietic System Reconstituted in Mice</b>	
Erik Young, Igor Shuryak, and Lubomir Smilenov.....	90
<b>New Approaches for Modeling Radiopharmaceutical Pharmacokinetics Using Continuous Distributions of Rates</b>	
Igor Shuryak and Ekaterina Dadachova .....	94
<b><u>CENTER FOR HIGH-THROUGHPUT MINIMALLY-INVASIVE RADIATION BIODOSIMETRY</u></b>	
<b>An Irradiator for Simulating Neutron Exposure from an Improvised Nuclear Device</b>	
Guy Garty, Yanping Xu, Gerhard Randers-Pehrson, Stephan A. Marino, Helen C. Turner, Adayabalam S. Balajee, and David J. Brenner .....	98
<b>Relative Biological Effectiveness of Neutrons and X-rays for Gene Induction</b>	
Sally A. Amundson and Constantinos G. Broustas .....	100
<b>Chromosomal Inversions as a Biomarker for Neutron Exposures</b>	
Adayabalam S. Balajee, Brian Ponnaiya, and David J. Brenner .....	102
<b>Response of Cell Cycle Genes in Mouse Blood after Exposure to Neutron or X-ray Irradiation</b>	
Constantinos G. Broustas and Sally A. Amundson .....	105
<b>Development of a Variable Dose-rate External <math>^{137}\text{Cs}</math> Irradiator (VADER)</b>	
Yanping Xu, Gerhard Randers-Pehrson, Guy Garty, and David J. Brenner .....	108
<b>Progress in Validation of an Anatomically Accurate Mouse Phantom using Radiographic Film Dosimetry and MCNP Simulations</b>	
David Welch, Gerhard Randers-Pehrson, and David J. Brenner.....	110
<b>Factors in the Reliability of <math>\gamma</math>-H2AX Scoring by Quantitative Fluorescence</b>	
Guy Garty, Helen C. Turner, Maria Taveras, and David J. Brenner .....	113

**In Vivo Response Patterns In Mice Exposed To The Internal Emitters Cesium-137 and Strontium-90**  
 Helen C. Turner, Igor Shuryak, Shanaz A. Ghandhi, Maryam Goudarzi, Waylon Weber, Melanie Doyle-Eisele, Raymond Guilmette, Dunstana Melo, Albert J. Fornace, Sally A. Amundson, and David J. Brenner ..... 116

*The Decade of the RABiT (2005-2015)*  
 Guy Garty, Helen C. Turner, Y. Lawrence Yao, and David J. Brenner ..... 121

**Automated High-Throughput Preparation and Analysis of Blood Samples in Biodosimetry using Commercial Biotech Robotic Systems**  
 Mikhail Repin, Sergey Pampou, and David J. Brenner ..... 125

**Lung Irradiation of Non-Human Primates Induces Persistent Gene Expression Changes in Peripheral Blood**  
 Shanaz A. Ghandhi, Jean Gardin, J. Mark Cline, and Sally A. Amundson..... 127

**Effects of DNA Repair Deficiency on the Transcriptional Radiation Response in Mouse Blood**  
 Nils Rudqvist, Evagelia C. Laiakis, Mashkura Chowdhury, Sunirmal Paul, M.A. Sureshkumar, Albert J. Fornace, and Sally A. Amundson ..... 129

**THE RADIOLOGICAL RESEARCH ACCELERATOR FACILITY – an NIH-Supported Resource Center**  
 Dir., David J. Brenner, PhD, DSc; Assoc. Dir. Gerhard Randers-Pehrson, PhD; Mgr., Stephen A. Marino, MS

**Research using RARAF** ..... 134

**Development of Facilities** ..... 137

**Singletron Utilization and Operation**..... 141

**Training** ..... 142

**Dissemination** ..... 142

**Personnel**..... 143

**Recent Publications of Work Performed at RARAF**..... 144

**PUBLICATIONS** ..... 146

## Collaborating Departments and Institutions

Individuals from the following departments and institutions collaborated with the Center's faculty and staff in the research reports included in this year's publication (for individual attributions see specific reports):

***Collaborating Columbia University Departments:***

- Department of Dermatology and Medicine
- Department of Environmental Health Sciences
- Department of Mechanical Engineering
- Department of Pathology and Cell Biology
- Department of Radiation Oncology
- Department of Surgery
- Department of Systems Biology
- Division of Infectious Diseases

***Collaborating Institutions:***

- Cytogenetic Biodosimetry Laboratory, Oak Ridge Institute for Science and Education, Oak Ridge, TN
- Department of Biochemistry and Molecular and Cellular Biology, Georgetown University, Washington, DC
- Department of Cell Biology and Physiology, Washington University in St. Louis, St. Louis, MO
- Department of Environmental and Radiological Health Sciences, Colorado State University, Fort Collins, CO
- Department of Mechatronics Engineering, Harbin Institute of Technology, Harbin, Heilongjiang, China
- Department of Oncology, Albert Einstein College of Medicine of Yeshiva University, New York, NY
- Department of Pathology, Wake Forest School of Medicine, Winston-Salem, NC
- Department of Radiation Oncology, Simmons Comprehensive Cancer Center, UT Southwestern, Dallas, TX
- Institute of Cancer Sciences, University of Manchester, Manchester, UK
- Instituto de Alta Investigación, Universidad de Tarapacá, Arica, Chile
- Lombardi Comprehensive Cancer Center, Georgetown University, Washington, DC
- Lovelace Respiratory Research Institute, Albuquerque, NM
- Rutgers University, Newark, NJ
- Surrey University, Guilford, UK
- University of Chile, Santiago, Chile
- University of Texas Health Science Center, San Antonio, TX

### *A Note About a Much Missed Collaborator*

Dr. Bill Morgan, a long time friend and collaborator with the Center for Radiological Research, passed away in 2015, very much mourned both by his many friends at our Center as well of course by his family and many friends elsewhere. Bill was first and foremost a radiation cytogeneticist, so it was natural that our paths crossed many times, while he was in San Francisco at UCSF and LBL, and particularly when he moved to the University of Maryland. By the time he moved on to Pacific Northwest National Lab, he was both a good friend of our Center and a valued collaborator in the microbeam / bystander effect business, and a staunch supporter and mentor of young scientists.

Our memories of Bill will always be happy ones - long talks about science, about politics, and about how to get things done....

RIP the Ram!



## Acknowledgement of Support

In 2015 the Center for Radiological Research was supported by competitively awarded grants from the following agencies:

- Department of Defense
  - Defense Threat Reduction Agency
- Department of Energy
  - Office of Science, Office of Biological and Environmental Research [Low Dose Radiation Research Program]
- Department of Health and Human Services
  - Biomedical Advanced Research and Development Authority
  - National Institutes of Health:
    - National Cancer Institute [Program Project (P01) and Individual Research Grants (R01s)]
- National Institute of Biomedical Imaging and Bio-engineering (P41)
- National Institute of Allergy and Infectious Disease (U19)
- National Institute of Environmental Health and Safety (R01s and R21)
- National Institute of General Medical Sciences (R01)
- National Aeronautics and Space Administration

## Websites

Center for Radiological Research.....<http://www.cumc.columbia.edu/crr/>  
Radiological Research Accelerator Facility.....<http://www.raraf.org>  
Center for High-Throughput Minimally-Invasive Radiation Biodosimetry.....<http://cmcr.columbia.edu>  
Mechanisms of Bystander Effects.....<http://www.radiation-bystander.columbia.edu>  
Web-Rad-Train.....<http://www.web-rad-train.org>  
Department of Radiation Oncology.....<http://www.cumc.columbia.edu/dept/radoncology>  
CRR Annual Reports (1999-present)..... <http://www.cumc.columbia.edu/crr/events/annual-reports>



*David Brenner being presented with the Weldon Memorial Prize by Sarah Darby. The Weldon Prize is awarded by Oxford University “to the person who, in the judgment of the electors, has, in the ten years next preceding the date of the award, published the most noteworthy contribution to the development of mathematical or statistical methods applied to problems in biology”. Previous recipients include some of the most recognized names in biostatistics and genetics, including Karl Pearson, RA Fisher, David Cox, JBS Haldane, and Sewall Wright.*

## Director's Introduction

Writing this in early 2016, we have reached our 100<sup>th</sup> anniversary! Founded in 1916 by Gioacchino Failla, our Center has spent the last 100 years focused on basic radiation science both to improve radiotherapy (at high radiation doses), as well as to improve our understanding of the health effects of low levels of radiation.

I would draw your attention to the excellent "history" sections in this report, but I would like to call out here a couple of scientists from our past, one in the radiotherapy field, and one in the low dose radiation risk field, who I think exemplify everything that our Center stands for.



In the field of Radiotherapy, Edith Quimby, joined Failla in 1919, and stayed here until 1978. If Failla was the first American Medical Physicist, Quimby was the undoubtedly the first woman Medical Physicist, worldwide. Like Failla, her early interest was in radium needle radiotherapy, particularly how to place the radium needles within a tumor for maximum therapeutic efficiency. The result was the "Quimby rules", a set of guidelines for exactly where to put the radium needles relative to one another.

These rules result in most of the dose being delivered at the center of the tumor, with less dose at the edge. Quimby based this on good science - the center of a tumor is typically more resistant to radiation than is the tumor edge. The alternative "Manchester" implant system gave a uniform dose over the whole tumor. The Quimby system continued to be used long after radium needles were replaced with iridium needles. It's fair to say that the Quimby vs. Manchester question is still being debated today, and the dogma that one needs a uniform radiation dose over the whole tumor - a dogma that Quimby actively rejected, is being increasingly questioned today.

Quimby was also a dedicated activist for the field of Medical Physics. In 1954, she became the first physicist (and the first woman) to be president of the American Radium Society, and she used her Presidential Speech to point out that while the UK had the British Hospital Physicists Association, no such Medical Physicist organization existed in the US. Very much because of her

influence, the American Association of Physicists in Medicine (AAPM) was founded in 1958.



**Albrecht Kellerer**

On the "low dose" side, Albrecht Kellerer arrived at our Center in 1968, having done his doctoral work with Otto Hug in Munich on the mathematical theory of dose-effect relations. This was a propitious time, because the new field of microdosimetry was just then getting major attention (the first of many International Microdosimetry Meetings was in 1967), very much due to our then Director, Harald Rossi's work.

The concept of microdosimetry is to think of radiation energy deposition from the perspective of individual cells. Because cells are so very small, and because radiation deposits its energy in a stochastic (random) way, a series of cells within an organ that is exposed to radiation will likely each have a different amount of energy deposited in them. This "microdosimetric distribution" of energy depositions in cells (the subject of microdosimetry) is different for different types of radiations - such as for neutrons vs. x rays. The rationale of microdosimetry is that these different microdosimetric distributions can be used to predict how much more hazardous one type of radiation (say neutrons) is, compared with, say, x rays.

So, when Kellerer arrived in 1968, Rossi had already come up with his brilliant ideas to measure these microdosimetric energy deposition distributions using so-called microdosimeters, which could simulate the size of a human cell - a few micrometers. Now Rossi was very much a "concepts" person - he dreamed up how an experimental microdosimeter might work, but it took the genius of Rudi Gand in our machine shop to actually build one (see pictures in "The Tools of the Trade"! ). Likewise, Rossi conceived of many of the ideas of microdosimetry, but it took the mathematical genius of Albrecht Kellerer to translate those ideas into numerical concepts, and we still use these same concepts today.

Quimby and Kellerer exemplify everything our Center stands for - now and into the next 100 years! Both were absolutely rigorous scientists, who also had their eyes very much on the end product - better cancer therapy for Quimby, a better understanding of low-level radiation risks for Kellerer. Both were also extraordinary teachers. Quimby mentored multiple generations of medical physicists, and Kellerer - I can only say that the first time I heard him lecture, I understood only a little of what he said - but I knew then that's what I wanted to do for the rest of my career!

-David Brenner ■

## Staff News

**Dr. David Brenner** was awarded the 2015 Weldon Memorial Prize and Medal, given by Oxford University for the development of mathematical methods in biology. He continued as a member of the National Academy of Sciences Nuclear and Radiation Studies Board, and was a member of a NAS study on “Research Directions in Human Biological Effects of Low Level Ionizing Radiation.” He is also a member of the New York City Radiological Advisory Committee. Dr. Brenner also continues to serve as an Associate Editor of the journal *Radiation and Environmental Biophysics*.

**Dr. Tom Hei** holds an Adjunct Professorship at the Chinese Academy of Sciences and a Chair Professorship at Soochow University. He serves as Editor in Chief of *Life Sciences in Space Research*, and as an Associate Editor of the *Journal of Radiation Research* and of *Translational Cancer Research*. Dr. Hei also serves on the NIH Cancer Etiology Study Section.

**Dr. Howard Lieberman** was a member of the Israel Cancer Research Fund Scientific Advisory Board, which awarded him the Elliot Osserman Award for Distinguished Service in 2015. He continued to serve as Associate Editor for both *Radiation Research* and the *Journal of Cellular Physiology*.

**Dr. Sally Amundson** completed her term on the Governing Council of the Radiation Research Society, and was appointed to the EPA Science Advisory Board. She completed service as the Chair of a NCRP commentary on integration of low dose radiation epidemiology and biology, and on a NAS study on backscatter x-ray machines for passenger screening. Dr. Amundson also continued as a member of NCRP, and as an Associate Editor of *Radiation Research*.

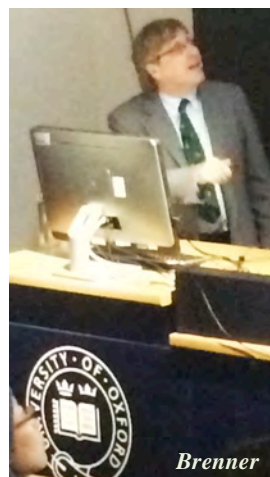
**Dr. Jingsong (Jason) Yuan**, previously of the MD Anderson Cancer Center, joined the CRR as an Assistant Professor. His lab focuses on the molecular mechanisms underlying DNA replication stress response and homologous recombination DNA repair, which is critical for preventing genomic instability and tumorigenesis. He is the recipient of both a Susan G. Komen Career Catalyst Research Grant, and a NCI Transition Career Development (K22) Award.

Dr. Eric Hall was the keynote speaker at Hiroshima University for an International Symposium on “Biological Effects of Low Dose Radiation”. Dr. Hall was also the keynote speaker at the American Society of Veterinarian Radiology at their annual meeting in San Antonio.

During the year, Brian Ponnaia was promoted to Research Scientist, and Manuela Buonanno was promoted to Associate Research Scientist.

Several new members also joined the Center in 2015; postdocs Dr. Nils Rudqvist in Dr. Amundson’s lab, and Drs. Mike Yuan-Cho Lee and Qing Zhou in Dr. Yuan’s lab. We also welcomed Mr. Matthew England, a graduate student at the University of Surrey as a Staff Associate at RARAF, Mr. Lance Redford, as Director of Development, and Qin Zhang as a Visiting Associate Research Scientist.

After 16 years as a key member of the CRR, **Dr. Adayabalam Balajee** left to become Director of the Cytogenetic Biodosimetry Lab at REAC/TS (Radiation Emergency Assistance Center/Training Site) at the Oak Ridge Institute for Science and Education. At the end of 2015 **Dr. Hongning Zhou** also left the CRR after 17 years with Dr. Hei. Drs. Alan Bigelow, Congju Chen, Stanley Lue, Sunil Panigrahi, Preety Sharma, and Erik Young, as well as Mr. Radoslaw Pieniazek and Mr. Dennis Keaveney also left the center in 2015. We wish them all well in the future. ■



Brenner



Lieberman



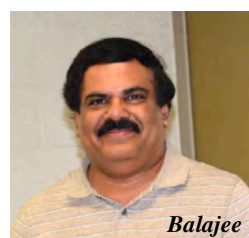
Amundson



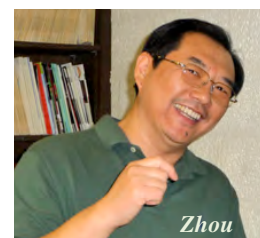
Hei



Yuan



Balajee



Zhou

## Laboratory Colloquia and Seminars

Periodically, the Center organizes morning-long colloquium sessions featuring presentations of recent work by Center researchers and guest speakers. These colloquia are attended by Center professional and technical staff and graduate students, as well as by physicians and scientists from other departments at CUMC. They serve as a forum for discussions and forging future collaborations. The 2015 Colloquium Series was organized and coordinated by Dr. Lubomir Smilenov.

### April Colloquium:

- Dr. Preeti Sharma, CRR: “Acute Effects of Radiation on the Human Endothelial Barrier.”
- Dr. Kunal Chaudhary, Department of Radiation Oncology, CUMC: “Determining Key Pathways Sensitizing Lung Cancer to Combined Chemoradiation Therapy using RNAi High-throughput Screen.”

Dr. Christopher Porada, Virginia Tech – Wake Forest University School of Biomedical Engineering and Sciences: “Direct and Biological Bystander Effects of Space Radiation on Human Hematopoiesis.”

In addition to our colloquium series, in 2015 we also hosted the first Radiation Oncology Research Retreat, and welcomed a number of distinguished guest speakers from around the country and around the world. Guest speakers during 2015 included the following:

- Dr. Günther Reitz, German Aerospace Center, Köln, Germany: “Radiation Exposures and Risks during Manned Space Missions.”
- Dr. Alexander Nesterov-Müller, Karlsruhe Institute of Technology, Karlsruhe, Germany: “Novel combinatorial chemistry for antibody profiling.”



*Audience at the first Department of Radiation Oncology Research Retreat, held in the Center for Radiological Research.*

## Faculty and Staff

### Faculty:

**DAVID J. BRENNER**, Ph.D., D.Sc.  
*Director*  
**RARAF Director**  
 Higgins Professor of Radiation Biophysics  
 Professor of Radiation Oncology  
 Professor of Environmental Health Sciences

**TOM K. HEL**, Ph.D.  
*Associate Director*  
**Vice-Chairman, Dept. of Radiation Oncology**  
 Professor of Radiation Oncology  
 Professor of Environmental Health Sciences

**ERIC J. HALL**, D.Phil., D.Sc., FACR, FRCR, FASTRO  
 Higgins Professor Emeritus  
 Special Lecturer in Radiation Oncology  
 Special Research Scientist

**CHARLES R. GEARD**, Ph.D.  
 Professor Emeritus of Clinical Radiation Oncology

**HOWARD B. LIEBERMAN**, Ph.D.  
 Professor of Radiation Oncology  
 Professor of Environmental Health Sciences

**SALLY A. AMUNDSON**, Sc.D.  
 Associate Professor of Radiation Oncology

**GUY GARTY**, Ph.D.  
 Associate Professor of Radiation Oncology (in the CRR) at the Columbia University Medical Center

**PETER GRABHAM**, Ph.D.  
 Assistant Professor of Radiation Oncology (in the CRR) at the Columbia University Medical Center

**LUBOMIR SMILENOV**, Ph.D.  
 Assistant Professor of Radiation Oncology (in the CRR) at the Columbia University Medical Center

**JINGSONG (JASON) YUAN**, M.D., Ph.D.  
 Assistant Professor of Radiation Oncology

**YONGLIANG ZHAO**, Ph.D.  
 Adjunct Assistant Professor

### Research Staff:

**GERHARD RANDERS-PEHRSON**, Ph.D.  
 Senior Research Scientist

**ADAYABALAM BALAJEE**, Ph.D.  
 Research Scientist

**VLADIMIR IVANOV**, Ph.D.  
 Research Scientist

**BRIAN PONNAIYA**, Ph.D.  
 Research Scientist

**HONGNING ZHOU**, M.D.  
 Research Scientist

**ALAN BIGELOW**, Ph.D.  
 Associate Research Scientist

**CONSTANTINOS BROUSTAS**, Ph.D.  
 Associate Research Scientist

**MANUELA BUONANNO**, Ph.D.  
 Associate Research Scientist

**CONGJU CHEN**, Ph.D.  
 Associate Research Scientist

**SHANAZ GHANDHI**, Ph.D.  
 Associate Research Scientist

**ANDREW HARKEN**, Ph.D.  
 Associate Research Scientist

**SUNIL PANIGRAHI**, Ph.D.  
 Associate Research Scientist

**MIKHAIL REPIN**, Ph.D.  
 Associate Research Scientist

**PREETY SHARMA**, Ph.D.  
 Associate Research Scientist

**IGOR SHURYAK**, M.D., Ph.D.  
 Associate Research Scientist

**HELEN TURNER**, Ph.D.  
 Associate Research Scientist

**LI WANG**, Ph.D.  
 Associate Research Scientist

**YANPING XU**, Ph.D.  
 Associate Research Scientist

**ERIK YOUNG**, Ph.D.  
 Associate Research Scientist

**GLORIA CALAF**, Ph.D.  
 Adjunct Associate Research Scientist

**ENYUAN SHANG**, Ph.D.  
 Adjunct Associate Research Scientist

**KEVIN M. HOPKINS**, M.S., Senior Staff Associate

**M. HASEEB DURRANI**, M.S., Staff Associate

**DENNIS FARRELL**, Staff Associate

**JAY PERRIER**, Staff Associate

**RADOSLAW PIENIAZEK**, Staff Associate

**MARIA TAVERAS**, R.N., Research Nurse

### Post-Doctoral Research Scientists:

**MIKE YUAN-CHO LEE**, Ph.D.

**STANLEY LUE**, Ph.D.

**NILS RUDQVIST**, Ph.D.

**GLICELLA SALAZAR-DE SIMONE**, Ph.D.

**DAVID WELCH**, Ph.D.

**DANNIS JINHUA WU**, Ph.D.

**VIVIAN QING ZHOU**, Ph.D.

### Graduate Student:

**MATTHEW ENGLAND**

### Design & Instrument Shop:

**GARY W. JOHNSON**, A.A.S., Senior Staff Associate  
*Design & Instrument Shop Director*

**DAVID CUNIBERTI**, B.A., Instrument Maker

**DENNIS KEAVENEY**, Instrument Maker

**ROBERT C. MORTON**, Instrument Maker

### Technical Staff:

**CUI-XIA KUAN**, Technical Assistant

**AESIS M. LUNA**, Senior Technician

**MASHKURA CHOWDHURY**, Technician B

### Administrative & Secretarial Staff:

**MARGARET ZHU**, M.A., Center Administrator

**LANCE REDFORD**, B.A., Director of Development

**ANGELA LUGO**, B.A., Business Manager

**ANNERYS RODRIGUEZ**, Junior Accountant

**MARGARET GERMAN**, B.A., Senior Clerk

## Faculty and Staff Photo



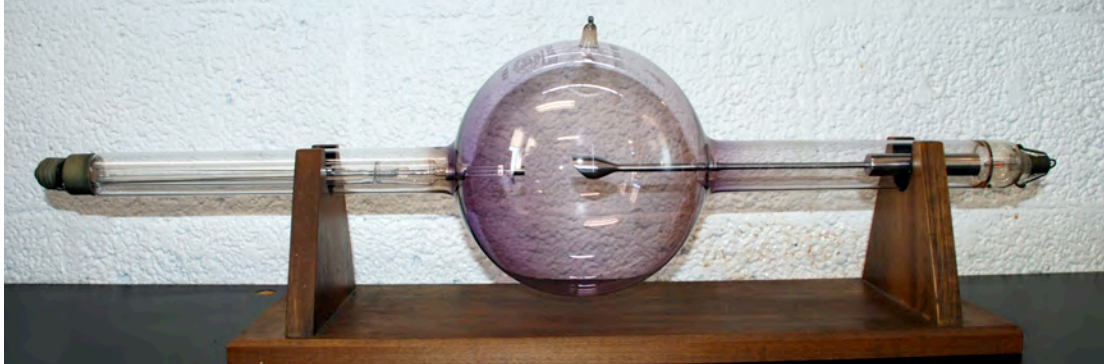
**Front Row** (l-r): Ms. Margaret Zhu, Dr. Gerhard Randers-Pehrson, Dr. David Brenner, Dr. Tom Hei, Dr. Sally Amundson, Dr. Howard Lieberman.

**2<sup>nd</sup> Row:** Mr. Gary Johnson, Dr. Constantinos Broustas, Dr. Jingsong Yuan, Dr. Vivian Qing Zhou, Ms. Aesis Luna, Dr. Mike Yuan-Cho Lee, Ms. Mashkura Chowdhury, Ms. Cui Xia Kuan, Dr. Yen-Ruh Wu, Dr. Shanaz Gandhi, Dr. Manuela Buonanno, Dr. Helen Turner, Dr. Igor Shuryak.

**3<sup>rd</sup> Row:** Dr. Guy Garty, Mr. Jay Perrier, Dr. Andrew Harkin, Qin Zhang, Mr. David Cuniberti, Dr. Jinhua Dannis Wu, Mr. Robert Morton, Dr. Kunal Choudhary, Dr. Mikhail Repin, Mr. Dennis Farrell, Dr. Lubomir Smilenov, Dr. Yanping Xu, Dr. David Welch, Dr. Peter Grabham, Mr. Lance Redford, Mr. Matthew England, Dr. Brian Ponnaiya.

**Not Pictured:** Dr. Adayabalam Balajee, Dr. Alan Bigelow, Dr. Gloria Calaf, Dr. Congju Chen, Dr. M. Haseeb Durrani, Dr. Charles Geard, Ms. Margaret German, Dr. Eric Hall, Mr. Kevin Hopkins, Dr. Vladimir Ivanov, Mr. Dennis Keaveney, Dr. Stanley Lue, Ms. Angela Lugo, Dr. Sunil Panigrahi, Mr. Radoslaw Pieniazek, Ms. Annerys Rodriguez, Dr. Nils Rudqvist, Dr. Glicella Salazar-de Simone, Dr. Enyuan Shang, Ms. Maria Taveras, Dr. Li Wang, Dr. Erik Young, Dr. Yongliang Zhao, Dr. Hongning Zhou, Dr. Qing Zhou.

## Tools of the Trade



Many artifacts of the work of our Center over the past hundred years are tucked away, both in the New York City lab and at RARAF. One of the most spectacular, and the oldest, is this high-vacuum Coolidge tube made by the Victor X-ray Corporation. Prior to 1923, this was the best high-voltage tube available, and was capable of running at up to 8 MA and 200 kV. Patent information printed on the tube suggests it was most likely manufactured some time in 1917, dating it to the Center's earliest days. The angled target in the center of the tube (and in close-up, upper right) produced a cone-shaped beam of x-rays leaving the tube in one direction. This tube was used rather heavily, as seen by the pitting of the target, and the strong violet color in the glass where the x-rays exited the tube. The violet tint indicates potassium in the glass. The evacuation port, visible at the top of the tube, and in the close up to the right, is a result of the early manufacturing process.



This is a Model CA-2 General Electric x-ray tube dating to the early 1930s. It was designed for x-ray diffraction analysis, and used filtration to produce a nearly monoenergetic x-ray beam. In contrast to medical tubes, this has a target (hidden inside the copper tube) perpendicular to the electron beam, resulting in the emission of x-rays in 360°. This is clearly seen by the darkening of the glass tube in a ring around the target location. Unlike the Victor tube, this tube was water cooled, and the two steel tubes on the far right would have connected to the water supply. The close up to the left shows the hemispherical focusing cup that conceals the cathode, and the bright yellow uranium glass stem holding the cathode wires.



*This is a General Electric model XR-T x-ray tube, also dating to the 1930s. It is a high-vacuum water-cooled (connection tubes on far right) direct current tube designed for x-ray therapy. The cathode is on the left, and the anode on the right. The Center has a matched pair of these tubes, which were used in a “double-headed” x-ray machine designed and built by Gioacchino Failla. The water-cooling system incorporated an ingenious fail-safe, which relied on a dessert spoon into which the water would flow. Any interruption of the water flow would cause the spoon to rise, tripping a switch to shut off the power and prevent over heating. This system was in use well into the 1970s, and Eric Hall recalls using it for many experiments. The very dark discoloration of the glass, with the orange tint indicating a high sodium glass, testifies to the extensive use of these tubes.*



*To the right is one of the earliest objects made by our machine shop. It is a radiation dose nomograph of an unusual cylindrical design. The rotating wheels are aligned to calculate radiation doses, quantities, effective half-lives, and other units. It was used by Harald Rossi, and likely also by Gioacchino Failla.*



*To the left is a Weston D.C. Voltmeter (Model 1) from 1951. It is in a fitted wooden case with a leather handle. The label pasted to the side declares it the property of Dr. G. Failla of the Radiological Research Laboratory.*



*This is a Model 70 Victoreen Condenser R Meter used by Edith Quimby. It was a battery-operated gamma and x-ray integrated air ionization meter. This model was manufactured c. 1948, and was last calibrated in 1963.*



*Above is an external meter from the Failla era that pre-dates solid state electronics.*



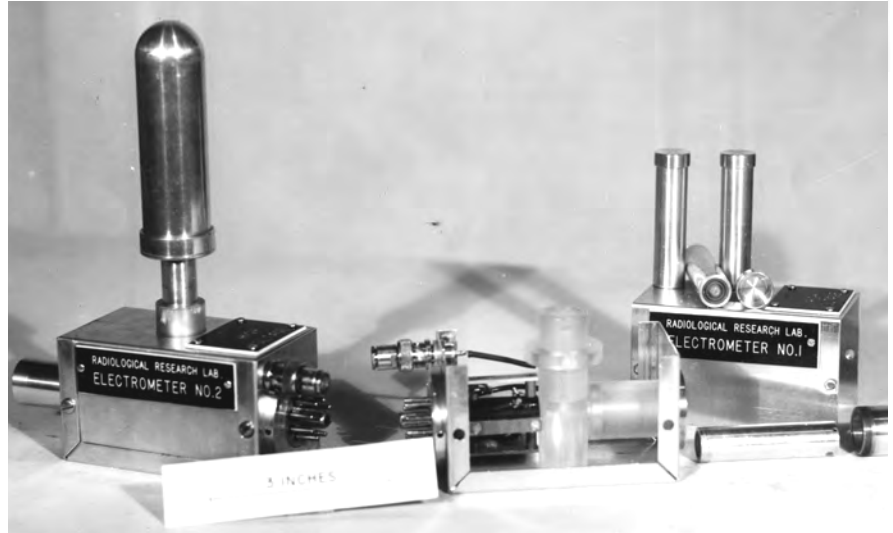
*Tracerlab RA-1 <sup>90</sup>Sr/<sup>90</sup>Y ophthalmic applicator dating to c. 1955. It was designed to produce a beta emission of 25-84 R/sec.*



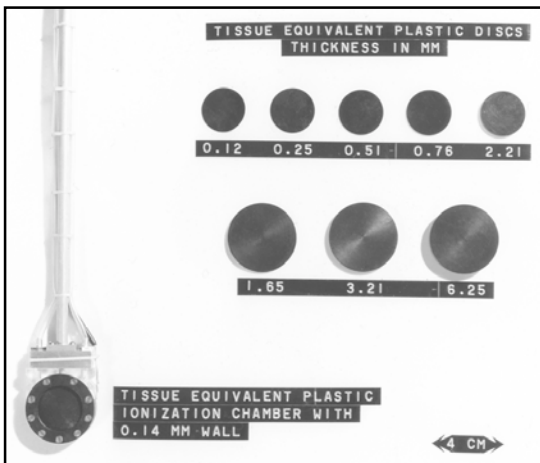
*Above is a Model E Braestrup condenser R meter used to measure the charge on condenser-type ion chambers exposed to radiation. It was stored with a card noting calibrations from 1946. The shipping label on the case indicates that this was one of the instruments Harald Rossi used to make measurements at the Nevada Proving Grounds. The story goes that they would drive "like a bat out of Hell" to their location, make the measurements, and drive like a bat out of Hell back to Camp Mercury.*



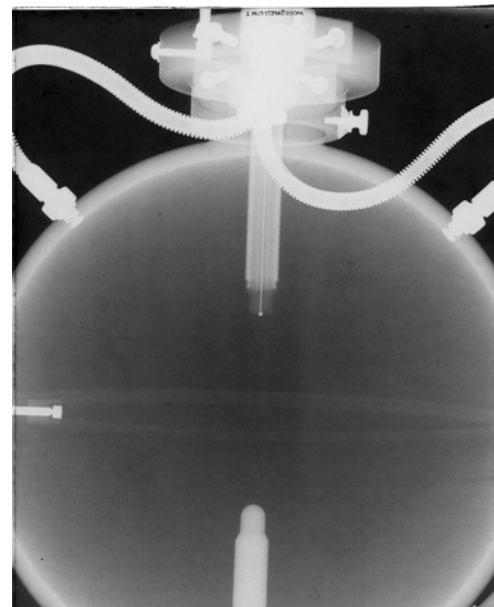
The above chamber, built by our shop for Eric Hall, is designed to grow seedlings under controlled levels of hypoxia. The growing root tips would be irradiated through the thin plastic wall in the square area outlined in the image above. These basic studies on hypoxia used some of the “beans” referred to in Eric Hall’s Failla Award Lecture (1991), which was entitled “From Beans to Genes: Back to the Future”.



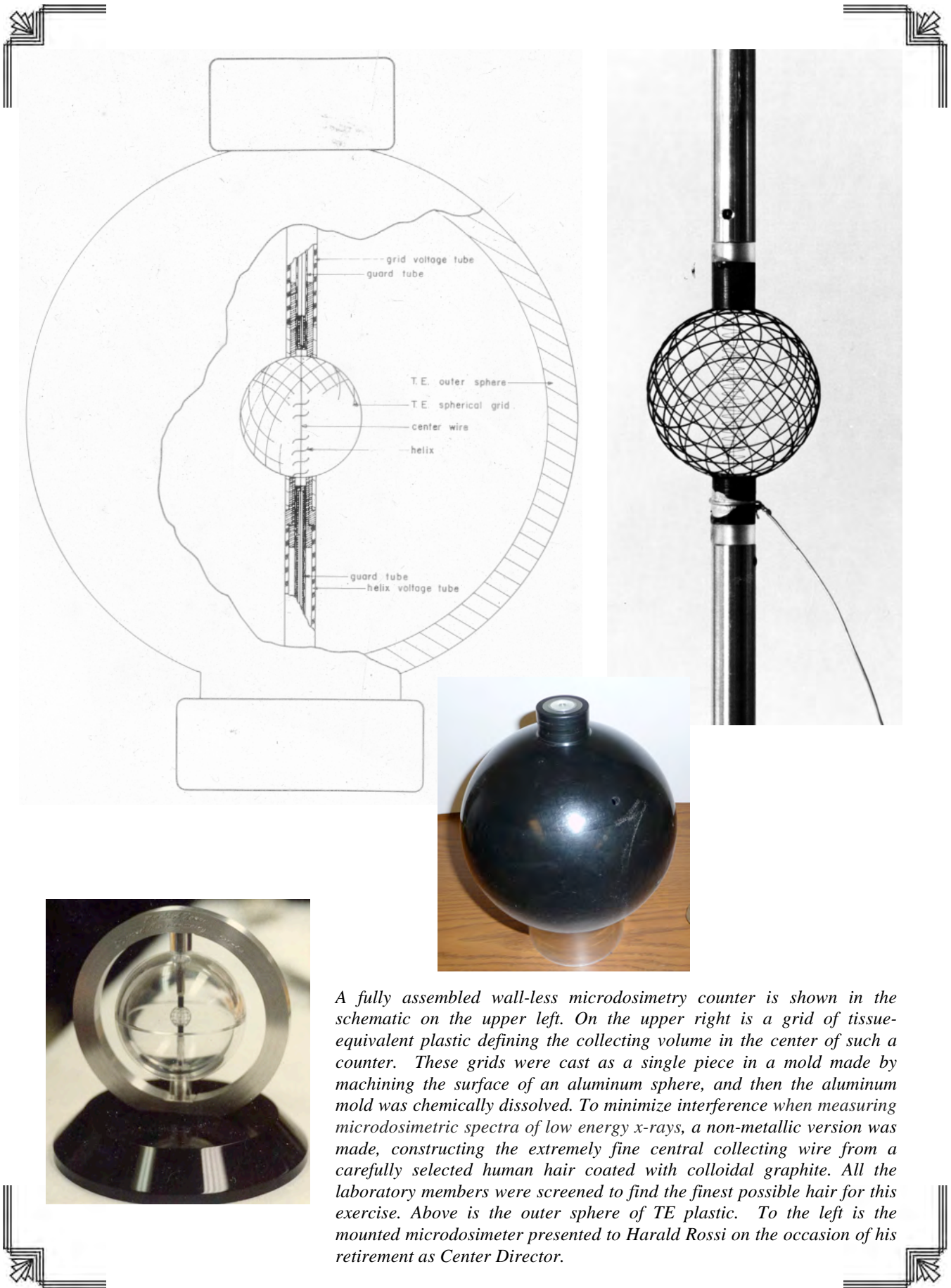
Quartz fiber electrometers designed by Leon Goodman in the early days of RARAF. The P chamber is about the size of a mouse and was designed to measure the average dose delivered to the body of the animal. Initially, the measurements were output to a chart recorder, and had to be integrated manually to obtain the dose.



Above is pictured a series of tissue equivalent (TE) plastic discs used to enable dose measurements corresponding to different depths in tissue. These were used by Bill Gross and Dee Colvett at the Princeton particle accelerator to measure at different points in high Z tracks and into the Bragg peak. They were used in 1964 at the Brookhaven Cosmotron, and for the measurement of monogenergetic neutron beams at RARAF.



An x-ray of a typical tissue-equivalent walled proportional counter used for microdosimetry is shown above. Harald Rossi developed these counters and launched the field of microdosimetry. This example of a “Rossi counter” uses a sphere of TE plastic filled with a low-pressure gas to enable precise measurements of low radiation doses in the equivalent of the volume of a single cell.



*A fully assembled wall-less microdosimetry counter is shown in the schematic on the upper left. On the upper right is a grid of tissue-equivalent plastic defining the collecting volume in the center of such a counter. These grids were cast as a single piece in a mold made by machining the surface of an aluminum sphere, and then the aluminum mold was chemically dissolved. To minimize interference when measuring microdosimetric spectra of low energy x-rays, a non-metallic version was made, constructing the extremely fine central collecting wire from a carefully selected human hair coated with colloidal graphite. All the laboratory members were screened to find the finest possible hair for this exercise. Above is the outer sphere of TE plastic. To the left is the mounted microdosimeter presented to Harald Rossi on the occasion of his retirement as Center Director.*

## The CRR in Pictures



*Founder and first Center Director Gioacchino (Gino) Failla working on his radium-emanation plant c. 1930. At a time when radium was being used for cancer treatment, but cost over \$178 million per ounce to produce, Failla and fellow Marie Curie student Dr. William Duane of Harvard devised this means of producing radon gas from radium and encasing it in gold or glass seeds for implantation into tumors, greatly improving the efficiency of radiotherapy.*



*L to R: “The Chief”, Gino Failla, in a photo as the Janeway Lecturer of the American Radium Society in 1939. Edith Quimby, as the Janeway Lecturer of the American Radium Society in 1940. She was the first non-MD to receive this award. (Eric Hall was the second, in 1992.) Titus Evans, a member of the Center in the 1940’s, later founded the Radiation Research Laboratory in Iowa, and became the first editor of Radiation Research. Ruth Hill, a radiobiologist at the Center for many years. These photographs were previously published in the special issue of Radiation Research marking our 75<sup>th</sup> anniversary (Hall EJ (1990) 75 years of radiological research. Radiat Res 124: S1-4.).*



**Top (l to r):** Gino Failla and his radon plant. Catharine Wingate, one of Failla's graduate students and later Executive Secretary of the Diagnostic Radiation Study Section at the NIH. (Image previously published in Hall EJ (1990) 75 years of radiological research. *Radiat Res* **124**: S1-4.)

**Middle (l to r):** Katie Johann, Failla's administrator, who remained with the Center for five decades. Roberts Rugh, a radiobiologist and embryologist at the Center from 1948 to 1971; Gino Failla and Henri Coutard, the originator of protracted fractionated radiotherapy, c. 1937 (Acc. 90-105 - Science Service, Records, 1920s-1970s, Smithsonian Institution Archives).

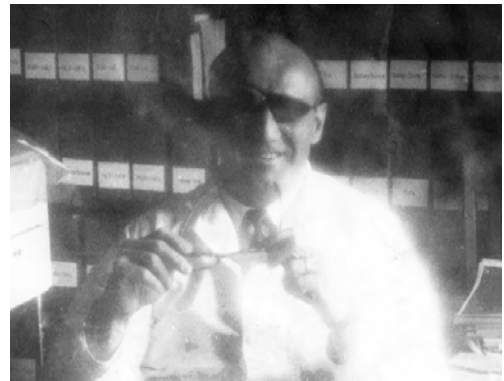
**Bottom:** Rudy Gand, longtime Director of the Design and Instrument Shop, who was hired by Failla and retired in 1989.



**Top** (l to r): Gino Failla and Hal Gray at an early International Congress of Radiation Research. (Image previously published in Hall EJ (1990) 75 years of radiological research. *Radiat Res* **124**: S1-4.). Roberts Rugh.

**Middle** (l to r): Edith Quimby; Drs. Shirley and Edith Quimby.

**Bottom** (l to r): The doctors Failla: Patricia and Gino. Pat Failla continued as an independent radiation researcher for decades after her husband's death in 1961. It is with sadness that the CRR learned of her death in early 2016, just a few months before the symposium celebrating our centennial.



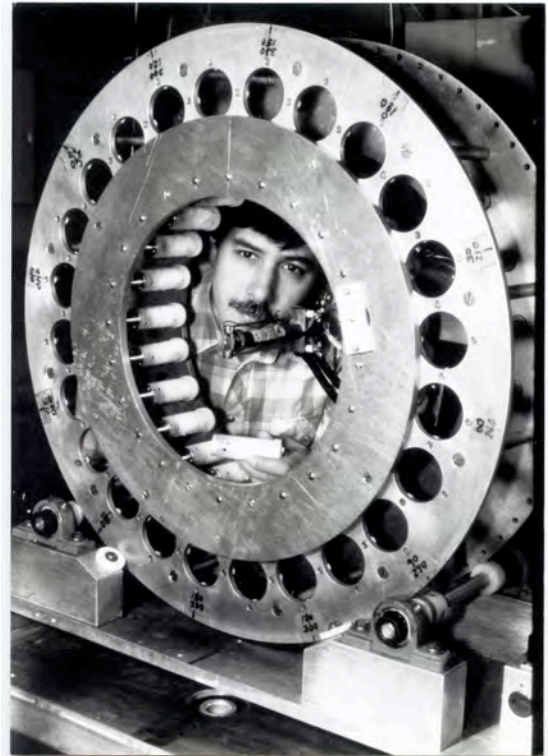
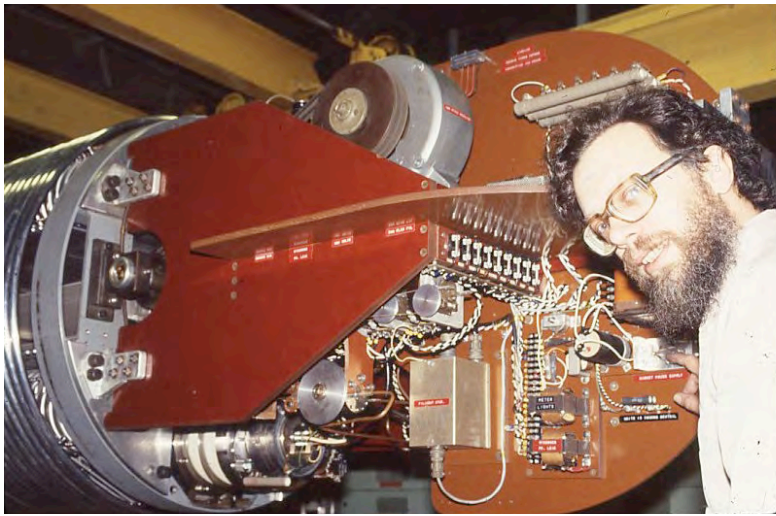
*Top (l to r): Katie Johanny; Bill Bell, Gino Failla, Harald H. Rossi, second Director of the Center, from 1960 to 1984.  
Middle (l to r): Katie Johanny, Harald Rossi; Roberts Rugh.  
Bottom (l to r): Pat Failla, Gino Failla.*



**Top** (l to r): Harald Rossi; Albrecht Kellerer (Images previously published in Hall EJ (1990) 75 years of radiological research. Radiat Res 124: S1-4).

**Middle:** Eric Hall (far left), at a symposium in New York in 1968 where he was recruited by Harald Rossi. On the far right is Larry Lanzi, a senior figure in the American Association of Physicists in Medicine, second from the right is John Laughlin, who took over as chairman of medical physics at Memorial when Failla left for Columbia.

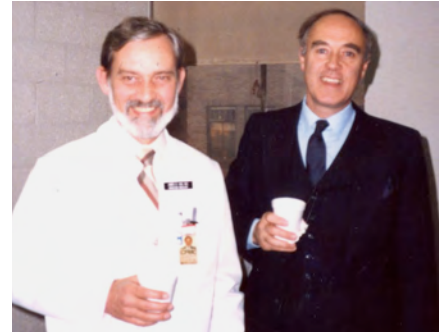
**Bottom:** Members of the Quantities and Units Committee in the gardens of Bushy House at the NPL in October 1978. (l to r) André Allisy, Harold O. Wyckoff, Albrecht M. Kellerer, Kurt Liden, W. Alan Jennings, Harald H. Rossi. Eric Hall and Juliana Denekamp (Image previously published in Hall EJ (1990) 75 years of radiological research. Radiat Res 124: S1-4).



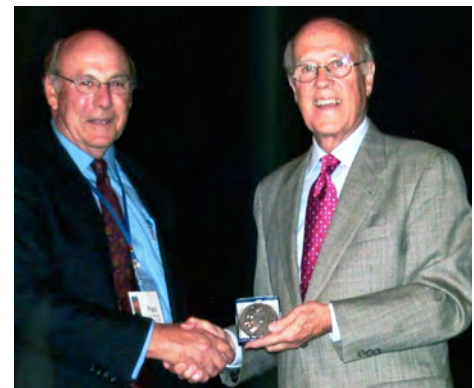
**Top** (l to r): Steve Marino, Gerhard Randers-Pehrson; Gerhard Randers-Pehrson; Susan Carlson (nee Munsterman), RARAF secretary. **Middle** (l to r): Gerhard Randers-Pehrson inside the Van de Graaff. Steve Marino setting up a neutron exposure experiment. **Left** (l to r): Leon J. Goodman (first Manager of RARAF), Steve Marino (Manager of RARAF until 2014).



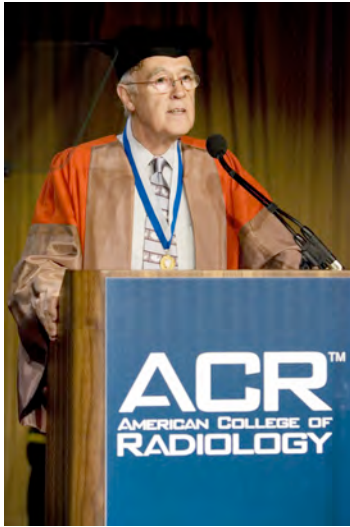
*Top (l to r): Charles Geard; Paul Kliauga, Kia-bao Li, Harald Rossi; Gary Johnson. 2<sup>nd</sup> Row (l to r): Eric Hall, Jeanne Kramer, Gary Johnson; Tom Hei, Robert Osmak, Richard Miller, Charles Geard. 3<sup>rd</sup> Row (l to r): Carmia Borek, Charles Geard; Richard Miller, Augustinus Ong, Tom Hei, Kenshi Komatsu, Yan-Chen Chang. Bottom Row (l to r): Eric Hall, Harald Rossi; Paul Kliauga, Rudy Gand, Carmia Borek, Eric Hall, Harald Rossi unwrapping a mounted microdosimeter presented to him on the occasion of his retirement in 1984. (A picture of the microdosimeter can be seen on p. 15 of this report.)*



**Top** (l to r): Joel Bedford, Martin Brown, Eric Hall, Ged Adams, Bob Sutherland; Jim Cox, at that time our Chairman of Radiation Oncology, and Eric Hall. **2<sup>nd</sup> Row** (l to r): Herb Mason, Elaine Sierra, Augustinus Ong; David Brenner (far right) playing for the Radiation Oncology "Photons" softball team. **3<sup>rd</sup> Row** (l to r): The 2000 Painter Debate - David Brenner (wearing the molecular clock), Julian Preston; Eric Hall, David Brenner; Laurie Roizin-Towle. **4<sup>th</sup> Row**: Tom Hei, Bob Osmak. **Right**: David Brenner taking part in the 2008 NCRP debate.



**Top** (l to r): John Ward receiving the Failla Gavel and the Presidency of the Radiation Research Society from Eric Hall (1984). Failla was one of the founding fathers of the RRS as well as its second president. He designed the ceremonial RRS gavel and had it made in our shop. Harald Rossi also served as RRS president (1974), as has Tom Hei, who received the gavel from Jacky Williams in 2012 (top right). **2<sup>nd</sup> Row** (l to r): David Brenner, honorary doctorate from Oxford University (1996); Sir Christopher Payne presents Eric Hall with the Edelstyn Medal of the Royal College of Radiology (1991); Roy Lam receives the Marie Curie Award from RRS President Tom Hei (2013). **3<sup>rd</sup> Row** (l to r): David Brenner Receives the Moseley Award from NCRP President Charles Meinhold (1992); Paul DeLuca, President of the ICRU awards the Gray Medal to Eric Hall (2007). **4<sup>th</sup> Row** (l to r): Appointment of Tom Hei as Adjunct Professor in the School of Public Health, Soochow University, China (2007); Igor Shuryak receives the Editor's Award from Radiation Research editor Marc Mendonca (2011).



**Top:** Eric Hall with several of his awards. (l to r) giving his Gold Medal Award lecture at the American College of Radiology (2008); Janeway Medal of the American Radium Society (1992); Failla Award, RRS (1991); Gold Medal of the Fletcher Society (1995). **2<sup>nd</sup> Row** (l to r): Tom Hei (center), the Distinguished Achievement Award by the Organization of Chinese Americans (2008); Former Michael Fry Award winners gather at the RRS Annual Meeting on the occasion of Sally Amundson receiving the award. Martin Brown (1980), David Brenner (1991), Bob Ullrich (1987), Sally Amundson (2004), Michael Fry, George Iliakis (1992), Kevin Prise (2001), Jim Mitchell (1989). **3<sup>rd</sup> Row** (l to r): Howard Lieberman (right) was elected a Fellow of the American Association for the Advancement of Science (2006); David Brenner congratulates Gary Johnson on winning the College of Physicians and Surgeons Award for Excellence (2014); David Brenner, Failla Award from RRS (2011). **4<sup>th</sup> Row** (l to r): Erik Young, Radiation Research Editor's Award (2012); Igor Shuryak, Jack Fowler Award presented by RRS President Frank Cucinotta (2014).

## CRR Group Photos

From the 1940's to the 1990's, a contract from first the Atomic Energy Commission, and later the Department of Energy, supported a large proportion of the Center's activities, and these activities were documented in a technical annual report. Towards the end of this era, as the scope of work at the CRR expanded the Center began producing its own Annual Report, which, starting in 1987, included group photos of Center members. These are reproduced in the following pages.

### 1987

**Front Row** (l-r): Ms. Miriam Weisbrot, Ms. Karen Smyth.

**2<sup>nd</sup> Row:** Ms. Miriam Battle, Dr. Laurie Roizin-Towle, Ms. C. Jeanne Kramer, Dr. Eric Hall, Mrs. Mary Coady, Dr. Carmia Borek, Ms. Gillian Bayne, Ms. Louise Guirguis.

**3<sup>rd</sup> Row:** Dr. Tien-Hsi Young, Dr. David Brenner, Dr. Kenshi Komatsu, Dr. Michael Marchese, Mr. John Pirro, Dr. Paul Kliauga, Dr. Howard Lieberman, Dr. Myles Astor, Mr. Joseph Smith, Mr. Nicholas Ludas, Dr. Tom Hei.

**4<sup>th</sup> Row:** Mr. Rudolph Gand, Dr. Paul Goldhagen, Dr. Marco Zaider, Mr. Stephen Marino, Dr. Richard Bird, Dr. Charles Geard, Mr. Steve Kushner, Mr. Gary Johnson.

**5<sup>th</sup> Row:** Dr. Gerhard Randers-Pehrson, Mr. Max Anchinovski.

### 1988

**Front Row** (l-r): Dr. Zhu-Ying He, Dr. Jaime Rubin, Dr. Laurie Roizin-Towle, Dr. Carmia Borek, Dr. Eric Hall, Ms. Louise Guirguis, Ms. Mary Coady, Ms. Michaela Delegianis, Ms. Miriam Battle.

**2<sup>nd</sup> Row:** Dr. Tom Hei, Dr. Myles Astor, Mr. Herbert Mason, Dr. David Brenner, Ms. Gloria Jenkins, Dr. Howard Lieberman, Dr. Marco Zaider, Ms. Maureen Laverty, Dr. Charles Geard, Dr. Paul Kliauga, Dr. Paul Goldhagen, Dr. Gerhard Randers-Pehrson, Mr. John Pirro, Mr. Stephen Marino, Mr. Nicholas Ludas, Mr. Freeman Suber, Mr. Augustinus Ong, Mr. Steven Kushner, Ms. Gillian Bayne, Mr. Dave Cassimy, Dr. Richard Miller.

### 1989

**Front Row** (l to r): Mrs. Marie Burchett, Dr. Zhu-Ying He, Dr. Jaime Rubin, Dr. Laurie Roizin-Towle, Dr. Eric Hall, Ms. Louise Guirguis, Mrs. Jeanne Kramer, Ms. Karen Evans, Ms. Marcia Richards.

**2<sup>nd</sup> Row** (l to r): Ms. Gloria Jenkins, Ms. Jacqueline Jones, Ms. Jiji Miranda, Ms. Maureen Laverty, Mr. John Pirro, Dr. Paul Kliauga, Mr. Steve Marino, Mr. Gilad Cohen, Dr. Marco Zaider, Dr. Tom Hei.

**3<sup>rd</sup> Row** (l to r): Mr. Herb Mason, Mr. Nick Ludas, Dr. David Brenner, Mr. Dave Cassimy, Dr. Myles Astor, Mr. Gary Johnson, Dr. Chang-Qing Piao, Dr. Roy Tishler, Dr. Howard Lieberman, Dr. Charles Geard, Mr. Augustinus Ong, Dr. Gerhard Randers-Pehrson, Dr. Richard Miller, Ms. Angela Reyes, Dr. Paul Goldhagen.

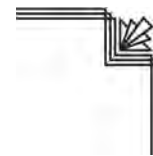
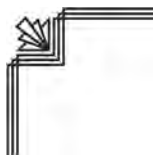
### 1990

**Front Row** (l to r): Dr. Jaime Rubin, Ms. Yvette Clausell, Dr. Diane Esposito, Dr. Laurie Roizin-Towle, Dr. Charles Geard, Dr. Eric Hall, Ms. Louise Guirguis, Dr. Carmia Borek, Mrs. Mary Coady, Mrs. Jeanne Kramer, Ms. Karen Evans.

**2<sup>nd</sup> Row** (l to r): Dr. Chang-Qing Piao, Dr. David Brenner, Mr. Jose Garcia, Ms. Jacqueline Jones, Mrs. Gloria Jenkins, Dr. Paul Kliauga, Mr. Gary Johnson, Mr. Nick Ludas, Mr. Kevin Hopkins, Dr. Tom Hei.

**3<sup>rd</sup> Row** (l to r): Dr. Marco Zaider, Dr. Myles Astor, Mr. Dave Cassimy, Mr. Gilad Cohen, Dr. Gerhard Randers-Pehrson, Ms. Angela Reyes, Dr. Richard Miller, Mr. Augustinus Ong, Dr. Howard Lieberman.





**1991**

**Front Row** (l to r): Dr. Laurie Towle, Dr. Charles Geard, Dr. Eric Hall, Ms. Louise Guirguis, Ms. Karen Evans.

**2<sup>nd</sup> Row** (l to r): Dr. Khalifah Sidik, Dr. Diane Esposito, Dr. Zhu-Ying He, Mrs. Mary Coady, Mrs. Jeanne Kramer.

**3<sup>rd</sup> Row** (l to r): Dr. David Brenner, Dr. Paul Kliauga, Dr. Jaime Rubin, Dr. Howard Lieberman, Ms. Julie Feinstein, Mrs. Marie Burchett, Dr. Gerhard Randers-Pehrson.

**4<sup>th</sup> Row** (l to r): Mr. Jose Garcia, Dr. Dave Cassimy, Mr. Gary Johnson, Dr. Tom Hei, Dr. Richard Miller, Ms. Gloria Jenkins, Mr. Nick Ludas, Dr. Marco Zaider, Mr. Marcus Geard, Mr. Chris Baird.

**5<sup>th</sup> Row** (l to r): Mr. Jesus Perez, Mr. Kevin Hopkins, Mr. Stephen Marino, Dr. Brad Loucas, Dr. Chang-Qing Piao, Dr. Yong Yu, Dr. Yuqi Zhao, Mr. Youping Huang, Mr. Albert Fung, Dr. Marjan Vracko Grobelsek.

**1992**

**Front Row** (l to r): Ms. Karen Evans, Mrs. Mary Coady, Mrs. Monique Rey, Dr. Eric Hall, Dr. Charles Geard, Mrs. Jeanne Kramer, Dr. Zhu-Ying He.

**2<sup>nd</sup> Row** (l to r): Dr. Tom Hei, Dr. Chang-Qing Piao, Ms. Gloria Jenkins, Ms. Yvette Clausell, Mrs. Marie Burchett, Dr. Marco Zaider, Dr. Gerhard Randers-Pehrson, Mr. Gary Johnson, Dr. Brad Loucas, Mr. Kevin Hopkins, Mr. Stephen Marino, Dr. Sewart Martin.

**3<sup>rd</sup> Row** (l to r): Dr. Howard Lieberman, Dr. Li Xun Zhu, Dr. Khalifah Sidik, Dr. Youg Yu, Dr. Yuqi Zhao, Dr. Marjan Vracko-Grobelsek, Mr. Albert Fung, Mr. Chris Baird, Mr. Marcus Geard, Dr. David Brenner.

**1993**

**Front Row** (l to r): Ms. Karen Evans, Mrs. Monique Rey, Dr. Eric Hall, Dr. Charles Geard, Mrs. Mary Coady, Dr. Jaime Rubin.

**2<sup>nd</sup> Row** (l to r): Dr. Tom Hei, Mrs. Gloria Jenkins, Mrs. Lakshmi Goriparthi, Dr. Chang-Qing Piao, Mr. Gary Johnson, Mr. Kevin Hopkins, Dr. Stewart Martin, Mr. Stephen Marino, Dr. C-Z Chen, Dr. Marco Zaider, Mr. Jose Garcia, Mr. Jesus Perez.

**3<sup>rd</sup> Row** (l to r): Dr. Howard Lieberman, Dr. Li Xun Zhu, Dr. Marjan Vracko-Grobelsek, Dr. Gerhard Randers-Pehrson, Mr. Augustinus Ong, Dr. Richard Miller, Mr. Nick Ludas, Dr. David Brenner.

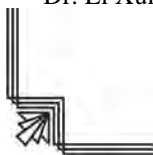
**1994**

**Front Row** (l to r): Ms. Karen Evans, Mrs. Mary Coady, Dr. Eric Hall, Dr. Charles Geard, Dr. Jaime Rubin.

**2<sup>nd</sup> Row** (l to r): Dr. Tom Hei, Mrs. Gloria Jenkins, Mrs. Lakshmi Goriparthi, Dr. Tej Pandita, Mr. Augustinus Ong, Mr. Dave Cassimy, Mr. Stephen Marino.

**3<sup>rd</sup> Row** (l to r): Dr. Haiying Hang, Dr. C-Z Chen, Dr. Brad Loucas, Mr. David Palmer, Dr. Paul Kliauga, Mr. Kevin Hopkins, Dr. Stewart Martin, Dr. Youping Huang.

**4<sup>th</sup> Row** (l to r): Dr. Howard Lieberman, Dr. Chang-Qing Piao, Dr. Keiji Suzuki, Mr. Nick Ludas, Mr. Gary Johnson, Dr. Li Xun Zhu, Dr. Ryuichi Okayasu, Dr. David Brenner.





**1995**

**Front Row** (l to r): Ms. Karen Evans, Ms. Monique Rey, Dr. Eric Hall, Dr. Charles Geard, Mrs. Mary Coady.

**2<sup>nd</sup> Row** (l to r): Dr. Marco Zaider, Dr. Howard Lieberman, Dr. Si-Xian Liu, Mrs. Lakshmi Goriparthi, Mrs. Gloria Jenkins, Dr. Paul Kliauga, Dr. Brad Loucas, Mr. Gary Johnson, Dr. Gerhard Randers-Pehrson, Mr. Stephen Marino, Mr. Kevin Hopkins, Dr. Li Xun Zhu, Dr. Tom Hei, Dr. David Brenner.

**3<sup>rd</sup> Row** (l to r): Dr. Chang-Qing Piao, Mr. Giulio Magrin, Dr. Scott Kahn, Dr. Yoshihiko Onizuka, Dr. Li Xun Zhu, Dr. Haiying Hang, Dr. Richard Miller, Ms. Noreen Duddy, Mr. Augustinus Ong.

**1996**

**Front Row** (l to r): Dr. Eileen Rakovitch, Mrs. Mary Coady, Dr. Eric Hall, Dr. Charles Geard, Ms. Monique Rey, Dr. Jaime Rubin.

**2<sup>nd</sup> Row** (l to r): Dr. Huijie Feng, Mr. Kevin Hopkins, Ms. Karen Evans, Ms. Marcia Richards, Dr. Wilfredo Mellado, Dr. Tej Pandita, Mr. Stephen Marino, Dr. Paul Kliauga, Mr. Gary Johnson, Dr. Scott Kahn, Dr. Roberto Antonacci, Dr. Satin Sawant, Ms. Diana Morrison, Dr. Tom Hei, Dr. Si-Xian Liu.

**3<sup>rd</sup> Row** (l to r): Dr. Richard Miller, Dr. Marco Zaider, Dr. Howard Lieberman, Dr. Haiying Hang, Dr. Lubomir Smilenov, Dr. Ding Bang Xu, Dr. Li-Jun Wu, Dr. Youping Huang, Dr. David Brenner.

**1997**

**Front Row** (l to r): Our Summer Students: Mr. Alan Lau, Columbia College, Mr. Alex Hu, Larchmont H.S., Mr. Raheel Ansari, Benjamin Cardozo H.S., Miss Alicia Pilgrim, Delaware State University, Miss Elizabeth Kim, School of Public Health, Columbia University, Mr. Yan Zheng, University of Wisconsin-Madison.

**2<sup>nd</sup> Row** (l to r): Ms. Karen Evans, Ms. Monique Rey, Dr. Eric Hall, Dr. Charles Geard, Dr. Jaime Rubin, Dr. Si-Xian Liu.

**3<sup>rd</sup> Row** (l to r): Dr. Marco Zaider, Dr. Haiying Hang, Mrs. Lakshmi Goriparthi, Dr. Richard Miller, Mr. David Cuniberti, Dr. Joseph Bargellini, Ms. Sarah Rauth, Dr. Dusan Srdoc, Dr. Andrew Risdale, Mr. Wei Zheng, Dr. Chang-Qing Piao, Dr. Howard Lieberman, Dr. Tom Hei.

**4<sup>th</sup> Row** (l to r): Mr. Gary Johnson, Mr. Arthur Geen, Dr. Tej Pandita, Dr. Willy Mellado, Dr. Lubomir Smilenov, Mr. Kevin Hopkins, Dr. Gerhard Randers-Pehrson, Dr. Li-Jun Wu, Dr. Satin Sawant, Dr. David Brenner.

**1998**

**Front Row** (l to r): Ms. Heidy Hernandez, Ms. Mary Coady, Dr. David Brenner, Dr. Charles Geard, Dr. Eric Hall, Ms. Monique Rey, Dr. Gloria Calaf, Dr. Jaime Rubin.

**2<sup>nd</sup> Row** (l to r): Mr. Gary Johnson, Mr. Carl Elliston, Ms. Gloria Jenkins, Dr. Debasish Roy, Ms. Whitney Clavin, Mr. Kevin Hopkins, Mr. David Cuniberti, Dr. Chang-Qing Piao, Mr. Wei Zheng, Dr. Howard Lieberman, Dr. Si-Xian Liu, Dr. Tom Hei.

**3<sup>rd</sup> Row** (l to r): Dr. Tej Pandita, Dr. Kirby Johnson, Dr. Haiying Hang, Ms. Mei Wang, Dr. Lubomir Smilenov, Dr. Gerhard Randers-Pehrson, Mr. Stephen Marino, Dr. Yong-Liang Zhao, Dr. Satin Sawant, Dr. Hongning Zhou, Ms. An Xu.



**1999**

**Front Row** (l to r): Ms. Monique Rey, Dr. Tom Hei, Dr. Charles Geard, Dr. Eric Hall, Dr. David Brenner, Dr. Howard Lieberman, Ms. Mary Coady.

**2<sup>nd</sup> Row** (l to r): Ms. Heidy Hernandez, Dr. Jaime Rubin, Mr. David Cuniberti, Ms. An Xu, Ms. Sonu Dhar, Ms. Gloria Jenkins, Ms. Mei Wang, Ms. Sarah Rauth, Dr. Gloria Calaf, Ms. Jian-Fen Guo, Dr. Si-Xian Liu, Ms. Annerys Rodriguez, Ms. Diana Morrison.

**3<sup>rd</sup> Row** (l to r): Dr. Tej Pandita, Mr. Jose Garcia, Dr. Adayabalam Balajee, Mr. Michael Chaplin, Dr. Satin Sawant, Dr. Haijun Song, Dr. Haiying Hang, Dr. Alexander Dymnikov, Dr. Chang-Qing Piao, Dr. Hongning Zhou, Mr. Wei Zheng.

**4<sup>th</sup> Row** (l to r): Dr. Yuxin Yin, Mr. Carl Elliston, Mr. Stephen Marino, Dr. Lubomir Smilenov, Dr. Brian Ponnaiya, Dr. Gerhard Randers-Pehrson, Mr. Kevin Hopkins, Dr. Masao Suzuki, Mr. Francois Lueg-Althoff, Mr. Robert Archigian.

**2000**

**Front Row** (l to r): Ms. Monique Rey, Dr. Tom Hei, Dr. Charles Geard, Dr. Eric Hall, Dr. David Brenner, Dr. Howard Lieberman, Ms. Mary Coady.

**2<sup>nd</sup> Row** (l to r): Dr. Tej Pandita, Dr. Yuxin Yin, Ms. Diana Morrison, Ms. Heidy Hernandez, Dr. Jaime Rubin, Ms. Sonu Dhar, Ms. An Xu, Dr. Gloria Calaf, Dr. Metka Filipic, Ms. Fei Song, Ms. C. Yuxin Liu, Ms. Jian-Fen Guo.

**3<sup>rd</sup> Row** (l to r): Mr. Gary Johnson, Mr. David Cuniberti, Mr. Robert Archigian, Dr. Lubomir Smilenov, Mr. Wei Zhang, Mr. Ronald Baker, Ms. Gloria Jenkins, Dr. Haiying Hang.

**4<sup>th</sup> Row** (l to r): Dr. Adayabalam Balajee, Dr. Prakash Hande, Dr. Hongning Zhou, Dr. Debashish Roy, Mr. Mutian Zhang, Mr. Stephen Marino, Dr. Satin Sawant, Dr. Alan Bigelow, Dr. Masao Suzuki.

**5<sup>th</sup> Row** (l to r): Dr. Arun Gupta, Dr. Girdhar Sharma, Mr. Carl Elliston, Mr. Kevin Hopkins, Dr. Gerhard Randers-Pehrson, Dr. Brian Ponnaiya, Dr. Yong-Liang Zhao.

**2001**

**Front Row** (l to r): Ms. Monique Rey, Dr. Tom Hei, Dr. Charles Geard, Dr. Eric Hall, Dr. David Brenner, Dr. Howard Lieberman, Ms. Mary Coady.

**2<sup>nd</sup> Row** (l to r): Ms. Yuxin C. Liu, Ms. Sonu Dhar, Dr. Dr. Su-Xian Liu, Ms. Xiaojian Wang, Dr. Gloria Calaf, Dr. Aiping Zhu, Dr. Alexander Dymnikov, Dr. Alan Bigelow, Ms. Heidy Hernandez, Ms. Diana Morrison.

**3<sup>rd</sup> Row** (l to r): Dr. Tej Pandita, Mr. Gary Johnson, Dr. Jaime Rubin, Mr. Robert Archigian, Mr. David Cuniberti, Mr. Carl Elliston, Ms. Gloria Jenkins-Baker, Dr. Gerhard Randers-Pehrson, Dr. Girdhar Sharma, Mr. Kevin Hopkins, Dr. Adayabalam Balajee.

**Back Row** (l to r): Dr. Haiying Hang, Dr. Brian Ponnaiya, Dr. Li Liu, Mr. Moshe Friedman, Dr. Debasish Roy, Dr. Yuxin Yin, Dr. Prakash Hande, Dr. Arun Gupta, Dr. Hongning Zhou, Dr. Lubomir Smilenov, Mr. Mutian Zhang, Mr. Stephen Marino, Dr. Yong-Liang Zhao, Chang-Qing Piao.

**2002**

**Front Row** (l to r): Ms. Diana Morrison, Dr. David Brenner, Dr. Howard Lieberman, Ms. Monique Rey, Dr. Eric Hall, Ms. Mary Coady, Dr. Charles Geard, Dr. Tom Hei.

**2<sup>nd</sup> Row** (l to r): Dr. Yuxin C. Liu, Mr. Gary Johnson, Dr. Su-Xian Liu, Ms. Alison Groome, Mrs. Cui-Xia Kuan, Dr. Peng He, Ms. Heidy Hernandez, Ms. Xiaojian Wang, Ms. Marni Hall, Dr. Aiping Zhu, Dr. Gloria Calaf, Ms. Gloria Jenkins-Baker, Dr. Catherine Mitchell, Dr. Alan Bigelow, Ms. Annerys Rodriguez, Mr. Kurt Michel.

**3<sup>rd</sup> Row** (l to R): Mr. Carl Elliston, Dr. Yuxin Yin, Dr. Haiying Hang, Mr. Robert Archigian, Dr. Debasish Roy, Mr. Ronald Baker, Dr. Stephen Mitchell, Mr. David Cuniberti, Dr. Chang-Qing Piao, Dr. Jianli Wang, Dr. Fu-Ru Zhan, Dr. Adayabalam Balajee.

**Back Row** (l to r): Mr. Moshe Friedman, Dr. Lubomir Smilenov, Dr. Rudranath Persaud, Dr. Brian Ponnaiya, Mr. Stephen Marino, Mr. Kevin Hopkins, Mr. Gregory Ross, Dr. Gerhard Randers-Pehrson, Dr. Oleg Belyakov, Dr. Yong-Liang Zhao, Dr. Hongning Zhou.



**2003**

**Front Row** (l to r): Dr. Tom Hei, Dr. Charles Geard, Ms. Monique Rey, Dr. Eric Hall, Ms. Mary Coady, Dr. David Brenner, Dr. Howard Lieberman, Dr. Sally Amundson.

**2<sup>nd</sup> Row** (l to r): Ms. Josephine Tsakok, Mr. Gary Johnson, Dr. Yuxin Yi, Mrs. Cui-Xia Kuan, Dr. Peng He, Ms. Jessica Berenguer, Dr. Corrine Leloup, Dr. Catherine Mitchell, Dr. Su-Xian Liu, Ms. Diana Morrison, Ms. Heidy Hernandez, Mr. Ronald Baker.

**3<sup>rd</sup> Row** (l to r): Dr. Brian Ponnaiya, Dr. Jaime Rubin, Ms. Xiaojian Wang, Dr. Aiping Zhu, Ms. Sarah Baker, Dr. Alan Bigelow, Dr. Stephen Mitchell, Dr. Vladimir Ivanov, Dr. Yong-Liang Zhao, Ms. Gloria Jenkins-Baker.

**4<sup>th</sup> Row** (l to r): Dr. Rajamanickam Baskar, Dr. Adayabalam Balajee, Dr. Haiying Hang, Mr. Robert Archigian, Dr. Lubomir Smilenov, Mr. David Cuniberti, Dr. Jianli Wang, Dr. Chang-Qing Piao.

**Back Row** (l to r): Mr. Moshe Friedman, Dr. Fu-ru Ahan, Dr. Hongning Zhou, Mr. Joseph Gillespie, Dr. Rudranath Persaud, Mr. Carl Elliston, Dr. Gerhard Randers-Pehrson, Mr. Gregory Ross, Mr. Stephen Marino, Dr. Guy Garty, Mr. Kevin Hopkins.

**2004**

**Front Row** (l to r): Dr. Howard Lieberman, Dr. Tom Hei, Ms. Monique Rey, Dr. Eric Hall, Ms. Mary Coady, Dr. Charles Geard, Dr. David Brenner, Dr. Sally Amundson.

**2<sup>nd</sup> Row** (l to r): Dr. Jaime Rubin, Dr. Wenhong Shen, Mrs. Cui-Xia Kuan, Ms. Sarah Huang, Ms. Xiaojian Wang, Dr. Corrine Leloup, Dr. Aiping Zhu, Mr. David Cuniberti, Ms. Gloria Jenkins-Baker, Dr. Catherine Mitchell, Dr. Su-Xian Liu, Ms. Heidy Hernandez, Ms. Diana Morrison, Dr. Hongning Zhou, Mr. Alan Wong, Dr. Koon Siew Lai, Mr. Gary Johnson.

**3<sup>rd</sup> Row** (l to r): Dr. Rudranath Persaud, Mr. Ronald Baker, Dr. Adayabalam Balajee, Dr. Genze Shao, Dr. Jianli Wang, Mr. Jaeyong Ahn, Dr. Alan Bigelow, Dr. Guy Garty, Dr. Chang-Qing Piao, Dr. Lubomir Smilenov, Mr. Joseph Gillespie, Dr. Vladimir Ivanov.

**Back Row** (l to r): Dr. Yuxin Yin, Dr. Yong-Liang Zhao, Mr. Moshe Friedman, Dr. Rajamanickam Baskar, Mr. Robert Archigian, Mr. Kevin Hopkins, Mr. Gregory Ross, Mr. Carl Elliston, Dr. Gerhard Randers-Pehrson, Dr. Giuseppe Schettino, Dr. Stephen Mitchell, Mr. Stephen Marino, Dr. Brian Ponnaiya.

**2005**

**Front Row** (l to r): Ms. Monique Rey, Dr. Sally Amundson, Dr. Tom Hei, Dr. Charles Geard, Dr. Eric Hall, Dr. David Brenner, Dr. Howard Lieberman, Ms. Mary Coady, Ms. Diana Morrison, Ms. Angela Lugo.

**2<sup>nd</sup> Row** (l to r): Dr. Adayabalam Balajee, Dr. Naved Alam, Ms. Jingjing Wu, Dr. Gengyun Wen, Dr. Wenhong Shen, Dr. Yu-Chen Lien, Mrs. Cui-Xia Kuan, Dr. Yanrong Su, Ms. Xiaojian Wang, Dr. Aiping Zhu, Ms. Gloria Jenkins-Baker, Dr. Corrine Leloup, Dr. An Xu, Dr. Aparajita Dutta, Dr. Shanaz Ghandhi, Ms. Sarah Huang, Ms. Anne Sutthoff, Mr. David Cuniberti, Ms. Heidy Hernandez, Mr. Yun Fei Chai, Dr. Vladimir Ivanov, Mr. Carl Elliston, Mr. Gary Johnson, Dr. Brian Ponnaiya.

**3<sup>rd</sup> Row** (l to r): Dr. Yuxin Yin, Dr. Genze Shao, Dr. Hongning Zhou, Dr. Shenbing Gu, Dr. Gengyun Wen, Dr. Guy Garty, Dr. Alan Bigelow, Mr. Jaeyong Ahn, Dr. Peter Grabham, Mr. Stephen Marino, Mr. Robert Archigian.

**Back Row** (l to r): Mr. Moshe Friedman, Dr. Igor Shuryak, Dr. Burong Hu, Dr. Lubomir Smilenov, Mr. Gregory Ross, Mr. Kevin Hopkins, Dr. Giuseppe Schettino, Dr. Michael Partridge, Dr. Tomoo Funayama, Dr. Gerhard Randers-Pehrson, Dr. Yong-Liang Zhao.

**2006**

**Front Row** (l to r): Dr. Gerhard Randers-Pehrson, Dr. Sally Amundson, Dr. Tom Hei, Dr. Charles Geard, Dr. Eric Hall, Dr. David Brenner, Dr. Howard Lieberman, Ms. Monique Rey.

**2<sup>nd</sup> Row** (l to r): Mrs. Cui-Xia Kuan, Dr. Natatia Sotnik, Dr. Wenhong Shen, Dr. Shanaz Ghandhi, Dr. Aparajita Dutta, Bingyan Li, Ms. Sarah Huang, Dr. Aiping Zhu, Ms. Xiaojian Wang, Dr. Corinne Leloup, Ms. Gloria Jenkins-Baker, Dr. Yu-Chen Lien, Ms. Anne Sutthoff, Ms. Sasha Lyulko, Ms. Jing Nie, Dr. An Xu, Dr. Jarah Meador, Ms. Yvette Acevedo, Dr. Yanrong Su, Ms. Angela Lugo, Dr. Vladimir Ivanov, Ms. Heidy Hernandez, Mr. Gary Johnson.

**3<sup>rd</sup> Row** (l to r): Dr. Ye Zhang, Mr. David Cunierti, Dr. Yuxin Yin, Dr. Lubomir Smilenov, Dr. Yong-Liang Zhao, Dr. Adayabalam Balajee, Dr. Hongning Zhou, Dr. Guy Garty, Dr. Guangming Zhou, Dr. Alan Bigelow, Dr. Yanping Xu.

**Back Row** (l to r): Mr. Yunfei Chai, Mr. Carl Elliston, Dr. Gengyun Wen, Mr. Robert Morton, Mr. Dimitar Zlatev, Dr. Andrew Harken, Dr. Brian Ponnaiya, Mr. Stephen Marino, Dr. Burong Hu, Mr. Kevin Hopkins.



**2007**

**Front Row** (l to r): Dr. Gerhard Randers-Pehrson, Dr. Sally Amundson, Dr. Tom Hei, Dr. Charles Geard, Dr. Eric Hall, Dr. David Brenner, Dr. Howard Lieberman, Dr. Yuxin Yin, Ms. Monique Rey.

**2<sup>nd</sup> Row** (l to r): Ms. Jennifer Maerki, Ms. Margaret Zhu, Mrs. Cui-Xia Kuan, Ms. Marisol Cruz, Dr. Corinne Leloup, Ms. Xiaojian Wang, Ms. Lilian Oling, Ms. Jing Nie, Dr. Mei Hong, Dr. Ling Han, Dr. Helen Turner, Mr. Gary Johnson.

**3<sup>rd</sup> Row** (l to r): Dr. Alexander Kofman, Dr. Alexandre Mezentsev, Dr. Shanaz Gandhi, Ms. Angela Lugo, Ms. Anne Sutthoff, Dr. Aiping Zhu, Ms. Yvette Acevedo, Ms. Jinshuang Lu, Mr. Kevin Hopkins, Dr. Chuanxin Huang, Dr. Burong Hu, Dr. Yongliang Zhao, Dr. Lubomir Smilenov, Dr. Vladimir Ivanov.

**4<sup>th</sup> Row** (l to r): Mr. Stephen Marino, Dr. Adayabalam Balajee, Mr. Dennis Keaveney, Dr. Alan Bigelow, Mr. Benjamin Yaghoubian, Dr. Sunirmal Paul, Dr. Guy Garty, Dr. Peter Grabham, Dr. Yanping Xu, Mr. Yunfei Chai.

**Back Row** (l to r): Dr. Brian Ponnaiya, Mr. David Cuniberti, Dr. Hongning Zhou, Dr. Michael Partridge, Dr. Andrew Harkin, Dr. Igor Shuryak, Mr. Robert Morton, Mr. Carl Elliston, Dr. Kenichi Tanaka, Dr. Gengyun Wen.

**2008**

**Front Row** (l to r): Dr. Gerhard Randers-Pehrson, Dr. Sally Amundson, Dr. Charles Geard, Dr. Tom Hei, Dr. David Brenner, Dr. Eric Hall, Dr. Howard Lieberman, Ms. Monique Rey.

**2<sup>nd</sup> Row** (l to r): Mr. Gary Johnson, Dr. Wenhong Shen, Mr. Yunfei Chai, Ms. Sarah Huang, Mrs. Cui-Xia Kuan, Ms. Suping Zhang, Ms. Tingting Gu, Dr. Corinne Leloup, Ms. Lilian Oling, Dr. Bo Shen, Dr. Aiping Zhu, Dr. Jarah Meador, Ms. Sasha Lyulko, Ms. Margaret Zhu, Ms. Angela Lugo, Dr. Antonella Bertucci.

**3<sup>rd</sup> Row** (l to r): Dr. Peter Grabham, Ms. Jinshuang Lu, Dr. Guy Garty, Dr. Ping Lu, Dr. Vladimir Ivanov.

**4<sup>th</sup> Row** (l to r): Dr. Mei Hong, Mr. David Cuniberti, Dr. Sunirmal Paul, Dr. Hongning Zhou, Ms. Xiaojian Wang, Dr. Alexandre Mezentsev, Dr. Shanaz Gandhi, Dr. Alan Bigelow, Ms. Yvette Acevedo, Mr. Dennis Keaveney.

**Back Row** (l to r): Dr. Yongliang Zhao, Mr. Ying Kong, Mr. Stephen Marino, Dr. Lubomir Smilenov, Mr. Kevin Hopkins, Dr. Thomas Templin, Dr. Igor Shuryak, Dr. Andrew Harken, Mr. Robert Morton.

**2009**

**Front Row** (l to r): Ms. Monique Rey, Dr. Sally Amundson, Dr. Tom Hei, Dr. David Brenner, Dr. Howard Lieberman, Dr. Charles Geard, Dr. Gerhard Randers-Pehrson.

**2<sup>nd</sup> Row** (l to r): Ms. Angela Lugo, Ms. Margaret Zhu, Mrs. Cui-Xia Kuan, Dr. Congju Chen, Ms. Lilian Oling, Dr. Corinne Leloup, Ms. Sasha Lyulko, Dr. Jarah Meador, Ms. Maria Taveras, Dr. Antonella Bertucci, Ms. Janice David.

**3<sup>rd</sup> Row** (l to r): Mr. Gary Johnson, Dr. Barbara Szolc, Ms. Annerys Rodriguez, Ms. Yvette Acevedo, Dr. Aiping Zhu, Ms. Jinshuang Lu, Dr. Helen Turner, Dr. Preety Sharma, Dr. Sarah Huang, Dr. Peter Grabham, Dr. Shanaz Gandhi, Dr. Vladimir Ivanov, Dr. Erik Young.

**4<sup>th</sup> Row** (l to r): Dr. Yongliang Zhao, Dr. Sunirmal Paul, Mr. Joshua Bernstock, Dr. Hongning Zhou, Mr. David Cuniberti, Dr. Guy Garty, Dr. Alan Bigelow, Dr. Ping Lu, Mr. Lihua Ming, Mr. Yunfei Chai.

**Back Row** (l to r): Dr. Igor Shuryak, Dr. Adayabalam Balajee, Dr. Thomas Templin, Mr. Kevin Hopkins, Mr. Carl Elliston, Dr. Lubomir Smilenov, Dr. Andrew Harken, Dr. Brian Ponnaiya, Mr. Robert Morton, Dr. Yanping Xu, Dr. Gengyun Wen.

**2010**

**Front Row** (l to r): Dr. Sally Amundson, Dr. Charles Geard, Dr. Tom Hei, Dr. David Brenner, Dr. Howard Lieberman, Dr. Gerhard Randers-Pehrson.

**2<sup>nd</sup> Row** (l to r): Ms. Annerys Rodriguez, Dr. Shanaz Gandhi, Dr. Helen Turner, Ms. Angela Lugo, Dr. Corinne Leloup, Ms. Lilian Oling, Dr. Congju Chen, Ms. Margaret Zhu, Ms. Sasha Lyulko, Ms. Yvette Acevedo, Mr. Hamin Jeon, Dr. Gengyun Wen, Dr. Vladimir Ivanov.

**3<sup>rd</sup> Row** (l to r): Mr. Gary Johnson, Dr. Winston Liao, Dr. Alan Bigelow, Dr. Guy Garty, Mr. Vatche Zohrabian, Dr. Constantinos Broustas, Dr. Peter Grabham, Mr. Joshua Bernstock, Dr. Hongning Zhou.

**Back Row** (l to r): Mr. Dennis Keaveney, Mr. Roy Lam, Dr. Hongbo Fang, Dr. Lubomir Smilenov, Mr. Stephen Marino, Dr. Andrew Harken, Dr. Igor Shuryak, Mr. Kevin Hopkins, Dr. Erik Young, Mr. David Cuniberti.



**2011**

**Front Row** (l-r): Dr. Eric Hall, Dr. Sally Amundson, Dr. Tom Hei, Dr. David Brenner, Dr. Howard Lieberman, Dr. Charles Geard, Ms. Monique Rey.

**2<sup>nd</sup> Row:** Mr. Gary Johnson, Dr. Preety Sharma, Ms. Erica Pena, Dr. Antonella Bertucci, Ms. Maria Taveras, Dr. Congju Chen, Ms. Lilian Oling, Dr. Jarah Meador, Dr. Sasha Lyulko, Dr. Manuella Buonanno, Dr. Bo Zhang, Dr. Ana Vasileva, Ms. Angela Lugo, Dr. Peter Grabham.

**3<sup>rd</sup> Row:** Mr. Radek Pieniazek, Dr. Constantinos Broustas, Ms. Annerys Rodriguez, Dr. Adayabalam Balajee, Dr. Helen Turner, Dr. Shanaz Ghandhi, Dr. Vladimir Ivanov, Dr. Lubomir Smilenov.

**Back Row:** Mr. Roy Lam, Dr. Sunirmal Paul, Dr. Thomas Templin, Mr. David Cuniberti, Mr. Stephen Marino, Dr. Mikhail Repin, Dr. Igor Shuryak, Dr. Guy Garty, Mr. Robert Morton, Dr. Alan Bigelow, Dr. Andrew Harkin, Dr. Hongning Zhou, Dr. Erik Young, Mr. Jay Perrier, Mr. Michael Grad, Dr. Winston Liao, Mr. Kevin Hopkins, Dr. Qingping Cui.

**2012**

**Front Row** (l-r): Dr. Peter Grabham, Dr. Gerhard Randers-Pehrson, Dr. Sally Amundson, Dr. Tom Hei, Dr. David Brenner, Dr. Howard Lieberman, Ms. Monique Rey, Dr. Lubomir Smilenov.

**2<sup>nd</sup> Row:** Mr. Gary Johnson, Ms. Annerys Rodriguez, Dr. Charles Geard, Dr. Helen Turner, Li Wang, Dr. Preety Sharma, Ms. Erica Pena, Ms. Maria Taveras, Ms. Cui-Xia Kuan, Ms. Lilian Oling, Dr. Bo Zhang, Dr. Sasha Lyulko, Dr. Ana Vasileva, Dr. Mikhail Repin, Mr. David Cuniberti, Dr. Vladimir Ivanov, Dr. Manuella Buonanno, Mr. Stephen Marino, Mr. Roy Lam.

**3<sup>rd</sup> Row:** Dr. Sunirmal Paul, Dr. Guy Garty, Dr. Xue-Zhong Gong, Mr. Haseeb Durrani, Dr. Adayabalam Balajee, Dr. Alan Bigelow, Mr. Jay Perrier, Dr. Yanping Xu, Dr. Stanley Lue.

**Back Row:** Youping Sun, Dr. Igor Shuryak, Dr. Constantinos Broustas, Dr. Sunil Panigrahi, Dr. Erik Young, Mr. Kevin Hopkins, Dr. Brian Ponnaiya, Mr. Robert Morton, Mr. Radek Pieniazek.

**2013**

**Front Row** (l-r): Ms. Erica Pena, Dr. Gerhard Randers-Pehrson, Dr. Tom Hei, Dr. David Brenner, Dr. Howard Lieberman, Dr. Sally Amundson, Dr. Eric Hall.

**2<sup>nd</sup> Row:** Mr. Gary Johnson, Ms. Annerys Rodriguez, Ms. Angela Lugo, Dr. Helen Turner, Ms. Maria Taveras, Ms. Cui-Xia Kuan, Dr. Ana Vasileva, Dr. Congju Chen, Dr. Jinhua Wu, Dr. Manuella Buonanno, Mr. Jay Perrier.

**3<sup>rd</sup> Row:** Mr. Haseeb Durrani, Dr. Chi Zhang, Dr. Kunal Chaudhary, Dr. Guy Garty, Mr. Radek Pieniazek, Dr. Peter Grabham, Dr. Alan Bigelow, Mr. Kevin Hopkins.

**Back Row:** Youping Sun, Dr. Hongning Zhou, Dr. Constantinos Broustas, Dr. Sunil Panigrahi, Mr. Robert Morton, Dr. Andrew Harkin, Dr. Lubomir Smilenov, Dr. David Welch.

**2014**

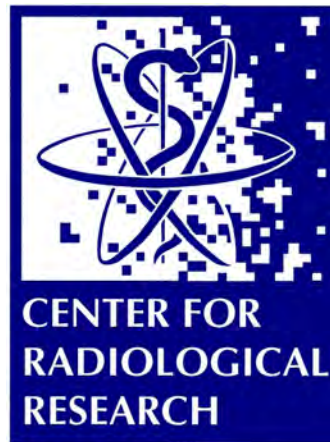
**Front Row** (l-r): Dr. Gerhard Randers-Pehrson, Dr. Sally Amundson, Dr. Eric Hall, Dr. David Brenner, Dr. Tom Hei, Dr. Howard Lieberman, Ms. Margaret Zhu.

**2<sup>nd</sup> Row:** Mr. Gary Johnson, Dr. Constantinos Broustas, Dr. Charles Geard, Ms. Sherry Yin, Dr. Li Wang, Ms. Mashkura Chowdhury, Dr. Preety Sharma, Dr. Jinhua (Dannis) Wu, Dr. Shanaz Ghandhi, Ms. Cui-Xia Kuan, Dr. Stanley Lue, Ms. Maria Taveras, Dr. Helen Turner, Ms. Margaret German, Dr. Peter Grabham, Mr. Dennis Keaveney, Ms. Angela Lugo, Dr. Lubomir Smilenov.

**Back Row:** Youping Sun (Radiation Oncology), Mr. Dennis Farrell, Mr. Robert Morton, Dr. Sunil Panigrahi, Mr. David Cuniberti, Dr. Mikhail Repin, Dr. Kunal Chaudhary (Radiation Oncology), Dr. Andrew Harkin, Mr. Stephen Marino, Dr. Igor Shuryak, Dr. Guy Garty, Mr. Kevin Hopkins, Dr. Alan Bigelow, Dr. Yanping Xu, Dr. Manuella Buonanno, Dr. Brian Ponnaiya, Mr. Haseeb Durrani.



# MICROBEAM AND SINGLE CELL STUDIES



# The Super Microbeam at RARAF

*Gerhard Randers-Pehrson, Andrew Harken, Guy Garty, Alan Bigelow, Yanping Xu, David Welch, Brian Ponnaiya, Dennis Farrell, Manuela Buonanno, Leah Turner<sup>a</sup>, and David J. Brenner*

## Introduction

The Super Microbeam at RARAF is a combined system to deliver a charged particle microbeam with a beam spot diameter of 75 nm in combination with a super resolution microscope with 75 nm imaging resolution. The charged particle beam will be focused with a superconducting solenoid magnet and will be installed in two phases. Phase 1 is the basic installation of the solenoid as a single lens, which will produce an initial beam size of 250 nm. Phase 2 is the installation of a double triplet electrostatic lens set as the initial focusing of the solenoid, which will allow for the final 75 nm beam spot. The super resolution microscope builds off our existing multi photon microscope with a second Stimulated Emission Depletion (STED) laser to suppress fluorescence into a sub-resolution spot allowing for super resolution imaging at 75 nm.

## The superconducting solenoid arrival and test installation

The Super microbeam has taken several steps toward the development of a 75 nm charged particle beam. The

main work this year was the receipt and test installation of the superconducting 7 Tesla solenoid in the microbeam laboratory.

This new system requires the use of a more substantial optical table to bear the weight of the magnet system and the other components of the microbeam. Figure 1 is a series of pictures of the optical table being lifted down to the microbeam level and being placed onto the stand legs in the microbeam lab.

Once the table was in place, we were able to place the solenoid onto the table. Figure 2 is a series of pictures of the RARAF staff delicately lifting and placing the new solenoid on the new optical table. The superconducting solenoid is cooled using a cryogen-free compressed helium gas cooling system. The vertical stack on the right side of the solenoid in Figure 2D is the cooling head. The helium compressor will be housed in the basement to prevent the vibration from affecting the microbeam.

The magnet has field restricting steel plates above and below the solenoid to limit the stray fields that may

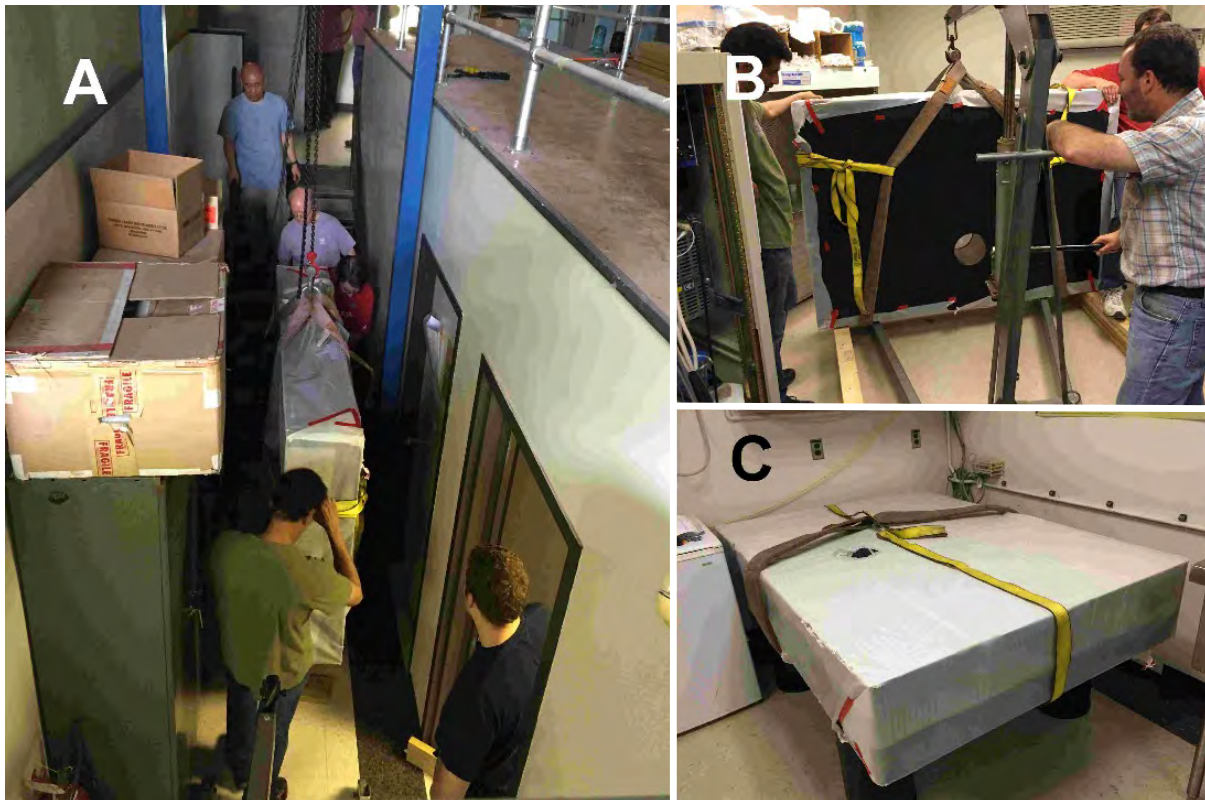


**Figure 1.** A) Lifting the table down to the Microbeam II room on the second mezzanine level of RARAF. B) Preparing to set the table onto the support legs in the microbeam lab. C) Table installed in corner location for initial testing of the super conducting solenoid.

<sup>a</sup>REU Summer Student from Lehigh University, Bethlehem, PA



**Figure 2.** A) Dr. Harken and Mr. Farrell centering the bottom field restriction plate on the table beam pipe through hole. B) Delicately lifting the solenoid down to the second mezzanine level at RARAF. C) Drs. Randers-Pehrson and Bigelow positioning the solenoid on the restrictor plate and table. D) Alignment of the solenoid to the bottom restrictor plate. E) Final testing assembly of the solenoid and both restrictor plates with cooling lines, monitoring sensors, current lines, and vacuum support connected.

interact with other components of the system. The magnet had not been tested with the steel restriction plates. This changed the eddy field forces on the solenoid such that it required several training quenches to obtain the full 7 Tesla field promised by the manufacturer. While not expected to be a significant issue, this will need to be monitored as we continue to move forward with equipment installation, as it will affect the fields and could cause further quenching.

The design and manufacturing of parts for the transfer of the microbeam endstation from the electrostatic microbeam to the solenoid microbeam is continuing. While very similar in its construction, the significant change in height and center reach of the solenoid system

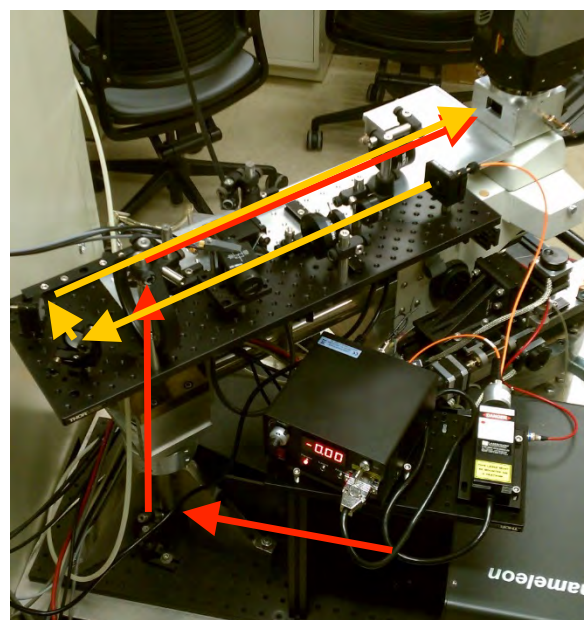


**Figure 3.** STED optics platform combined with multi-photon microscope on the back of the microbeam endstation. Arrows show light pathways for the multi-photon laser (red) and the STED laser (yellow).

will require several modifications of the endstation technology.

### Super resolution microscope laser alignment and testing

The second half of the super microbeam is the super resolution imaging. This past year has seen many improvements in the optical pathway for the STED beam as well as the receipt of the 2W continuous wave laser for the formation of the STED suppression beam.

The most challenging part of developing the STED imaging system is the co-alignment of the STED suppression beam with that of the multi-photon microscope, our excitation beam. This alignment is not only required in the laboratory optical space on the beam introduction benches, but also microscopically in the focal plane of the endstation microscope. The STED suppression donut not only needs to be aligned in the 2-D imaging plane of the microscope, but must also match the excitation spot in the z-axis as well. This total alignment required the matching of the transmission optics combining the beams externally on the bench in combination with any achromatic effects from the optics in the endstation microscope.

While the initial alignment has been performed using the low power alignment laser, no imaging has yet been performed, as the alignment laser does not have sufficient power to suppress the fluorescence. The installation of the higher power 2W laser will make imaging possible in early 2016, as we prepare the endstation for the transfer. The initial alignment procedures, determined with the low power laser, will make the minor adjustments needed for

the high power laser alignment both easier and safer for the operator.

**Summary**

We plan to have the Phase 1 (250 nm beam spot) Super Microbeam operational for the Microbeam Training Course in May. The design of the custom vacuum system

for the electrostatic lenses for Phase 2 (75 nm beam spot) is also underway and will begin construction when Phase 1 becomes operational. The STED super resolution imaging will become available in Spring of 2016, beginning with the imaging and targeting tests needed to prepare for the Phase 2 development in the summer and fall. ■



**Top row** (l to r): Guy Garty, Patricia Farrell, Dennis Farrell, Andrew Harkin, Matt England; David Brenner. **Second row** (l to r): Tom Hei, Sally Amundson; David Brenner, Shanaz Ghandhi, Sally Amundson, Aesis Luna, Nils Rudqvist, Mashkura Chowdhury; Tom Hei. **Third row** (l to r): Lubo Smilenov; Howard Lieberman, Cui-Xia Kuan; Ashish Jani, Cheng-Shie Wu, Anand Shah. **Bottom row** (l to r): Angela Lugo, Yvette Acevedo.



# AMOEBA: Unlocking the Potential of Vertical Focused Ion Beams to Examine the Long Term Effects of Radiation on Cells and the Effects of Hypoxia on Cellular Radiation Response

Matthew England<sup>a</sup>, Michael Merchant<sup>b</sup>, Alan Bigelow, David Welch, Andrew Harken, Guy Garty, Eirini Velliou<sup>a</sup>, David J. Brenner, and Karen Kirkby<sup>b</sup>

Glioblastoma multiforme (GBM) is a grade 4 astrocytoma. GBM and anaplastic astrocytoma are the most common types of brain tumours in adults. GBM tumors are often found deep within a patient's brain. As a result the patients benefit from particle therapy. As with any large cancerous tumor, large parts of a GBM are under low oxygen conditions (Figure 1). As a result it is important to understand how glioblastoma tumors respond to radiation in low oxygen conditions. It has also been shown that radiation can increase the movement of Glioblastoma cells [1, 2].

Vertical Focused Ion Beams such as the Vertical Nanobeam at Surrey University [3] or the Electrostatic Microbeam at RARAF (Radiation Research Accelerator Facility) [4] are useful tools for examining the effects of radiation on DNA, allowing for simultaneous particle irradiation and observation of cells using both bright field and fluorescence microscopy techniques. Despite their great potential, such facilities have their drawbacks. Irradiations of cells using vertical focussed ion beams are carried out in lab (benchtop) conditions. This is of significance because of the difference in environmental conditions between the incubator, where cells are cultured in a humid environment at 37°C and 5% carbon dioxide, as opposed to lab conditions. This leads to a change in the pH and the evaporation of the cell media during the irradiation. Another limiting factor is that they are unable to carry out experiments in extreme oxygen conditions such as hypoxia.

To unlock the potential of Vertical Focused Ion Beams and explore the effects of radiation and oxygen on the movement of glioblastoma cells the AMOEBA (Automated Microbeam Observation Endstation for Biological Analysis) and  $\mu$ AMOEBA (a microfluidic AMOEBA system) are being developed. The AMOEBA is a flexible environmental control system designed for Vertical Focused Ion beams allowing long-term observation and irradiation of cells. The  $\mu$ AMOEBA allows for the creation of controlled oxygen conditions (including hypoxia) at the end of the beam line.

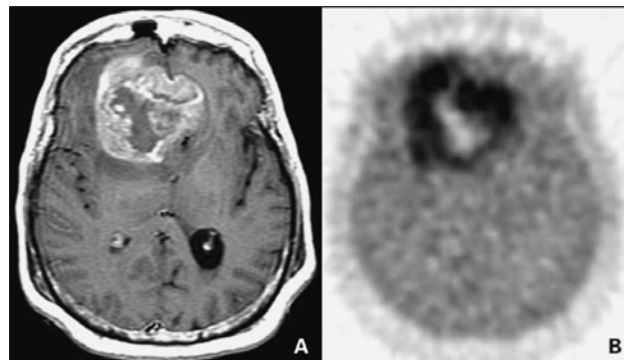


**Figure 1.** A) An MRI image of a ring-shaped glioblastoma multiforme tumor. B) A PET scan of the same tumor shown in image A. The dark areas correspond to the areas with hypoxia due to low blood flow.

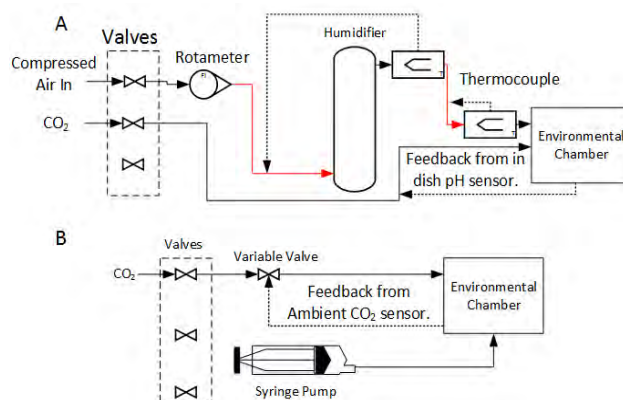


**Figure 2.** A) AMOEBA system in the humid air configuration and carbon dioxide control using an in-dish pH sensor. B) Syringe pump AMOEBA system with pH control using an ambient carbon dioxide sensor and variable valve. The solid arrows show pipes and their direction indicates gas flow. The red arrows are heated pipes. The dotted lines demonstrate feedback within the system.

## Methods

The AMOEBA system has been designed with a modular approach. Each AMOEBA module is connected to the other modules by a single CAN bus down which all the modules communicate using a common protocol. The modules are controlled and monitored by a server module that is connected to a computer by a USB connection. The main parameters controlled by the AMOEBA system

<sup>a</sup>Surrey University, Guilford, UK

<sup>b</sup>University of Manchester, Manchester, UK

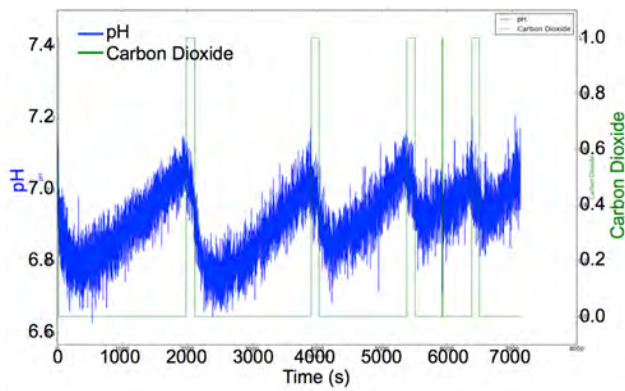


Figure 3. pH Control carried out by an AMOEBA system at Surrey University.

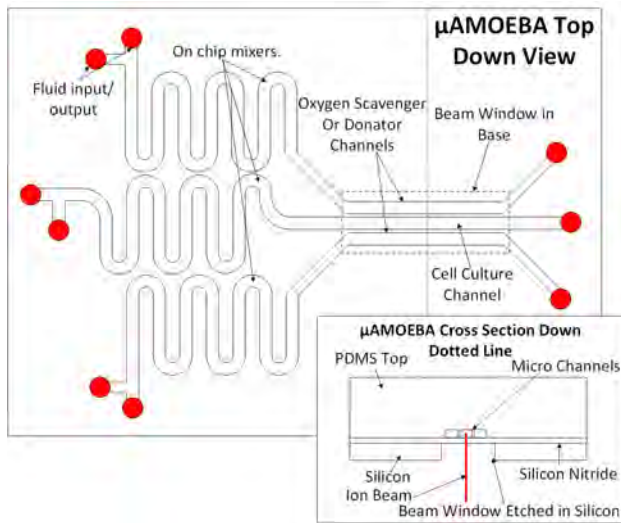


Figure 4. Concept design for the μAMOEBa.

controls are cell media levels, cell media pH and cell media temperature.

The AMOEBA system at RARAF can work in two ways to maintain cell media levels. The first method uses a syringe pump to replace cell media lost due to evaporation, and the second method blows warm air (with a relative humidity of 100%) over the cell dish. For system overview diagrams of these systems see Figure 2. Cell media pH is controlled by flowing carbon dioxide over the cells, and this is achieved in one of two ways. Firstly by monitoring the pH using a Lazar-PHR146 flexible pH micro electrode, where the flow of carbon dioxide from a gas cylinder is turned on when the pH goes above a certain threshold and then turned off when the pH drops below a second threshold (Figure 3). The second method uses a valve that controls the gas flow rate using a SprintIR WR 100% CO<sub>2</sub> monitor and an electronically controlled variable valve to regulate the carbon dioxide flow rate ensuring that the atmosphere above the cell dish contains 5% carbon dioxide to mimic the environment of an incubator. These AMOEBA configurations are illustrated in Figure 2. The Cell media temperature is controlled using an under-dish heater that reads the temperature of the cell media using an in-cell media thermocouple.

The μAMOEBa (a microfluidic AMOEBA system) is designed with a thin base that allows ions to pass into the device. A concept drawing of the μAMOEBa can be seen in Figure 4. The device will be a PDMS soft top hard bottom microfluidic device that will allow cells to be grown on chip in a microfluidic channel where oxygen levels can be controlled. The device consists of three parallel channels: the central channel is used to grow the cells, while the two outer channels are used to control oxygen levels. By flowing oxygen scavengers through these channels, oxygen can be drawn out from the central channel creating a hypoxic environment. A device similar to this was created by Chen et al [5], and was able to create hypoxic environments.

To allow ions to enter the μAMOEBa, the device must have a thin base that ions can penetrate. Therefore the μAMOEBa will be built on a 500 μm thick silicon wafer with a 300 nm silicon nitride layer. To create a substrate that low energy hadrons can pass through, the silicon layer is etched away leaving only the thin 300 nm Silicon Nitride window.

Results so Far

So far a functional AMOEBA system has been built at the University of Surrey that uses a humid air system to stop cell media evaporation. Currently, a similar system is being built for the Permanent Magnet Microbeam and the Electrostatic Microbeam at RARAF. The system at Surrey University was able to maintain cell media levels over a 24-hour period while observing the cell dish. It was also able to maintain cell media temperature at 37°C using a heated microscope objective cover (the Surrey System uses an immersion objective).

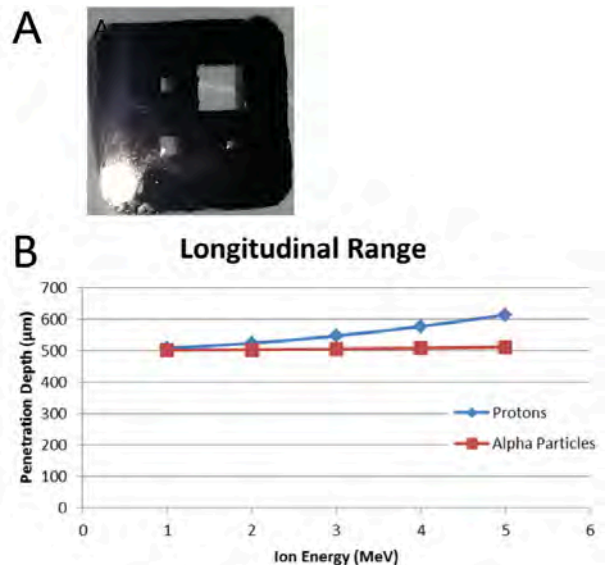


Figure 5. A) Silicon nitride windows created in a silicon nitride coated silicon wafer. The windows are sized 1 mm by 1 mm, 1.5 mm by 1.5 mm, 2 mm by 2 mm and 4 mm by 4 mm. All of these except the 4 mm by 4 mm windows survived the etching process. B) Results for SRIM simulation. Each simulation consisted of 100,000 ions fired into a substrate that consisted of a 500 nm silicon nitride beam window, a 500 μm air gap, a 300 nm silicon nitride beam window, and a water layer.

The functional Surrey AMOEBA system is also able to control cell media pH by flowing carbon dioxide over the cell dish (Figure 3). Since the RARAF AMOEBA system is based on Surrey's system, there should be no difficulties with the pH control.

The  $\mu$ AMOEBA is still in design, but it has two key components: the ability to control oxygen concentrations and the ability to irradiate cells within the device. The oxygen scavenging system has been proven to work by Chen et al [5] and a similar device has also been shown to work using deoxygenated water [6]. Both these devices were PDMS soft top hard bottom devices similar to the  $\mu$ AMOEBA design.

The second essential part of the  $\mu$ AMOEBA is the thin base that allows ions to enter the device. 300 nm thick Silicon Nitride windows have been created in a silicon nitride coated silicon wafer by etching away from the back of the wafer through the silicon (Figure 5A). Also a series of SRIM (Stopping and Range of Ions in Matter) simulations [7] have been carried out to show that ions are able to penetrate the device (Figure 5B).

#### References

- Steinle M, Palme D, Misovic M, Rudner J, Dittmann K, Lukowski R, Ruth P and Huber SM (2011) Ionizing radiation induces migration of glioblastoma cells by activating BK K(+) channels. *Radiother Oncol* **101**: 122-126.
- Wild-Bode C, Weller M, Rimner A, Dichgans J and Wick W (2001) Sublethal irradiation promotes migration and invasiveness of glioma cells: implications for radiotherapy of human glioblastoma. *Cancer Res* **61**: 2744-2750.
- Merchant MJ, Jeynes JC, Grime GW, Palitsin V, Tullis ID, Barber PR, Vojnovic B, Webb RP and Kirkby KJ (2012) A focused scanning vertical beam for charged particle irradiation of living cells with single counted particles. *Radiat Res* **178**: 182-190.
- Bigelow AW, Randers-Pehrson G, Garty G, Geard CR, Xu Y, Harken AD, Johnson GW and Brenner DJ (2010) Ion, X-ray, UV and Neutron Microbeam Systems for Cell Irradiation. *AIP Conf Proc* **1336**: 351-355.
- Chen YA, King AD, Shih HC, Peng CC, Wu CY, Liao WH and Tung YC (2011) Generation of oxygen gradients in microfluidic devices for cell culture using spatially confined chemical reactions. *Lab Chip* **11**: 3626-3633.
- Grist S, Yu L, Chrostowski L, and Cheung CK (2012) Microfluidic cell culture systems with integrated sensors for drug screening. *Proc. SPIE* **8251**: 825103.
- Ziegler JF, Biersack JP and Littmark U (1985) The stopping and range of ions in solids. Pergamon, New York. ■

## Development of a Cell System to Investigate the Repair of Telomeres After Targeted Microbeam Induced Damage

Brian Ponnaiya, Andrew Harken, Susan Bailey<sup>a</sup>, and David J. Brenner

Telomeres are nucleoprotein complexes comprised of tandem arrays of repetitive DNA sequence that serve to protect chromosomal termini from inappropriate degradation, as well as to prevent these natural DNA ends from being recognized as broken DNA (double-strand breaks) and triggering of inappropriate DNA damage responses [1, 2]. Telomere-specific binding proteins include the telomere repeat factors 1 and 2 (TRF1 and TRF2), which bind double-stranded telomeric DNA, and protection of telomeres 1 (POT1), which binds single-stranded telomeric DNA [3, 4]. Direct links between telomere dysfunction (in terms of either significant shortening or compromise of end-capping structure/

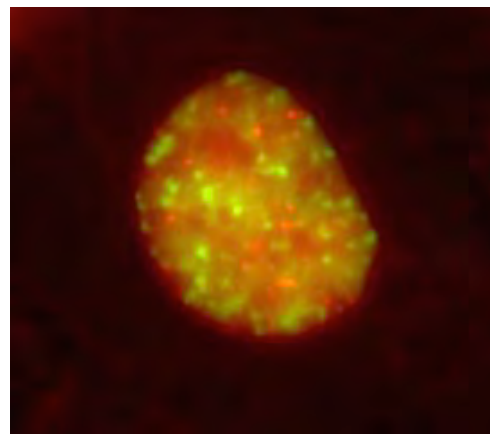


**Figure 1.** Induction of MDC1 foci (green) 5 minutes after exposure to 5 Gy x-rays. Telomeres (red spots) are visualized with the mCherry-TRF1 tag.

<sup>a</sup>Department of Environmental and Radiological Health Sciences, Colorado State University, Fort Collins, CO

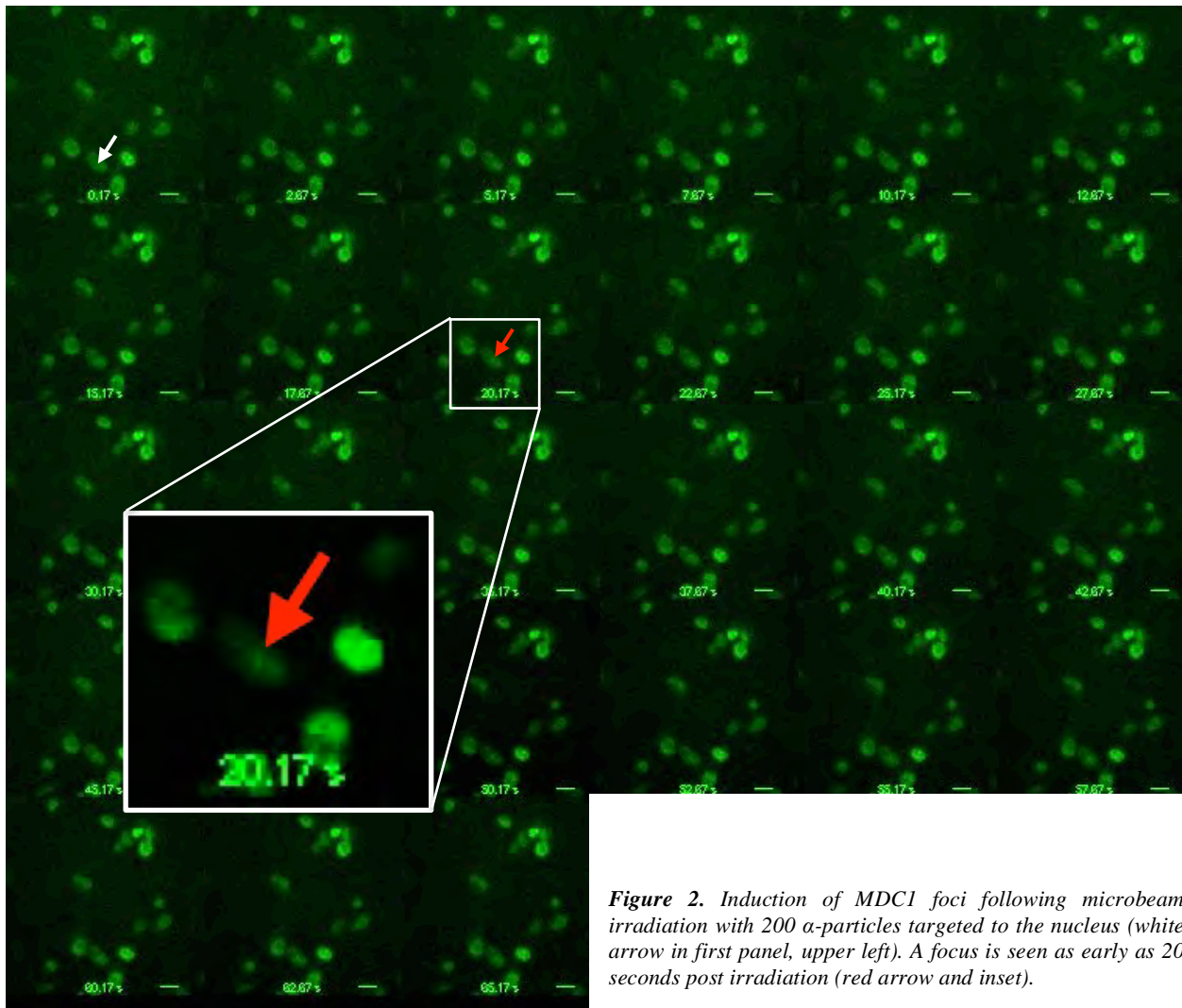


**Figure 2.** Induction of MDC1 foci following microbeam irradiation with 200  $\alpha$ -particles targeted to the nucleus (white arrow in first panel, upper left). A focus is seen as early as 20 seconds post irradiation (red arrow and inset).

function) and genomic instability and cancer, as well as senescence- and age related degenerative pathologies have been demonstrated [5-7].

Early studies by Bradshaw et al. [8] reported that TRF2 accumulates at nuclear sites damaged by high-intensity laser beams, presumptively in response to DNA double-strand breaks (DSBs), and that TRF2 arrives before other DNA repair-related proteins, including ATM. However, subsequent studies using the Columbia University microbeam to deposit particles in defined sub-micron regions of the cellular nucleus failed to detect the recruitment of TRF2 to the sites of DNA damage [9]. To date there are conflicting reports on whether telomeres are repaired. On one hand, proteins from multiple DNA repair pathways have been shown to associate with telomere proteins [10-12], while on the other hand, there is indirect evidence that damaged telomeres remain unrepaired [13, 14].

To examine the cellular consequences of damage to telomeres in a definitive way, we have developed a system that allows for the simultaneous live-cell visualization of both TRF1 and MDC1 (a DNA repair

protein). GFP-MDC1 (Addgene # 26284) and mCherry-TRF1 (a kind gift from Dr. E. Blackburn) were co-transfected into HT1080 cells, and single cell clones of stable transfectants expressing both constructs were obtained under drug selection. Initial experiments tested the ability of these cells to form MDC1 foci in response to x-rays. Cells were seeded onto collagen coated glass coverslips and irradiated with 5 Gy x-rays (250 kV, 15 mA). As can be seen in Figure 1, MDC1 foci were observed by 5 minutes after irradiation, the earliest observation time possible.

Subsequent studies examined the formation of MDC1 foci as a consequence of microbeam irradiation. For these experiments, cells were cultured on conventional microbeam dishes and one cell in a 60X field of view was irradiated through the nucleus with 200  $\alpha$ -particles (white arrow in Figure 2). Starting immediately after the irradiation (~1 sec), cells were continuously imaged every second. As can be seen in Figure 2, at ~20 seconds post irradiation, a focus first appears at the site of irradiation (red arrow in Figure 2). Optimization of culturing and imaging parameters are currently ongoing.

In conclusion, a system has been developed that will allow for the direct visualization of the recruitment of DNA repair proteins and telomere proteins to the sites of DNA damage. While present technology cannot target telomeres, the super microbeam that is currently under development will have the capability of delivering charged particles to individual telomeres. This will allow for the direct observation of whether or not damaged telomeres are repaired.

### References

1. Moyzis RK, Buckingham JM, Cram LS, Dani M, Deaven LL, Jones MD, Meyne J, Ratliff RL, Wu JR. A highly conserved repetitive DNA sequence, (TTAGGG)<sub>n</sub>, present at the telomeres of human chromosomes. *Proceedings of the National Academy of Sciences of the United States of America*. 1988;85(18):6622-6. PMID: PMC282029.
2. de Lange T. Shelterin: the protein complex that shapes and safeguards human telomeres. *Genes & Development*. 2005;19(18):2100-10.
3. Bianchi A, Smith S, Chong L, Elias P, de Lange T. TRF1 is a dimer and bends telomeric DNA. *The EMBO Journal*. 1997;16(7):1785-94. PMID: PMC1169781.
4. Broccoli D, Smogorzewska A, Chong L, de Lange T. Human telomeres contain two distinct Myb-related proteins, TRF1 and TRF2. *Nature Genetics*. 1997;17(2):231-5.
5. DePinho RA. The age of cancer. *Nature*. 2000;408(6809):248-54.
6. Murnane JP, Sabatier L. Chromosome rearrangements resulting from telomere dysfunction and their role in cancer. *BioEssays : News and Reviews in Molecular, Cellular and Developmental Biology*. 2004;26(11):1164-74.
7. Haycock PC, Heydon EE, Kaptoge S, Butterworth AS, Thompson A, Willeit P. Leucocyte telomere length and risk of cardiovascular disease: systematic review and meta-analysis. *BMJ*. 2014;349:g4227. PMID: PMC4086028.
8. Bradshaw PS, Stavropoulos DJ, Meyn MS. Human telomeric protein TRF2 associates with genomic double-strand breaks as an early response to DNA damage. *Nature Genetics*. 2005;37(2):193-7.
9. Williams ES, Stap J, Essers J, Ponnaiya B, Luijsterburg MS, Krawczyk PM, Ullrich RL, Aten JA, Bailey SM. DNA double-strand breaks are not sufficient to initiate recruitment of TRF2. *Nature Genetics*. 2007;39(6):696-8; author reply 8-9.
10. Jia P, Her C, Chai W. DNA excision repair at telomeres. *DNA Repair*. 2015;36:137-45. PMID: PMC4688237.
11. Doksan Y, de Lange T. The role of double-strand break repair pathways at functional and dysfunctional telomeres. *Cold Spring Harbor Perspectives in Biology*. 2014;6(12):a016576.
12. Longhese MP. DNA damage response at functional and dysfunctional telomeres. *Genes & Development*. 2008;22(2):125-40. doi: 10.1101/gad.1626908. PMID: PMC2731633.
13. Fumagalli M, Rossiello F, Clerici M, Barozzi S, Cittaro D, Kaplunov JM, Bucci G, Dobrev M, Matti V, Beausejour CM, Herbig U, Longhese MP, d'Adda di Fagagna F. Telomeric DNA damage is irreparable and causes persistent DNA-damage-response activation. *Nature Cell Biology*. 2012;14(4):355-65. doi: 10.1038/ncb2466. PMID: PMC3717580.
14. Hewitt G, Jurk D, Marques FD, Correia-Melo C, Hardy T, Gackowska A, Anderson R, Taschuk M, Mann J, Passos JF. Telomeres are favoured targets of a persistent DNA damage response in ageing and stress-induced senescence. *Nature Communications*. 2012;3:708. doi: 10.1038/ncomms1708. PMID: PMC3292717. ■



*Tom Hei (right) with Geisha.*

# A Microfluidic Array for Parallelized Transcriptional Profiling of Single cells

Hao Sun<sup>a,b</sup>, Tim Olsen<sup>b</sup>, Jing Zhu<sup>b</sup>, Jianguo Tao<sup>a</sup>, Brian Ponnaiya, Sally A. Amundson, David J. Brenner, and Qiao Lin<sup>b</sup>

Existing methods for single-cell transcript measurements include quantitative reverse transcription polymerase chain reaction (RT-qPCR) [1], emulsion-based methods [2, 3] and RNA fluorescence in situ hybridization (FISH) [3]. Of these, RT-qPCR combines the advantages of high accuracy, specificity, and sensitivity, and has been broadly employed to measure transcript levels of small quantities of mRNA [1, 4]. We have developed a microfluidic device for coupling to our microbeam, which can perform parallelized, quantitative analysis of low-abundance mRNA from single cells *via* RT-qPCR (Fig. 1). The device accomplishes arrayed RT-qPCR analysis of cells by leveraging concurrent control of a set of parallel microchannels. Combined with bead-based reactions, this enables parallelized handling and processing of multiple single cells.

To test the robustness of the device, stress induced gene expression in single cells was investigated by treating cells with methyl methanesulfonate (MMS), an alkylating agent, and then analyzing them by on-chip RT-qPCR. We first measured the transcript levels of *CDKN1A* and the housekeeping gene *GAPDH* in MMS treated (120  $\mu\text{g}/\text{mL}$  for 2.5 h) and untreated single MCF-7 cells using the microfluidic array.

In each test, five MMS treated or untreated single cells were isolated and immobilized in five separate analysis units of the array, and the remaining unit was used as a no-template control. After cell trapping and lysis, a two-step RT-qPCR was initialized. The fluorescent intensity was detected and assayed using hydrolysis probe/primer sets for *CDKN1A* and *GAPDH* respectively during the qPCR process (Fig. 2a).

The mean  $C_q$  value of *CDKN1A* in untreated single cells was 33.5 with a standard deviation of 0.54 (Fig. 2b). After treatment with 120  $\mu\text{g}/\text{mL}$  of MMS for 2.5 h, the mean  $C_q$  value decreased to 30.5 with a standard deviation of 0.23. No fluorescent signal was detected in the no-template control samples. The difference between the  $C_q$  of treated and untreated cells,  $\Delta C_q$ , was determined to be 3.0 for *CDKN1A*, and for the housekeeping gene *GAPDH*,  $\Delta C_q$  was found to be approximately 0.5. Thus, treatment with MMS significantly upregulated the transcript levels of *CDKN1A* in single cells. Conversely, the transcript level of *GAPDH* was found to be very consistent, as

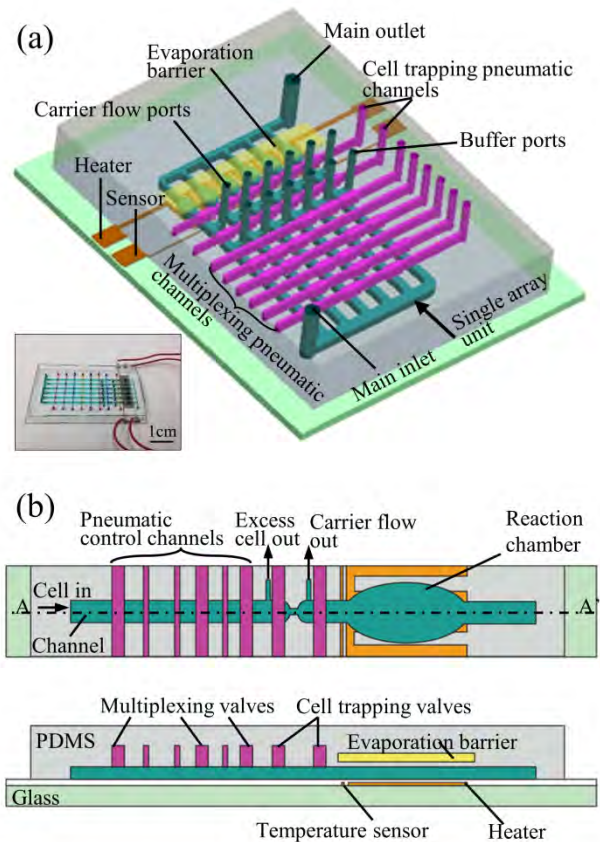


**Figure 1.** The microfluidic RT-qPCR array, experimental procedure and setup. (a) Schematic of the microfluidic array with a photograph of a packaged device in the inset. (b) Schematic (top and side views) of a single unit.

reported earlier [5]. These results demonstrate the ability of our approach to analyze alterations in transcript levels in single mammalian cells in a parallelized fashion.

We next assayed the effect of drug exposure time on transcript levels of *CDKN1A* in single MCF-7 cells. First, five suspension cell cultures were exposed to MMS for different time durations (from 0.5 to 4.5 hours). Following exposure to MMS, the cell suspensions from the five separate culture media were diluted and introduced to five analysis units on the microchip.  $C_q$  values of *CDKN1A* RT-qPCR in MMS-treated single cells and mean 3-D qPCR amplification curves were plotted for this scenario (Fig. 2c).

The mean  $C_q$  values decreased from 32.9 to 28.1 when the exposure time was increased from 0.5 to 4.5 h. Also, the standard deviation of  $C_q$  decreased (from 0.5 to 0.2) as the exposure time increased. Furthermore, the exposure

<sup>a</sup>Department of Mechatronics Engineering, Harbin Institute of Technology, Harbin, Heilongjiang, China

<sup>b</sup>Department of Mechanical Engineering, Columbia University, New York, NY

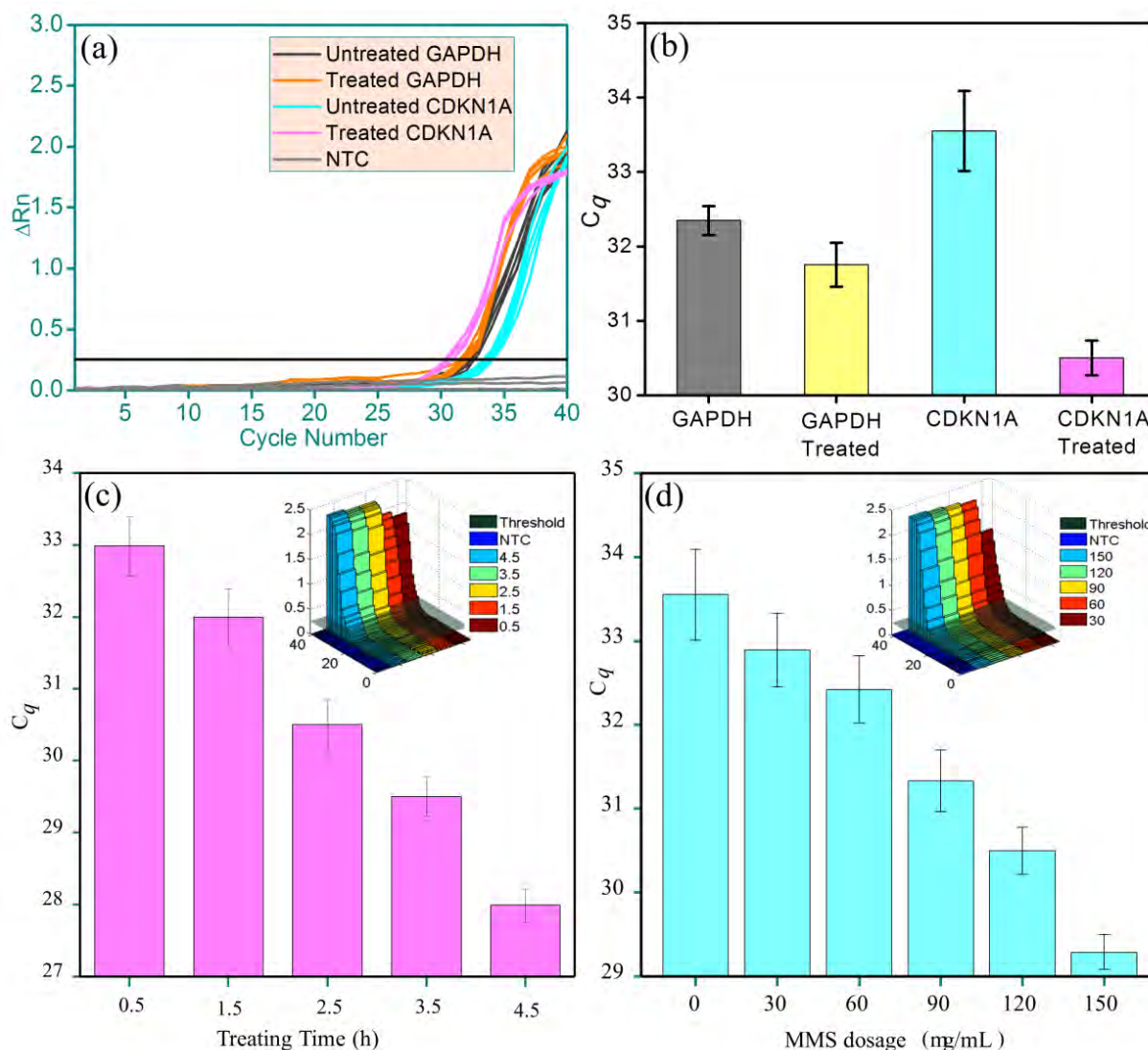


**Figure 2.** (a) The amplification curves of CDKN1A and GAPDH in MMS treated, untreated single MCF-7 cells and no-template control (NTC) by the microfluidic array. (b) qPCR  $C_q$  values of CDKN1A and GAPDH in MMS treated and untreated single MCF-7 cells. (c) qPCR  $C_q$  values with amplification curves shown in the inset of CDKN1A in single cells exposed to MMS for different time durations. (d) qPCR  $C_q$  values with amplification curves shown in the inset of CDKN1A in single cells treated with different doses of MMS. Each experiment was repeated three times and error bars represent standard deviations.

time did not have a linear relationship with CDKN1A expression, as seen from the increased inter-unit  $C_q$  differences with increasing exposure durations. As the exposure time increased beyond 2.5 h, the 3D amplification curves became saturated before 40 cycles of qPCR. We can conclude that the upregulation of CDKN1A expression caused by MMS was positively correlated with treatment duration in the range of 0.5 to 4.5 h.

To further investigate the effect of MMS treatment on gene expression levels of CDKN1A in single cells, we treated MCF-7 cells with different doses of MMS and then performed on-chip RT-qPCR. First, cells ( $\sim 1 \times 10^6$  cells in a 10 cm dish) in five cultures were exposed to different doses of MMS (from 30 to 150  $\mu\text{g/ml}$ ) for 2.5 h at 37 °C in an incubator. After treating, cells were introduced to the arrayed microfluidic device for single-

cell processing and RT-qPCR following the above described protocol.

In the five separate analysis units, increasing the drug concentration from 30 to 150  $\mu\text{g/ml}$ , resulted in a decrease in the mean  $C_q$  value from 33.5 to 29.3 while the standard deviation of this  $C_q$  decreased from 0.5 to 0.2 (Fig. 2d). In addition, by plotting the mean qPCR data in a three-dimensional bar graph, it appears that after 40 PCR cycles the amplification of samples that were treated with doses of MMS from 60 to 150  $\mu\text{g/ml}$  became saturated. In contrast, for the 30  $\mu\text{g/ml}$  MMS-treated sample, the amplification yield at the end of 40-cycle PCR was lower than the other four cases. Furthermore, the inter-unit  $C_q$  differences for CDKN1A were found to be 0.4, 0.7, 1.3 and 0.7, indicating that the intracellular DNA damage was greatest when MMS dosage increased from 90 to 120  $\mu\text{g/ml}$ . The upregulation of CDKN1A expression caused

by MMS treatment was positively correlated with MMS dosage in the range from 30 to 150 µg/ml.

These results demonstrate that the presented microfluidic array is capable of detecting alterations in transcript levels of single cells and can potentially perform parallelized single-cell analysis. The next step will be development of the front end to allow microfluidic integration with the microbeam.

**References**

1. Stahlberg A, Rusnakova V, Kubista M. (2013) The added value of single-cell gene expression profiling. *Briefings in Functional Genomics* **12(2)**:81-9. doi: 10.1093/bfgp/elt001.
2. Zhang H, Jenkins G, Zou Y, Zhu Z, Yang CJ (2012) Massively parallel single-molecule and single-cell emulsion reverse transcription polymerase chain reaction using agarose droplet microfluidics. *Analytical Chemistry* **84(8)**:3599-606. doi: 10.1021/ac2033084.
3. Ludlow AT, Robin JD, Sayed M, Litterst CM, Shelton DN, Shay JW, Wright WE (2014) Quantitative telomerase enzyme activity determination using droplet digital PCR with single cell resolution. *Nucleic Acids Research* **42(13)**:e104. doi: 10.1093/nar/gku439. PMID: PMC4117742.
4. Bustin SA, Benes V, Garson JA, Hellems J, Huggett J, Kubista M, Mueller R, Nolan T, Pfaffl MW, Shipley GL, Vandesompele J, Wittwer CT (2008) The MIQE guidelines: minimum information for publication of quantitative real-time PCR experiments. *Clinical Chemistry* **55(4)**:611-22. doi: 10.1373/clinchem.2008.112797.
5. Schmittgen TD and Zakrajsek BA (2000) Effect of experimental treatment on housekeeping gene expression: validation by real-time, quantitative RT-PCR. *J Biochem Biophys Methods* **46**: 69-81. ■



**Top** (l to r): Tom Hei, Margaret Zhu; Kunal Chaudhary, Vladimir Ivanov, David Cuniberti; Eric Hall, Norm Kleiman.  
**Middle** (l to r): David Cuniberti, Rob Morton; David Brenner, Kunal Chaudhary, Aesis Luna, Igor Shuryak, Yen-Ruh Wu, David Welch, Angela Lugo, Mashkura Chowdhury, Andrew Harkin, Rob Morton, Tom Hei, Kevin Hopkins.  
**Bottom** (l to r): Manuela Buonanno, Aesis Luna, Angela Lugo.

# Cytoplasmic Irradiation Induces Metabolic Shift in Small Airway Epithelial Cells via Activation of PIM1 Kinase

Jinhua Wu, Qin Zhang<sup>a</sup>, Yen-Ruh Wu<sup>a</sup>, Sirui Zou<sup>b</sup>, and Tom K. Hei

The unique molecular consequences of cytoplasmic damage caused by ionizing radiation have been unveiled by the use of a precision microbeam irradiator. Our recent results suggest that targeted cytoplasmic irradiation induces a metabolic shift from an oxidative to glycolytic phenotype in small airway epithelial (SAE) cells. At 24 hours after irradiation, there was an increase in the mRNA expression level of key glycolytic enzymes as well as lactate secretion in SAE cells. Using RNA-sequencing analysis to compare genes that are responsive to cytoplasmic vs. nuclear irradiation, we found a glycolysis related gene, PIM1, was significantly upregulated only by cytoplasmic irradiation. Inhibition of PIM1 activity using the selective pharmaceutical inhibitor Smi-4a significantly reduced the level of lactate production and glucose uptake after cytoplasmic irradiation. In addition, PIM1 also inhibited AMPK (protein kinase, AMP-activated, alpha 1 catalytic subunit) activity, which is a well-characterized negative regulator of glycolysis. In an

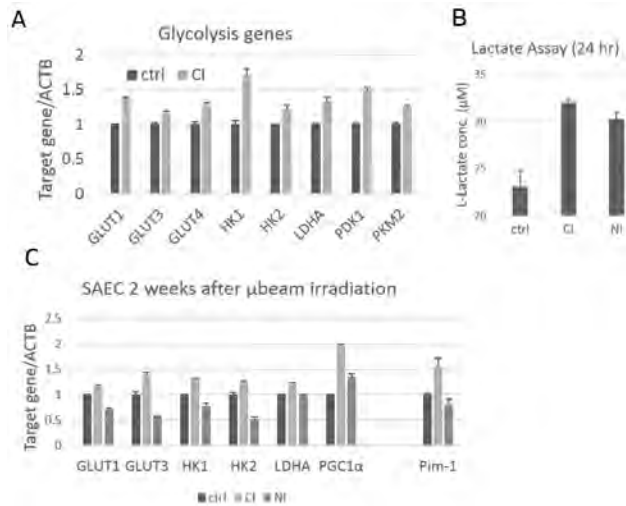


**Figure 1.** Targeted cytoplasmic irradiation increases glycolysis in SAE cells. A) 24 hours after irradiation, SAE cells were lysed in Trizol. RNA extraction and qRT-PCR (quantitative RT-PCR) were performed following manufacturers' protocols. Data were calculated using the  $\Delta\Delta C_t$  method using  $\beta$ -actin as a control gene. B) Culture media were collected from SAE cells 24 hours after irradiation. Lactate concentrations were measured using a L-lactate assay kit according to manufacturer's instructions. Three individual samples were used in each group. C) SAE cells were cultured for two weeks after irradiation. RNA extraction and qRT-PCR were performed as described for A.

<sup>a</sup>Department of Pathology and Cell Biology, CUMC

<sup>b</sup>Department of Environmental Health Sciences, CUMC

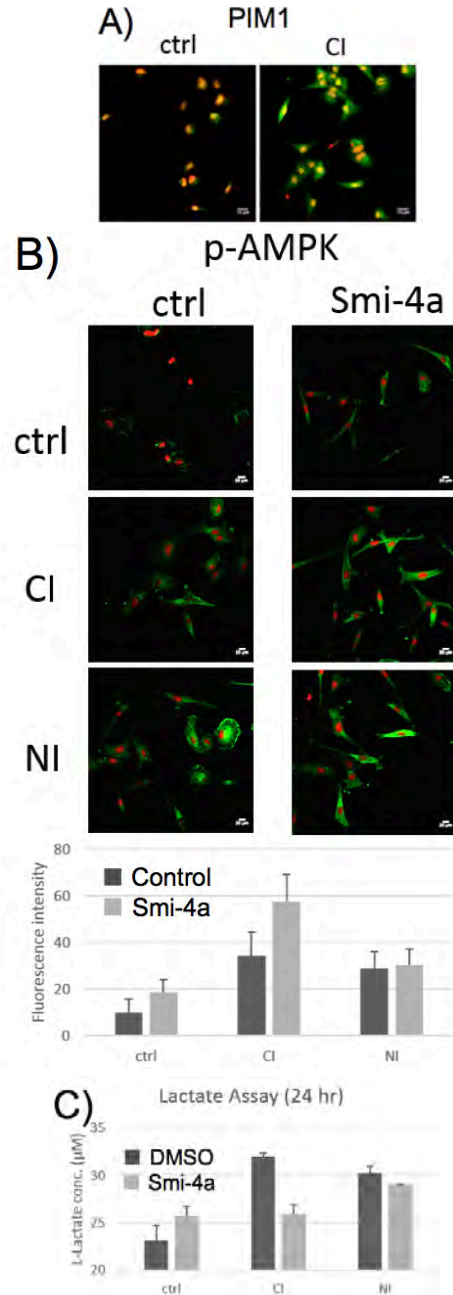


**Figure 2.** Involvement of PIM1 in cytoplasmic irradiation mediated glycolysis. A) 24 hours after irradiation, SAE cells were fixed with paraformaldehyde and immunofluorescence staining was performed to evaluate PIM1 expression levels. B) Phosphorylation of p-AMPK in SAE cells was examined 24 hour after irradiation. Smi-4a was added 30 minutes prior to irradiation and maintained after irradiation to inhibit PIM1 activity. Fluorescence intensity was measured using Image-J. C) Smi-4a inhibited glycolysis 24 hours after cytoplasmic irradiation.

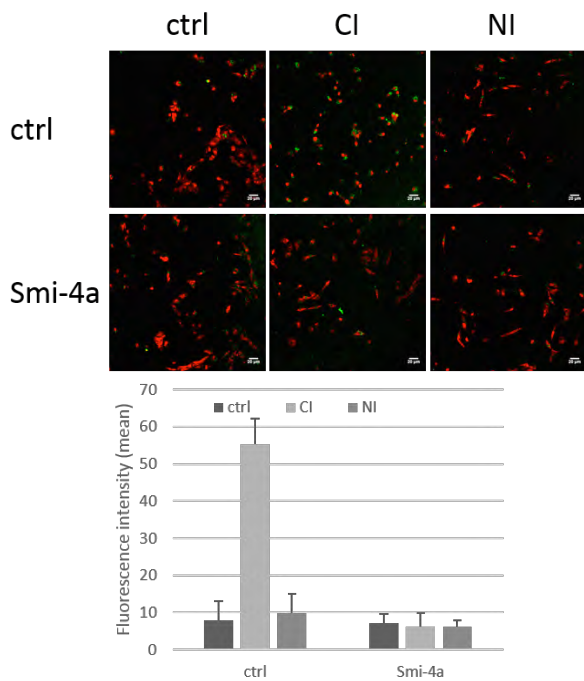


**Figure 3.** Glucose uptake was increased by PIM1 only in cytoplasmic irradiated cells. SAE cells were irradiated with cytoplasmic- or nuclear-targeted irradiation with or without Smi-4a. 2-NBDG was added to cells after irradiation for 24 hours. Cells were counter-stained with propidium iodide to visualize nuclei. Green fluorescence intensity was calculated using Image-J.

effort to explore the underlying mechanism, we found that inhibition of mitochondrial fission using the cell-permeable selective inhibitor mdivi-1 suppressed the induction of PIM1, further confirming that PIM1 was a downstream target of cytoplasmic irradiation. Our data show for the first time that cytoplasmic irradiation mediates expression of PIM1, which leads to a glycolytic shift in normal SAE cells. Additionally, since glycolysis is frequently linked to cancer cell metabolism, our findings further suggest a role of cytoplasmic damage during neoplastic transformation.

Based on RNA sequencing data, we found many glycolysis-related genes were upregulated in SAE cells 24 hours after cytoplasmic irradiation. As shown in Figure 1A, several key enzymes involved in glycolysis pathways were significantly increased, including glucose transporters (*GLUT1-4*) in glucose transportation, Hexokinases (*HK1* and *HK2*) in glycolysis initiation, pyruvate kinase M2 (*PKM2*) in generation of pyruvate and pyruvate dehydrogenase kinase (*PDK1*) necessary for the production of lactate. Consistent with the increased expression of glycolytic genes, glycolysis levels in SAE cells, measured by the concentration of lactate secreted in the medium, was also increased by 40% (Figure 1B). An increase of lactate production was also found in nuclear-irradiated SAE cells (Figure 1B). The elevated levels of glycolytic enzymes were maintained even 2 weeks after cytoplasmic irradiation (Figure 1C). However, the increase of glycolysis following nuclear irradiation was

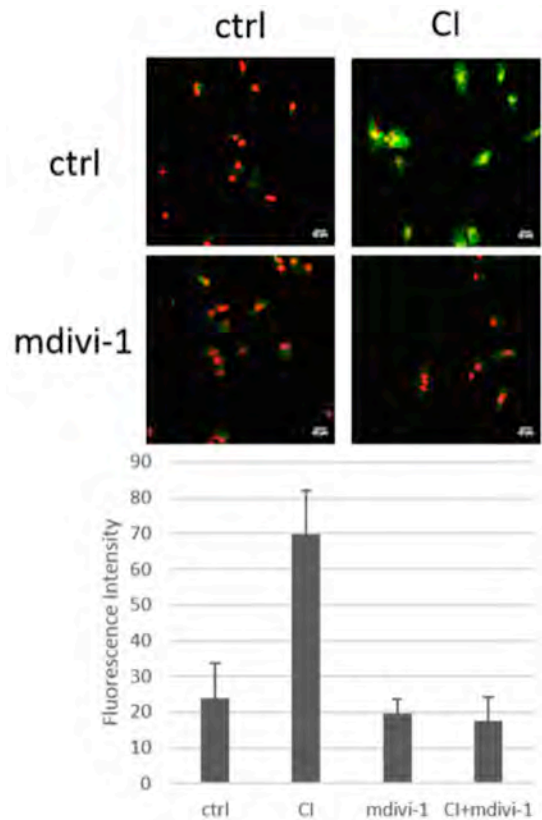


**Figure 4.** PIM1 expression was regulated by mitochondrial fission. Mitochondrial fission inhibitor mdivi-1 was added to SAE cells 30 minutes before cytoplasmic irradiation and kept in the culture medium for 6 hours before washing away with new medium. PIM1 expression was examined 24 hours after irradiation using immunofluorescence.

transient, as no significant increases of glycolytic genes were observed 2 weeks after nuclear irradiation (Figure 1C), which was consistent with previously published data on irradiated tumor cells [1].

Among the genes that are regulated by cytoplasmic but not nuclear irradiation, we identified the proto-oncogene serine/threonine-protein kinase (*PIM1*) as a potential regulator of glycolysis. Consistent with RNA-Seq results, increased expression of *PIM1* was observed after cytoplasmic irradiation (Figure 2A). *PIM1* has been reported to mediate energy metabolism by regulating AMPK activity [2]; therefore we tested the effect of *PIM1* inhibitor Smi-4a on AMPK activity. As shown in Figure 2B, both cytoplasmic and nuclear irradiation increased AMPK phosphorylation, suggesting activation of AMPK in response to radiation. Cytoplasmic irradiation in combination with Smi-4a resulted in a further increase of AMPK phosphorylation. Interestingly, Smi-4a increased AMPK phosphorylation in control and cytoplasmic-irradiated SAE cells, but not in nuclear-irradiated cells, suggesting that increase of AMPK activity by nuclear irradiation was not dependent on *PIM1*.

To further confirm the role of *PIM1* in cytoplasmic irradiation mediated glycolysis, we also tested the effect of Smi-4a in the lactate assay (Figure 2C). The induction

of lactate generation by cytoplasmic irradiation was abolished in the presence of Smi-4a, while no change was observed in nuclear irradiated cells.

Measurement of glucose uptake can also be used to confirm an increased level of glycolysis in cytoplasmic-irradiated SAE cells. A fluorescent d-glucose analog, 2-[N-(7-nitrobenz-2-oxa-1,3-diazol-4-yl) amino]-2-deoxyglucose (2-NBDG) was used to monitor glucose uptake. As shown in Figure 3, fluorescence intensity increased in SAE cells only after cytoplasmic irradiation, and it was reduced back to control levels when PIM1 activity was inhibited using Smi-4a. This result further confirmed the role of PIM1 in increasing the glycolytic rate.

Our previous results suggested the unique effect of cytoplasmic irradiation was due to oxidative stress and mitochondrial fission. In an effort to explore the molecular mechanism of *PIM1* induction, mdivi-1, a mitochondrial fission inhibitor, was used to block mitochondrial fission after cytoplasmic irradiation. As shown in Figure 4, the induction of PIM1 by cytoplasmic irradiation was diminished with inhibition of mitochondrial fission. Hence, the shift of metabolism was also a downstream outcome of mitochondrial dysfunction.

#### ACKNOWLEDGEMENTS

The authors thank Drs. Guy Garty, Andrew Harkins, Alan Bigelow and Yanping Xu for their assistance with the microbeam irradiations. This research was supported by NIH grants 5P01-CA49062-22 and 5R01-ES12888-07. The Radiological Research Accelerator Facilities is an NIH sponsored Resource Center through grant EB-002033 (National Institute of Biomedical Imaging and Bioengineering).

#### References

1. Fujibayashi Y, Waki A, Sakahara H, Konishi J, Yonekura Y, Ishii Y, et al. Transient increase in glycolytic metabolism in cultured tumor cells immediately after exposure to ionizing radiation: from gene expression to deoxyglucose uptake. *Radiation research* 1997;147(6):729-34.
2. Beharry Z, Mahajan S, Zemskova M, Lin YW, Tholanikunnel BG, Xia Z, et al. The Pim protein kinases regulate energy metabolism and cell growth. *Proceedings of the National Academy of Sciences of the United States of America* 2011;108(2):528-33. ■

## Live Cell Imaging of Connexin 43: Towards Visualizing Cell-to-cell Communication of Bystander Responses Following Microbeam Irradiation

Brian Ponnaiya, David Piston<sup>a</sup>, and David J. Brenner

Radiation induced bystander responses have now been well established for a variety of cellular end points. Signaling molecules appear to be transferred from irradiated cells to neighboring non-irradiated cells primarily via two mechanisms. The first is via media transfer, wherein the irradiated cells secrete into the media specific molecule/s that induce bystander responses in neighboring cells. Alternatively, signaling molecules may pass directly from the irradiated to the bystander cells via gap junctions.

Support for the role of connexins in the propagation of bystander responses have come from both *in vitro* and *in vivo* studies. Azzam *et al.* initially presented direct evidence for the requirement of connexin 43 (Cx43) in the transmission of bystander signals that resulted in the induction of WAF1 in bystander cells [1]. Subsequent

studies from the group have demonstrated that gap junction intercellular communication contributes to the spread of radiation-induced toxic and clastogenic effects from normal human cells directly traversed by HZE particles to bystander normal cells in the vicinity. Importantly, they have shown that Cx26 and Cx43 channels mediated intercellular effects leading to DNA damage in bystander normal cells [2-4]. Mancuso *et al.* have demonstrated an *in vivo* oncogenic bystander response in Patched-1 heterozygous mice after x-ray exposure and that gap junction communication was responsible for the propagation of signals from irradiated to non-irradiated regions in the mice [5]. More recently, the group has demonstrated that upregulation of Cx43 is required for this transmission of oncogenic bystander signals [6].

To develop a cellular system that would allow the direct visualization of gap junction communication in bystander responses a Cx43-GFP vector was transfected into HeLa cells and single cell clones of stable

<sup>a</sup>Department of Cell Biology and Physiology, Washington University in St. Louis, St. Louis, MO

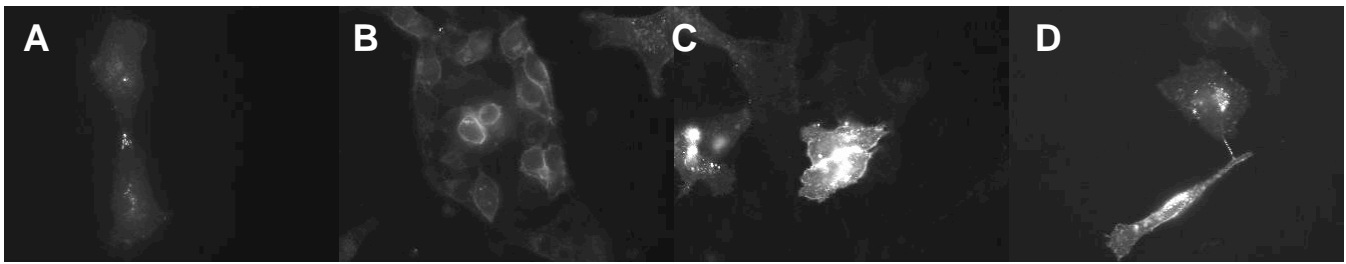


**Figure 1.** Examples of patterns of expression of Cx43-GFP in four different HeLa clones.

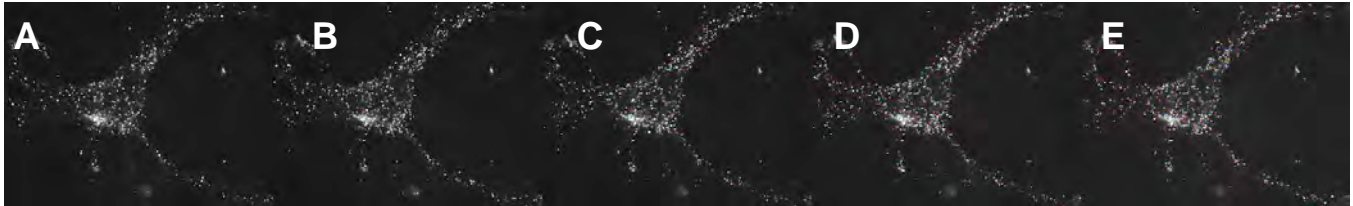


**Figure 2.** Time-lapse images of a single Cx43-GFP expressing HeLa cell. Images were acquired at 1-minute intervals for 10 minutes. Panels A to E are images taken at 1, 3, 5, 7 and 9 minutes respectively.

transfectants were obtained under drug selection. The differing patterns of expression of Cx43 among clones are presented in Figure 1. Cx43 appears to be concentrated at the site of contact between cells (eg. panel A) or more diffused along the entire perimeter of cells (eg. panels B and C), with some clones demonstrating this diffuse pattern in addition to more concentrated staining along regions of contact between cells (panel C). Furthermore, in cells that are adjacent but have little or no direct contact with each other, Cx43 appears to move towards the potential contact sites (panel D).

To further investigate the movement of Cx43, cells were seeded at sparse densities and individual, non-contacting, cells were imaged over 10 minute intervals (Figure 2).

A particle tracking module in ImageJ was used to measure the movement of these Cx43 aggregates over this time frame (Figure 3). As can be seen in the figure, almost all aggregates moved, although there does not

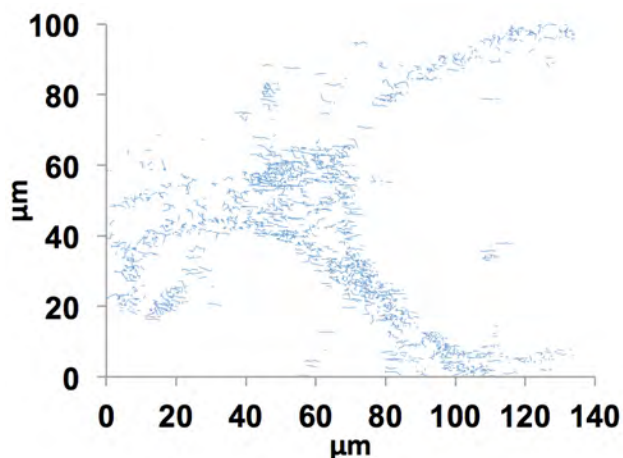


**Figure 3.** Movement of Cx43-GFP aggregates in the image series in Figure 2. Each line represents the movement of a single aggregate over the course of 10 minutes.

appear to be a specific direction associated with this movement. Aggregate movement ranged from 0.2 to 2  $\mu\text{m}$  over 10 minutes, with a mean of about 1  $\mu\text{m}$ .

In conclusion, a system has been developed that allows for the visualization of gap junctions between cells. In conjunction with the charged particle microbeam's ability to target individual cell nuclei, this will allow a more direct visualization of communication between irradiated and bystander cells.

## References

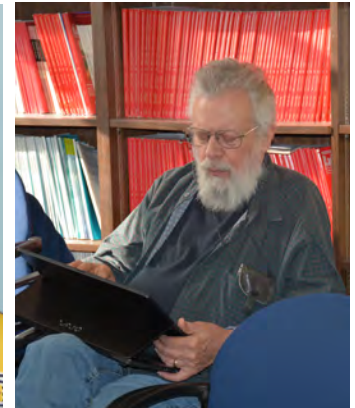
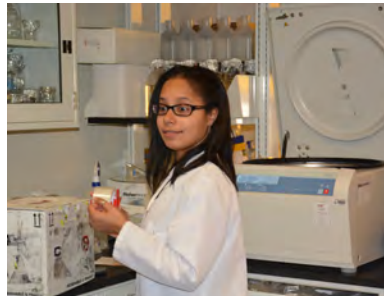
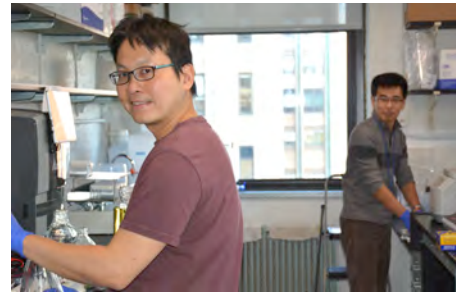
1. Azzam EI, de Toledo SM, Little JB. Direct evidence for the participation of gap junction-mediated intercellular communication in the transmission of damage signals from alpha -particle irradiated to nonirradiated cells. *Proceedings of the National Academy of Sciences of the United States of America*. 2001;98(2):473-8. doi: 10.1073/pnas.011417098.
2. Autsavapromporn N, Suzuki M, Funayama T, Usami N, Plante I, Yokota Y, Mutou Y, Ikeda H, Kobayashi K, Kobayashi Y, Uchihori Y, Hei TK, Azzam EI, Murakami T. Gap junction communication and the propagation of bystander effects induced by microbeam irradiation in human fibroblast cultures: the impact of radiation quality. *Radiation research*. 2013;180(4):367-75. doi: 10.1667/RR3111.1.
3. Autsavapromporn N, Suzuki M, Plante I, Liu C, Uchihori Y, Hei TK, Azzam EI, Murakami T. Participation of gap junction communication in potentially lethal damage repair and DNA damage in human fibroblasts exposed to low- or high-LET radiation. *Mutation research*. 2013;756(1-2):78-85. doi: 10.1016/j.mrgentox.2013.07.001.
4. Autsavapromporn N, de Toledo SM, Little JB, Jay-Gerin JP, Harris AL, Azzam EI. The role of gap junction communication and oxidative stress in the

propagation of toxic effects among high-dose alpha-particle-irradiated human cells. *Radiation research*. 2011;175(3):347-57. doi: 10.1667/RR2372.1.

5. Mancuso M, Pasquali E, Leonardi S, Tanori M, Rebessi S, Di Majo V, Pazzaglia S, Toni MP, Pimpinella M, Covelli V, Saran A. Oncogenic bystander radiation effects in Patched heterozygous mouse cerebellum. *Proceedings of the National*

*Academy of Sciences of the United States of America*. 2008;105(34):12445-50. doi: 10.1073/pnas.0804186105.

6. Mancuso M, Pasquali E, Leonardi S, Rebessi S, Tanori M, Giardullo P, Borra F, Pazzaglia S, Naus CC, Di Majo V, Saran A. Role of connexin43 and ATP in long-range bystander radiation damage and oncogenesis in vivo. *Oncogene*. 2011;30(45):4601-8. doi: 10.1038/onc.2011.176. ■



**Top** (l to r): Jay Perrier; Igor Shuryak; Mike Yuan-Cho Lee, Jingsong Yuan. **Second row** (l to r): Tom Hei; Maria Taveras; Kevin Hopkins. **Third row** (l to r): David Brenner, Charles Geard, Gerhard Randers-Pehrson; Lance Redford; Howard Lieberman; Mikhail Repin. **Fourth Row** (l to r): Andrew Harkin, Margaret Zhu; Gerhard Randers-Pehrson.

# CELLULAR AND MOLECULAR STUDIES



# The Impact of MEK5 on Prostate Cancer Cell Survival

Stephanie Sanchez<sup>a</sup>, Howard B. Lieberman, and Constantinos G. Broustas

## Introduction

Prostate cancer is the second most common cancer in men. The family of mitogen-activated protein kinases (MAPK) plays an essential role in the initiation and progression of prostate cancer. Moreover, aberrant activation of MAPKs interferes with anti-cancer treatment of human prostate tumors.

Mitogen-activated protein kinase kinase 5 (MAP2K5, MEK5, or MKK5), belongs to the family of MAP kinases [1]. It is activated by the upstream kinases MEKK2 and MEKK3 at S<sup>311</sup>/T<sup>315</sup>, or in some cases directly by c-Src. MEK5, in turn, phosphorylates and activates extracellular signal-regulated kinase 5 (ERK5) at T<sup>218</sup>/Y<sup>220</sup>. ERK5 constitutes a unique class of MAPKs that can modify the activity of targets not only as a kinase through phosphorylation, but also via physical interactions by acting as a transcriptional cofactor in a nonkinase manner. The MEK5/ERK5 pathway can be activated by various stimuli such as oxidative stress, growth factors, and mitogens downstream of receptor tyrosine kinases, and G protein-coupled receptors, and culminates in the activation of a large number of transcription factors, including c-JUN, NF-κB, CREB, and transcription factors that control the epithelial-mesenchymal transition (EMT) program [1].

Evidence supports a major role of MEK5/ERK5 in human tumorigenesis, although mechanistic studies in most cases are still lacking. It has been shown that MEK5 is constitutively active in human prostate cancer cells and MEK5 overexpression is associated with metastatic prostate cancer [2]. High expression of ERK5 in prostate cancer has also been found to correlate with poor disease-specific survival and could serve as an independent prognostic factor [3]. Furthermore, ERK5 expression in prostate cancer is associated with an invasive phenotype, whereas ERK5-overexpressing PC3 cells show increased migration and invasion *in vitro* and are dramatically more efficient in forming tumors *in vivo* [4].

## Results

To elucidate the role of MEK5 in prostate cancer cell viability we employed both genetic and pharmacological approaches. DU145 and PC3 prostate cancer cells were transiently transfected with either a specific, short interfering (si) RNA against *MEK5* or *luciferase* (*siLuc*; control) siRNA. In *siMEK5* transfected cells, MEK5 protein abundance was reduced by more than 90% in both cell lines, relative to *siLuc* transfected cells (Fig. 1A).

<sup>a</sup>Department of Environmental Health Sciences, Columbia University, New York, NY

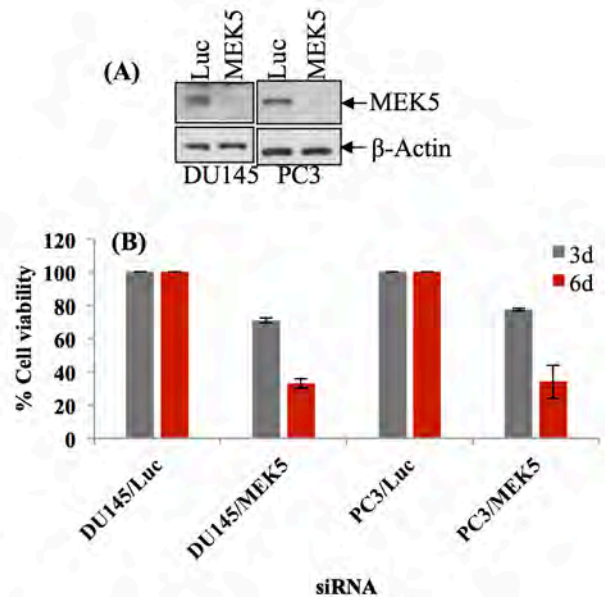


**Fig. 1.** Prostate cancer cell viability after knockdown of MEK5. (A) DU145 and PC3 cells were transiently transfected with a specific MEK5 siRNA or a control (*luciferase*) siRNA and three days later, cell lysates were immunoblotted with anti-MEK5 and anti-β-actin (loading control) antibodies. (B) Transiently transfected DU145 and PC3 cells with MEK5 or luciferase siRNA were seeded into 96-well plates and cell viability was assayed after 3 and 6 days post-transfection using the CellTiter 96 non-radioactive cell viability assay. Data are mean ± SD (n=3).

Next, we studied the impact of MEK5 depletion on DU145 and PC3 cell viability. Cells were transiently transfected with *MEK5* or *luciferase* siRNA and a day later cells were seeded into 96-well plates, in triplicate. Cell viability was measured after 3 and 6 days by using the CellTiter 96 non-radioactive cell viability assay (Promega). Control (*luciferase* siRNA) cell viability was set at 100%. Three days post-transfection, viability of *siMEK5* cells was 71 ± 1.4% and 77.5 ± 0.7% for DU145 and PC3 cells, respectively, compared with control cells (Fig. 1B). However, after 6 days, the percentage of viability was reduced to 33 ± 2.8% and 34 ± 9.9% for DU145 and PC3, respectively, compared with control cells (Fig. 1B). These results demonstrate that MEK5 is required for prostate cancer cell viability.

To confirm the role of MEK5 in prostate cancer cell survival, we used a small-molecule inhibitor, BIX02189, which is a highly selective MEK5 inhibitor [5]. This inhibitor does not display appreciable activity towards a panel of 79 kinases, including MEK1/2 kinases, which are closely related to MEK5 in terms of sequence similarity and phosphorylation of consensus motif (threonine-glutamate-tyrosine, TEY) [5]. As this inhibitor has not

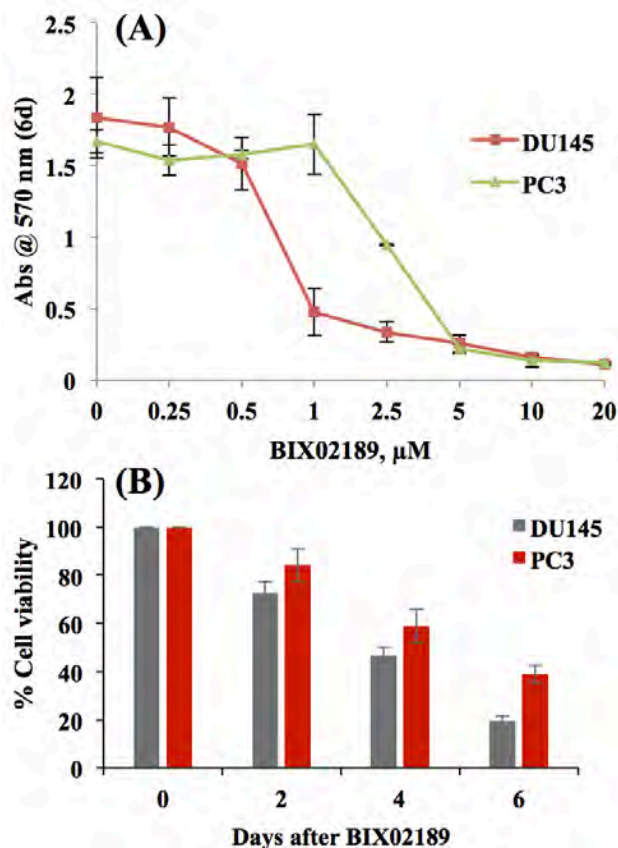


**Fig. 2.** Prostate cancer cell viability after inhibiting MEK5 activity. (A) DU145 and PC3 cells were treated with the indicated concentrations of BIX02189 inhibitor and cell viability was measured 6 days later with the CellTiter 96 non-radioactive cell viability assay. (B) DU145 and PC3 cells were treated with the MEK5-specific inhibitor BIX02189 (10  $\mu\text{M}$ ) and cell viability was assessed after 0, 2, 4, and 6 days as described in (A). Data are mean  $\pm$  SD ( $n=3$ ).

been previously used with prostate cancer cells, we performed a dose-response experiment with different concentrations of the inhibitor and assessed the impact on DU145 and PC3 cell viability after 6 days of incubation. As depicted in Fig. 2A, BIX02189 reduced both DU145 and PC3 cell viability. The  $\text{GI}_{50}$  (drug concentration required to achieve 50% growth inhibition) was 0.75  $\mu\text{M}$  and 2.50  $\mu\text{M}$  for DU145 and PC3 cells, respectively.

Finally, we carried out a time-course experiment with the inhibitor. Treatment of DU145 and PC3 cells with 10

$\mu\text{M}$  of BIX02189 resulted in progressively less viability for both cell lines, at 0, 2, 4, and 6 days after addition of the inhibitor (Fig. 2B). At these times DU145 cell viability was 100%,  $72.7 \pm 4.7\%$ ,  $46.8 \pm 3.4\%$ ,  $19.3 \pm 2.1\%$ , whereas the corresponding values for PC3 cells were 100%,  $84.3 \pm 6.8\%$ ,  $59 \pm 7\%$ , and  $39 \pm 3.8\%$ . These results provide further evidence that MEK5 is essential for the viability of prostate cancer cells.

## Conclusions

MEK5 activity has a profound impact on prostate cancer cell viability as can be assessed by MEK5 knockdown, as well as kinase activity inhibition using a MEK5-specific small-molecule inhibitor. The mechanistic details of MEK5/ERK5 function on prostate cancer cells are currently not known and will be the subject of future studies.

## References

1. Drew BA, Burow ME, Beckman BS. (2012). MEK5/ERK5 pathway: the first fifteen years. *Biochim Biophys Acta.* 1825:37-48.
2. Mehta PB, Jenkins BL, McCarthy L, Thilak L, Robson CN, Neal DE, Leung HY. (2003). MEK5 overexpression is associated with metastatic prostate cancer, and stimulates proliferation, MMP-9 expression and invasion. *Oncogene.* 22:1381-9.
3. McCracken SR, Ramsay A, Heer R, Mathers ME, Jenkins BL, Edwards J, Robson CN, Marquez R, Cohen P, Leung HY. (2008). Aberrant expression of extracellular signal-regulated kinase 5 in human prostate cancer. *Oncogene.* 27:2978-88.
4. Ramsay AK, McCracken SR, Soofi M, Fleming J, Yu AX, Ahmad I, Morland R, Machesky L, Nixon C, Edwards DR, Nuttall RK, Seywright M, Marquez R, Keller E, Leung HY. (2011). ERK5 signalling in prostate cancer promotes an invasive phenotype. *Br J Cancer.* 104:664-72.
5. Tataka RJ, O'Neill MM, Kennedy CA, Wayne AL, Jakes S, Wu D, Kugler SZ Jr, Kashem MA, Kaplita P, Snow RJ. (2008). Identification of pharmacological inhibitors of the MEK5/ERK5 pathway. *Biochem Biophys Res Commun.* 377:120-5. ■



(l to r): Gerhard Randers-Pehrson, Lubomir Smilenov, Guy Garty and Hal Swartz, Andrew Harkin.

# RAD9 Knockdown Represses Metastasis-associated Gene Anterior Gradient 2 in Prostate Cancer

Constantinos G. Broustas and Howard B. Lieberman

## INTRODUCTION

Despite successes in treating localized primary prostate tumors, metastatic prostate cancer poses a real challenge and remains essentially incurable. Therefore, elucidating the mechanism of metastasis will offer rational approaches to intervention with great benefit for the patient in the clinic.

RAD9 displays pleiotropic functions [1]. As part of the RAD9-HUS1-RAD1 complex, it acts as a sensor of DNA damage that enables ATR kinase to phosphorylate and activate its downstream effector CHK1. In addition, RAD9 promotes base excision repair, nucleotide excision repair, mismatch repair, and homologous recombination. Moreover, human RAD9 can function as a sequence-specific transcription factor. Specifically, RAD9 can bind to p53 DNA-binding consensus sequences in the promoter region of *CDKN1A* (p21<sup>Waf1/Cip1</sup>) [2] and *NEIL1* [3], and enhance transcription of these genes.

Aberrant RAD9 expression has been associated with breast, lung, skin, thyroid, and gastric cancers [1]. We have shown previously that RAD9 is overexpressed in human prostate cancer specimens as well as prostate cancer cell lines [4]. Most importantly, down-regulation of RAD9 in human tumor cell line xenografts impairs growth in nude mice, thus establishing a causative role for RAD9 in prostate cancer [4]. Furthermore, immunohistochemical analysis of non-cancer and tumor prostate specimens showed that RAD9 expression increased along with cancer progression stages, suggesting a role for RAD9 in prostate malignant progression [4].

The AGR2 protein is a member of the oxidoreductase family of protein disulphide isomerases (PDIs) [5]. The protein is localized in various cellular compartments, including the endoplasmic reticulum, the cytosol, the plasma membrane, and the nucleus, as well as the extracellular space. AGR2 is involved in numerous biological processes including cell transformation, cell migration and invasion, cell adhesion, as well as regulation of p53 [5]. Moreover, increased levels of AGR2 in various tumors have been associated with increased tumor growth, metastasis, and drug resistance. AGR2 protein levels are elevated in prostate cancer and downregulation of AGR2 decreases metastatic behavior [6]. Given the roles of RAD9 and AGR2 in prostate cancer, we addressed whether the two proteins are mechanistically related.

## RESULTS

We have shown previously that RAD9 has a functional role in human prostate tumorigenesis and is associated with metastasis [4]. Furthermore, RAD9 affects a number of *in vitro* characteristics of metastasis, such as cell motility, invasion, anoikis resistance, and anchorage-independent growth [7]. Moreover, RAD9 silencing causes a reduction in integrin  $\beta 1$  (ITGB1) protein levels in prostate cancer cells, whereas ectopic expression of RAD9 results in increased levels of ITGB1 [7]. Interestingly, recent experimental evidence has shown that in addition to ITGB1, RAD9 is required to stabilize a number of proteins, including DDB2 (damage-specific DNA binding protein 2) [8], ATRIP (ATR interacting protein) [9], and NEIL1 (nei1-like DNA glycosylase 1) [3] by an as yet unknown mechanism. As AGR2 can act as a chaperone to stabilize various proteins, we examined the relationship between RAD9 and AGR2. We found that RAD9 controls AGR2 mRNA and protein levels in prostate cancer cells.

### **RAD9 silencing causes decreased mRNA levels of AGR2 in PC3 human prostate cancer cells**

Preliminary experiments showed that AGR2 protein is abundantly expressed in PC3 cells with somewhat lower levels in LNCaP cells, whereas it is hardly detectable in DU145 cells. Thus, we used PC3 cells for our RAD9 knockdown experiments. We first performed quantitative RT-PCR to examine mRNA levels of AGR2 in PC3 cells that stably expressed an insertless retroviral vector (*shControl*) or *shRAD9* (clones 1 and 2), and the results were normalized against expression of glyceraldehyde-3-phosphate dehydrogenase (GAPDH) mRNA. As shown in Fig. 1A, AGR2 mRNA levels in both clones of

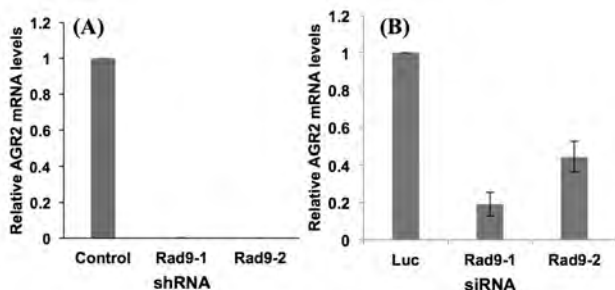


**Figure 1.** Depletion of RAD9 in PC3 cells reduces AGR2 mRNA. (A) Quantitative RT-PCR using RNA isolated from PC3 cells stably expressing *shControl*, or *shRAD9* (two clones) were assayed for AGR2 expression. (B) Quantitative RT-PCR using RNA isolated from PC3 cells transiently expressing control luciferase or two non-overlapping RAD9 siRNAs. AGR2 mRNA level was normalized against GAPDH mRNA abundance. Data are mean  $\pm$  SD (n=3).

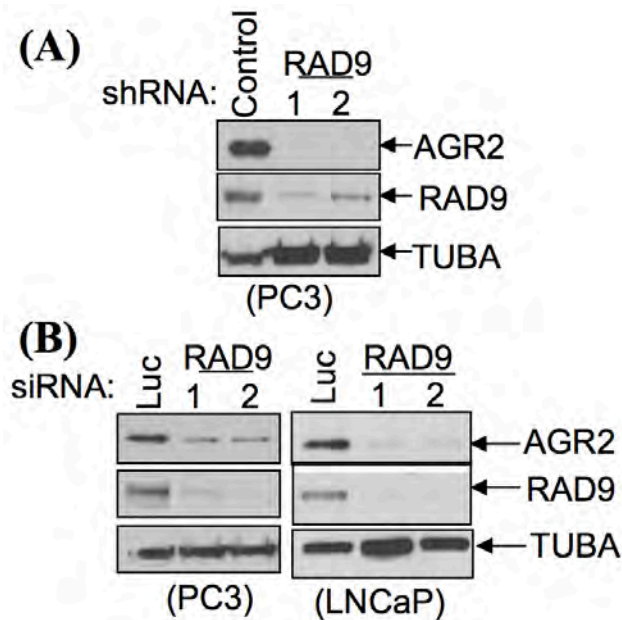


**Figure 2.** *Rad9* expression modulates *AGR2* protein levels. (A) Stable down-regulation of *RAD9* in PC3 (two clones) results in diminished levels of *AGR2* protein compared with shControl cells. (B) PC3 (left) or LNCaP (right) cells were transiently transfected with control (*luciferase*) or *RAD9-1*, or *RAD9-2* siRNAs and immunoblotted sequentially with *AGR2*, *RAD9* and  $\alpha$ -tubulin (loading control) antibodies.

PC3/sh*RAD9* cells were reduced by more than 90% compared with *AGR2* mRNA from PC3/shControl cells. We then transiently transfected PC3 cells with two non-overlapping *RAD9* or a control (*luciferase*) siRNAs, and two days later, we analyzed *AGR2* transcript levels. We found that there was a 60-80% reduction in *AGR2* mRNA in *RAD9* siRNA-transfected cells (Fig. 1B).

#### Targeted reduction of endogenous *RAD9* protein levels in human prostate cancer cells causes decreased levels of *AGR2* protein

We then proceeded to evaluate *AGR2* protein levels in *RAD9*-depleted cells. Stable knockdown of *RAD9* in PC3 cells (two clones) resulted in a dramatic reduction in *AGR2* protein levels (Fig. 2A). In contrast, *AGR2* knockdown in PC3 cells did not affect *RAD9* protein levels (not shown), implying that *RAD9* lies upstream of *AGR2*. Finally, transient transfection of PC3 cells with two different *RAD9* siRNAs diminished *AGR2* protein levels by approximately 80% (Fig. 2B, left panel). These results were further corroborated by transiently transfecting a second prostate cancer cell line, LNCaP (Fig. 2B, right panel), and demonstrating a more than 90% decrease in *AGR2* protein levels.

#### CONCLUSIONS

We provide *in vitro* evidence that supports the association of *RAD9* with *AGR2* in PC3 and LNCaP prostate cancer cell lines. Silencing of *RAD9* diminishes pro-metastatic *AGR2* at both the mRNA and protein levels. Future studies will determine (1) how *RAD9* controls *AGR2* gene expression, and (2) what is the contribution of *AGR2* to *RAD9*-induced cell motility and invasion, as well as anoikis resistance.

#### References

1. Broustas CG, Lieberman HB. Contributions of *RAD9* to tumorigenesis. (2012) *J Cell Biochem* 113:742-51.
2. Yin Y, Zhu A, Jin YJ, Liu YX, Zhang X, Hopkins KM, Lieberman HB. (2004) Human *RAD9* checkpoint control/proapoptotic protein can activate transcription of p21. *Proc Natl Acad Sci U S A*. 101:8864-9.
3. Panigrahi SK, Hopkins KM, Lieberman HB. (2015). Regulation of NEIL1 protein abundance by *RAD9* is important for efficient base excision repair. *Nucleic Acids Res*. 43:4531-46.
4. Zhu A, Zhang CX, Lieberman HB. (2008) *Rad9* has a functional role in human prostate carcinogenesis. *Cancer Res*. 68:1267-74.
5. Brychtova V, Mohtar A, Vojtesek B, Hupp TR. (2015). Mechanisms of anterior gradient-2 regulation and function in cancer. *Semin Cancer Biol*. 33:16-24.
6. Zhang Y, Ali TZ, Zhou H, D'Souza DR, Lu Y, Jaffe J, Liu Z, Passaniti A, Hamburger AW. (2010). *ErbB3* binding protein 1 represses metastasis-promoting gene anterior gradient protein 2 in prostate cancer. *Cancer Res*. 70:240-8.
7. Broustas CG, Zhu A, Lieberman HB. (2012). *Rad9* protein contributes to prostate tumor progression by promoting cell migration and anoikis resistance. *J Biol Chem* 287:41324-41333.
8. Li T, Wang Z, Zhao Y, He W, An L, Liu S, Liu Y, Wang H, Hang H. (2013). Checkpoint protein *Rad9* plays an important role in nucleotide excision repair. *DNA Repair (Amst)*. 12:284-92.
9. Peng XJ, Liu SJ, Bao CM, Liu YZ, Xie HW, Cai YH, Li BM, Hang HY, Ding X. (2015). Regulation of ATRIP protein abundance by *RAD9* in the DNA damage repair pathway. *Cell Mol Biol (Noisy-le-grand)*. 61:31-6. ■

# DNA Damage Repair Protein Rad9 Regulates Abundance of the MRN Complex Proteins Mre11 and Nbs1

Li Wang and Howard B. Lieberman

Genetic material must be maintained throughout life so that it remains functionally intact and is faithfully transmitted to progeny. To meet this challenge, cells have evolved a set of complementary DNA damage response (DDR) pathways and dedicated protein machineries that arrest cell cycle progression, thus providing a time window for repair. DNA damage response and repair proteins are centrally involved in genome maintenance pathways. The heterotrimeric Rad9-Rad1-Hus1 (9-1-1) complex is a PCNA-like clamp that is loaded onto DNA at structures resulting from damage and is important for initiating and maintaining the checkpoint response. The DNA damage repair protein Rad9 is regulated by phosphorylation and by differential interactions with several protein partners, which likely determines the multiple functions of Rad9.

The MRN (Mre11-Rad50-Nbs1) complex has been implicated in many aspects of the DNA damage response. It is a major sensor of DNA double strand breaks that plays essential roles in DNA repair processes and in the DDR. The MRN complex also has a key role in activation of ATM (ataxia telangiectasia mutated), in particular the nuclease activity of Mre11 plays an important role in the activation of Chk1 in response to stalled replication forks. Meanwhile, the activation of Chk1 in response to stalled replication forks involves a complex pathway including Rad9, suggesting that this protein and the MRN complex might be connected in a unique pathway. So far, very few papers have addressed how MRN complex expression is controlled, most often only reporting on its deregulation in cancer cells. Indeed, *Mre11* and *Rad50* are repressed by p63 and p73 in response to anticancer drugs [1], while Foxm1 and c-Myc stimulate and hypoxia represses *Nbs1* expression [2-4]. Intriguingly, constitutive *Mre11*, *Nbs1* or *Rad50* knockout mice are inviable, indicating that all three components are involved in pathway/s whose integrity is essential for mammalian development.

Here, we show that Rad9 transcriptionally controls expression of two components of the MRN complex, *Mre11* and *Nbs1*, but not *Rad50* in mouse embryo stem cells (Figure 1). Future work will focus on exploring the functional connections between Rad9 and the MRN complex.

## References

1. Lin YL, Sengupta S, Gurdziel K, Bell GW, Jacks T, Flores ER. p63 and p73 transcriptionally regulate genes involved in DNA repair. *PLoS Genet* 2009; 5: e1000680.
2. Chiang YC, Teng SC, Su YN, Hsieh FJ, Wu KJ. c-Myc directly regulates the transcription of the NBS1 gene involved in DNA double-strand break repair. *J Biol Chem* 2003; 278: 19286–19291.
3. Khongkow P, Karunarathna U, Khongkow M, Gong C, Gomes AR, Yague E et al. FOXM1 targets NBS1 to regulate DNA damage-induced senescence and epirubicin resistance. *Oncogene* 2014; 33: 4144–4155.
4. To KK, Sedelnikova OA, Samons M, Bonner WM, Huang LE. The phosphorylation status of PAS-B distinguishes HIF-1alpha from HIF-2alpha in NBS1 repression. *EMBO J* 2006; 25: 4784–4794. ■

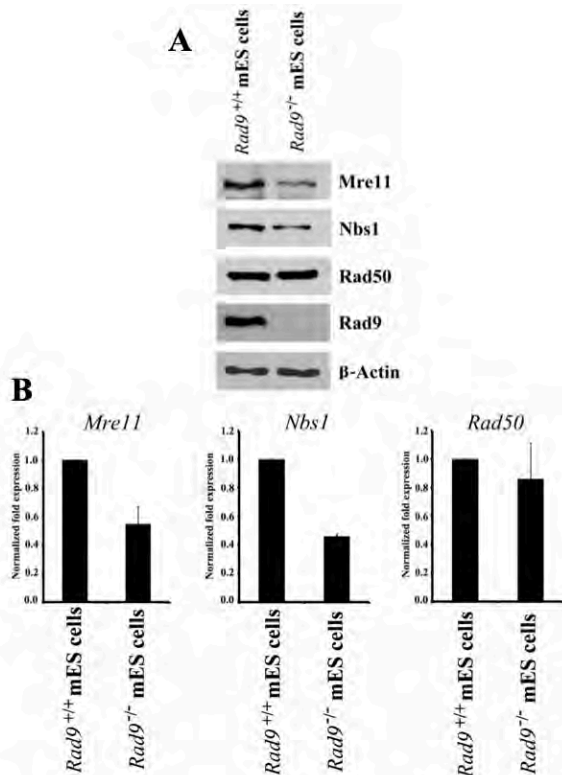


**Figure 1.** Expression of the MRN complex is transcriptionally controlled by Rad9 in mES cells (A) Analysis of MRN complex expression in Rad9<sup>+/+</sup> and Rad9<sup>-/-</sup> mES cell lines. Whole extracts isolated from cells were analyzed by immunoblotting using either anti-Mre11, Nbs1, or Rad50 antibodies. β-actin served as a loading control. (B) Total RNA from Rad9<sup>+/+</sup> and Rad9<sup>-/-</sup> mES cells was used to perform qRT-PCR with *Mre11*, *Nbs1* and *Rad50* gene-specific primers. Error bars represent the standard deviation of three experiments.

# Mechanistic Modeling of Dose and Dose Rate Dependencies of Radiation-Induced DNA Double Strand Break Rejoining Kinetics in *Saccharomyces cerevisiae*<sup>a</sup>

Igor Shuryak

Mechanistic modeling of DNA double strand break (DSB) rejoining is important for quantifying and medically exploiting radiation-induced cytotoxicity (e.g. in cancer radiotherapy). Most radiation-induced DSBs are quickly-rejoinable and are rejoined within the first 1-2 hours after irradiation. Others are slowly-rejoinable (persist for several hours), and yet others are essentially unrejoinable (persist for >24 hours). The dependencies of DSB rejoining kinetics on radiation dose and dose rate remain incompletely understood. We hypothesize that the fraction of slowly-rejoinable and/or unrejoinable DSBs increases with increasing dose/dose rate. This radiation-dependent (RD) model was implemented using differential equations for three DSB classes: quickly-rejoinable, slowly-rejoinable and unrejoinable. Radiation converts quickly-rejoinable to slowly-rejoinable, and slowly-rejoinable to unrejoinable DSBs.

In the proposed RD model (schematically summarized in Fig 1), radiation (with dose rate R) produces three DSB classes (DSB1, DSB2, DSB3) with yields (per unit dose) of  $k_1$ ,  $k_2$  and  $k_3$ , respectively. Quickly-rejoinable DSBs (DSB1) and slowly-rejoinable DSBs (DSB2) are rejoined with rates  $v_1$  and  $v_2$ , respectively; DSB3 are unrejoinable. Radiation converts DSB1 to DSB2 and DSB2 to DSB3 with rates proportional to parameters  $q_1$  and  $q_2$ , respectively. The model contains seven parameters:  $k_1$ ,  $k_2$ ,  $k_3$ ,  $v_1$ ,  $v_2$ ,  $q_1$  and  $q_2$ . These assumptions are mathematically represented by the following system of differential equations:

$$\begin{aligned}\frac{dDSB_1(t)}{dt} &= k_1 \times R - (v_1 + q_1 \times R) \times DSB_1(t); \\ \frac{dDSB_2(t)}{dt} &= k_2 \times R - (v_2 + q_2 \times R) \times DSB_2(t) \\ &\quad + q_1 \times R \times DSB_1(t); \\ \frac{dDSB_3(t)}{dt} &= k_3 \times R + q_2 \times R \times DSB_2(t)\end{aligned}$$

These equations are analytically solvable. Linear quadratic (LQ) approximations to these solutions (which are computationally convenient and can be compared to analogous approximations of other kinetic models) are also easily obtainable.

In the two-lesion kinetic (TLK) model [1] (schematically summarized in Fig 1), radiation also

produces three DSB classes with yields (per unit dose) of  $c_1$ ,  $c_2$  and  $c_3$ , respectively; DSB1 and DSB2 are rejoined with rates  $\lambda_1$  and  $\lambda_2$ , respectively; DSB3 are unrejoinable. DSB1 and DSB2 are “fixed” to become DSB3 with rates  $\varepsilon_1$  and  $\varepsilon_2$ , respectively. DSB1 interact with each other (by quadratic mis-rejoining) with rate  $\eta_1$ , and DSB2 interact with each other with rate  $\eta_2$ . DSB1 interact with DSB2 with rate  $\eta_{1,2}$ . The model contains ten parameters:  $c_1$ ,  $c_2$ ,  $c_3$ ,  $\lambda_1$ ,  $\lambda_2$ ,  $\varepsilon_1$ ,  $\varepsilon_2$ ,  $\eta_1$ ,  $\eta_2$ , and  $\eta_{1,2}$ . These assumptions are represented by the following system of differential equations:

$$\begin{aligned}\frac{dDSB_1(t)}{dt} &= c_1 \times R - (\varepsilon_1 + \lambda_1) \\ &\quad \times DSB_1(t) - (\eta_1 \times DSB_1(t) \\ &\quad + \eta_{1,2} \times DSB_2(t)) \times DSB_1(t); \\ \frac{dDSB_2(t)}{dt} &= c_2 \times R - (\varepsilon_2 + \lambda_2) \\ &\quad \times DSB_2(t) - (\eta_2 \times DSB_2(t) \\ &\quad + \eta_{1,2} \times DSB_1(t)) \times DSB_2(t); \\ \frac{dDSB_3(t)}{dt} &= c_3 \times R + \varepsilon_1 \times DSB_1(t) + \varepsilon_2 \times DSB_2(t)\end{aligned}$$

Here, we have included a term for direct yield of unrejoinable DSBs (parameter  $c_3$ ) for completeness, because although this term was absent from the original TLK model [1], it was introduced in subsequent similar formalisms. There is no analytical solution to the TLK model.

We used large published data sets on DSB rejoining in yeast exposed to sparsely-ionizing (electrons and  $\gamma$ -rays, single or split-doses, high or low dose rates) and densely-ionizing ( $\alpha$ -particles) radiation [2-5] to compare the performance of the proposed RD formalism and the established TLK model. These yeast DSB rejoining data were measured within the radiation dose range relevant for clonogenic cell survival, whereas in mammalian cells DSB rejoining is usually measured only at supra-lethal doses for technical reasons.

Best-fit predictions of the RD and TLK models after single-dose exposures are compared with the data (Figs 2-4). Visual inspection clearly shows that at long times ( $\geq 24$  h) after sparsely-ionizing or densely-ionizing radiation only the RD model reproduced the upwardly-curving dose responses for remaining unrejoined DSBs, whereas the TLK model predicted linear dose responses and

<sup>a</sup>Adapted from: Shuryak I (2016) *PLoS One* 11: e0146407; 10.1371/journal.pone.0146407.

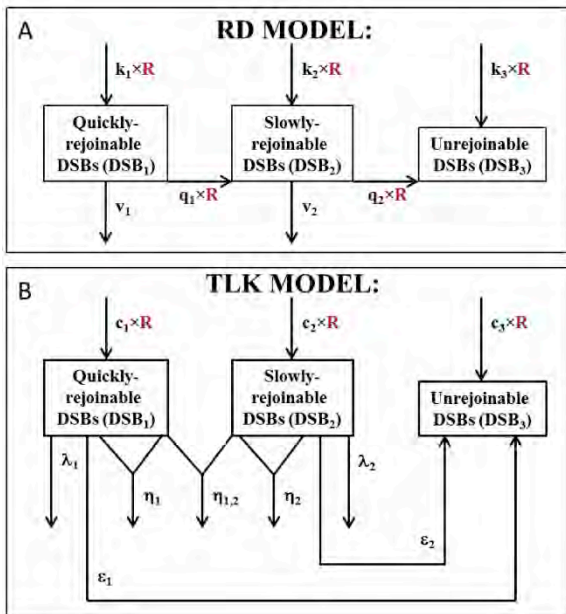


**Figure 1.** Schematic representations of the RD (panel A) and TLK (panel B) models. In the RD model, radiation (with dose rate  $R$ ) produces three DSB classes ( $DSB_1$ ,  $DSB_2$ ,  $DSB_3$ ) with yields (per unit dose) of  $k_1$ ,  $k_2$  and  $k_3$ , respectively.  $DSB_1$  and  $DSB_2$  are rejoined with rates  $v_1$  and  $v_2$ , respectively;  $DSB_3$  are unrejoinable. Radiation converts  $DSB_1$  to  $DSB_2$  and  $DSB_2$  to  $DSB_3$  with rates proportional to parameters  $q_1$  and  $q_2$ , respectively. In the TLK model, radiation also produces three DSB classes with yields (per unit dose) of  $c_1$ ,  $c_2$  and  $c_3$ , respectively;  $DSB_1$  and  $DSB_2$  are rejoined with rates  $\lambda_1$  and  $\lambda_2$ , respectively;  $DSB_3$  are unrejoinable.  $DSB_1$  and  $DSB_2$  are "fixed" to become  $DSB_3$  with rates  $\epsilon_1$  and  $\epsilon_2$ , respectively.  $DSB_1$  interact with each other (by quadratic mis-rejoining) with rate  $\eta_1$ , and  $DSB_2$  interact with each other with rate  $\eta_2$ .  $DSB_1$  interact with  $DSB_2$  with rate  $\eta_{1,2}$ .

underestimated the data. For example, the mean measured number of DSBs/cell 72 hours after 2400 Gy of high dose rate (HDR) 30 MeV electrons was 30.2 (range: 24.7-35.6). The corresponding best-fit prediction from the RD model was 28.4, whereas the TLK model predicted 19.5 (Fig 2). The mean measured number of DSBs/cell 72 hours after 600 Gy of  $\alpha$ -particles was 20.1 (range: 9.6-30.9). The corresponding best-fit prediction from the RD model was 17.0, whereas the TLK model predicted 14.5 (Fig 4). Therefore, the tendency of the TLK model to underestimate the data at long times and high doses was evident for both sparsely- and densely-ionizing radiations, although it was more clear with the former. The number of split-dose data points (10) was too small for robust conclusions (i.e. both models visually approximated these data reasonably), and consequently we did not show the fits to these data graphically.

Although the number of HDR data points (157) for sparsely-ionizing radiation was much larger than the number of low dose rate (LDR) points (29), the RD model reasonably described DSB yields at both high and low dose rates using one set of parameters (Fig 4). In contrast, the TLK model was unable to do so: its fit was dominated

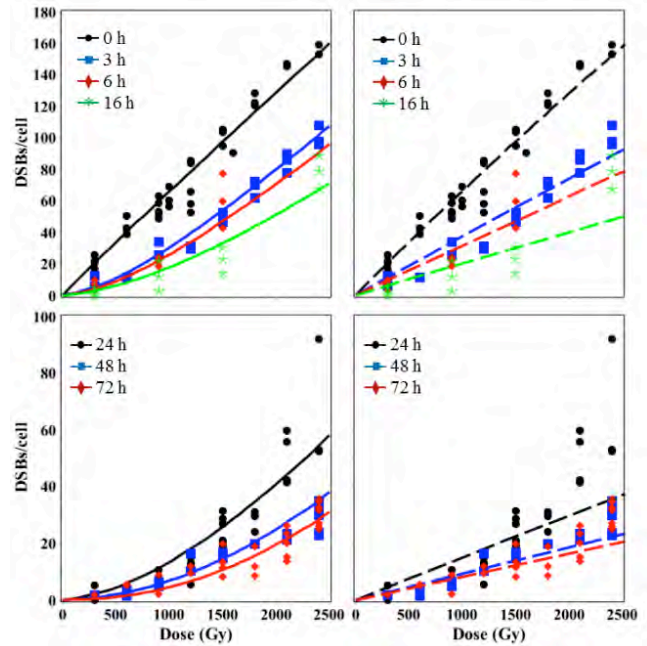


**Figure 2.** Dose dependence of best-fit model predictions (curves) for 30 MeV electron data (symbols). Solid lines = RD model, dashed lines = TLK model. The legend indicates times after HDR single-dose irradiation when DSBs were measured. In this and the following Figs, the left-most panels compare both models, the middle panels show the RD model only, and the right-most panels show the TLK model only.

by HDR data and LDR data were strongly overestimated (Fig 3). For example, the mean measured number of DSBs/cell 22 hours after 1650 Gy of LDR  $\gamma$ -rays was 5.6 (range: 4.2-6.4). The corresponding best-fit prediction from the RD model was 4.0, whereas the TLK model predicted 16.8 (Fig 3).

These visually apparent differences in model performance were quantified by relative and absolute goodness of fit (GOF) assessments. The RD model described both sparsely-ionizing and densely-ionizing

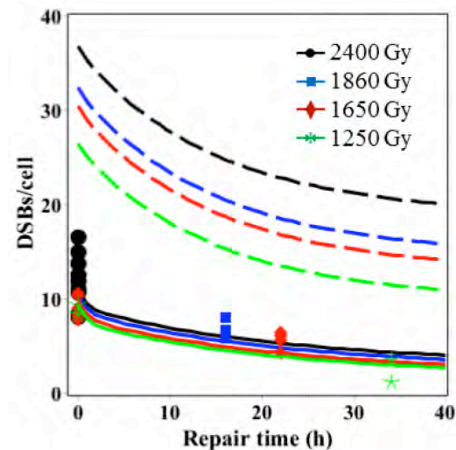


**Figure 3.** Time dependence of best-fit model predictions (curves) for LDR  $\gamma$ -ray data (symbols). Solid lines = RD model, dashed lines = TLK model. The legend indicates radiation doses.

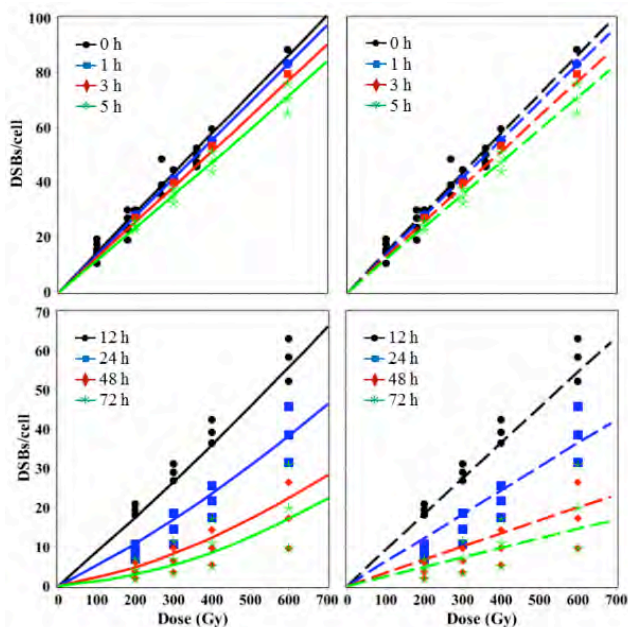


**Figure 4.** Dose dependence of best-fit model predictions (curves) for  $\alpha$ -particle data (symbols). Solid lines = RD model, dashed lines = TLK model. The legend indicates times after HDR single-dose irradiation when DSBs were measured.

radiation data much better than the TLK model: by 217 and 14 sample-size-adjusted Akaike information criterion units, respectively. This occurred because: the RD (but not the TLK) model reproduced the observed upwardly-curving dose responses for slowly-rejoinable/unrejoinable DSBs at long times after irradiation; the RD model adequately described DSB yields at both high and low dose rates using one parameter set, whereas the TLK model overestimated low dose rate data.

Because the TLK and RD models are based on different mechanistic assumptions, comparison of their performances on the same data enabled us to make the following observations about which putative mechanisms are most (or least) useful for describing DSB rejoining kinetics.

The TLK model contains 3 parameters ( $\eta_1$ ,  $\eta_2$ , and  $\eta_{1,2}$ ) for quadratic interactions between different DSBs within/between DSB classes (Fig 1). If some/all of these parameters have positive values, the model structure (Eq. 2) implies that, as the dose of HDR radiation (and hence the yield of DSBs just after irradiation) increase, the rate of DSB removal increases because quadratic interactions between DSBs become more frequent. Consequently, the quadratic interactions mechanism predicts that the fraction of DSBs that remain unrejoined at a given time after irradiation should decrease with increasing radiation dose. The dose response for unrejoined DSBs at a given time after irradiation is, therefore, predicted to be downwardly-curving (i.e. to have a negative second derivative).

In contrast, the data analyzed here suggest the opposite pattern: at higher doses, the fraction of DSBs that remain unrejoined at each measured time after irradiation increases, rather than decreases (Figs 2, 3, 4). Consequently, the observed dose response for unrejoined DSBs at a given time after irradiation is upwardly-curving (i.e. has a positive second derivative). This disparity between predictions and observations explains why the best-fit values of parameters  $\eta_1$ ,  $\eta_2$ , and  $\eta_{1,2}$  in the TLK model became zero: when quadratic interactions between DSBs do not occur, the TLK model predicts a linear dose response for unrejoined DSBs (Figs 2 and 4), which is closer to the data than a downwardly-curving one.

An important drawback of the TLK model's reliance on unrejoinable DSBs to approximate HDR data was that the best-fit yield of such DSBs (parameter  $c_3$ ) was too high to describe LDR data, leading to overestimation of these data (Fig 3). In other words, in the context of the TLK model, the observed DSB data at long times after HDR sparsely-ionizing radiation exposure appeared to be inconsistent with the data after LDR exposure.

In contrast, the proposed mechanism of radiation-dependent conversion of DSB classes present in the RD model (Fig 1) allowed the upwardly-curving dose response shape for DSBs left unrejoined after HDR

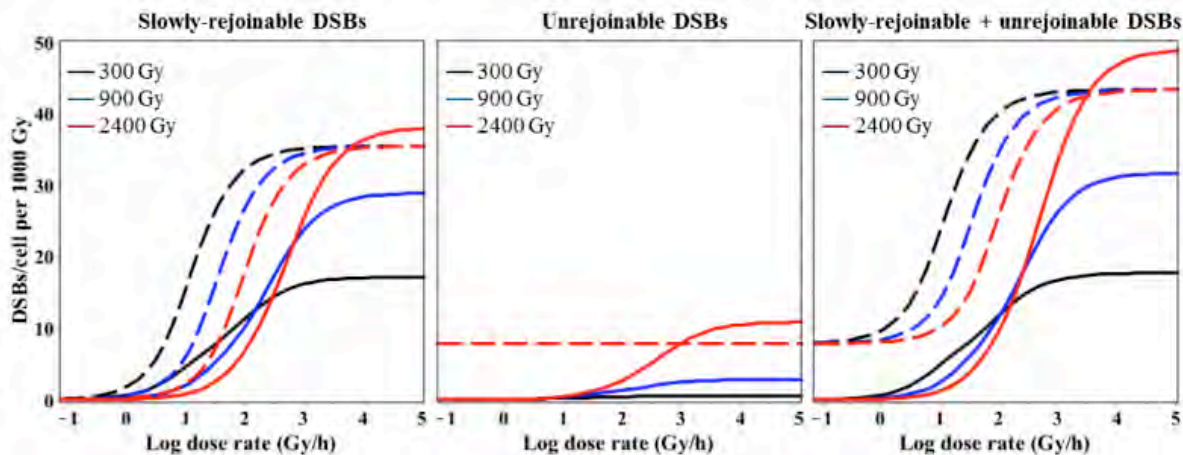


**Figure 5.** Dose rate dependence of best-fit model predictions for sparsely-ionizing radiation. Solid lines = RD model, dashed lines = TLK model. The legend indicates radiation doses.

radiation to be reproduced (Figs 2, 4). There was also no inconsistency between HDR and LDR data in the context of the RD model (Figs 2-4): both data sets were described with adequate GOF using one set of best-fit parameters. These results were obtained thanks to the fact that the RD model predicts that, at increasing doses/dose rates, DSB rejoining is increasingly impeded because more and more quickly-rejoinable DSBs are converted to slowly-rejoinable DSBs, some of which are in turn converted to unrejoinable ones.

The qualitative differences in dose and dose rate dependences of DSB rejoining predicted by the RD and TLK models (using best-fit parameter values) can be summarized as follows. The TLK model predicts that the yield of unrejoinable DSBs per unit dose is independent of both dose and dose rate, whereas the yield of slowly-rejoinable DSBs depends on dose rate but not on dose. The RD model, however, predicts that the yields of both slowly-rejoinable and unrejoinable DSBs depend on both dose and dose rate.

Our analysis suggests that the proposed mechanism of radiation-dependent conversion of DSB classes, which supports the hypothesis that DSB rejoining is progressively impeded at increasing radiation doses/dose rates, strongly enhanced the ability of kinetic models to describe DSB rejoining in yeast. In contrast, the analyzed data did not support the notion (represented in the TLK model) that interactions between different DSBs constitute an important route of DSB removal. However, interactions between DSBs which lead to transition into a different class of DSB would still be compatible with the

data. Our analysis also suggests that the time needed to rejoin a particular DSB depends mainly on the properties of this DSB and/or on radiation damage to nearby chromatin. These factors can be represented by the generic term “DSB complexity”, which depends not only on radiation type, but also on dose and dose rate.

### References

1. Stewart RD. Two-lesion kinetic model of double-strand break rejoining and cell killing. *Radiation Research*. 2001;156(4):365-78. 2. Frankenberg-Schwager M, Frankenberg D, Blocher D, Adamczyk C. Repair of DNA double-strand breaks in irradiated yeast cells under nongrowth conditions. *Radiation research*. 1980;82(3):498-510.
3. Frankenberg-Schwager M, Frankenberg D, Blocher D, Adamczyk C. Effect of dose rate on the induction of DNA double-strand breaks in eukaryotic cells. *Radiation research*. 1981;87(3):710-7.
4. Frankenberg-Schwager M, Frankenberg D, Harbich R, Beckonert S. Evidence against the "oxygen-in-the-track" hypothesis as an explanation for the radiobiological low oxygen enhancement ratio at high linear energy transfer radiation. *Radiat Environ Biophys*. 1994;33(1):1-8.
5. Frankenberg D, Frankenberg-Schwager M, Blocher D, Harbich R. Evidence for DNA double-strand breaks as the critical lesions in yeast cells irradiated with sparsely or densely ionizing radiation under oxic or anoxic conditions. *Radiation research*. 1981;88(3):524-32. ■



*Hongning Zhou, Ashish Jani, Chung-Man Leung (visiting fellow from Taiwan), Kunal Chaudhary, Youping Sun, Mercy Davidson, Simon Cheng, Dannis Wu, Christine Hellweg, Sherry Yan (medical student), Enyuan Shang, Winsome Walker, Vladimir Ivanov.*

# Genes Targeted by Therapeutic Drugs and an Antioxidant in a Breast Cancer Model

Gloria M. Calaf<sup>a,b</sup>, Richard Ponce-Cusi<sup>b</sup>, and Marcela Gallardo<sup>c</sup>

Breast carcinogenesis is a multistage process that involves mutations and cellular phenotypic alterations attributed to exposure both to exogenous environmental substances and endogenous agents, such as female hormones. In this study, we investigated expression of several genes that have been implicated in breast carcinogenesis, including *c-Ha-ras* and *Rho-A* from the Ras signaling pathway, the tumor suppressor *TP53*, and *caveolin*. *Rho-A* is a small GTPase protein known to regulate the actin cytoskeleton in the formation of stress fibers, and it is generally distributed in the nuclei of cancer cells [1, 2]. *TP53* is known as the guardian of the genome and it responds to stress signals and activates the transcription of genes, such as *BAX*, that are involved in cellular mechanisms including cell cycle control and apoptosis [3]. *Caveolin* forms specialized lipid rafts in the plasma membrane of mesenchymal cells [4].

Several candidates for treatment of breast cancer were tested in the current study. Pamidronate (Pam), one of the nitrogen-containing bisphosphonates, is used in the treatment of breast cancer metastases. It has recently been reported that it also can have an impact on cell proliferation and apoptosis [5-6]. 5-Fluorouracil (5-FU) is a chemotherapeutic agent used in the treatment of many solid cancers. 5-FU is known to arrest cell cycle and induce apoptosis in cancer cells [7]. Curcumin (Cur) is an antioxidant known as a natural yellow dietary pigment derived from the rhizome of the herb *Curcuma longa* [8], and is reported to have anti-cancer properties.

The aim of this study was to evaluate the expression of selected genes that could be regulated by these agents in a breast carcinogenesis *in vitro* model [9]. The model used for this study was developed from a normal immortalized breast epithelial cell line, MCF-10F, that was exposed to low doses of high LET (linear energy transfer) alpha particles (150 keV/ $\mu$ m), and cultured in the presence of 17 $\beta$ -estradiol. The model consists of the following cell lines: i) MCF-10F, ii) Alpha3 (malignant but non-tumorigenic), iii) Alpha5 (tumorigenic) and iv) Tumor2 (derived from Alpha5 after injection into nude mice). Previous results showed that compared with MCF-10F, Alpha5 and Tumor2 had increased cell proliferation and presented anchorage independence, invasive capabilities, and tumor formation in nude mice. Pam has

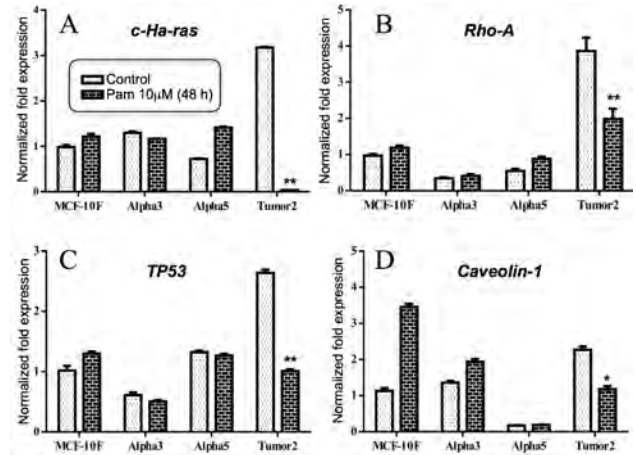


**Figure 1.** Effect of pamidronate (10  $\mu$ M for 48h) on A) *c-Ha-ras*, B) *Rho-A*, C) *TP53* and D) *Caveolin-1* gene expression evaluated by RT-qPCR. Bars represent the mean  $\pm$  S.E.M. of  $n=3$  experiments. Significance: \* $p<0.05$ , \*\* $p<0.01$ .

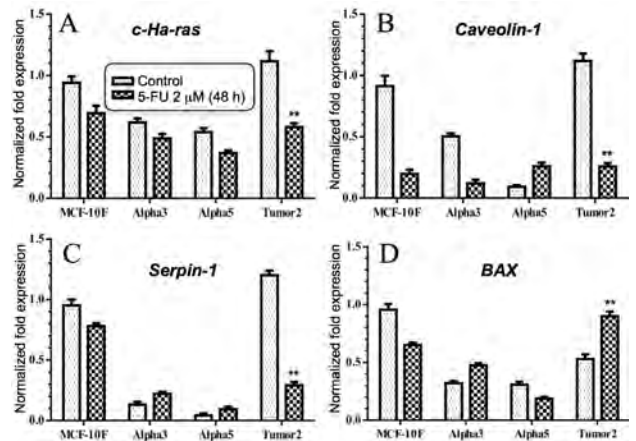


**Figure 2.** Effect of 5-FU (2  $\mu$ M for 48h) on A) *c-Ha-ras*, B) *Caveolin-1*, C) *Serpin-1* and D) *Bax* gene expression evaluated by RT-qPCR. Bars represent the mean  $\pm$  S.E.M. of  $n=3$  experiments. Significance: \* $p<0.05$ , \*\* $p<0.01$ .

also been shown to inhibit migration and invasion in both Alpha5 and Tumor2 cell lines [10].

For the gene expression study, MCF-10F and its derivatives were exposed to the LD<sub>50</sub> of Pam (10  $\mu$ M), 5-FU (2  $\mu$ M), and Cur (30  $\mu$ M), and mRNA levels for the selected genes were measured 48 hours later by RT-qPCR. LD<sub>50</sub> values were determined previously using a 48-hour MTT (3-(4,5-dimethylthiazol-2-yl)-2,5-diphenyltetrazolium bromide) assay. Pam treatment significantly decreased *c-Ha-ras*, *Rho-A*, *TP53* and *Caveolin-1* gene expression in the Tumor2 cell line (Figure 1). Similarly, 5-FU also significantly decreased

<sup>a</sup>Center for Radiological Research

<sup>b</sup>Instituto de Alta Investigación, Universidad de Tarapacá, Arica, Chile

<sup>c</sup>University of Chile, Santiago, Chile

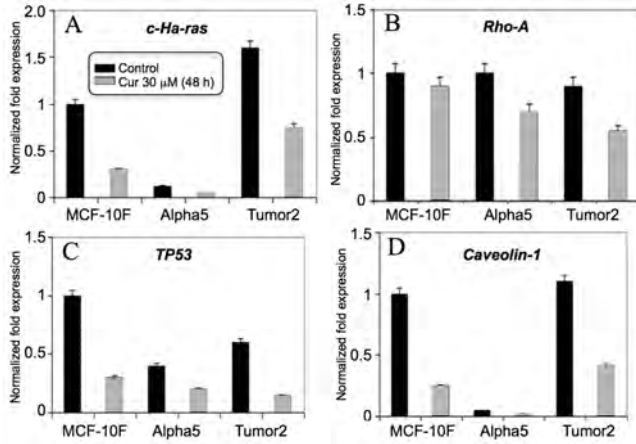


**Figure 3.** Effect of Curcumin (30 μM for 48h) on A) *c-Ha-ras*, B) *Rho-A*, C) *TP53* and D) *Caveolin-1* gene expression evaluated by RT-qPCR. Bars represent the mean±S.E.M. of n=3 experiments. Significance: \*p<0.05, \*\*p<0.01.

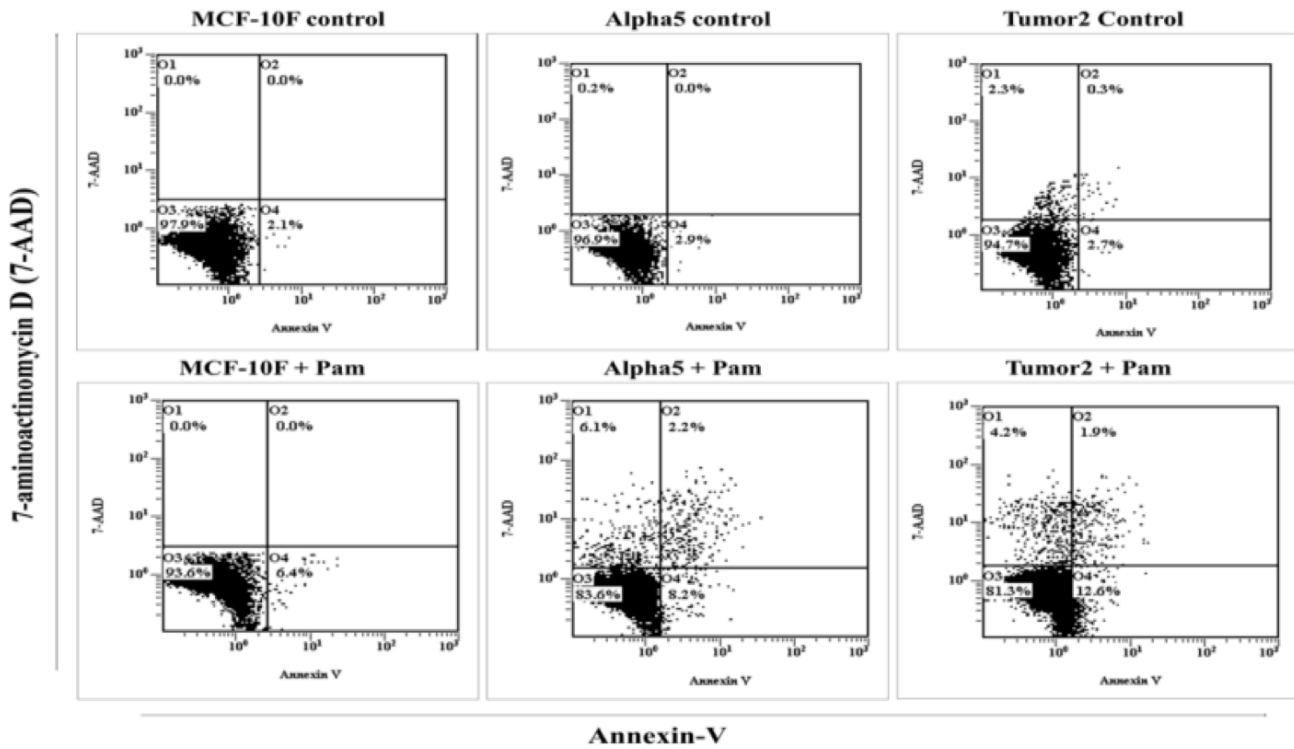


**Figure 4.** Apoptotic analysis of breast cancer cell lines by flow cytometry: Apoptotic effects of pamidronate (10 μM for 48h) was evaluated in MCF-10F, Alpha5 and Tumor2 cell lines compared to untreated controls. The upper left quadrant (O1) indicates cells undergoing necrosis; the upper right quadrant (O2), cells at the end stage of apoptosis; the lower left quadrant (O3), cells that are viable, or have no measurable apoptosis, and the lower right quadrant (O4), cells undergoing apoptosis. The percentage of the cells in apoptosis was determined by CXP analysis software.

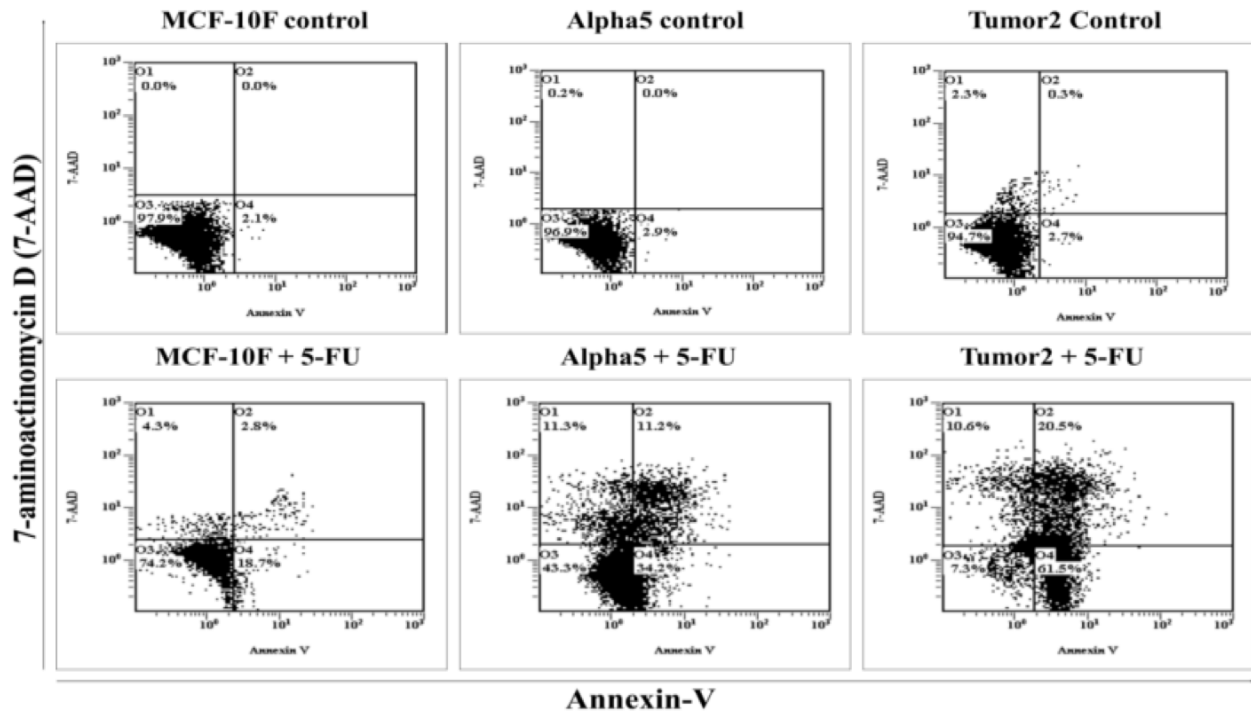


**Figure 5.** Apoptotic analysis of breast cancer cell lines by flow cytometry: The apoptotic effects of 5-FU (2  $\mu$ M for 48h) were evaluated in MCF-10F, Alpha5 and Tumor2 cell lines compared with untreated controls. The upper left quadrant (O1) indicates cells undergoing necrosis; the upper right quadrant (O2), cells at the end stage of apoptosis; the lower left quadrant (O3), cells that are viable, or have no measurable apoptosis, and the lower right quadrant (O4), cells undergoing apoptosis. The percentage of the cells in apoptosis was determined by CXP analysis software.

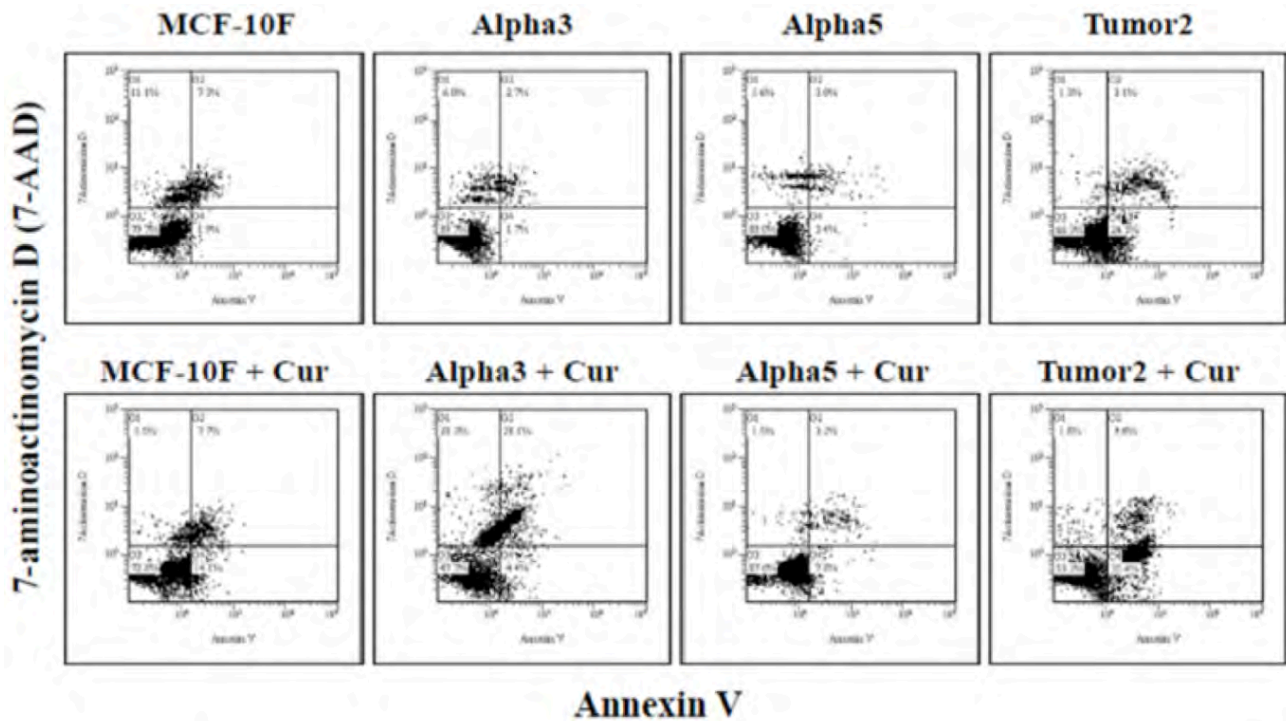


**Figure 6.** Apoptotic analysis of breast cancer cell lines by flow cytometry: Apoptotic effects of Curcumin (30  $\mu$ M for 48h) was evaluated in MCF-10F, Alpha5 and Tumor2 cell lines compared with their untreated controls. The upper left quadrant (O1) indicates cells undergoing necrosis; the upper right quadrant (O2), cells at the end stage of apoptosis; the lower left quadrant (O3), cells that are viable, or have no measurable apoptosis, and the lower right quadrant (O4), cells undergoing apoptosis. The percentage of the cells in apoptosis was determined by CXP analysis software.

expression of the *c-Ha-ras*, *Caveolin-1*, and *Serpin-1* genes in the Tumor2 cell line, but lead to a significant increase in *BAX* expression (Figure 2). Curcumin also decreased *c-Ha-ras*, *Rho-A*, *TP53*, and *Caveolin-1* gene expression in Tumor2, with a similar trend of decrease in the other cell lines (Figure 3).

The increased expression of the *BAX* gene observed in the Tumor2 cell line following 5-FU treatment may be related to the mechanism of apoptosis. Significant apoptotic activity was observed in both the Alpha5 and Tumor2 cell lines by flow cytometry (Figures 4-6). It can be concluded that in this cellular model of breast cancer, the therapeutic agents tested result in alterations of gene expression and induction of apoptosis.

*Grant support: FONDECYT #1120006 (GMC) and MINEDUC-UTA (GMC)*

### References

- Ridley AJ, Hall A. The small GTP-binding protein rho regulates the assembly of focal adhesions and actin stress fibers in response to growth factors. *Cell* 70: 389-399, 1992.
- Ridley AJ, Paterson HF, Johnston CL, Diekmann D and Hall A. The small GTP-binding protein rac regulates growth factor-induced membrane ruffling. *Cell* 70: 401-410, 1992.
- Donehower LA, Godley LA, Aldaz CM, Pyle R, Shi YP, Pinkel D, Gray J, Bradley A, Medina D and Varmus HE. The role of p53 loss in genomic instability and tumor progression in a murine mammary cancer model. *Prog Clin Biol Res* 395: 1-11, 1996.
- Witkiewicz AK, Dasgupta A, Sammons S, Er O, Potoczek MB, Guiles F, Sotgia F, Brody JR, Mitchell EP and Lisanti MP. Loss of stromal caveolin-1 expression predicts poor clinical outcome in triple negative and basal-like breast cancers. *Cancer Biol Ther* 10: 135-143, 2010.
- Wada K, Fukui K, Sawai Y, Imanaka K, Kiso S, Tamura S, and Hayashi N. Pamidronate induced anti-proliferative, apoptotic, and anti-migratory effects in hepatocellular carcinoma. *J Hepathology* 44: 142, 2006.
- Riebeling C, Forsea A-M, Raisova M, Orfanos CE, Geilen CC. The bisphosphonate pamidronate induces apoptosis in human melanoma cells in vitro. *Br J Cancer* 87: 366-371, 2002.
- Longley DB, Harkin DP and Johnston PG. 5-fluorouracil: Mechanism of action and clinical strategie. *Nat Rev Cancer* 3: 330-338, 2003.
- Reuter S, Eifes S, Dicato M, Aggarwal BB and Diederich M. Modulation of anti-apoptotic and survival pathways by curcumin as a strategy to induce apoptosis in cancer cells. *Biochemical Pharmacology* 76: 1340-1351, 2008.
- Calaf GM and Hei TK. Establishment of a radiation- and estrogen-induced breast cancer. *Carcinogenesis* 21: 769-776, 2000.
- Ponce-Cusi R and Calaf GM. Antitumor activity of pamidronate in a breast cancer model by targeting Rho-A gene expression. *Center for Radiological Research 2014 Annual Report*: 41-43, 2015. ■

## Oxygen Level Effects on Gene Expression in Aging IMR-90 Fibroblasts

*Shanaz A. Ghandhi, Xiuquan Luo<sup>a</sup>, David Boothman<sup>a</sup>, and Sally A. Amundson*

Cellular senescence in human fibroblasts is a well characterized phenomenon [1] accompanied by phenotypic changes in aging cells that gradually overtake the culture until almost all cells are terminally differentiated and will not divide further. Senescence in IMR-90 fibroblasts occurs at population doubling level (PDL) of ~65 [2], when cells are grown at normal atmospheric oxygen levels of 20%. However, this oxygen level is high compared with physiological levels, which

vary between 2-12%, depending on the tissue and location [3]. When IMR-90 cells are grown at 2% oxygen, their lifespan in culture can be further extended to >80 PDL, which may be a better representation of their growth potential.

We hypothesized that although there is no morphological difference between IMR-90 cells sub-cultivated to senescence at 2% oxygen and those cultured at 20% oxygen, gene expression may differ in these two conditions due to the triggering of different stress pathways. To examine this, we isolated total RNA from young and senescent IMR-90 cells cultured at 2% and 20% oxygen. We focused our analyses on a panel of ~96 genes, selected based on previous studies of stress-

<sup>a</sup>Department of Radiation Oncology, Simmons Comprehensive Cancer Center, UT Southwestern, Dallas, TX.

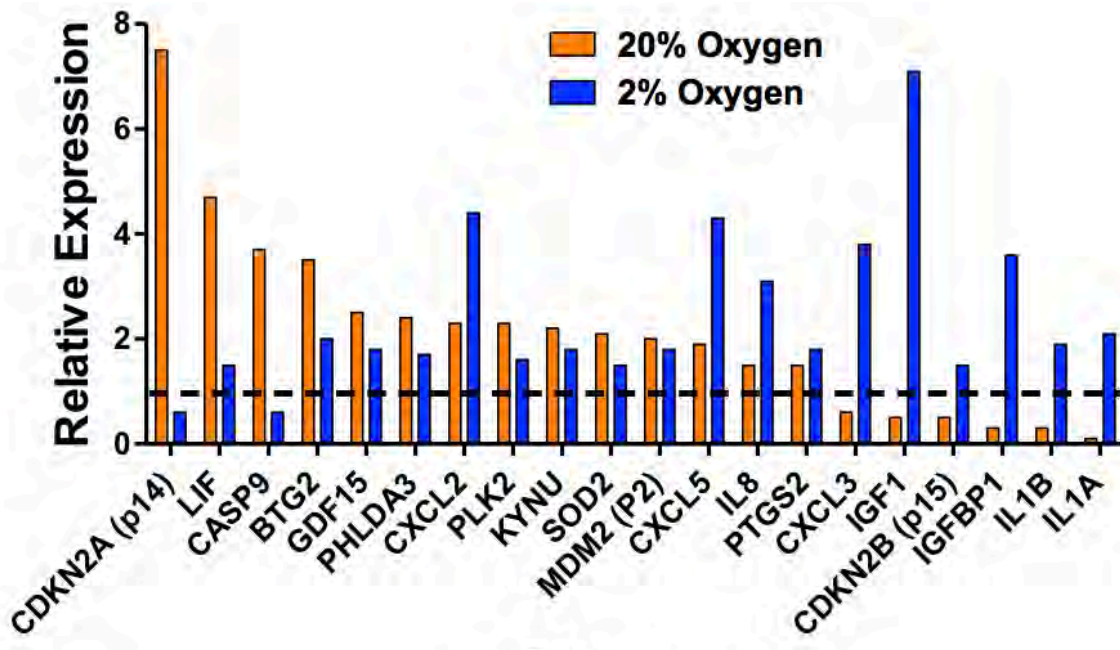


**Figure 1.** Effect of aging on gene expression in IMR-90 cells. Genes that were significantly ( $p < 0.05$ ) affected by aging are shown here and listed in decreasing order of fold change in senescent cells at 20% oxygen (yellow bars). The level of gene expression change in senescence IMR-90 cells at 2% oxygen is shown in blue bars. Fold change for each gene is the average of three independent experiments.

response signaling in IMR-90 cells after irradiation [4]. Expression of these genes was quantified using a Taqman® Low Density Array (TLDA) platform, and relative gene expression levels were calculated using corresponding young IMR-90 cells as calibrators and *UBC* (ubiquitin C) as the housekeeping gene.

Results from real time qRT-PCR analysis of gene expression in young and senescent IMR-90 cells are shown in Figure 1. Most of the genes were differentially expressed at the mRNA level based on age. Many of the genes chosen were known targets of p53, such as *GDF15*, *PHLDA3*, *PLK2* and *MDM2*, and responded similarly in senescent cells at both oxygen conditions.

It is interesting to note that gene expression changes were not always in the same direction, either up or down-regulated by age. Oxygen levels affected the age-associated expression of some genes, such as *p14<sup>ARF</sup>* and *CASP9*, which were up regulated in senescent IMR-90 at 20%, but down regulated in senescent IMR-90 at 2% oxygen. All fold change levels illustrated in Figure 1 were calculated using the corresponding young IMR-90 cells as calibrators, but some genes were also differentially expressed in young cells depending on the oxygen level. *CASP9* and *p14<sup>ARF</sup>* were 9.7 and 6.7 fold higher, respectively, in young cells at 2% compared to 20% oxygen, perhaps contributing to the observed different direction of expression change as the cells aged.

Other genes were expressed at higher levels in senescent IMR-90 at 2% oxygen, and at lower levels at 20%. These genes were *CXCL3*, *IGF1*, *CDKN2B (p15)*, *IGFBP1*, *IL1B* and *IL1A*. Differences seen here may

result from alterations in the NFκB signaling pathway in aging cells. The mRNA expression levels of these genes in young cells were not significantly different, with the exception of *IL1B* mRNA, which was 3.4 fold higher in young cells at 2% oxygen compared to 20%. The opposite effect of aging on the group of mRNA related to stress signaling pathways involving the transcription factor NFκB at 2% vs 20% oxygen is intriguing, and follow-up studies are needed to elucidate which stress response pathways may be involved in shaping the differential transcriptional landscape of aging cells cultured under different oxygen conditions.

## References

1. Lopez-Otin C, Blasco MA, Partridge L, Serrano M, Kroemer G: **The hallmarks of aging.** *Cell* 2013, **153**(6):1194-1217.
2. Luo X, Suzuki M, Ghandhi SA, Amundson SA, Boothman DA: **ATM regulates insulin-like growth factor 1-secretory clusterin (IGF-1-sCLU) expression that protects cells against senescence.** *PLoS One* 2014, **9**(6):e99983.
3. Atkuri KR, Herzenberg LA, Niemi AK, Cowan T, Herzenberg LA: **Importance of culturing primary lymphocytes at physiological oxygen levels.** *Proc Natl Acad Sci U S A* 2007, **104**(11):4547-4552.
4. Ghandhi SA, Yaghoubian B, Amundson SA: **Global gene expression analyses of bystander and alpha particle irradiated normal human lung fibroblasts: synchronous and differential responses.** *BMC Med Genomics* 2008, **1**:63. ■

# Sensitization of Glioblastoma Cells to Apoptosis by Combined Treatment with Cannabidiol, $\gamma$ -Irradiation, and Specific Inhibitors of Signaling Pathways

Vladimir N. Ivanov and Tom K. Hei

Glioblastoma is the most common primary malignant brain tumor affecting more than 10,000 new patients in the US each year. Despite advances in therapy, outcomes remain really poor with a median survival time of 12-15 months after initial diagnosis [1]. Ionizing radiation either alone or in combination with chemotherapy (using temozolomide, a DNA methylating agent with DNA damaging activity) is the main treatment procedure for brain tumors including glioblastoma. Glial cells exhibit a substantial degree of radioresistance, however, while adult neurons and endothelial cells can be significantly damaged by ionizing radiation. Furthermore, oligodendrocyte precursor cells (OPC) and neural stem and progenitor cells (NSC/NPC), which have significant proliferative capacities, are highly sensitive to ionizing radiation, especially in combination with chemotherapy. Clinical observations and experiments with animals have demonstrated that cranial irradiation used for tumor treatment may cause substantial cognitive deficits due to neuronal and endothelial cell damage, as well as inhibition of proliferation and induction of death of OPC and NSC/NPC [2-9]. The challenge for glioblastoma treatment is thus to find a way to radiosensitize glioblastoma cells while protecting neurons, OPC, and NSC/NPC.

Investigations of the somatic genomic landscape of glioblastoma have demonstrated a connection between gene alteration and signaling pathway modifications in glioblastoma cells, including RTK pathways (EGFR1, FGFR2 or PDGFRA), the PI3K/PTEN-AKT pathway, MAPK pathways, the p53 pathway (together with MDM2) and the RB1 pathway [8, 10]. A role for the IKK-NF $\kappa$ B pathway via activating mutations was also demonstrated in some types of glioblastoma. Ionizing radiation causes DNA damage via generation of reactive oxygen species (ROS), which further affect cell signaling pathways with corresponding gene expression changes, followed by inhibition of proliferation, induction of DNA repair mechanisms and, finally, either cell survival or cell death via apoptosis, necrosis and destructive autophagy [11, 12]. The tumor microenvironment is actively involved in the regulation of cell signaling pathways, gene expression and survival of glioblastoma cells [13].

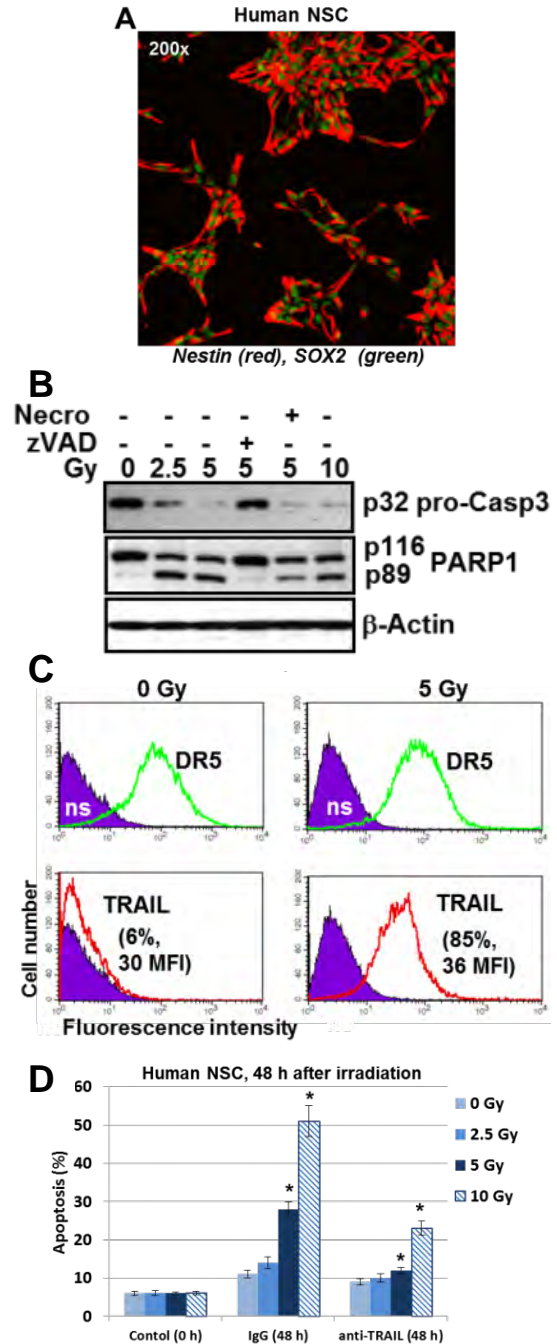


**Figure 1.** NSC before and after  $\gamma$ -irradiation at 5 Gy. **A)** Confocal image of NSC: Nestin, an early neuroprogenitor marker (red), and SOX2, a pluripotency marker (green). **B)** Induction of caspase-3-dependent apoptosis in NSC 6 h after irradiation. Caspase-3-dependent cleavage of PARP-1 was revealed by Western blot. **C)** The surface expression of TRAIL-R2 (DR5) and death ligand TRAIL in control and irradiated NSC, 16h after irradiation. **D)** Apoptotic levels 48 h after irradiation of NSC determined by PI staining and FACS analysis. Anti-TRAIL antibody in the cell media partially suppressed radiation-induced apoptosis. Non-specific IgG was used as a control.

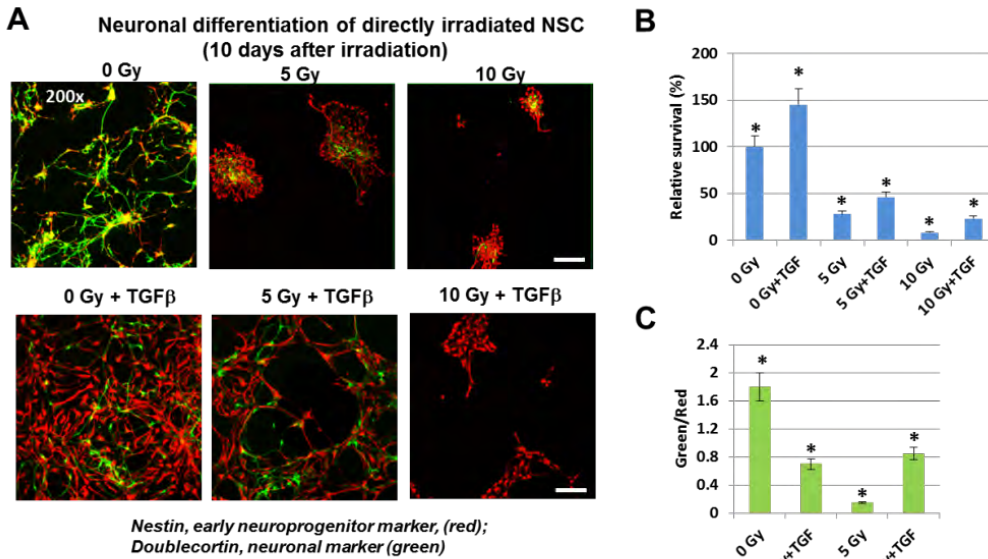


**Figure 2.** Effects of  $\gamma$ -irradiation on levels of neuronal differentiation of NSC/NPC in the absence or in the presence of TGF $\beta$  (20  $\mu$ M). A) Immunostaining with Nestin (red), an early neuroprogenitor marker, and Doublecortin (green), a neuronal marker. Bar = 50 $\mu$ M. B) Relative survival and C) Green/Red ratio, indicating the degree of neuronal differentiation.

Furthermore, radiation induces a signal transfer from treated tumors to non-irradiated bystander cells, including NSC/NPC in the brain, via expression and secretion of cytokines, death ligands, prostaglandins and endocannabinoids [14-16]. Numerous studies of the radiation-induced effects generated in cancer cells and expressed in non-targeted normal cells have dramatically changed the paradigm of radiobiology concerning the general regulation of the response to radiation [14, 15, 17].

In the present study, we elucidated a probable mechanism of radiosensitization of glioblastoma cells using cannabinoids, intercellular lipid messengers, and intercellular protein messengers, specifically proinflammatory cytokines that regulate the signaling cascades in the recipient cells [18, 19]. From the numerous members of the cannabinoid family, we have focused on the actions of cannabidiol (CBD), which is without psychogenic activity, alone or in combination with  $\gamma$ -irradiation, for induction of cell death via apoptosis in human glioblastoma cells. During the last year, we have investigated radiation-induced signaling pathways in normal stem cells and cancer cells with the goal of enhancing apoptosis in cancer cells while suppressing death pathways in normal cells [9, 16, 20-26]. Some essential data related to the present project are described below.

Human NSCs (H9 line) are very sensitive to  $\gamma$ -radiation, demonstrating apoptotic commitment 6 h after exposure (Fig. 1A and B). This is a result of combined effects of direct irradiation and radiation-induced TRAIL expression accompanied by TRAIL-mediated caspase-3-dependent apoptosis that targets PARP1 6-48 h after exposure (Fig. 1C). Indeed, anti-TRAIL antibody (5  $\mu$ g/ml) in the cell media, but not non-specific IgG, protects NSC/NPC against apoptosis (Fig.1D).

Neuronal differentiation of directly irradiated NSC/NPC was significantly disturbed 10 days after

irradiation (Fig. 2A). The presence of TGF $\beta$  (20  $\mu$ M) in the cell media partially restored differentiation of NPC after treatment with irradiation at 5 Gy, but not 10 Gy (Fig. 2 A-C).

In contrast to NSC/NPC, relative survival of the total U87MG glioblastoma cell population after irradiation was significantly higher (Fig. 3A), correlating with the basal upregulation of several survival pathways, such as AKT and IKK-NF- $\kappa$ B, and suppression of pro-apoptotic pathways, including p53 inactivation, BAX down-regulation and blockage of caspase-3 activation in

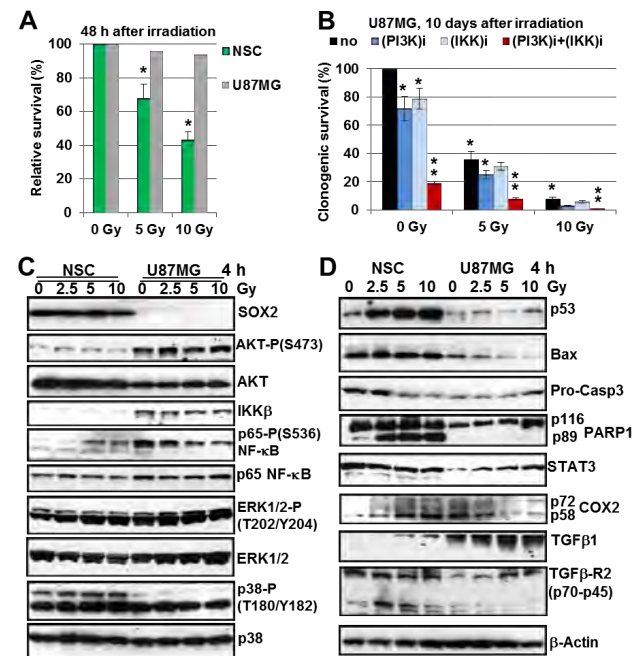


**Figure 3.** A) Relative survival of NSC and U87MG cells after  $\gamma$ -irradiation. B) combined treatment of U87MG cells by irradiation in the presence of inhibitors of cell signaling: PI3K-AKT and IKK-NF- $\kappa$ B. C) and D) Levels and activation of main signaling proteins in NSC and U87MG glioblastoma cells (by Western blot) after  $\gamma$ -irradiation.

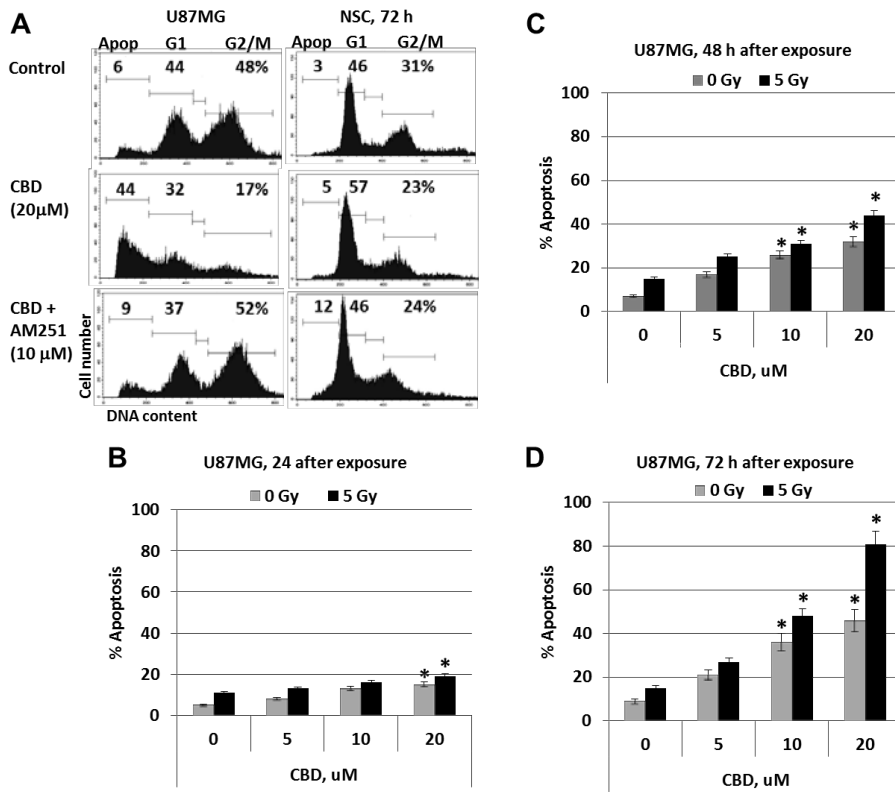


**Figure 4.** Dose-dependent effects of cannabidiol (CBD) on apoptosis of U87MG glioblastoma cells and an additional increase induced by  $\gamma$ -irradiation at 5 Gy. Cell cycle-apoptosis analysis was performed using PI staining of DNA and flow cytometry. A) typical result demonstrating differential effects of CBD or CBD plus AM251, an inhibitor of cannabinoid receptor mediated signaling, on U87MG glioblastoma cells and neural stem/progenitor cells (NSC). Percent of apoptotic U87MG cells B) 24 h, C) 48 h, or D) 72 h after 5 Gy irradiation with 0-20  $\mu$ M CBD. Pooled results of four independent experiments are shown in the panels. Error bars represent  $\pm$ S.D. An asterisk indicates significance ( $p < 0.05$ , Student's  $t$  test).

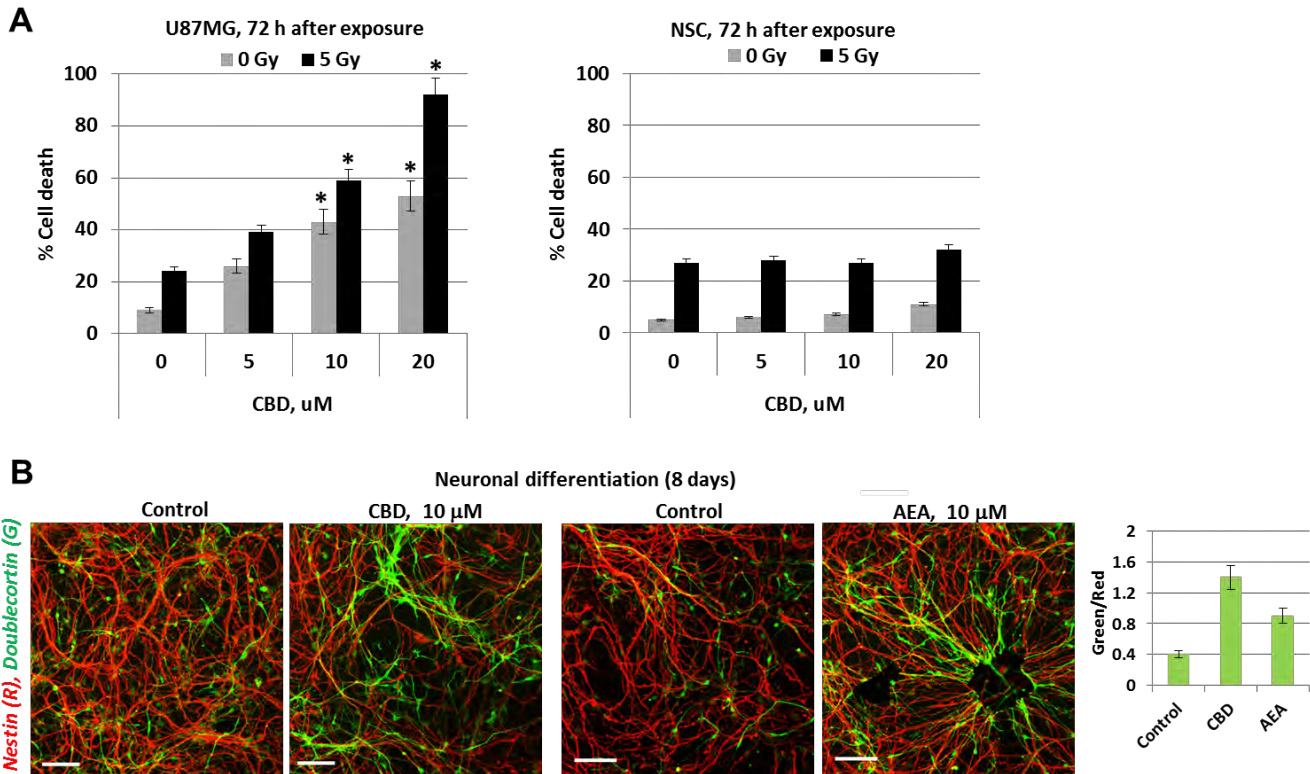


**Figure 5.** A) Total levels of cell death in U87MG cells (left panel) and NSC/NPC (right panel) were determined 72 h after treatment with CBD and  $\gamma$ -irradiation. B) Effect of the cannabinoids CBD and AEA on neuronal differentiation of NSC/NPC. Immunostaining with Nestin (red), an early neuroprogenitor marker, and Doublecortin (green), a neuronal marker. Bar = 50  $\mu$ M. The green/Red ratio (bar graph) reflects the degree of neuronal differentiation.

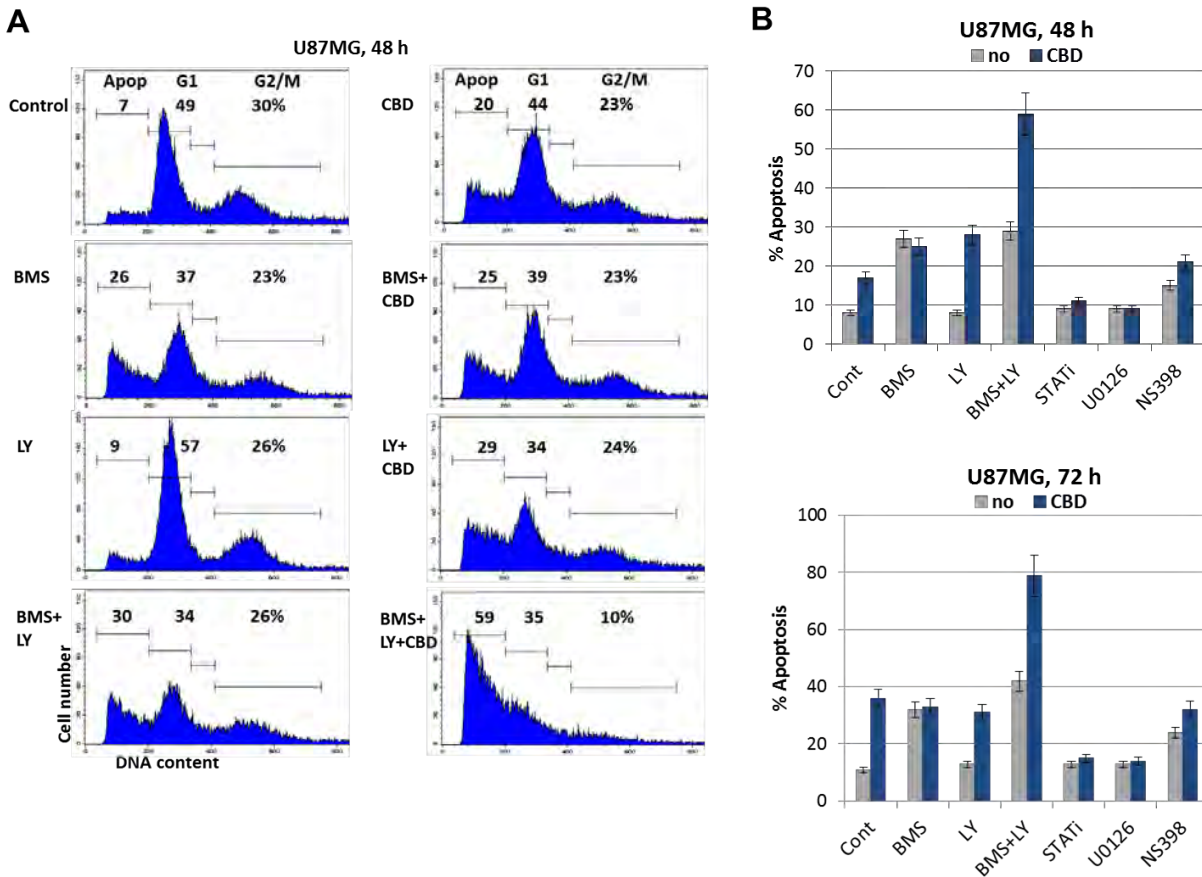


**Figure 6.** Substitution of irradiation: Dramatic upregulation of glioblastoma apoptosis by CBD+BMS+LY. A) Typical experiment: U87MG cells were treated with BMS345541 (BMS), an IKK-NF-κB inhibitor, LY294002 (LY), an PI3K-AKT inhibitor or CBD (20 μM) in the indicated combinations. Cell cycle-apoptosis analysis was performed using PI staining of DNA and FACS analysis. The combination of BMS, LY and CBD was very effective for killing of U87MG glioblastoma cells. B) Percentage of apoptotic cells at 48 h (top panel) and 72 h (bottom panel) after treatment. Results are the mean of four independent experiments.

U87MG cells (Fig. 3C and D). Hence, U87MG glioblastoma cells exhibiting high levels of radioresistance require special pre-treatments for induction of cell death (Fig. 3). Indeed, additional suppression of pro-survival pathways could substantially increase radiosensitivity of U87MG cells. Measurement of clonogenic survival demonstrated a substantial downregulation of U87MG cell survival after irradiation in the presence of inhibitors of PI3K-AKT (LY294002) and IKK-NF-κB (BMS345541) (Fig.3B). Unfortunately, these inhibitors also affected normal stem cells, especially NSC/NPC.

As an alternative modality, we tested pretreatment with NS398, a COX2 inhibitor, which we had previously used in combination with γ-irradiation. Unfortunately, we observed only modest upregulation of glioblastoma apoptosis. Similar results were found with STAT-inhibitor-6 and U0126, a MEK-ERK inhibitor (data not shown). Our next targets were cannabinoids, especially CBD. We used CBD (5-20 μM) for treatment of U87MG human glioblastoma cells and observed pronounced effects on induction of apoptosis 48-72 h after exposure. Simultaneously, NSC/NPC did not respond by induction of apoptosis after CBD treatment (Fig.4A). Ionizing

radiation at 5 Gy in combination with 20 μM CBD dramatically increased apoptotic (Fig. 4B-D) and total cell death levels in glioblastoma cells, while death levels in NSC/NPC cell populations did not further increase after combined treatment, compared to irradiation alone (Fig. 5A). The effects of CBD were dependent on CB1 receptor mediated signaling, because AM251 (10 μM), a CB1 inhibitor, blocked apoptotic development (Fig. 4A). The presence of the cannabinoids CBD or anandamide (AEA) also accelerated neuronal differentiation of NPC (Fig. 5B).

We previously observed notable levels of apoptosis induced in glioblastoma cells by combination of BMS345541 (10 μM), an IKK-NF-κB inhibitor, and LY294002 (40 μM), a PI3K-AKT inhibitor (Fig. 6A). The triple combination of these inhibitors with CBD (20 μM) demonstrated synergistic effects on U87MG glioblastoma cell apoptosis, highlighting a possibility for substitution of irradiation with small molecular inhibitors of survival signaling pathways (Fig. 6). Taken together, our results demonstrate that radiation-induced death of glioblastoma cells could be enhanced by cannabidiol-mediated signaling pathways in concert with their relatively neutral effects on NSC/NPC. This will allow selection of efficient

targets for radiosensitization of glioblastoma while overcoming cancer therapy-induced severe adverse sequelae.

### References

1. Porter KR, McCarthy BJ, Freels S, Kim Y, Davis FG. Prevalence estimates for primary brain tumors in the United States by age, gender, behavior, and histology. *Neuro-oncology*. 2010;12(6):520-7. Epub 2010/06/01. doi: 10.1093/neuonc/nop066. PMID: 20511189; PMCID: 2940648.
2. Monje ML, Mizumatsu S, Fike JR, Palmer TD. Irradiation induces neural precursor-cell dysfunction. *Nat Med*. 2002;8(9):955-62. Epub 2002/08/06. doi: 10.1038/nm749. PMID: 12161748.
3. Mizumatsu S, Monje ML, Morhardt DR, Rola R, Palmer TD, Fike JR. Extreme sensitivity of adult neurogenesis to low doses of X-irradiation. *Cancer Res*. 2003;63(14):4021-7. Epub 2003/07/23. PMID: 12874001.
4. Acharya MM, Lan ML, Kan VH, Patel NH, Giedzinski E, Tseng BP, Limoli CL. Consequences of ionizing radiation-induced damage in human neural stem cells. *Free Radic Biol Med*. 2010;49(12):1846-55. Epub 2010/09/10. doi: 10.1016/j.freeradbiomed.2010.08.021. PMID: 20826207.
5. Acharya MM, Christie LA, Lan ML, Giedzinski E, Fike JR, Rosi S, Limoli CL. Human neural stem cell transplantation ameliorates radiation-induced cognitive dysfunction. *Cancer Res*. 2011;71(14):4834-45. Epub 2011/07/16. doi: 10.1158/0008-5472.CAN-11-0027. PMID: 21757460; PMCID: 3517293.
6. Hellstrom NA, Bjork-Eriksson T, Blomgren K, Kuhn HG. Differential recovery of neural stem cells in the subventricular zone and dentate gyrus after ionizing radiation. *Stem Cells*. 2009;27(3):634-41. Epub 2008/12/06. doi: 10.1634/stemcells.2008-0732. PMID: 19056908.
7. Greene-Schloesser D, Robbins ME, Peiffer AM, Shaw EG, Wheeler KT, Chan MD. Radiation-induced brain injury: A review. *Front Oncol*. 2012;2:73. Epub 2012/07/27. doi: 10.3389/fonc.2012.00073. PMID: 22833841; PMCID: 3400082.
8. Brennan CW, Verhaak RG, McKenna A, Campos B, Noshmehr H, Salama SR, Zheng S, Chakravarty D, Sanborn JZ, Berman SH, Beroukhi R, Bernard B, Wu CJ, Genovese G, Shmulevich I, Barnholtz-Sloan J, Zou L, Vegesna R, Shukla SA, Ciriello G, Yung WK, Zhang W, Sougnez C, Mikkelsen T, Aldape K, Bigner DD, Van Meir EG, Prados M, Sloan A, Black KL, Eschbacher J, Finocchiaro G, Friedman W, Andrews DW, Guha A, Iacocca M, O'Neill BP, Foltz G, Myers J, Weisenberger DJ, Penny R, Kucherlapati R, Perou CM, Hayes DN, Gibbs R, Marra M, Mills GB, Lander E, Spellman P, Wilson R, Sander C, Weinstein J, Meyerson M, Gabriel S, Laird PW, Haussler D, Getz G, Chin L, Network TR. The somatic genomic landscape of glioblastoma. *Cell*. 2013;155(2):462-77. Epub 2013/10/15. doi: 10.1016/j.cell.2013.09.034. PMID: 24120142; PMCID: 3910500.
9. Ivanov VN, Hei TK. A role for TRAIL/TRAIL-R2 in radiation-induced apoptosis and radiation-induced bystander response of human neural stem cells. *Apoptosis: an international journal on programmed cell death*. 2014;19(3):399-413. Epub 2013/10/26. doi: 10.1007/s10495-013-0925-4. PMID: 24158598; PMCID: PMC3945673.
10. Cancer Genome Atlas Research N. Comprehensive genomic characterization defines human glioblastoma genes and core pathways. *Nature*. 2008;455(7216):1061-8. Epub 2008/09/06. doi: 10.1038/nature07385. PMID: 18772890; PMCID: 2671642.
11. Okada H, Mak TW. Pathways of apoptotic and non-apoptotic death in tumour cells. *Nat Rev Cancer*. 2004;4(8):592-603. PMID: 15286739.
12. Hitomi J, Christofferson DE, Ng A, Yao J, Degtrev A, Xavier RJ, Yuan J. Identification of a molecular signaling network that regulates a cellular necrotic cell death pathway. *Cell*. 2008;135(7):1311-23. Epub 2008/12/27. doi: 10.1016/j.cell.2008.10.044. PMID: 19109899; PMCID: 2621059.
13. Persano L, Rampazzo E, Basso G, Viola G. Glioblastoma cancer stem cells: role of the microenvironment and therapeutic targeting. *Biochem Pharmacol*. 2013;85(5):612-22. Epub 2012/10/16. doi: 10.1016/j.bcp.2012.10.001. PMID: 23063412.
14. Hei TK, Zhou H, Chai Y, Ponnaiya B, Ivanov VN. Radiation induced non-targeted response: mechanism and potential clinical implications. *Current molecular pharmacology*. 2011;4(2):96-105. PMID: 21143185; PMCID: 3356574.
15. Prise KM, O'Sullivan JM. Radiation-induced bystander signalling in cancer therapy. *Nat Rev Cancer*. 2009;9(5):351-60. Epub 2009/04/21. doi: nrc2603 [pii] 10.1038/nrc2603. PMID: 19377507; PMCID: 2855954.
16. Ivanov VN, Hei TK. Radiation-induced glioblastoma signaling cascade regulates viability, apoptosis and differentiation of neural stem cells (NSC). *Apoptosis*. 2014;19(12):1736-54. Epub 2014/10/03. doi: 10.1007/s10495-014-1040-x. PMID: 25273222; PMCID: PMC4378234.
17. Morgan WF. Non-targeted and delayed effects of exposure to ionizing radiation: I. Radiation-induced genomic instability and bystander effects in vitro. *Radiat Res*. 2003;159(5):567-80. Epub 2003/04/25. PMID: 12710868.

18. Brown I, Cascio MG, Rotondo D, Pertwee RG, Heys SD, Wahle KW. Cannabinoids and omega-3/6 endocannabinoids as cell death and anticancer modulators. *Prog Lipid Res.* 2013;52(1):80-109. doi: 10.1016/j.plipres.2012.10.001. PMID: 23103355.
19. Scott KA, Dalglish AG, Liu WM. The combination of cannabidiol and Delta9-tetrahydrocannabinol enhances the anticancer effects of radiation in an orthotopic murine glioma model. *Mol Cancer Ther.* 2014;13(12):2955-67. doi: 10.1158/1535-7163.MCT-14-0402. PMID: 25398831.
20. Ivanov VN, Zhou H, Partridge MA, Hei TK. Inhibition of ataxia telangiectasia mutated kinase activity enhances TRAIL-mediated apoptosis in human melanoma cells. *Cancer research.* 2009;69(8):3510-9. doi: 10.1158/0008-5472.CAN-08-3883. PMID: 19351839.
21. Zhou H, Ivanov VN, Lien YC, Davidson M, Hei TK. Mitochondrial function and nuclear factor-kappaB-mediated signaling in radiation-induced bystander effects. *Cancer research.* 2008;68(7):2233-40. Epub 2008/04/03. doi: 10.1158/0008-5472.can-07-5278. PMID: 18381429; PMCID: PMC3715144.
22. Ivanov VN, Zhou H, Ghandhi SA, Karasic TB, Yaghoubian B, Amundson SA, Hei TK. Radiation-induced bystander signaling pathways in human fibroblasts: a role for interleukin-33 in the signal transmission. *Cellular signalling.* 2010;22(7):1076-87. doi: 10.1016/j.cellsig.2010.02.010. PMID: 20206688; PMCID: 2860693.
23. Karasic TB, Hei TK, Ivanov VN. Disruption of IGF-1R signaling increases TRAIL-induced apoptosis: a new potential therapy for the treatment of melanoma. *Experimental cell research.* 2010;316(12):1994-2007. Epub 2010/04/27. doi: 10.1016/j.yexcr.2010.04.014. PMID: 20417200; PMCID: PMC2878841.
24. Ivanov VN, Partridge MA, Huang SX, Hei TK. Suppression of the proinflammatory response of metastatic melanoma cells increases TRAIL-induced apoptosis. *J Cell Biochem.* 2011;112(2):463-75. Epub 2011/01/27. doi: 10.1002/jcb.22934. PMID: 21268068; PMCID: PMC4378843.
25. Ivanov VN, Hei TK. Induction of apoptotic death and retardation of neuronal differentiation of human neural stem cells by sodium arsenite treatment. *Experimental cell research.* 2013;319(6):875-87. doi: 10.1016/j.yexcr.2012.11.019. PMID: 23219847; PMCID: 3593966.
26. Ivanov VN, Wen G, Hei TK. Sodium arsenite exposure inhibits AKT and Stat3 activation, suppresses self-renewal and induces apoptotic death of embryonic stem cells. *Apoptosis : an international journal on programmed cell death.* 2013;18(2):188-200. doi: 10.1007/s10495-012-0779-1. PMID: 23143138; PMCID: 3552097. ■



(l to r): Alan Bigelow, David Welch, Yanping Zhou, Charles Geard, David Brenner, Gerhard Randers-Pehrson, Steve Marino, Andrew Harkin, Guy Garty, Dennis Farrell, Manuela Buonanno.

# The Effects of Ionizing Radiation on the Structure and Function of Human Blood Capillaries

Peter Grabham, Preety Sharma, Burong Hu, Thomas Templin, Alan Bigelow, and Charles R. Geard

Although the endothelial cells in micro-capillaries rarely develop cancer, they are of critical importance to some of the non-cancer related effects of radiation exposure. Ionizing radiation can cause dysfunction of the endothelial cells in blood micro-capillaries or microvessels, which can in turn lead to many serious pathologies, particularly degenerative disorders of the cardiovascular and central nervous systems.

A vast network of tens of thousands of miles of microvessels permeates every tissue at the microscopic level, and this is therefore a major target for an agent like ionizing radiation that originates from a source and passes through the body. The types of radiation and means of exposure include: photons (gamma rays) from nuclear accidents or explosions, photons and charged particles (protons and carbon ions) used in radiotherapy, and different species of charged particles (light ions and heavy ions) encountered in the space environment. The specific effects of ionizing radiation on the biology of endothelial cells in the micro-capillaries are crucial to the understanding of the short-term and long-term non-cancer effects of radiation. To achieve this, relevant experimental models are needed, models that reflect as closely as possible the responses in human beings. In this report we summarize the effects of ionizing radiation on human 3D micro-capillary tissue models. We have examined the effects of both photons and charged particles on five key endpoints that give information on the biology of endothelial responses and their relevance to pathologies – cell death (apoptosis), capillary structure, endothelial barrier function, angiogenesis, and the production of endothelial microparticles. The results indicate that there are a variety of different responses that could lead to pathologies depending on the type and dose of radiation. Furthermore, not all responses are linked directly to cell death since some effects occur at doses well below those required for an apoptotic response.

## Vessel models

We established a 3D tissue model to use in our investigations [1]. After 7 days in culture within matrix gels, human endothelial cells have formed tubes with lumens of diameters comparable to those of capillaries *in vivo* (Figure 1). The cells in the tissue display a more differentiated phenotype than cells cultured in monolayers. There are over 120 gene expression changes, in addition to differences in secreted proteins. The rate of mitosis is very low and the occurrence of spontaneous DNA repair foci is also very low, although after irradiation, the nuclei still display the DNA damage and

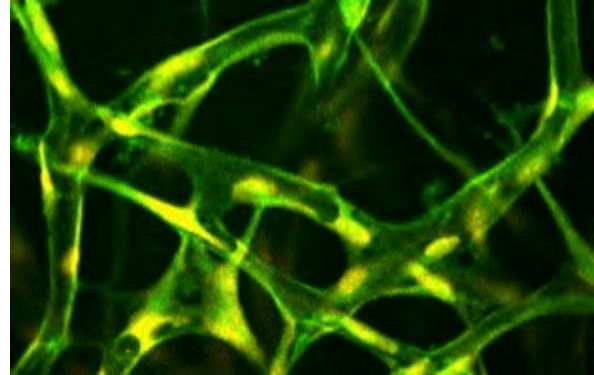


**Figure 1.** Human microvessel model grown from Human Umbilical Vein Cells (HUVEC). All structures are labeled green and nuclei are labeled red resulting in a merged yellow color.

repair characteristics typical of the dose and type of radiation [2]. There are also tight junctions between the cells, indicating the presence of an endothelial barrier. These characteristics make the model closer to *in vivo* capillaries and thus a more relevant and accurate experimental model.

## Apoptosis

Many of the harmful effects of radiation, particularly at higher doses, can be simply attributed to radiation-induced death of the cells in the tissue, which then results in dysfunction and eventual pathologies. Cells in tissues with a high rate of mitosis, such as the intestines, are particularly sensitive. However, endothelial cells in vessels have a very low mitotic index and therefore a

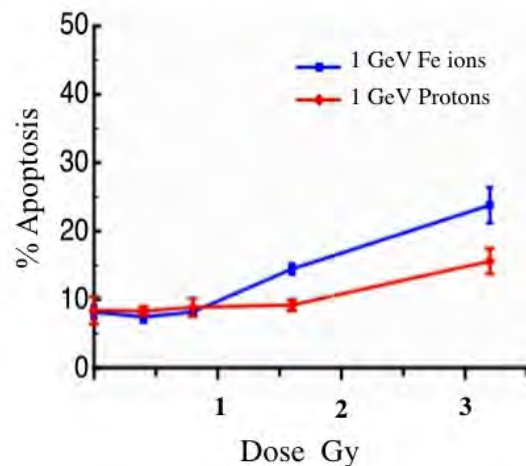


**Figure 2.** Apoptosis by TUNEL assay in human microvessel models exposed to light ions (protons) and heavy ions (Fe). Heavy ions have a higher RBE than light ions.

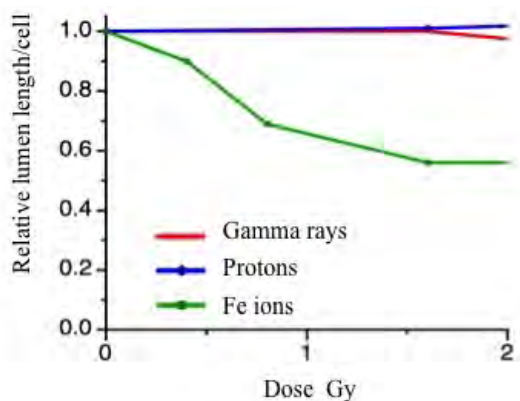


**Figure 3.** Effects of gamma rays, protons, and Fe ions on mature vessel structure. Length of vessel with lumen is calculated relative to the control (50 mm/cell).

higher resistance to radiation-induced apoptosis. Our studies on apoptosis in vessel models show this to be the case, although the relative biological effects (RBE) of photons, light charged particles, and heavy charged particles are typical of many responses to radiation, especially cytotoxic responses. TUNEL assays show that high-energy heavy ions are most effective, causing a projected 25% apoptosis at 4.5 Gy, whereas protons are less effective, causing a projected 25% apoptosis at 6.5 Gy (Figure 2). Photons (Gamma rays) were even less effective at inducing apoptosis, producing 25% labeled (apoptotic) nuclei at a dose of 22 Gy (not shown). While the expected RBE hierarchy is maintained with these types of radiation, cell death of microvessels requires much higher doses than those known to cause other microvessel-related problems (described below).

### Capillary structure

The integrity of the capillary structure is critical to its function. Loss or collapse of vessels compromises their ability to transport blood to the tissue they provide with

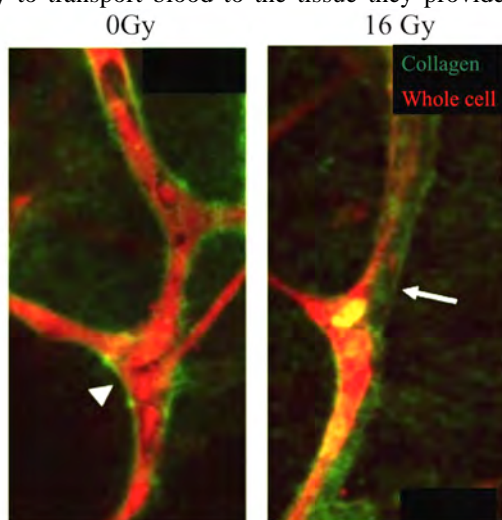


**Figure 4.** Effects of gamma rays on mature vessel structure. The control image shows the vessels (red) surrounded closely by collagen (green) lining the cavity (arrowhead). A dose of 16 Gy causes the vessels to collapse leaving gaps between the collagen and cell material.

nutrients and oxygen. The tissue can become hypoxic or even necrotic. The effect can be long-term and incremental, causing degenerative pathologies. Experiments in which mature tissue models are exposed to photons and charged particles show that heavy ions (1 GeV/n Fe ions) have the highest RBE for vessel collapse (Figure 3) [1]. Fe ions cause full morphological breakdown at a dose of 1.5 Gy. We did not observe any effect by low LET protons up to 3.2 Gy, a dose well above the dose encountered in the space environment.

Gamma rays caused collapse at 10-15 Gy (Figure 4), a relatively high dose in comparison to conventional radiotherapy delivered in fractions of 2 Gy, although the higher dose is relevant to stereotactic brain radiotherapy, which is used at doses above 10 Gy.

### Endothelial barrier function

The endothelial barrier regulates the exchange of fluid and solutes between the vascular compartment and the interstitial space. It is the interface between the blood and all tissues. The disruption of endothelial barrier function is not only a primary event in a range of degenerative diseases but is also an important influencing factor in many others.

We used a set of established and novel endpoints to assess barrier function after exposure to radiation. These include trans-endothelial electrical resistance (TEER), morphological effects, localization of adhesion and cell junction proteins (in 2D monolayers and in 3D tissue models), and permeability of molecules through the endothelial barrier. Gamma rays caused two distinct effects. One is an early transient loss in barrier function and the shedding of endothelial microparticles (see below). The second effect occurs at 24-48 hours after exposure to doses of 8 Gy and above. There is a breakdown of all cell-cell junctions and an increase in TEER. The barrier is destroyed at these doses, similar to doses that also cause significant cytotoxic effects such as apoptosis and vessel collapse. For low LET protons there were no observed effects after exposures up to a dose of 4 Gy. Heavy ions, however, were found to compromise the endothelial barrier by affecting tight junctions at a dose as low as 0.25 Gy (Figure 5) [3], well below doses that cause apoptosis.

### Angiogenesis

Angiogenesis is the growth of new blood vessels. For adults, it is important in maintaining the microvasculature by replacing damaged or dysfunctional blood vessels. Without it there is a gradual decline in the blood microvessels (rarefaction) as capillaries are damaged but not replaced. It is especially critical when an agent like radiation causes capillary dysfunction in addition to inhibiting angiogenesis. Now the damaged vessel is prevented from being repaired. Tissues can be left without nutrients or oxygen for longer periods of time leading to hypoxia and necrosis. We assay for angiogenesis by irradiating cultures only one day after

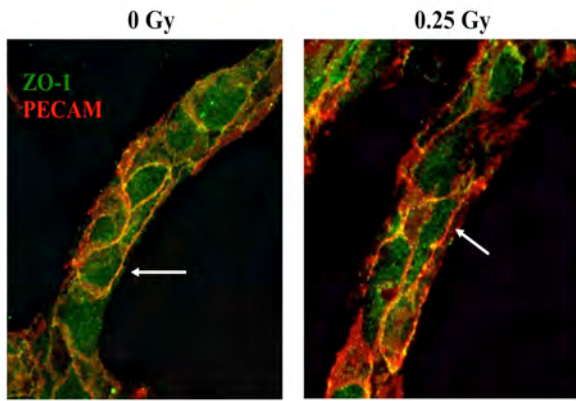


**Figure 5.** Irradiation induced changes in the tight junctions of 3-Dimensional human vessel models. Control cultures and 0.25 Gy Fe ion irradiated cultures were immunostained for ZO-1 (green) and for PECAM-1 (red). Control cultures show good co-localization of the two proteins as a merged yellow color (arrow). Irradiated cultures show areas where the ZO-1 distribution is disrupted (arrow) while the red PECAM-1 staining remains intact.

seeding in the matrix and following the effects over the vessel growth period. Gamma rays inhibit angiogenesis fully at 8-10 Gy [1] a dose high enough to cause cytotoxicity as well as loss of barrier function. This becomes a beneficial effect on the tumor vasculature in stereotactic radiotherapy, where the doses are large enough to cause dysfunctional angiogenesis, unlike conventional fractionated radiotherapy that, in fact, increases angiogenesis.

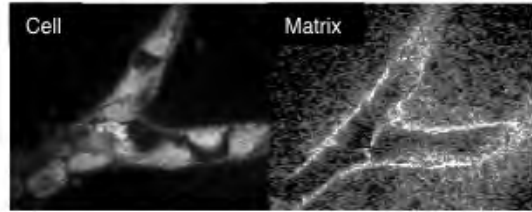
On the other hand, charged particles (high and low LET) cause the inhibition of capillary growth at much lower doses, well below the dose required for any detectable apoptosis. Furthermore, low LET charged particles cause inhibition at a dose comparable to that required with heavy ions (50% effect at 40 cGy). This is an unexpected result, since heavy ions have consistently shown a much higher RBE than protons or helium ions.

Further investigation showed that each is inhibiting angiogenesis by distinct mechanisms [4, 5]. Low LET charged particles inhibit the early stages of vasculogenesis when tip cells have motile protrusive structures and are creating narrow pioneer guidance tunnels through the matrix (Figure 6). High LET charged particles do not affect the early stages of vasculogenesis but they do affect the later stages when the endothelial cells migrate and expand to form tubes (tubulogenesis). The high RBE for protons and heavy ions in the inhibition of angiogenesis make them relevant to the tumor vasculature in particle cancer radiotherapy (protons and Carbon ions). This effect could also negatively impact astronaut health in the space environment.

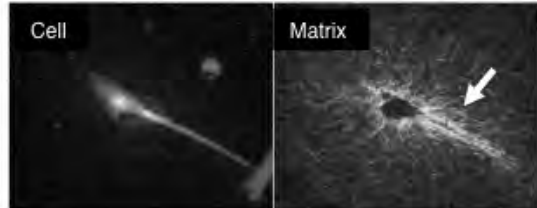
### Endothelial microparticles

Circulating extracellular vesicles comprise a heterogeneous population of vesicular structures released from cells under stress or activation stimuli. They include exosomes, microparticles and apoptotic bodies.

### A Control



### B Fe ions



### C Protons

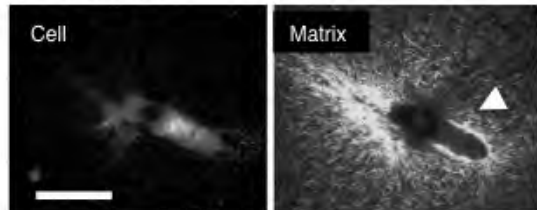


**Figure 6.** Uncoupling of PECAM-1 after exposure to 5 Gy Gamma rays. Immunocytochemistry with DTAF (stains all proteins green) and anti PECAM-1 antibody (red) shows PECAM-1 negative (arrowhead) and positive microparticles (arrow) are released and held in the extracellular matrix.

Microparticles have been of particular recent interest because they express markers that indicate changes in the activation state or apoptosis of their cell of origin. Within the last 1-2 decades it has been shown that microparticles are useful blood surrogate markers for different pathological conditions, such as vascular inflammation. Furthermore, it has recently been indicated that they may be causative agents of certain pathologies. Endothelial microparticles (EMPs) are identified by the presence of PECAM-1, are associated with many pathological conditions, and their molecular make up is characteristic of different pathologies.

As yet there is very little information on the induction of microparticle shedding by ionizing radiation, although we have detected it in human endothelial cells. It was first seen as a transient dip in TEER after exposure to gamma rays as low as 2 Gy. It is associated with transient barrier dysfunction and the uncoupling of the cell adhesion molecule – PECAM-1 [6]. At the same time PECAM-1 positive (and negative) microparticles are shed from the endothelial layer (Figure 7). In our models the particles are held in the gel matrix but *in vivo* they would be expected to float in the blood and deposit elsewhere. This effect is relevant to all gamma cancer radiotherapy (fractionated and stereotactic), but not with charged particle radiation, since these microparticles were not detected at the same time after proton and heavy ion

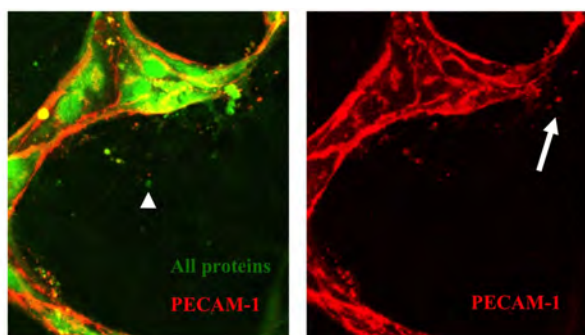


**Figure 7.** Uncoupling of PECAM-1 after exposure to 5 Gy Gamma rays. Immunocytochemistry with DTAF to show all proteins and anti PECAM-1 antibody, shows PECAM-1 negative (arrowhead) and positive microparticles (arrow) are released and held in the extracellular matrix.

exposure. Although it is not known if there are other particles induced by charged particles at other times.

### Summary

These studies highlight the fact that there are a number and variety of non-cancer responses of the microvasculature to ionizing radiation, and that the kind of response is dependent on the type and dose of radiation in addition to the status of the cells at the time of exposure. The effects on human capillaries can be divided into two broad categories. Those that involve cytotoxicity, and those that occur at much lower doses (Table 1). For those that involve cytotoxicity, the dose is large enough and enough energy is absorbed, that a threshold level is reached, causing cell shutdown and death. Obviously, structure and function (e.g. Barrier function) of the microvessels is compromised as the cells die. This kind of effect is only seen in situations like nuclear accidents and explosions, and some types of cancer radiotherapy. It is, however, dependent on radiation quality, such that different doses of each type of radiation are required to produce the effect. As with many endpoints, heavy ions have the highest RBE and photons the lowest.

The effects that are seen at doses much lower than those required for cell death reveal several important points about non-cancer radiation effects. First, not all responses are related to cytotoxic effects. There are other cellular mechanisms that are triggered by ionizing radiation. Second, heavy ions are particularly potent in this respect. Low doses are sufficient to elicit many responses (especially disruptions of barrier function in these studies) making these particles, which are present in the space environment, a concern for astronaut health. Third, the fluence and pattern of energy deposition can determine the mechanism of biological response by the cell. An example here is the inhibition of angiogenesis by heavy and light charged particles. While the dose is the same for each, the type of biological inhibition, like the fluence and LET, is entirely different. The target structures within the cell may be important here. Targets like membrane proteins and enzymes that are widespread

**Table 1.** Summary of the non-cancer effects of ionizing radiation on human blood microcapillaries.

	Photons	Light Ions	Heavy Ions
Capillary Structure	10-15 Gy	> 4 Gy	<b>1.5 Gy*</b>
Cell Death Apoptosis	25% at 22 Gy	25% at 6.5 Gy	25% at 4.5 Gy
Barrier Function	16 Gy	> 4 Gy	<b>0.25 Gy</b>
Angiogenesis	8 Gy	<b>50% at 0.4 Gy</b>	<b>50% at 0.4 Gy</b>
Microparticle Production	<b>2 Gy</b>	No Effect	No Effect

\*Orange = below the dose where cytotoxicity is observed.

over the cell will receive more traversals by high fluence low LET radiation. Fourth, the effect on the cell is also determined by the context of the cell behavior and activation. Inhibition of angiogenesis by protons has a much higher RBE than apoptosis and barrier function effects. During angiogenesis the cells are known to be in an activated state (they are secreting the cytokine IL-6, unpublished observations) and many signaling pathways for cell stress are shared with the pathways for motility. The cell could be closer to a threshold level that shuts down a biological process. Finally, random effects specific to a particular type radiation are possible. While photons generally have a low RBE they are effective at inducing the shedding of microparticles, even though charged particles are not.

### References

1. Grabham P, Hu B, Sharma P and Geard C (2011) Effects of ionizing radiation on three-dimensional human vessel models: differential effects according to radiation quality and cellular development. *Radiat Res* **175**: 21-28.
2. Grabham P, Bigelow A and Geard C (2012) DNA damage foci formation and decline in two-dimensional monolayers and in three-dimensional human vessel models: differential effects according to radiation quality. *Int J Radiat Biol* **88**: 493-500.
3. Sharma P, Guida P and Grabham P (2014) Effects of Fe particle irradiation on human endothelial barrier structure and function. *Life Sci Space Res* **2**: 29-37.
4. Grabham P and Sharma P (2013) The effects of radiation on angiogenesis. *Vasc Cell* **5**: 19.
5. Grabham P, Sharma P, Bigelow A and Geard C (2013) Two distinct types of the inhibition of vasculogenesis by different species of charged particles. *Vasc Cell* **5**: 16.
6. Sharma P, Templin T and Grabham P (2013) Short term effects of gamma radiation on endothelial barrier function: uncoupling of PECAM-1. *Microvasc Res* **86**: 11-20. ■

# Isolation and Analysis of mRNA from Urinary Exosomes as Potential Markers for Prostate Cancer

Kevin M. Hopkins and Howard B. Lieberman

Prostate cancer will be diagnosed in about 1 of every 7 men during their lifetime. The American Cancer Society estimates that 220,800 new cases arose and 27,540 deaths occurred because of this disease in the year 2015. Standard initial diagnostic tests include assessment of PSA levels in blood, and digital rectal examination of the prostate. These tests are useful but not completely accurate, as false positives and false negatives can occur. For example, conditions other than prostate cancer can affect PSA level. Prostatitis, ejaculation, or old age can be factors that contribute to raised PSA levels. In contrast, certain herbal mixtures, aspirin, obesity or statins can lower levels, unrelated to prostate cancer status. Furthermore, even if cancer is present, it is not always clear whether the disease is dangerous and life threatening. The results of initial diagnosis could lead to unnecessary follow up biopsy, or inappropriate treatment for disease that would remain indolent or advance aggressively in an unpredictable manner. Therefore, an important clinical need is a diagnostic tool, preferably non-invasive or minimally invasive, that ideally would permit accurate detection and assessment of prostate cancer, to inform treatment strategy early in the process when any intervention is most effective.

Characteristics of an ideal diagnostic test should include accuracy, reproducibility, and preferably a non-invasive avenue to obtain patient specimens for analyses. Exosomes in urine offer an attractive opportunity. Exosomes are small membrane bound nanovesicles secreted by mammalian cells into the extracellular environment, which includes urine and also blood. They contain many proteins, mRNAs and the small non-coding RNAs called miRNAs, all potentially capable of serving as sensitive biomarkers for disease [1, 2]. Advantages of the use of urine exosomes include ease of obtaining large quantities, their composition is less complex than that of cells or tissues, and their contents reflect alterations in the urogenital system [3, 4]. Furthermore, compared to whole cells, exosomes might better protect RNA during

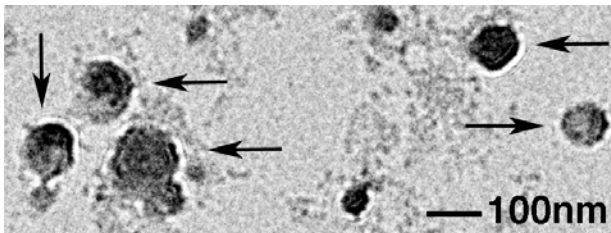


**Figure 1.** Transmission electron microscopy used to visualize exosomes from the urine of a male donor who did not have prostate cancer. Arrows indicate exosomes, which are typically 50-100 nm.

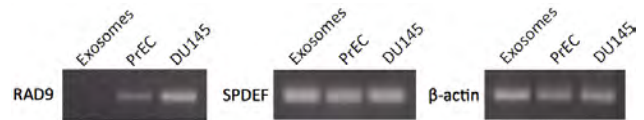


**Figure 2.** RT-PCR amplification of specific RNAs within male urine exosomes, the non-cancer prostate cells PrEC, and prostate cancer cells (DU145). RNAs were RAD9 (cancer marker), SPDEF (general prostate marker) and  $\beta$ -actin (general marker). RAD9 is most abundant in DU145 and similar levels of SPDEF and  $\beta$ -actin were detected in all three samples tested using 40 PCR cycles, as predicted.

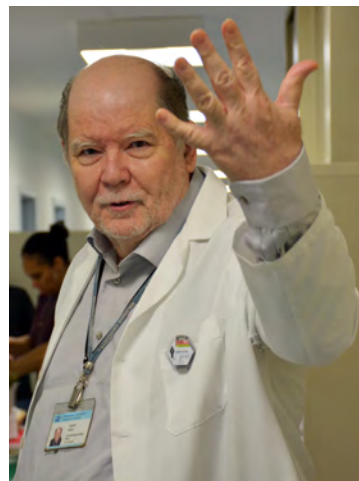
passage through urine, and are thus a more amenable source for biomarker evaluation [5].

The overall goal of this study is to isolate exosomes from male urine, and establish a gene expression profile within that indicates if the donor has prostate cancer. Further, correlations with details about the disease, and ability to stratify cancer severity will also be evaluated. Fig. 1 indicates that we can successfully isolate urinary exosomes from a male without prostate cancer, as viewed by transmission electron microscopy (images obtained by Dr. Chris Goulbourne, Electron Microscopy Laboratory, Columbia University). Further, we harvested RNA from these vesicles, and performed RT-PCR to assess levels of specific RNA species. For these initial experiments, we used 40 PCR cycles, a high number, to insure that any mRNA present would generate a signal. Indicated in Fig. 2 are agarose gels depicting amplified cDNA bands from RNA within urine exosomes, as well as from cultured normal prostate epithelial cells (PrEC) and prostate cancer cells (DU145). As predicted, SPDEF (prostate specific marker; 6) and  $\beta$ -actin (general marker) are present at equivalent levels in all samples but RAD9 (cancer marker; 7, 8) is most abundant in DU145. Experiments for future studies will use qRT-PCR to carefully quantify the expression of genes with potential as biomarkers of prostate cancer.

## References

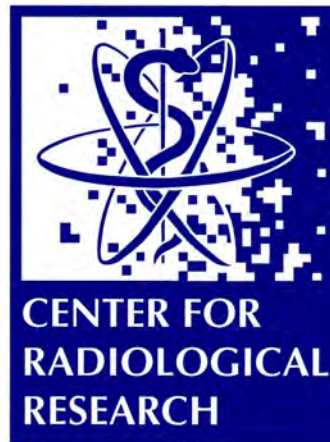
1. Dijkstra S, Mulders PF, Schalken JA. (2014b) Clinical use of novel urine and blood based prostate cancer biomarkers: a review. Clin Biochem. 47(10-11):889-96.
2. Drake RR, Kislinger T. (2014) The proteomics of prostate cancer exosomes. Expert Rev Proteomics. 11(2):167-77.
3. Hessvik NP, Sandvig K, Llorente A. (2013) Exosomal miRNAs as Biomarkers for Prostate Cancer. Front Genet. 4:36.

4. Soekmadji C, Russell PJ, Nelson CC. (2013) Exosomes in prostate cancer: putting together the pieces of a puzzle. *Cancers (Basel)*. 5(4):1522-44.
5. Miranda KC, Bond DT, McKee M, Skog J, Păunescu TG, Da Silva N, Brown D, Russo LM. (2010) Nucleic acids within urinary exosomes/microvesicles are potential biomarkers for renal disease. *Kidney Int*. 78(2):191-9.
6. Oettgen P, Finger E, Sun Z, Akbarali Y, Thamrongsak U, Boltax J, Grall F, Dube A, Weiss A, Brown L, Quinn G, Kas K, Endress G, Kunsch C, Libermann TA (2000). "PDEF, a novel prostate epithelium-specific ets transcription factor, interacts with the androgen receptor and activates prostate-specific antigen gene expression". *J Biol Chem*. 275(2):1216–25
7. Zhu A, Zhang CX, Lieberman HB. (2008) Rad9 has a functional role in human prostate carcinogenesis. *Cancer Res*. 68(5):1267-74.
8. Broustas CG, Zhu A, Lieberman HB. (2012) Rad9 protein contributes to prostate tumor progression by promoting cell migration and anoikis resistance. *J Biol Chem*. 287(49):41324-33. ■



**Top** (l to r): Peter Grabham; Qin Zhang; Shanaz Ghandhi; Howard Lieberman.  
**Bottom** (l to r): David Brenner, Eric Hall, Gerhard Randers-Pehrson; Vladimir Ivanov; Mashkura Chowdhury.

# TRANSLATIONAL STUDIES



# Far-UVC Light: A Promising Tool for Safe Low-cost Reduction of Surgical Site Infections

Manuela Buonanno, Sheetal Trivedi<sup>a</sup>, Milda Stanislaukas<sup>b</sup>, Brian Ponnaiya, Alan W. Bigelow, Gerhard Randers-Pehrson, Franklin D. Lowy<sup>a</sup>, Henry M. Spotnitz<sup>c</sup>, Scott M. Hammer<sup>a</sup>, David M. Owens<sup>b,d</sup>, and David J. Brenner

## INTRODUCTION

It is estimated that between 2% and 5% of clean surgeries result in surgical site infections (SSI) [1]. Despite improvements in operating room practices, SSIs result in substantial morbidity, prolonged hospital stays, and increased direct patient cost [2]. This is due to the increasing number of SSIs that are attributable to antibiotic-resistant pathogens such as methicillin-resistant *S. aureus* (MRSA) [3], one of the leading causes of SSIs in community hospitals. Although recommendations for reducing the risk of SSIs are routinely applied in hospitals, there is no single effective strategy for prevention, containment and treatment of MRSA infections. Therefore, novel infection control techniques are necessary.

Conventional germicidal UVC lamps are very effective at killing both bacteria and viruses. A particular advantage of UVC-mediated bacterial killing is that it is essentially independent of acquired drug resistance [3, 4]. The downside to the more widespread use of germicidal UVC radiation in hospital (or other) environments, is that it is a human health hazard, being both carcinogenic and cataractogenic [4].

We have developed an approach for UV-based sterilization using single-wavelength UVC light to kill bacteria, but potentially without harming human cells and tissues [5]. It involves the use of far-UVC radiation generated by inexpensive filtered excimer lamps that emit primarily a single UVC wavelength; in particular, our approach has used krypton-bromine (Kr-Br) or krypton-chlorine (Kr-Cl) excimer lamps that produce high-intensity light at 207 nm or 222 nm, respectively [6].

The mechanistic background to this approach is that far UVC light in the wavelength range around 200 to 220 nm is strongly absorbed by proteins, and so its ability to penetrate biological material is very limited. The very short half value distance of ~200-nm UV light in biological material means that, while it can penetrate bacteria and viruses that are typically smaller than 1  $\mu\text{m}$  in size, it cannot penetrate the human stratum corneum (the outer dead-cell skin layer, thickness 5-20  $\mu\text{m}$ ), nor the ocular cornea (thickness ~500  $\mu\text{m}$ ), nor even the cytoplasm of individual human cells (Fig. 1).

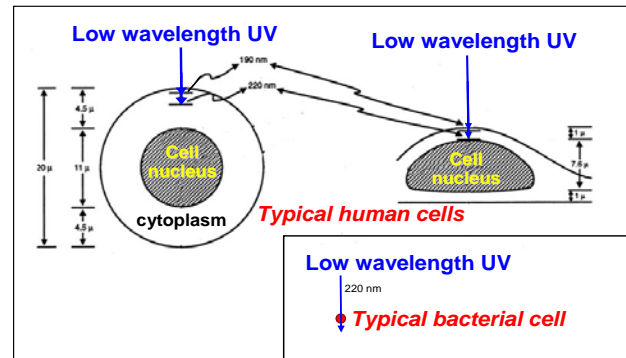


**Figure 1.** A typical human cell nucleus in a spherical or flattened geometry, illustrating the penetration into a human cell of UV radiation with wavelength of ~200 nm. No UV of this wavelength can reach the cell nucleus, which contains the radiation-sensitive DNA, whereas it can penetrate microbes that are generally much smaller in size. Adapted from [7].

Here we show *in vitro* that far-UVC light (207- and 222-nm light) has a bactericidal efficacy similar to that of conventional germicidal light (254 nm) but without inducing skin and eye damage *in vivo*.

## IN VITRO STUDIES

### MRSA Survival

We measured cell survival in MRSA (strain USA300) exposed to UV light generated by a 254-nm germicidal lamp, or by 207-nm or 222-nm light from filtered excilamps (Fig. 2). We found that far-UVC light kills MRSA as efficiently as 254-nm light. A fluence of ~20  $\text{mJ}/\text{cm}^2$  provided up to four logs of MRSA cell killing.

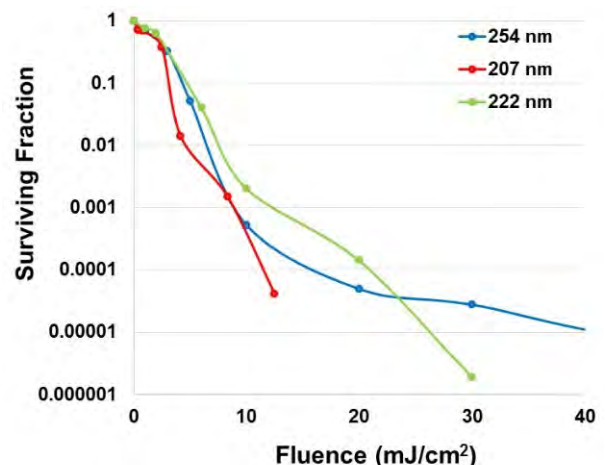


**Figure 2.** UVC survival of methicillin-resistant *S. aureus* (USA300). Far-UVC light (207- and 222-nm) is as efficient as conventional germicidal UV (254 nm) at killing MRSA.

<sup>a</sup>Division of Infectious Diseases, CUMC;

<sup>b</sup>Departments of Dermatology and Medicine, CUMC;

<sup>c</sup>Department of Surgery, CUMC;

<sup>d</sup>Department of Pathology & Cell Biology, CUMC

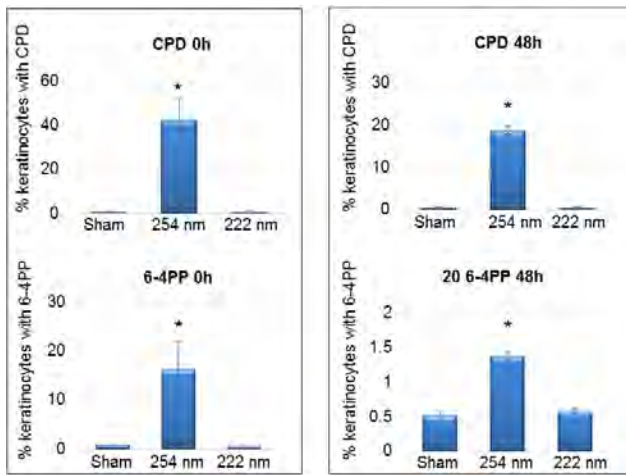


**Figure 3.** DNA photodamage in 3-D skin tissues exposed to 20 mJ/cm<sup>2</sup> from a conventional germicidal lamp (254 nm) or an excilamp (222 nm). In a 3-D human skin tissue model, pre-mutagenic DNA lesions were observed only in keratinocytes exposed to UV from the 254-nm germicidal lamp (\*p < 0.0001).

**DNA Photodamage in a 3-D Skin Tissue Model**

Figure 3 shows the measured induced yields of cyclobutane pyrimidine dimers (CPD) and pyrimidine-pyrimidone 6-4 photoproducts (6-4PP) [8] in keratinocytes of a full thickness MatTek 3-D skin tissue model immediately or 48 h after exposure to 20 mJ/cm<sup>2</sup> from a conventional germicidal UV lamp (peak 254 nm) or from 222-nm light generated by a Kr-Cl excilamp. As expected, at both time points the germicidal lamp induced high yields of both pre-mutagenic skin DNA lesions. However, following 222-nm exposure, neither lesion showed an induced yield that was significantly elevated above zero.

*IN VIVO* STUDIES

**Epidermal Thickness and Keratinocyte Proliferation in Hairless Mouse Skin**

To extend the far-UVC light safety studies [9] *in vivo*, we used a hairless mouse skin model. Mice were exposed to a cumulative fluence of 67 mJ/cm<sup>2</sup> delivered over a 7-hour period. This fluence is ~20 times higher than that required from a conventional germicidal lamp to inactivate 90% of *S. aureus* on surfaces [10].

At 48 h post-exposure, fixed dorsal skin sections were stained with hematoxylin and eosin (H&E) for analysis of epidermal thickness (Fig. 4). Figure 4A shows typical H&E-stained cross-sections of dorsal skin of sham-exposed mice (top panel), of mice exposed to 254-nm light (middle panel), and of mice exposed to 207-nm light (bottom panel). Exposure to conventional germicidal UV light (254 nm) caused a ~ 2.8-fold increase in the average mouse epidermal thickness (p < 0.0001) (Fig. 4B). In contrast, the epidermal thickness of the skin of mice exposed to the 207-nm excimer lamp was not statistically different from the skin of unexposed mice (p = 0.54) (Fig. 4B).

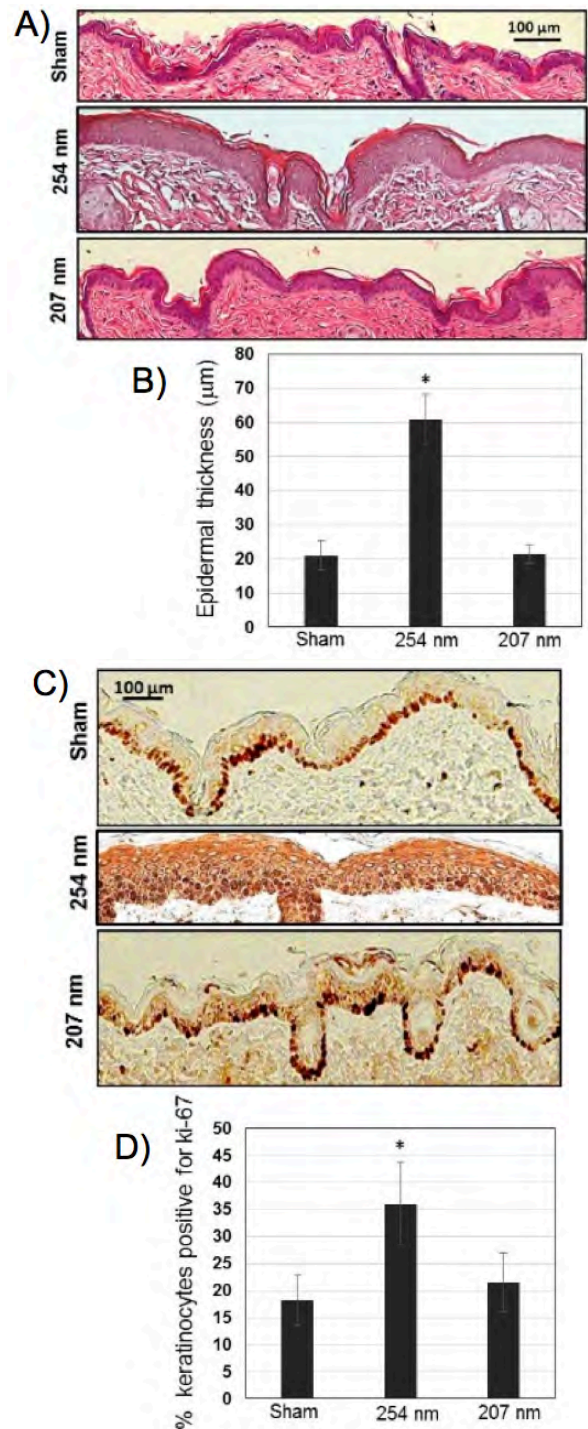


**Figure 4.** Epidermal thickness and expression of the proliferative marker Ki-67 in hairless mouse skin exposed to UVC light. A) Representative cross-sectional images of H&E-stained mouse dorsal skin comparing the epidermal thickness in sham-exposed mice (top panel), and mice exposed to 254-nm (middle panel) or 207-nm light (bottom panel) with B) relative quantification. C) Ki-67-positive keratinocytes (dark-stained cells) in typical cross-sections of skin of sham-exposed mice (top panel), and mice exposed to 254-nm (middle panel) or 207-nm light (bottom panel) with D) relative quantification. Values represent the average ± SD measured in at least 6 randomly selected fields of view per mouse (n=3). \*p < 0.0001

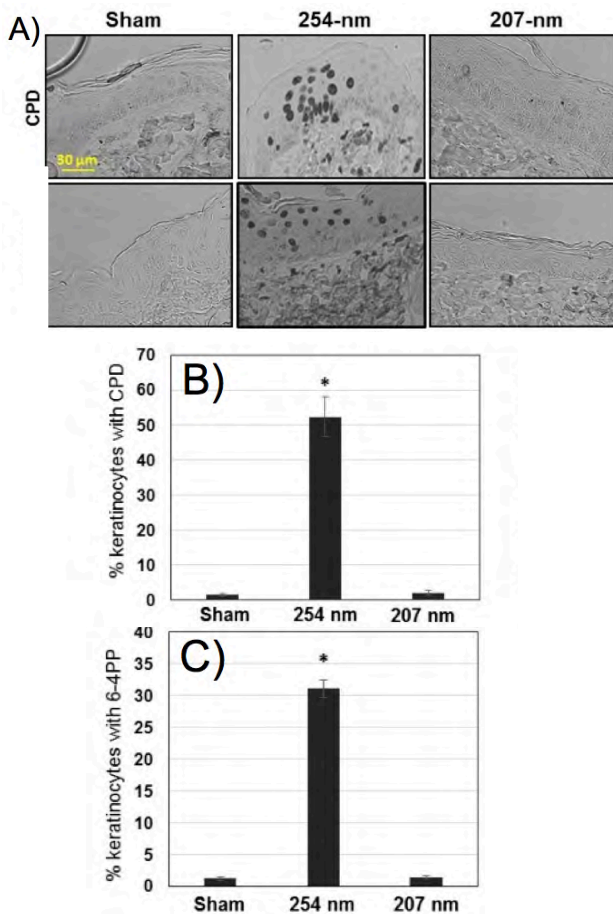


**Figure 5.** UVC-induced pre-mutagenic DNA lesions in hairless mouse skin. A) Representative cross-sectional images of dorsal skin samples comparing pre-mutagenic skin lesions CPD (top row, dark-stained cells) and 6-4PP (bottom row, dark stained cells) in the epidermis of sham-exposed mice (left column), of mice exposed to 254-nm light (middle column), or of mice exposed to 207-nm light (right column). Quantification of the percentage of keratinocytes showing B) CPD or C) 6-4PP. Values represent the average  $\pm$  SD of cells exhibiting dimers measured in nine randomly selected fields of view per mouse ( $n=3$ ). \* $p<0.0001$ .

254-nm light induced hyperplasia was associated with a hyper-proliferative epithelium as measured by the expression of the cell proliferation marker Ki-67 antigen [11]. Figure 4C shows representative cross-sectional images of skin samples comparing Ki-67 expression (dark-stained cells) in sham-exposed mice (top panel), in skin exposed to 254-nm UV light (middle panel), and in skin exposed to 207-nm light (bottom panel). In the skin of mice exposed to 254-nm UV light, the percentage of epidermal cells expressing the proliferative marker Ki-67 increased 2 fold ( $p<0.0001$ ) relative to sham-irradiated mouse skin (Fig. 4D). In contrast, Ki-67 expression in the keratinocytes of skin exposed to the 207-nm excimer lamp was not statistically different from controls ( $p=0.19$ ) (Fig. 4D).

**Pre-Mutagenic UV-Associated DNA Lesions in Hairless Mice Skin**

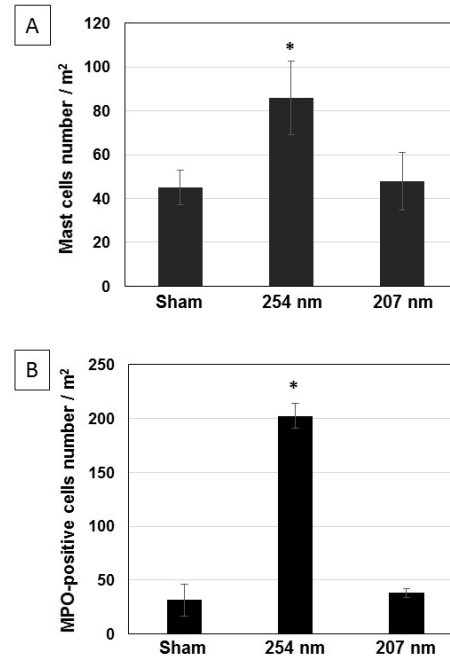


**Figure 6.** UVC-induced inflammation in hairless mouse skin. Density of A) mast cells and B) cells expressing the myeloperoxidase (MPO) enzyme (i.e. neutrophils) in the epidermis of UVC-exposed mouse skin. Values represent the average  $\pm$  SD of the number of cells / m² measured in six randomly selected fields of view per mouse ( $n=3$ ). \* $p<0.0001$

Figure 5A shows representative cross-sectional images of skin samples comparing pre-mutagenic skin lesions CPD and 6-4PP (dark-stained keratinocytes in the top and bottom row, respectively) with relative quantifications (Fig. 5B and 5C, respectively). In agreement with our previous findings in a human skin model [8], exposure to 67 mJ/cm² from 254-nm light resulted in ~ 35-fold increase in CPD and ~ 26-fold increase in 6-4PP relative to controls ( $p<0.0001$ ), whereas skin exposed to the same fluence of 207 nm UV light showed no statistically significant increases (Fig. 5B and 5C) for either CPD ( $p=0.44$ ) or 6-4PP ( $p=0.65$ ).

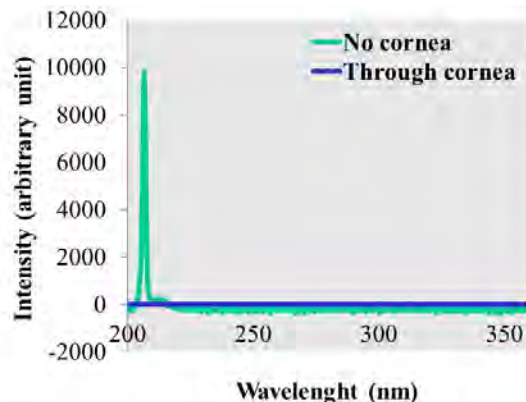


**Figure 7.** Measured UV emission spectra from filtered 207-nm excilamp through porcine cornea explants. Porcine cornea explants were mounted on a custom-designed fixture and positioned between the UV source and the fiber-optic guide to the spectrometer.



**Figure 8.** Slit lamp image of UVC-irradiated mouse eyes. 24 h post exposure to 600 mJ/cm<sup>2</sup> from 254-nm, but not 222-nm light, inflammation was induced in mouse eyes.

### Inflammation in Hairless Mouse Skin

To assess UV-induced tissue inflammation, we measured mast cell number by toluidine stain and the expression of the neutrophil myeloperoxidase (MPO) enzyme as a marker of neutrophil number [12]. Relative to controls, the density of both cell types doubled in the skin of mice chronically exposed to 254-nm light ( $p < 0.0001$ ) (Fig. 6A), while neutrophil density increased by 5.8-fold (Fig. 6B). By contrast, in mouse skin chronically exposed to 207-nm light, the density of mast cells (Fig. 6A) and of cells expressing MPO (Fig. 6B) was not statistically distinguishable from controls ( $p = 0.42$  and  $p = 0.76$ , respectively).

### Preliminary Eye Studies

Together with the skin, the eye is the most sensitive organ to UV damage. As shown by the emission spectra in Fig. 7, filtered UV from a 207-nm excilamp does not transmit through porcine cornea explants.

However, the most important target from the perspective of UV risk is the lens [13]. Although it can be predicted that penetration of ~200-nm light through the cornea to the lens would be essentially zero because the lens is located distal to the cornea, which is sufficiently thick (~500  $\mu\text{m}$  [14]) to completely block 200-nm light, it is nevertheless important to confirm that neither photokeratitis nor ultimately cataracts will be induced several months after exposure to far-UVC light. Preliminary results (Fig. 8) show severe inflammation 24 h after a mouse eye was acutely exposed to 600 mJ/cm<sup>2</sup> from conventional germicidal light (254-nm) (left panel), but not to far-UVC light (222-nm) (right panel).

### CONCLUSIONS

Our *in vitro* [5] and *in vivo* [9] studies suggest that far-UVC light (207- and 222-nm) generated by excilamps is approximately equitoxic to MRSA bacteria as 254-nm UV from a germicidal lamp, but without associated skin and eye damage risks. Our approach may have the potential to safely and inexpensively reduce surgical site infection rates [15], including those due to drug-resistant bacteria, and to continuously and safely sterilize any indoor environment. The low cost of such lamps may make them an attractive option, particularly in low-income countries.

### References

1. Rosenthal, V.D., et al., *International Nosocomial Infection Control Consortium (INICC) report, data summary of 36 countries, for 2004-2009*. Am J Infect Control, 2012. 40(5): p. 396-407.
2. Barie, P.S. and S.R. Eachempati, *Surgical site infections*. The Surgical clinics of North America, 2005. 85(6): p. 1115-35, viii-ix.
3. Jarvis, W.R. and R.L. Sinkowitz-Cochran, *Emerging healthcare-associated problem pathogens in the United States*. Postgraduate medicine, 2001. 109(2 Suppl): p. 3-9.
4. Koch-Paiz, C.A., et al., *Functional genomics of UV radiation responses in human cells*. Mutation research, 2004. 549(1-2): p. 65-78.
5. Buonanno, M., et al., *207-nm UV light - a promising tool for safe low-cost reduction of surgical site infections. I: in vitro studies*. PLoS One, 2013. 8(10): p. e76968.
6. Sosnin, E.A., Oppenlander, T. and Tarasenko, F.V. , *Applications of capacitive and barrier discharge excilamps in photoscience*. J Photochem Photobiol, 2006. C(7): p. 145-163.
7. Coohill, T.P., *Virus-cell interactions as probes for vacuum-ultraviolet radiation damage and repair*. Photochem Photobiol, 1986. 44(3): p. 359-63.
8. Pfeifer, G.P. and A. Besaratinia, *UV wavelength-dependent DNA damage and human non-melanoma and melanoma skin cancer*. Photochem Photobiol Sci, 2012. 11(1): p. 90-7.
9. Buonanno, M., et al., *207-nm UV Light - A Promising Tool for Safe Low-Cost Reduction of Surgical Site Infections. II: In-Vivo Safety Studies*. PLoS One In Press, 2015.
10. Kowalski, W., *Ultraviolet Germicidal Irradiation Handbook*. MyCopy, ed. SpringerLink. 2009: Springer.
11. Scholzen, T. and J. Gerdes, *The Ki-67 protein: from the known and the unknown*. J Cell Physiol, 2000. 182(3): p. 311-22.
12. Hawk, J.L., G.M. Murphy, and C.A. Holden, *The presence of neutrophils in human cutaneous ultraviolet-B inflammation*. Br J Dermatol, 1988. 118(1): p. 27-30.
13. Jose, J.G. and D.G. Pitts, *Wavelength dependency of cataracts in albino mice following chronic exposure*. Exp Eye Res, 1985. 41(4): p. 545-63.
14. Doughty, M.J. and M.L. Zaman, *Human corneal thickness and its impact on intraocular pressure measures: a review and meta-analysis approach*. Surv Ophthalmol, 2000. 44(5): p. 367-408.
15. Ritter, M.A., E.M. Olberding, and R.A. Malinzak, *Ultraviolet lighting during orthopaedic surgery and the rate of infection*. J Bone Joint Surg Am, 2007. 89(9): p. 1935-40. ■

# Targeting Lung Cancer Stem Cell Factor BMI-1 to Sensitize Non-small Cell Lung Cancer to Chemotherapy and Radiation Therapy

Kunal Chaudhary<sup>a</sup>, Haiying Cheng<sup>b</sup>, Balazs Halmos<sup>b</sup>, Jose Silva<sup>c</sup>, Tom K Hei, Simon Cheng<sup>a</sup>

Lung cancer is known to be the most common type of cancer and the leading cause of cancer-related death in men and women worldwide. Despite treatment advances, patient outcomes remain dismal and overall survival at 5 years is only 15%. The resistance mechanisms for concurrent chemoradiation therapy are poorly studied. Cancer stem cells have been proposed to be the driver for many cancers including lung cancer and may also be responsible for therapy resistance. We sought therefore to identify therapy resistance pathways in lung cancer by using genome-wide RNAi high-throughput screening using a shRNA viral library containing approximately 60,000 individual shRNAs on a human lung adenocarcinoma cell line (PC9), as reported in last year's annual report.

Interestingly, from the cisplatin and radiation screen, analysis of the top 100 potential hits showed several cancer stem cell markers including Sox, Lrg6, and the Hedgehog signaling pathway members PTCH1 and BMI1. FACS analysis showed increased stem cell markers CD133, ABCG2 and CXCR4 expression on PC9 cells treated multiple times with cisplatin and radiation compared to non-treated cells, pointing towards acquired

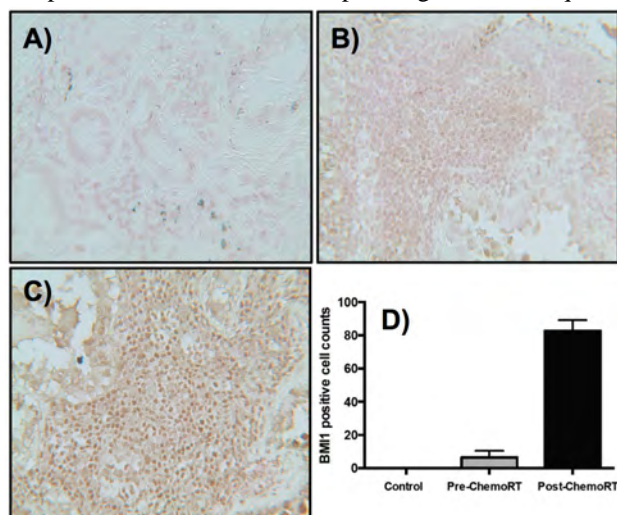


**Figure 1.** NSCLC tissue samples stained for BMI1. A) Staining control, B) Pre-chemoradiation treatment, C) 24 hours after chemoradiation. D) The percentage of BMI1 positive cells.

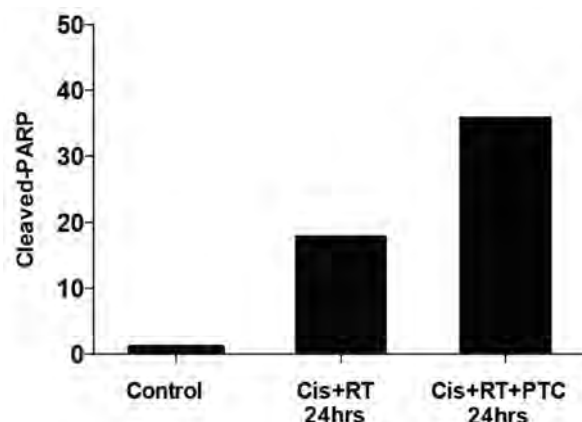


**Figure 2.** PARP cleavage (% cells positive for C-PARP antibody) as measured by flow cytometry. PC9 cells were exposed to cisplatin (Cis; 1  $\mu$ M) and X-rays (RT; 2 Gy) in the presence or absence of BMI1 inhibitor PTC-09 (PTC; 10  $\mu$ M). Bars are the mean of 3 experiments.

stemness of lung cancer cells after treatment and subsequently resistance to treatment. Furthermore, immunohistochemistry of NSCLC patient's tissue slides revealed elevated levels of BMI-1 positive cells post chemoradiation therapy compared to pre-treatment (Figure 1). Cells treated with cisplatin and radiation in combination with the Bmi1 inhibitor PTC-209 showed increased staining of cleaved PARP compared to control cells treated with combined chemoradiation (Figure 2).

We further determined the effects of BMI1 on therapy resistance by performing survival assays with PC9 cells treated with PTC-09. MTT cell survival and clonogenic assays were performed by treating PC9 cells with PTC-09 in triplicate and then treating with increasing doses of cisplatin (0.1, 1 and 10  $\mu$ M) or X-ray radiation (2, 4 and 6 Gy). Significantly decreased cell survival was observed in PC9 cells treated with cisplatin or radiation in the presence of PTC-09 compared to controls and to cells treated with cisplatin or radiation alone. Further clonogenic assay of PC9 cells treated with 2 Gy X-rays plus 1  $\mu$ M cisplatin and increasing dosage of PTC-09 showed a significant decrease in the ability of cells to form colonies compared to controls (Figure 3).

By performing an unbiased genome wide screen for therapeutic resistance, we have successfully identified and validated a target in the cancer stem cell pathway. We are further evaluating the effects of BMI1 using a CRISPR knock out model and downstream targets. ■

<sup>a</sup>Department of Radiation Oncology, CUMC;

<sup>b</sup>Department of Oncology, Albert Einstein College of Medicine of Yeshiva University, New York, NY;

<sup>c</sup>Department of Pathology and Cell Biology, CUMC;

# The Effect of High LET Radiation on a Human Hematopoietic System Reconstituted in Mice

*Erik Young, Igor Shuryak, and Lubomir Smilenov*

## The hematopoietic system and space radiation

The main goal of the NASA radiation program is to reduce the uncertainties in space radiation risk projections for cancer and for CNS and other degenerative tissue diseases. During the past 50 years of human spaceflight, especially during the space shuttle era, a number of important physiological changes to humans in spaceflight have been observed ([1-3] and NCRP reports No.132 and No. 153).

Of major concern to NASA are short- and long-term radiation-induced injuries to the hematopoietic system. The hematopoietic compartment is one of the most radiosensitive tissues in the human body, given that it is comprised of a large number of continuously and rapidly proliferating cells. Effects of exposure to the space environment are illustrated in studies that show changes in the immune response of T lymphocytes following space flight, as well as decreases in the numbers of T and B cells observed in crewmembers of STS-41B and STS-41D [4]. Altered differentiation of human bone marrow hematopoietic progenitor cells was also demonstrated during STS-63 and STS-69 [5].

Effects of spaceflight on the hematopoietic systems of animals have also been reported. Studies in mice that were aboard STS-108 showed hematologic changes of CD34<sup>+</sup> cells, early blast cells, and macrophage progenitors in the bone marrow[6]. Mouse studies during STS-118 revealed alterations in leukocyte subpopulations of the bone marrow and spleen [7, 8]. Other work in both nonhuman primates and mice shows a suppression of hematopoietic differentiation of macrophages and other blood cells [9, 10].

These in-flight studies are bolstered by ground-based findings that the high-LET radiation present in the space environment may have an impact on the immune system. Indeed, changes in virtually all blood cell populations from generative compartments of bone marrow and spleen to mature populations in circulating blood are evident in mice after irradiation with protons, carbon ions or iron ions [11, 12]. There are, in addition, supporting 'real world' forensic dosimetry findings that report lesions in astronauts' peripheral blood lymphocytes after long-term missions [13, 14]. Together, these data support a consensus that space radiation may have important short- and long-term effects on the hematopoietic system.

The main goal of our study is to obtain data on the early and late effects of high LET radiation on the human hematopoietic system. We hypothesized that studies of

the effects of high-LET radiation on a human hematopoietic system reconstituted in immunodeficient mice will provide meaningful information on both post-radiation depletion and repopulation kinetics and tumor formation. Such information can then be applied to space radiation risk assessment. The study has two key objectives: The first is to characterize the early and late response of a human immune system reconstituted in mice to high LET radiation and gamma-rays. The second objective is to characterize the tumors (of human and mouse origin) that may arise in the irradiated and non-irradiated mice. Here we present data on the high LET radiation induced depletion and recovery kinetics of human peripheral blood cells that were produced in immunodeficient mice engrafted with a human immune system.

## Model system description

In this study we used the NSG mice (strain NOD-*scid* IL2Rg<sup>null</sup>). The advantages of the NSG mouse model include long lifespan (>100 weeks), low frequency of lymphomas, and high engraftment of human hematopoietic stem cells [15]. Numerous studies have demonstrated that transplantation of the human CD34<sup>+</sup> cell fraction leads to the *in vivo* development of human hematopoietic progenitors and differentiated cells in the mouse bone marrow, spleen and thymus, culminating in a functional immune system [16-18]. Using this model allows, for the first time, detailed short- and long-term studies of the response of human hematopoietic cells to diverse radiation exposure scenarios in an *in-vivo* environment.

## Assessment of the early effect of high Let <sup>28</sup>Si radiation on the peripheral blood cell counts of irradiated mice

For these studies we produced 73 mice engrafted with a human hematopoietic system. Forty nine mice were irradiated at the NASA Space Radiation Laboratory (NSRL) with 0.4 Gy of 350 MeV/n <sup>28</sup>Si ions, which are part of the high energy spectrum of galactic cosmic rays. Twenty-four mice were used as non-irradiated controls. For blood cell count assessment, blood samples (around 50 µl per mouse) were obtained at 3 weeks before the irradiation, and at 7 and 30 days after the irradiation.

## Statistical analysis

The analysis of the data was performed using three methods: 1. Student's t-test with Bonferroni correction of the p-values for multiple comparisons; 2. Machine learning by random forests (RF) [19]; and 3. Parametric modeling by mixed effect linear models. In methods 2 and 3, the variables evaluated as potential predictors of the

outcome were: time, time<sup>2</sup>, radiation dose, human donor from which the cells were derived, and sex of the recipient mouse.

**Results and discussion**

It is well known that an insult to the hematopoietic system will generate effects that are not limited in scope to hematologic endpoints. There is an interrelationship between the correct function of the hematopoietic system and other organ systems. Systemic infections and mortality are known to accompany the reduction of peripheral blood cell counts that result from low LET radiation exposure [20, 21]. Blood cell populations are an important indicator of the functional status of the hematopoietic system. The mean dose of high LET radiation that a human hematopoietic system can

autonomously recover from is not known and extrapolating from mouse data to answer this question is difficult. Mice are more radioresistant, possessing a gamma-ray LD<sub>50</sub> nearly twice that of humans [22]. Recently two very important studies have shown that the response of mouse and human hematopoietic stem cells (HSC) to radiation is different. The mouse response is biased toward the induction of pro-survival signaling pathways due to the activation of p53 dependent double-strand break (DSB) repair. This results in increased radioresistance and HSC protection but this mechanism leads also to accumulation of DNA damage [23]. In contrast, human HSC respond with a bias toward apoptosis, sacrificing the damaged HSC population in favor of genomic integrity [24]. An important hypothesis

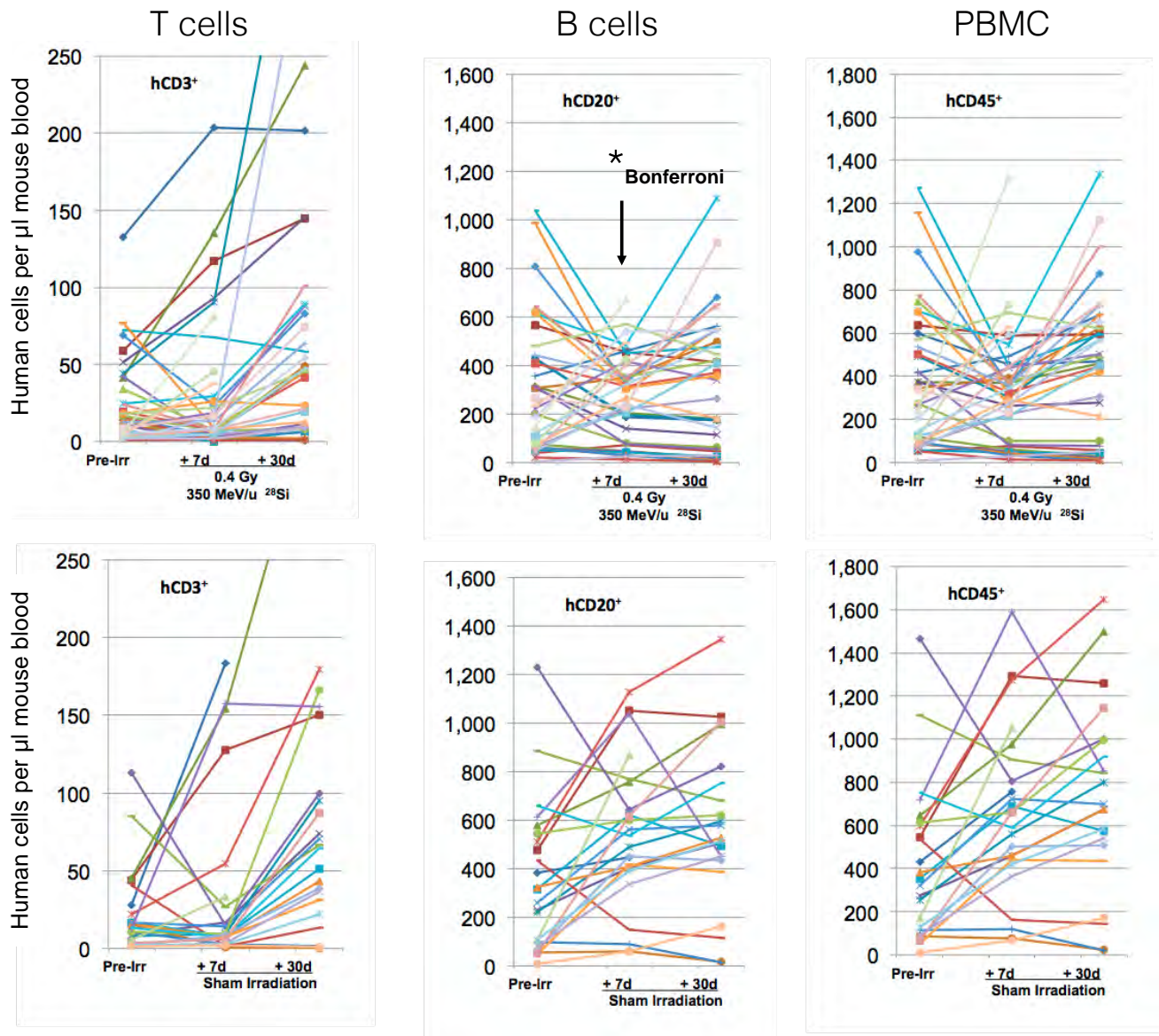


**Figure 1.** Depletion and recovery kinetics of human peripheral blood cells after irradiation with 350 MeV/n <sup>28</sup>Si ions (top row) and controls (bottom row). Peripheral blood cell counts (T cells, B cells and PBNC) were measured 21 days before the irradiation (Pre-irr) and 7 days and 30 days after irradiation. Each colored line represents the blood cell counts of a single mouse taken at the different time points. The asterisk indicates a statistically significant Bonferroni-corrected p-value (p<0.05) between B cell counts in irradiated and control mice 7 days after irradiation.

can be formulated based on these results. Specifically, mice and humans employ different strategies in responding to hematopoietic genotoxic insults. Given the species-specific nature of these response strategies, it is important that an experimental system that informs risk assessment is comprised of human cells and human systems.

A very important question regarding the effect of high LET radiation on human blood cells is related to its effects on the human blood cell counts. Two very important endpoints can be measured by determining the blood cell counts at different periods after irradiation, and these are cell killing and depletion and recovery kinetics. Any detectable loss of cells as a result of radiation will be a measure of the radiation damage to the hematopoietic system. Monitoring the peripheral blood cell counts for extended periods of time may show the depletion and recovery kinetics of peripheral blood cells, which will be a measure of the degree and sustainability of the radiation induced damage, and also the ability of the human hematopoietic system to recover after radiation induced cell losses.

The depletion/recovery kinetics data are shown in Fig. 1. Based on the statistical analysis of these results, we draw the following main conclusions:

Direct t-testing with Bonferroni correction of the p-values for multiple comparisons of irradiated vs. non-irradiated mouse data showed statistically significant differences only between the B cell counts of irradiated and non-irradiated mice at day 7 after the irradiation ( $p = 3.16 \times 10^{-4}$ ). The differences in the cell counts at all other time points were not statistically significant for any of the cell types.

The machine learning analysis by RF identified the most important variables for predicting the kinetics of both CD20 and CD3 cells were **time** and the human **donor** from which the cells were derived: these variables were 4.7-5.8-fold more important for describing the data than random noise. In other words, there was strong evidence that cell numbers changed (grew) over time and that there was a lot of inter-donor variability. The effect of radiation was quite important for CD20 cells (4.4-fold more important than random noise), but barely detectable for CD3 cells (only 1.1-fold more important than random noise). This is consistent with experimental data showing that B-cells (CD20) are more radiosensitive than T-cells (CD3). Another factor that may have influenced these results is the relatively low counts for T cells specifically at the pre-irradiation time point and at day 7 after the irradiation time point. Sex of the mouse, however, was not important for predicting the kinetics of either CD20 or CD3 cells.

Parametric analysis by mixed effect linear models confirmed the conclusion that **inter-donor variability** in response to radiation and proliferation rates over time were very important. For CD20 cells, a linear model with

no random effects of donor identity on radiation response or proliferation rate (i.e. a fixed effect only model) achieved a coefficient of determination ( $R^2$ ) of only 0.25. In other words, when inter-donor variability was not accounted for, only 25% of the variance could be explained. In contrast, when inter-donor variability was included by adding random effects of donor to the radiation response and proliferation rate, the fraction of explained variance (conditional  $R^2$ ) rose to 58%. The corresponding numbers for CD3 cells were 51% and 72%, respectively.

Two conclusions can be derived from the data analysis. The first one is that a human hematopoietic system, reconstituted in mice, is affected by 0.4 Gy of 350 MeV/n  $^{28}\text{Si}$ -ions. Secondly, the engrafted hematopoietic system does recover after some period of time. Important questions arise from these results. What is the effect of the  $^{28}\text{Si}$ -ion irradiation on the HSC and progenitor cells? Is the depletion of the peripheral blood human cells a result of their high radiation sensitivity, or it is a result of reduction of the HSC and progenitor cell numbers in the bone marrow? If the later is true, then the radiation effect can be qualified as significant and has to be investigated further. Future experiments aiming to answer this question are being scheduled at NSRL for the summer of 2016.

## References

1. Suda, T., *Lessons from the space experiment SL-J/FMPT/L7: the effect of microgravity on chicken embryogenesis and bone formation*. Bone, 1998. **22**(5 Suppl): p. 73S-78S.
2. Chapes, S.K., *Lessons from Immune 1-3: what did we learn and what do we need to do in the future?* J Gravit Physiol, 2004. **11**(2): p. P45-8.
3. Charles, D., *Science on the shuttle. NASA's busload of science*. Science, 2011. **333**(6038): p. 28-9.
4. Taylor, G.R., L.S. Neale, and J.R. Dardano, *Immunological analyses of U.S. Space Shuttle crewmembers*. Aviat Space Environ Med, 1986. **57**(3): p. 213-7.
5. Davis, T.A., et al., *Effect of spaceflight on human stem cell hematopoiesis: suppression of erythropoiesis and myelopoiesis*. J Leukoc Biol, 1996. **60**(1): p. 69-76.
6. Pecaut, M.J., et al., *Genetic models in applied physiology: selected contribution: effects of spaceflight on immunity in the C57BL/6 mouse. I. Immune population distributions*. J Appl Physiol, 2003. **94**(5): p. 2085-94.
7. Gridley, D.S., et al., *Spaceflight effects on T lymphocyte distribution, function and gene expression*. J Appl Physiol, 2009. **106**(1): p. 194-202.
8. Ortega, M.T., et al., *Shifts in bone marrow cell phenotypes caused by spaceflight*. J Appl Physiol, 2009. **106**(2): p. 548-55.

9. Sonnenfeld, G., et al., *Effect of space flight on cytokine production and other immunologic parameters of rhesus monkeys*. J Interferon Cytokine Res, 1996. **16**(5): p. 409-15.
10. Sonnenfeld, G., et al., *Spaceflight alters immune cell function and distribution*. J Appl Physiol, 1992. **73**(2 Suppl): p. 191S-195S.
11. Gridley, D.S. and M.J. Pecaut, *Whole-body irradiation and long-term modification of bone marrow-derived cell populations by low- and high-LET radiation*. In Vivo, 2006. **20**(6B): p. 781-9.
12. Maks, C.J., et al., *Analysis of white blood cell counts in mice after gamma- or proton-radiation exposure*. Radiation research, 2011. **176**(2): p. 170-6.
13. George, K., L.J. Chappell, and F.A. Cucinotta, *Persistence of space radiation induced cytogenetic damage in the blood lymphocytes of astronauts*. Mutat Res, 2010. **701**(1): p. 75-9.
14. Obe, G., et al., *Chromosomal aberrations in blood lymphocytes of astronauts after long-term space flights*. International journal of radiation biology, 1997. **72**(6): p. 727-34.
15. Shultz, L.D., et al., *Humanized mice for immune system investigation: progress, promise and challenges*. Nat Rev Immunol, 2012. **12**(11): p. 786-98.
16. Traggiai, E., et al., *Development of a human adaptive immune system in cord blood cell-transplanted mice*. Science, 2004. **304**(5667): p. 104-7.
17. Andre, M.C., et al., *Long-term human CD34+ stem cell-engrafted nonobese diabetic/SCID/IL-2R gamma(null) mice show impaired CD8+ T cell maintenance and a functional arrest of immature NK cells*. Journal of immunology, 2010. **185**(5): p. 2710-20.
18. Shultz, L.D., et al., *Generation of functional human T-cell subsets with HLA-restricted immune responses in HLA class I expressing NOD/SCID/IL2r gamma(null) humanized mice*. Proceedings of the National Academy of Sciences of the United States of America, 2010. **107**(29): p. 13022-7.
19. Breiman, L., *Random forests*. Machine learning, 2001. **45**(1): p. 5-32.
20. Dainiak, N., et al., *First global consensus for evidence-based management of the hematopoietic syndrome resulting from exposure to ionizing radiation*. Disaster Med Public Health Prep, 2011. **5**(3): p. 202-12.
21. Brook, I., et al., *Management of postirradiation sepsis*. Mil Med, 2002. **167**(2 Suppl): p. 105-6.
22. Hall EJ, G.A., *Radiobiology for the radiologists*. 2006, Philadelphia: Lippincott Williams&Wilkins.
23. Mohrin, M., et al., *Hematopoietic stem cell quiescence promotes error-prone DNA repair and mutagenesis*. Cell Stem Cell, 2010. **7**(2): p. 174-85.
24. Milyavsky, M., et al., *A distinctive DNA damage response in human hematopoietic stem cells reveals an apoptosis-independent role for p53 in self-renewal*. Cell Stem Cell, 2010. **7**(2): p. 186-97. ■



**Top row (l to r):** Matt England, Peter Grabham, Cui-Xia Kuan, Haseeb Durrani.  
**Bottom row (l to r):** Rob Morton, David Cuniberti, Kunal Chaudhary.

# New Approaches for Modeling Radiopharmaceutical Pharmacokinetics Using Continuous Distributions of Rates

Igor Shuryak and Ekaterina Dadachova<sup>a</sup>

Radiopharmaceutical pharmacokinetics are usually approximated by sums of discrete first-order rates, using 3 or more parameters. We hypothesized that pharmacokinetic processes can be modeled even better by continuous probability distributions (CPD) of rates, using only 1–2 parameters.

To test this hypothesis, we used biodistribution data for <sup>188</sup>Re-labeled melanin-specific antibody in blood, kidneys, liver, bone marrow, and lungs of melanoma xenograft-bearing mice [1]. We used three discrete-rate models (mono-exponential (ME), mono-exponential with constant (MEC), and bi-exponential (BE) and 4 CPD models (stretched-exponential (SE) [2], modified stretched-exponential (MSE) [2], simplified versions of stretched-exponential, and modified stretched-exponential (SSE and SMSE, respectively). They were compared by sample-size-corrected Akaike information criterion. Total time integrals of radioactivity were computed for each model and averaged across all models.

Radioactivity pharmacokinetics can be approximated by two phases. The first is distribution, during which the radioactive material spreads throughout various organs/tissues, reaching organ-specific concentrations. The second is elimination, during which the material is eliminated by biochemical processes and by physical radioisotope decay. Ideally, both phases should be described by suitable mathematical models. However, the main focus of the current study was on the second (elimination) phase—namely to investigate whether this phase can be

reasonably described by formalisms that assume CPDs of first-order rates, and to compare the performance of such formalisms to that of the commonly used sum of 2 discrete rates. Consequently, the distribution phase was left beyond the scope of this study.

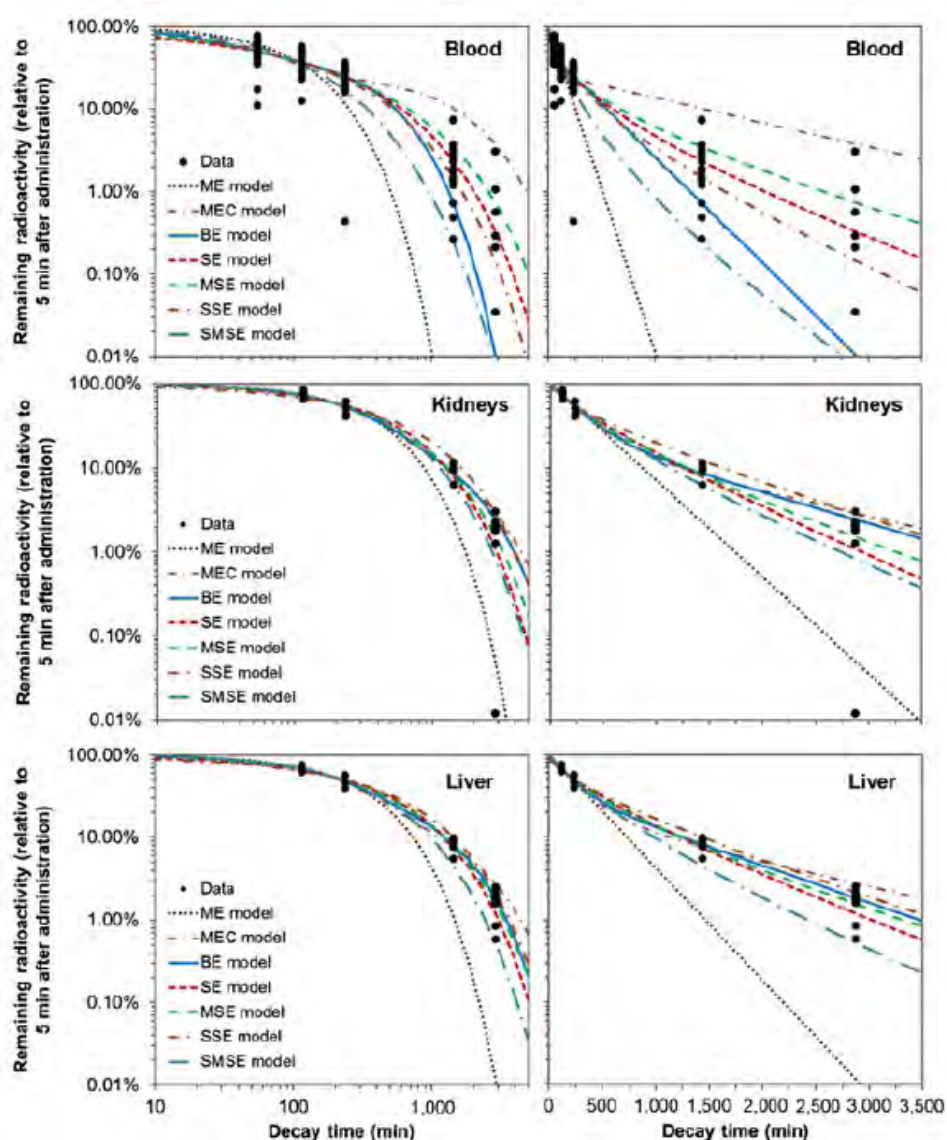


**Figure 1.** Data and best-fit model predictions for pharmacokinetics of <sup>188</sup>Re-labeled antibody to melanin in mouse blood, kidneys, and liver. Model abbreviations are described in the main text. Data and curves in left and right panels are same, and panels differ only by linear or logarithmic scaling of the x-axis (time).

<sup>a</sup>Department of Radiology and Department of Microbiology and Immunology, Albert Einstein College of Medicine, Bronx, New York

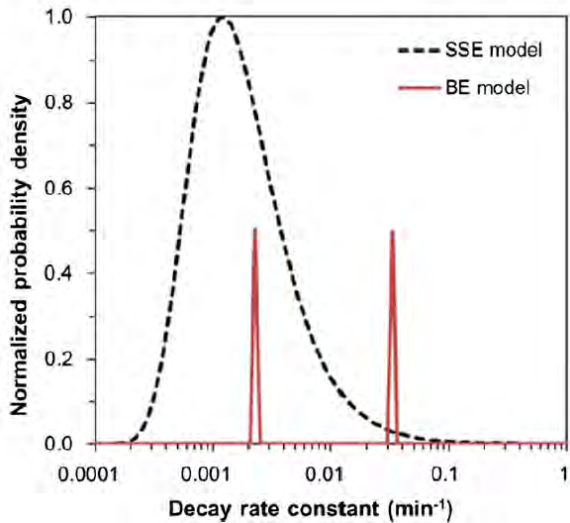


**Figure 2.** Distributions of pharmacokinetic rates predicted for blood data by BE and SSE models, using best-fit parameter values. For BE model, the heights of both peaks sum to 1. For SSE model, the probability density function was normalized (divided by its maximum value) to facilitate visual comparison with BE model on same scale.

To focus on the elimination phase, we selected five organs/tissues (blood, kidneys, liver, bone marrow, and lungs) with clinical relevance regarding radiation-induced toxicity, in which the distribution phase is rapid and maximum radioactivity concentrations are reached within 5 min after radioactivity administration.

We constructed the mathematical models to analyze these data as follows: Physical decay of  $^{188}\text{Re}$  is represented by the function  $g(t) = \exp[-(\ln(2)/\tau_0)t]$  where  $\tau_0$  is the half-life. The ME model is represented by the equation  $g(t) \exp[-t/\tau_1]$ . The MEC and BE models are represented by equations  $g(t) (w_1 \exp[-t/\tau_2] + 1 - w_1)$  and  $g(t) (w_2 \exp[-t/\tau_3] + (1 - w_2) \exp[-t/\tau_4])$ , respectively. The SE and MSE models are represented by equations  $g(t) \exp[-(t/\tau_5)^{\gamma_1}]$  and  $g(t) \exp[1 - (1 + t/\tau_6)^{\gamma_2}]$ , respectively. The SSE and SMSE models are represented by equations  $g(t) \exp[-(t/\tau_7)^{1/2}]$  and  $g(t) \exp[1 - (1 + t/\tau_8)^{1/2}]$ , respectively. All model parameters labeled  $\tau$  have units of minutes, and all parameters labeled  $w$  or  $\gamma$  are unit-less.

Visual inspection of model fits to blood data (Fig. 1) suggests that the SE and SSE models described the pharmacokinetics better than other tested formalisms. Information theoretic analysis supported this conclusion:

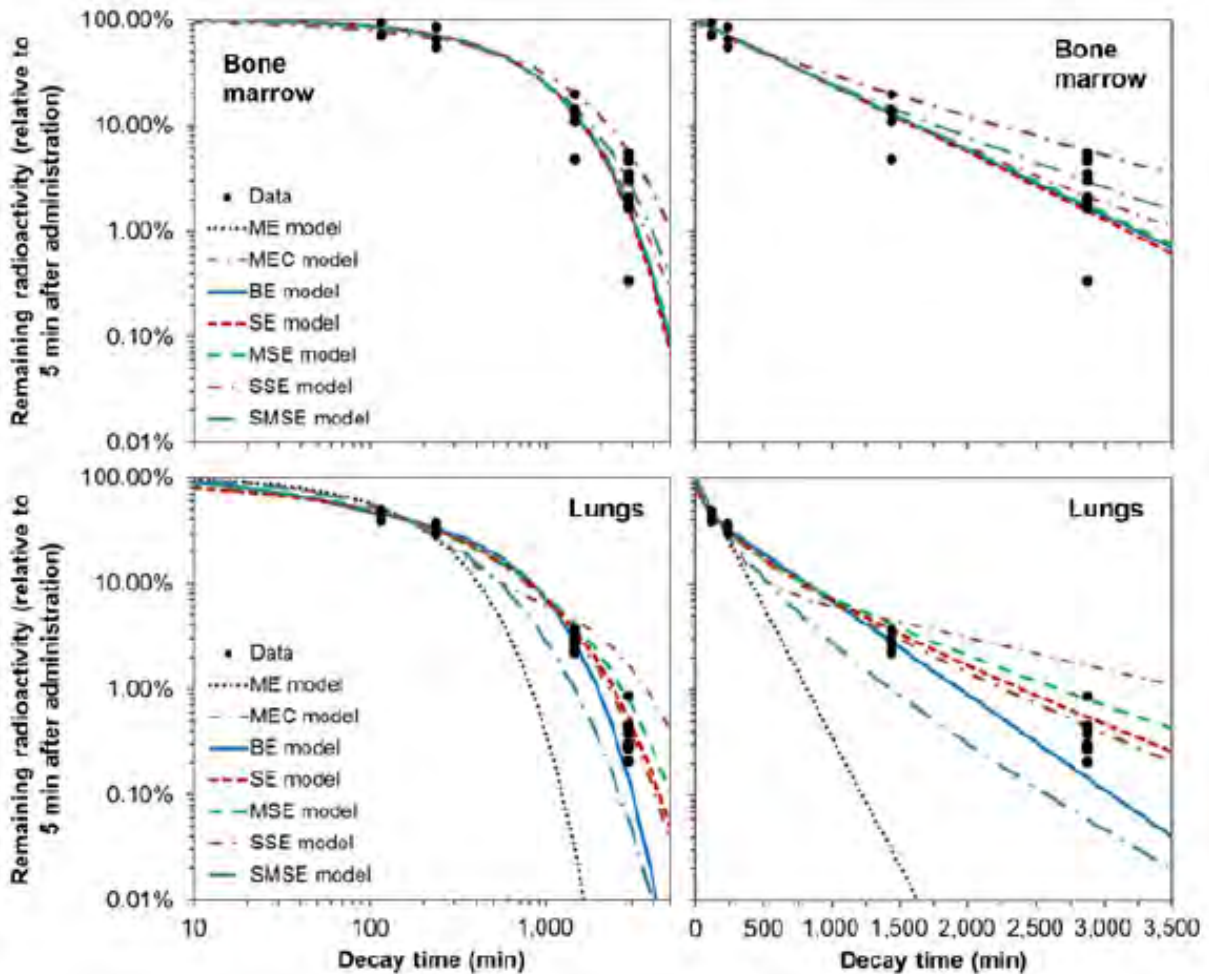


**Figure 3.** Data and best-fit model predictions for pharmacokinetics of  $^{188}\text{Re}$ -labeled antibody to melanin in mouse bone marrow and lungs.

the SSE model had the highest Akaike weight, followed by the SE model, indicating that these models had the strongest support from the data. The commonly used BE model described the blood data reasonably well at short decay times but underestimated them at long times (Fig. 1).

A visual comparison of the best-fit rate distributions from the SSE and BE models for blood data is shown in Fig. 2. The rate distribution underlying the SSE model in this case resembles the lognormal distribution, with a somewhat enlarged tail toward larger rates. The distribution underlying the BE model in this case is almost a 50:50 combination of 2 discrete peaks, which represent rates roughly an order of magnitude apart.

For kidney, liver, bone marrow, and lung data, the ratios of combined weight of evidence for CPD versus discrete-rate models were 0.81, 0.73, 0.99, and 2.7, respectively. Visual inspection of the model fits and the data (Figs. 1 and 3) supported these findings. This pattern may imply that for some organs/tissues (e.g., kidneys, liver, bone marrow) pharmacokinetics were simple and hence well described by ME or MEC models, whereas for others (e.g., blood, lungs) pharmacokinetics were complex and well described by only CPD models. The commonly used BE model did not have the best AICc ranking in any of the five analyzed organs/tissues and sometimes clearly underestimated the data at long decay times.

The ratio of weights of evidence for CPD versus discrete-rate models was high for blood (12.2) and lungs (2.7), almost unity (0.99) for bone marrow, and slightly lower for kidneys (0.81) and liver (0.73). In all organs or tissues except lungs, model-averaged time integrals were 12.7%–54.0% higher than bi-exponential model estimates. Therefore, our analysis suggests that simple

CPD models often outperform more complex discrete-rate models on pharmacokinetic data. Radioactivity time integrals are more robustly estimated by multimodel inference than by using any single model.

Pharmacokinetic data are essential for translating pharmaceutical agents from the bench to the clinic. For radiopharmaceuticals, pharmacokinetic data are also essential for dosimetry calculations to predict radiation doses to tumors and healthy tissues. In this study, we applied simple mechanistically plausible models, which assume CPDs of pharmacokinetic rates to data on biodistribution of <sup>188</sup>Re-labeled melanin-specific antibodies in melanoma-bearing mice, and observed that these models described the data better than the more complex biexponential model. Therefore, such models should be taken into consideration for describing radiopharmaceutical pharmacokinetics.

*This research was originally published in JNM. Shuryak I and Dadachova E. New Approaches for Modeling Radiopharmaceutical Pharmacokinetics Using Continuous Distributions of Rates. J Nucl Med. 2015; 56: 1622-1628. © by the Society of Nuclear Medicine and Molecular Imaging, Inc.*

#### References

1. Dadachova E, Revskaya E, Sesay MA, et al. Pre-clinical evaluation and efficacy studies of a melanin-binding IgM antibody labeled with 188Re against experimental human metastatic melanoma in nude mice. *Cancer Biol Ther.* 2008;7:1116-1127.
2. Berberan-Santos M, Bodunov E, Valeur B. Mathematical functions for the analysis of luminescence decays with underlying distributions 1. Kohlrausch decay function (stretched exponential). *Chem Phys.* 2005;315:171-182. ■



*Eric Hall (right) with the President of the American Society of Veterinarian Radiology after giving his keynote address at their annual meeting.*

**CENTER FOR HIGH-THROUGHPUT  
MINIMALLY-INVASIVE RADIATION  
BIOSIMETRY**



# An Irradiator for Simulating Neutron Exposure from an Improvised Nuclear Device

Guy Garty, Yanping Xu, Gerhard Randers-Pehrson, Stephan A. Marino, Helen C. Turner, Adayabalam S. Balajee, and David J. Brenner

Several scenarios of large-scale radiological events include the use of an improvised nuclear device (IND). An IND may produce a significant neutron component with the prompt radiation exposure [1], qualitatively similar to that of the gun-type 15 kT device exploded over Hiroshima [2]. In order to assess the significance of the neutron exposure in this type of scenario, a new broad-energy neutron irradiator was designed [3] and built [4] at the Columbia University Radiological Research Accelerator Facility (RARAF).

## Irradiator Design

This accelerator-driven neutron irradiator provides a neutron field with energies from below 0.2 MeV to 9 MeV, produced by a mixed beam composed of 5 MeV atomic (hydrogen) and molecular (deuterium) ions bombarding a thick beryllium (Be) target.

This mixed beam produces a neutron spectrum that is the sum of the spectra from the  $9\text{Be}(d,n)10\text{B}$  and  $9\text{Be}(p,n)9\text{B}$  reactions for all the incident ions (monatomic, diatomic and triatomic). In general, the  $9\text{Be}(d, n)$  reaction provides a spectrum with higher-energy neutrons (above 1 MeV) and the  $9\text{Be}(p,n)$  reaction provides a spectrum with neutrons below 1 MeV. These nuclear reactions generate a combined neutron spectrum with a wide range of energies, similar to that of the Hiroshima bomb neutron spectrum (Figure 1), which can be used for irradiating biological samples and small animals (e.g., mice) for radiobiology studies. The beam composition in the present setup is approximately a 1:2

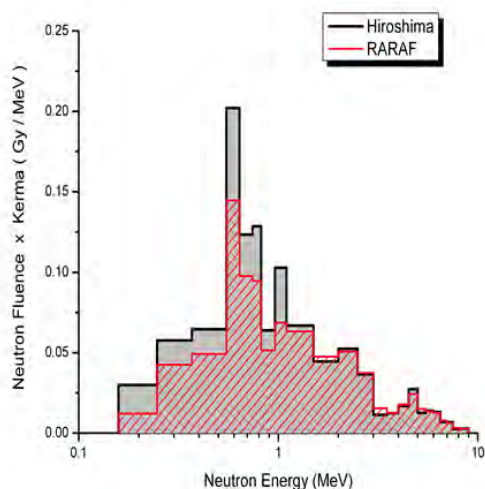


**Figure 1.** A comparison of the kerma-weighted neutron spectrum generated from our neutron irradiator with that at 1.5 km from Hiroshima ground zero.

ratio of protons to deuterons. However, for other scenarios, the shape of the neutron spectrum can be modified by adjusting the ratio of protons to deuterons.

Due to the requirement for a mixed hydrogen/deuterium beam, the irradiation facility was set up using an un-deflected (zero degree angle) beam line in the RARAF accelerator facility (Figure 2). Sample holder tubes (for either blood or mice) were mounted on a vertical Ferris wheel-like fixture for rotation around the Be target. A water cooling chamber cooled the Be target by impinging water onto its copper backing plate [3]. The sample holders for both mice and ex-vivo irradiated blood are standard 50 ml conical centrifuge tubes, which have been modified to allow mounting from rods on the wheel, with a constant horizontal orientation at a distance of 190 mm from the center of the target and an angle of  $60^\circ$  to the ion beam axis. The tubes used for blood irradiations have been fitted with a customized cap, designed to hold a 4 ml vacutainer tube centered within the conical tube. The tubes used for mouse irradiations have been fitted with a cap that allows the tail to pass through and are perforated to provide breathing holes. As the neutron dose is not azimuthally uniform, the fixture rotates up to 18 samples about the beam axis, providing a more uniform dose. Additionally, the sample tubes are flipped front to back halfway through the irradiation.

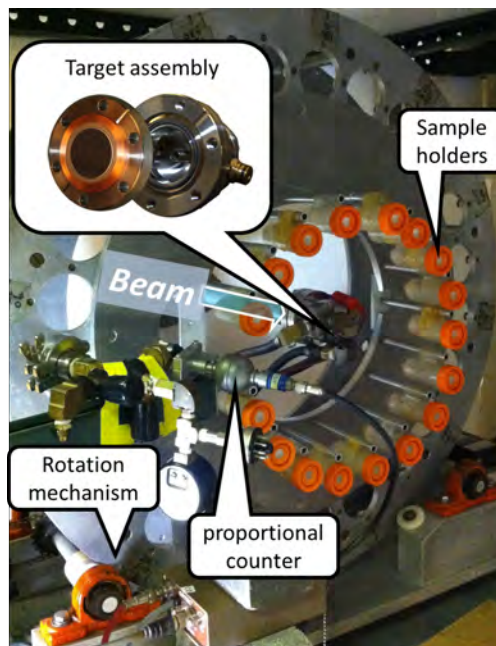


**Figure 2.** Target and sample fixture. Insert shows the Be-coated copper target and cooling system.

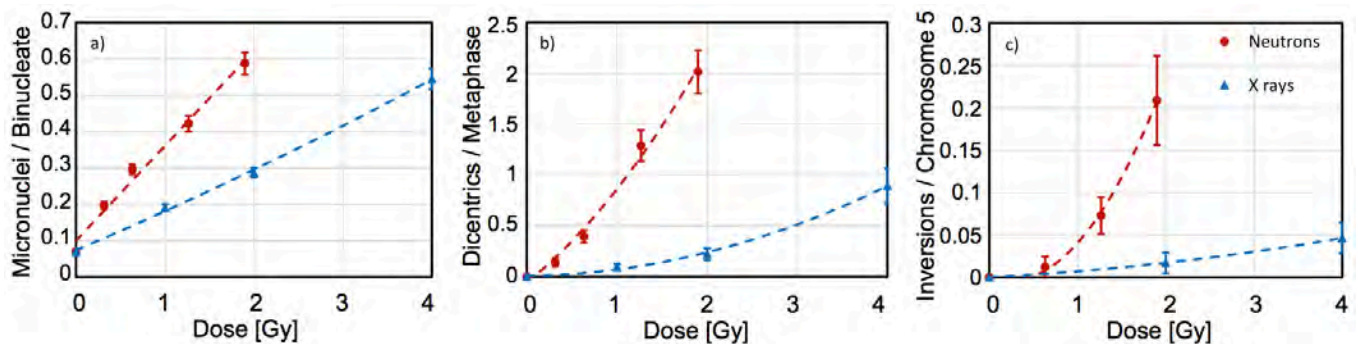


**Figure 3.** Yields of a) micronuclei, b) dicentric chromosomes and c) inversions in chromosome 5 in human peripheral blood lymphocytes exposed *in vivo* to neutrons or X-rays. The mixed field yields are plotted vs total dose (neutrons +  $\gamma$  rays). The solid lines indicate a linear-quadratic fit.

### Dosimetry

During calibration of the irradiator, the total dose for the IND-like neutron/gamma mixed-field, at the position of the irradiated samples, was measured using a custom A-150 muscle tissue-equivalent (TE) gas ionization chamber [5]. To extract the neutron dose,  $\gamma$ -ray dosimetry was performed separately with a compensated Geiger-Mueller dosimeter [6], which has a very low response to neutrons.

To verify the energy spectrum of the RARAF IND-spectrum neutron irradiation facility, spectroscopy measurements were performed at the sample position as described in [7]. Briefly, an EJ-301 liquid-filled scintillation detector and a gas proportional counter filled with 3 atmospheres of hydrogen were used for measuring neutron energies above and below 1.0 MeV respectively. The combination of the two detection systems covers a wide energy range, from 0.2 MeV to >9 MeV. The recoil pulse height spectra acquired by the detector systems were carefully evaluated using different quasi-monoenergetic neutron beams (0.2 to 9 MeV) available at the RARAF accelerator, discriminating the  $\gamma$ -ray signals from the raw acquisition data, using pulse rise time [7].

During biological irradiations, neutron flux is monitored using a TE gas ionization chamber mounted at a fixed location downstream of the neutron target at an angle of  $\sim 12^\circ$  relative to the ion beam direction. The incident charged particle beam current is also recorded with an electrometer coupled to the end of the beamline, which is a Faraday cup-like isolated beam pipe with the target at the end.

### Biomarker yields

Figure 3 shows the yields of three cytogenetic biomarkers, following neutron and X-ray irradiations

a) **Micronuclei:** The micronucleus assay quantifies radiation-induced chromosome damage expressed as post-mitotic micronuclei. Lymphocytes are cultured to division, but cytokinesis is blocked, preventing separation of the two daughter cells; healthy lymphocytes form binucleate cells, while those with chromosome damage can additionally contain one or more micronuclei

containing chromosomal fragments. The data shown here were obtained using the micro-culture assay [8] we developed for high throughput screening.

b) **Dicentric chromosomes:** The dicentric assay [9] is the gold standard of biodosimetry. Metaphase spreads are formed and chromosomes having two centromeres are scored. The yield of dicentric chromosomes correlates with the yield of inter-chromosome rearrangements.

c) **Chromosome inversions:** The mBAND [10] assay uses partial chromosome paints to “barcode” a chromosome (in this case chromosome 5). Intra-chromosomal rearrangements are identified as changes in the order of the bands, typically a group of bands that appears in reverse order within an otherwise normal sequence of bands.

In all cases, the neutron induced yields are much higher than the X-ray induced ones. The linear component of the dose response curve is also larger, indicating that much more of the damage is due to single traversals, whereas in X-rays, most of the persistent damage is due to multiple photon events. The relative biological effectiveness (RBE) values for the different assays are also very different, as can be expected due to the varying cross sections of the relevant targets (e.g. to get an inversion, double-strand breaks (DSBs) need to be formed in two positions in the same chromosome, whereas to get a dicentric, two DSBs must be formed on two different chromosomes, which is easier to achieve at the lower ionization density of X-rays). Consequently, by using a combination of the assays, the relative dose of neutrons and X-rays can be, in principle, unfolded from a mixed exposure.

### References

1. Homeland Security Council, National planning scenarios (final version 21.3). 2006.
2. Egbert, S.D., Kerr, G.D., and Cullings, H.M., DS02 fluence spectra for neutrons and gamma rays at Hiroshima and Nagasaki with fluence-to-kerma coefficients and transmission factors for sample measurements. *Radiat Environ Biophys*, 2007. 46(4): p. 311-25.

3. Xu, Y., et al., Novel neutron sources at the Radiological Research Accelerator Facility. *Journal of Instrumentation*, 2012. 7(03): p. C03031.
4. Xu, Y., et al., Accelerator-Based Biological Irradiation Facility Simulating Neutron Exposure from an Improvised Nuclear Device. *Radiation Research*, 2015. 184(4): p. 404-410.
5. Rossi, H.H., et al., The dependence of RBE on the energy of fast neutrons: 1. Physical design and measurement of absorbed dose. *Radiation Research*, 1960. 13(4): p. 503-520.
6. Wagner, E.B. and Hurst, G.S., A Geiger-Mueller  $\gamma$ -ray dosimeter with low neutron sensitivity. *Health Physics*, 1961. 5(1): p. 20-26.
7. Xu, Y., et al., Broad energy range neutron spectroscopy with a liquid scintillator and a proportional counter: application to a neutron spectrum similar to that from an improvised nuclear device. *Nuclear Instruments and Methods in Physics Research Section A: Accelerators, Spectrometers, Detectors and Associated Equipment*, 2015. 794: p. 234-239.
8. Lue, S., et al., Development of a high-throughput and miniaturized cytokinesis-block micronucleus assay for use as a biological dosimetry population triage tool. *Radiation Research*, 2015. 184(2): p. 134-142.
9. M'kacher, R., et al., New tool for biological dosimetry: Reevaluation and automation of the gold standard method following telomere and centromere staining. *Mutation Research/Fundamental and Molecular Mechanisms of Mutagenesis*, 2014. 770(0): p. 45-53.
10. Mitchell, C.R., et al., Stable intrachromosomal biomarkers of past exposure to densely ionizing radiation in several chromosomes of exposed individuals. *Radiation Research*, 2004. 162(3): p. 257-263.
11. Fenech, M., Cytokinesis-block micronucleus cytome assay. *Nature Protocols*, 2007. 2(5): p. 1084-1104.
12. Wuttke, K., Müller, W.-U., and Streffer, C., The sensitivity of the in vitro cytokinesis-blocked micronucleus assay in lymphocytes for different and combined radiation qualities. *Strahlentherapie und Onkologie*, 1998. 174(5): p. 262-268.
13. Huber, R., et al., Dose-response relationships of micronuclei in human lymphocytes induced by fission neutrons and by low LET radiations. *Mutation Research/Fundamental and Molecular Mechanisms of Mutagenesis*, 1994. 306(2): p. 135-141. ■

## Relative Biological Effectiveness of Neutrons and X-rays for Gene Induction

*Sally A. Amundson and Constantinos G. Broustas*

In the event of the detonation of an Improvised Nuclear Device (IND), the prompt radiation exposure would likely include a neutron component constituting several percent of the total dose. As neutrons generally have a high Relative Biological Effectiveness (RBE) for most physiological endpoints, it is important to understand the impact that neutrons would have on the biodosimetry methods that are being developed for medical triage purposes.

As part of our development of gene expression signatures for radiation biodosimetry, we have exposed peripheral blood from healthy donors to graded doses of neutrons using the IND-spectrum neutron irradiator developed at RARAF [1, 2]. This novel neutron source provides a spectrum of neutron energies comparable to that at 1.5 km from the epicenter of the Hiroshima detonation, dominated by neutrons with energies between 0.2 and 9 MeV, and with about 20% gamma-ray contribution [2].

The initial analysis of gene expression in response to IND-spectrum neutrons focused on a 1 Gy dose, compared with a 1 Gy dose of X-rays from a 250 kVp orthovoltage X-ray machine. RNA was harvested from peripheral blood samples from five independent donors 24 hours after ex vivo exposure, and hybridized to Agilent whole-genome microarrays. Class comparison analysis of the data using BRB-Array Tools [3] identified 327 genes differentially expressed ( $p < 0.110$ ; False Discovery Rate (FDR)  $< 3\%$ ) after 1 Gy neutron exposure, compared to 82 unique genes differentially expressed ( $p < 0.001$ ;  $FDR \leq 10\%$ ) after 1 Gy X-rays. Sixty-nine genes were found to be significantly differentially expressed following both exposures (Figure 1).

We used DAVID [4] to compare the biological processes and pathways significantly enriched among the genes responding to the two radiation qualities. Consistent with previous findings, the X-ray induced genes were dominated by functions related to DNA

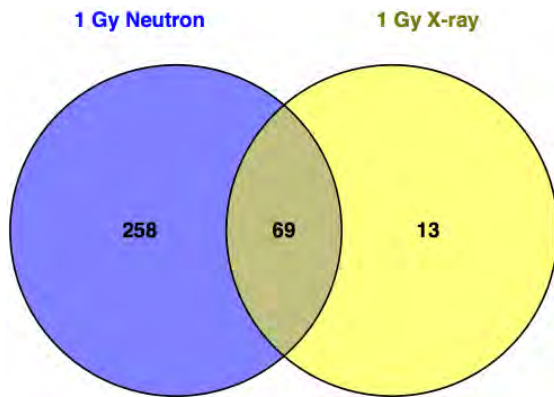


**Figure 1.** Numbers of genes differentially expressed by microarray at 24 hours after ex vivo exposure of human peripheral blood to 1 Gy of neutrons or X-rays.

damage response and activation of the p53 pathway, with the top functions being “p53 signaling pathway” (Benjamini-corrected p-value =  $2.1 \times 10^{-5}$ ), and “response to DNA damage stimulus” (Benjamini-corrected p-value = 0.0037). The neutron response showed similar functions, for example “p53 signaling pathway” (Benjamini-corrected p-value = 0.0038) and “apoptosis” (Benjamini-corrected p-value = 0.046), but in addition, many immune and inflammation related functions, such as “natural killer cell mediated immunity” (Benjamini-corrected p-value =  $8.2 \times 10^{-7}$ ) and “cytokine” (Benjamini-corrected p-value = 0.01), were also significant following the neutron exposure. The pattern observed is consistent with what would be expected following a higher dose of X-ray, consistent with the expectation that neutrons have a greater biological effect per unit dose than X-rays.

The majority (84%) of the genes significantly differentially expressed following X-ray exposure were also differentially expressed after neutron exposure. The genes in common to both exposures included many commonly included in biodosimetry signatures. Figure 2

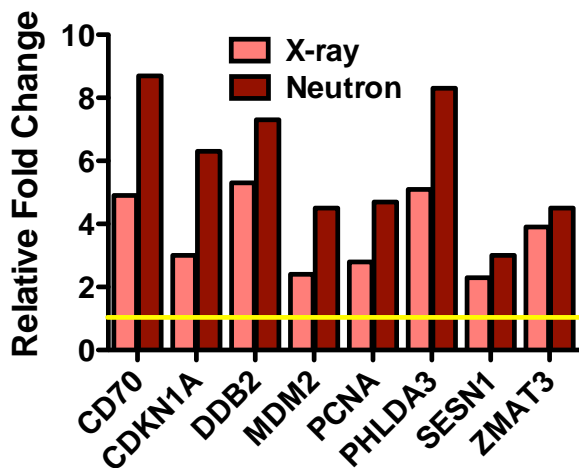


**Figure 2.** Fold-change of common biodosimetry genes in human peripheral blood 24 hours after ex vivo exposure to 1 Gy of neutrons (dark red bars) or X-rays (pink bars). Bars represent the mean response of 5 donors. The yellow line indicates the level of controls.

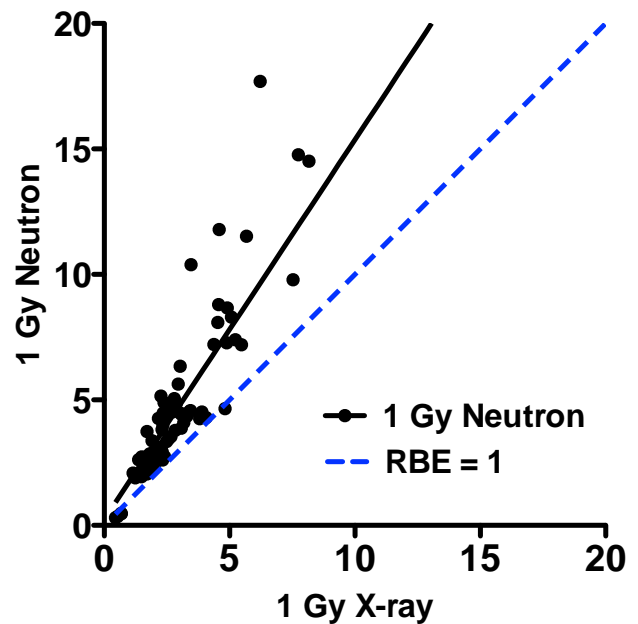


**Figure 3.** The fold change in response to neutrons plotted against the fold change for the same gene in response to X-rays. The same fold change in response to both qualities of radiation would be a RBE of 1, indicated by the dashed blue line. The majority of significantly differentially expressed genes fall above the blue line, indicating RBE > 1.

shows the relative fold change for some of these genes, illustrating that some (e.g. *SESN1* and *ZMAT3*) respond very similarly to the two qualities of radiation, and others (e.g. *CDKN1A* and *MDM2*) show a larger differential, with markedly greater response after neutron exposure.

Even from this small sampling, it appeared that there is not a single RBE for gene induction. In order to compare RBE across all the differentially expressed genes, we plotted relative fold change after 1 Gy neutron for all differentially expressed genes (including those significant only for one type of exposure) as a function of fold change after 1 Gy X-ray (Figure 3). While a small number of genes had very similar magnitudes of response to 1 Gy radiation, whether it was delivered as X-rays or IND-spectrum neutrons, the vast majority of responding genes showed a greater response to the neutron dose, and the average of all RBE values at 1 Gy was 1.9.

The complex patterns of response to different quality radiation may provide an opportunity to detect a neutron component in the radiation response of exposed individuals following an IND event. Potentially, genes with an RBE close to 1 could be used to provide reliable overall dose estimates. Additional information on the neutron component, which could have implications for the extent of radiological injury to be expected, could be derived from the response of genes that show a large RBE. In ongoing experiments, we plan to determine if RBE changes with dose, and if gene expression analysis can be used to detect a small percentage neutron component in a mixed exposure, such as might be expected after an IND.

References

1. Xu Y, Garty G, Marino SA, Massey TN, Randers-Pehrson G, Johnson GW and Brenner DJ (2012) Novel neutron sources at the Radiological Research Accelerator Facility. *J Instrum* **7**: C03031.
2. Xu Y, Randers-Pehrson G, Turner HC, Marino SA, Geard CR, Brenner DJ and Garty G (2015) Accelerator-Based Biological Irradiation Facility Simulating Neutron Exposure from an Improvised Nuclear Device. *Radiat Res* **184**: 404-410.
3. Simon R, Lam A, Li M-C, Ngan M, Meneses S and Zhao Y (2007) Analysis of gene expression data using BRB-Array Tools. *Cancer Informatics* **2**: 11-17.
4. Huang DW, Sherman BT and Lempicki RA (2009) Systematic and integrative analysis of large gene lists using DAVID bioinformatics resources. *Nat Protoc* **4**: 44-57. ■

# Chromosomal Inversions as a Biomarker for Neutron Exposures

Adayabalam S. Balajee<sup>a</sup>, Brian Ponnaiya, and David J. Brenner

A likely scenario for an Improvised Nuclear Device is a gun-type detonation using highly enriched uranium [1]; in this case, the prompt exposure will be  $\gamma$ -rays combined with a device-dependent dose of fast neutrons [2]. Fast neutrons are known to have very high biological effectiveness, so the motivation of this study is to investigate the potential to estimate separately the photon and the neutron doses after a mixed photon / neutron exposure. A series of mechanistic, *in-vitro* and epidemiological results, from our group and others [3-8] have suggested that chromosomal inversions represent a high-specificity biomarker for the presence of densely-ionizing radiations such as neutrons.

Track structure calculations predict a much higher induction of close-proximity double strand breaks (DSB) by high LET radiation relative to sparsely ionizing radiations [3, 9-11]. Biophysical modeling studies based on DSB proximity and track structure suggest that high LET radiations, such as neutrons, should result in increased frequencies of intra-chromosomal exchanges, particularly intra-arm exchanges, owing to closely spaced DSB. To examine the feasibility of using these exchanges as a biomarker for neutron exposures, frequencies of inversions were examined in blood samples exposed to either X-rays or neutrons.

**Interchromosomal exchanges**

The frequencies of interchromosomal exchanges (dicentrics and translocations) involving chromosomes 1 and 5 induced by different doses of X-rays and neutrons are shown in Fig. 1A. Comparison of interchromosomal exchanges between chromosomes 1 and 5 revealed a

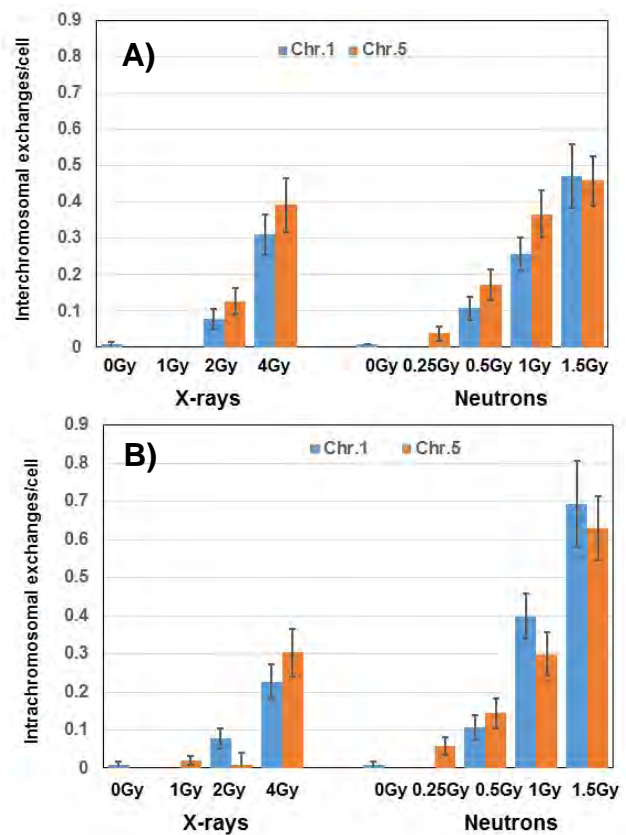
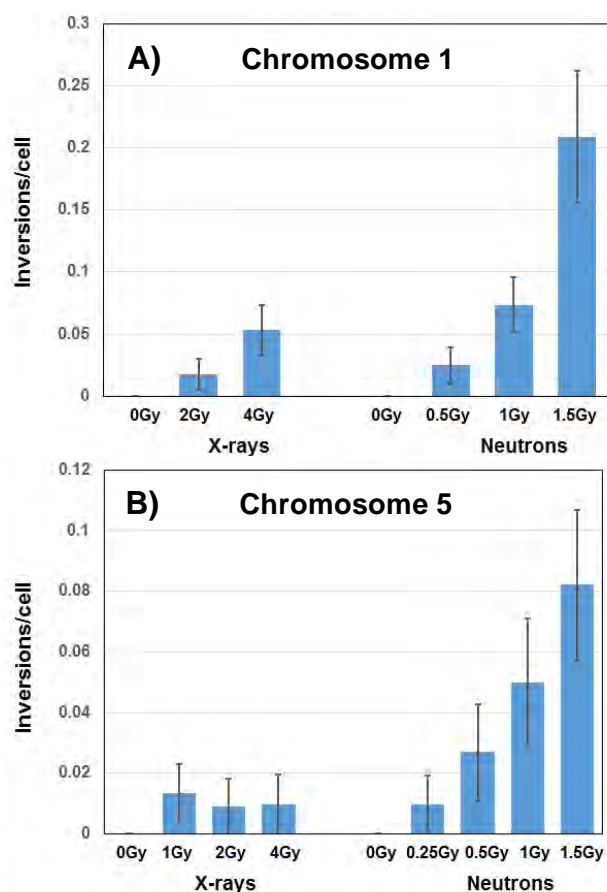


Fig. 1. Frequencies of A) interchromosomal and B) intrachromosomal exchanges detected in chromosomes 1 and 5 following exposure to different doses of X-rays and neutrons. Error bars indicate SEM.

slightly enhanced frequency of involvement in chromosome 5 relative to chromosome 1. The fold increase in interchromosomal exchange frequencies involving chromosome 5 over chromosome 1 was found

<sup>a</sup>Cytogenetic Biodosimetry Laboratory, Oak Ridge Institute for Science and Education, Oak Ridge, TN



**Fig. 2.** Frequencies of inter-arm and intra-arm exchanges in A) chromosome 1 and B) chromosome 5 of human lymphocytes irradiated with different doses of X-rays and neutrons. Error bars indicate SEM.

to be 1.53 and 1.25 for 2 Gy and 4 Gy of X-rays respectively and 1.7 and 1.44 for 0.5 Gy and 1 Gy of neutrons respectively. Both chromosomes displayed a dose dependent increase in the frequencies of interchromosomal exchanges. Among the aberrations, non-reciprocal translocations accounted for 83-92% of the total interchromosomal exchanges.

### Intrachromosomal exchanges

In contrast to interchromosomal exchanges, which were grossly similar in X-ray and neutron irradiated samples, intrachromosomal exchanges involving insertions, inversions, rings and fragments in chromosome 1 were much more common after neutron doses of 1 Gy and 1.5 Gy than after 4 Gy of X-rays (Fig. 1B). At the highest dose of X-rays, chromosome 5 showed a 1.3 fold increase in intrachromosomal exchange frequencies relative to chromosome 1. Likewise, intrachromosomal frequencies observed after 1 Gy (1.3 fold) and 1.5 Gy (1.1 fold) of neutron irradiation were slightly higher in chromosome 1 than chromosome 5, indicating that the chromosome length may modulate the intrachromosomal aberration frequencies induced by densely ionizing radiations.

Earlier studies have suggested that the frequencies of high LET radiation induced inter- and intra-arm exchange events (pericentric and paracentric inversions) were significantly higher than those induced by low LET radiation. In view of these observations, particular attention was paid in the present study to inversion events induced by X-rays and neutrons involving chromosomes 1 and 5. mBAND analysis revealed that among the intrachromosomal aberrations (insertions, inversions, rings and fragments), inversions involving chromosomes 1 and 5 were distinctly elevated in neutron irradiated samples relative to X-ray irradiated samples (Fig. 2). Induction of inversions in chromosome 1 by X-rays (0.017/cell for 2 Gy and 0.053/cell for 4 Gy) and neutrons (0.025/cell for 0.5 Gy, 0.073/cell for 1 Gy and 0.208/cell for 1.5 Gy) was much higher than in chromosome 5 (0.013/cell for 1 Gy, 0.01/cell for both 2 and 4 Gy of X-rays; 0.01/cell for 0.25 Gy, 0.027/cell for 0.5 Gy, 0.05/cell for 1 Gy and 0.08/cell for 1.5 Gy of neutrons). In general, neutron irradiated samples showed a 3- to 8.7-fold increase in the yield of inversions compared to X-ray irradiated samples. While identical frequencies of inversions were observed for both chromosomes for 0.5Gy of neutrons, increased inversion frequencies were observed for chromosome 1 relative to chromosome 5 at neutron doses higher than 0.5 Gy (1.4 fold and 2.5 fold more for 1 Gy and 1.5 Gy neutron doses, respectively). These results were not found to be statistically significant. Observation of higher frequencies of both intra-arm and inter-arm exchanges in chromosome 1 relative to chromosome 5 for both X-rays and neutrons seems to suggest that chromosome length may be a critical determinant for chromosome inversion events induced by both low and high LET radiations.

In conclusion, the present study has confirmed earlier observations that intrachromosomal exchanges are induced at higher frequencies by neutrons as compared to X-rays, and that these exchanges may provide a suitable biomarker for neutron exposures.

### References

1. Homeland\_Security\_Council. National Planning Scenarios (Final Version 21.3). Washington DC2006.
2. Egbert SD, Kerr GD, Cullings HM. DS02 fluence spectra for neutrons and gamma rays at Hiroshima and Nagasaki with fluence-to-kerma coefficients and transmission factors for sample measurements. *Radiat Environ Biophys.* 2007;46(4):311-25..
3. Brenner DJ, Sachs RK. Chromosomal "fingerprints" of prior exposure to densely ionizing radiation. *Radiat Res.* 1994;140(1):134-42.
4. Hande MP, Azizova TV, Geard CR, Burak LE, Mitchell CR, Khokhryakov VF, Vasilenko EK, Brenner DJ. Past exposure to densely ionizing radiation leaves a unique permanent signature in the genome. *Am J Hum Genet.* 2003;72(5):1162-70.

5. Mitchell CR, Azizova TV, Hande MP, Burak LE, Tsakok JM, Khokhryakov VF, Geard CR, Brenner DJ. Stable intrachromosomal biomarkers of past exposure to densely ionizing radiation in several chromosomes of exposed individuals. *Rad Res.* 2004;162(3):257-63.
6. Hada M, Zhang Y, Feiveson A, Cucinotta FA, Wu H. Association of inter- and intrachromosomal exchanges with the distribution of low- and high-LET radiation-induced breaks in chromosomes. *Radiat Res.* 2011;176(1):25-37. Epub 2011/04/07.
7. Bauchinger M, Schmid E. LET dependence of yield ratios of radiation-induced intra- and interchromosomal aberrations in human lymphocytes. *Int J Radiat Biol.* 1998;74(1):17-25.
8. Schmid TE, Oestreicher U, Molls M, Schmid E. Alpha particles induce different F values in monocellular layers of settled and attached human lymphocytes. *Radiat Res.* 2011;176(2):226-33. Epub 2011/06/03. doi: 10.1667/RR2574.1 [pii].
9. Burkart W, Jung T, Frasch G. Damage pattern as a function of radiation quality and other factors. *Comptes rendus de l'Academie des sciences Serie III, Sciences de la vie.* 1999;322(2-3):89-101. Epub 1999/04/10.
10. Sachs RK, Brenner DJ, Chen AM, Hahnfeldt P, Hlatky LR. Intra-arm and interarm chromosome intrachanges: tools for probing the geometry and dynamics of chromatin. *Radiation research.* 1997;148(4):330-40. Epub 1997/10/27.
11. Sachs RK, Chen AM, Brenner DJ. Review: proximity effects in the production of chromosome aberrations by ionizing radiation. *International journal of radiation biology.* 1997;71(1):1-19. Epub 1997/01/01.
12. Hande MP, Azizova TV, Burak LE, Khokhryakov VF, Geard CR, Brenner DJ. Complex chromosome aberrations persist in individuals many years after occupational exposure to densely ionizing radiation: an mFISH study. *Genes, chromosomes & cancer.* 2005;44(1):1-9. Epub 2005/05/25.
13. Hande MP, Azizova TV, Geard CR, Burak LE, Mitchell CR, Khokhryakov VF, Vasilenko EK, Brenner DJ. Past exposure to densely ionizing radiation leaves a unique permanent signature in the genome. *American journal of human genetics.* 2003;72(5):1162-70. Epub 2003/04/08.
14. Mitchell CR, Azizova TV, Hande MP, Burak LE, Tsakok JM, Khokhryakov VF, Geard CR, Brenner DJ. Stable intrachromosomal biomarkers of past exposure to densely ionizing radiation in several chromosomes of exposed individuals. *Radiation research.* 2004;162(3):257-63. Epub 2004/09/24. ■



**Top** (l to r): David Cuniberti, Haseeb Durrani, Stan Leu, Hongning Zhou, Youping Sun, (Igor Shuryak), Guy Garty, Nils Rudqvist, Mikhail Repin, Cui-Xia Kuan; Sally Amundson, Helen Turner. **Bottom** (l to r): David Bremner, Gerhard Randers-Pehrson, Steve Marino, Charles Geard, Tom Hei; Manuela Buonanno.

# Response of Cell Cycle Genes in Mouse Blood after Exposure to Neutron or X-ray Irradiation

Constantinos G. Broustas and Sally A. Amundson

## Introduction

Accurate prediction of radiation dose during the first week after a large-scale radiation emergency is a central goal of radiation biodosimetry, but most development efforts have focused on external gamma- or X-ray exposures. The detonation of an improvised nuclear device (IND) would likely produce a significant neutron component along with the prompt gamma radiation, however. Compared to gamma rays, neutrons and other high linear energy transfer radiations cause more complex and difficult to repair damage to cellular components, such as DNA, and may produce more severe health consequences for a given dose. Identifying the contribution of neutrons to an estimated dose could thus provide valuable information for those making treatment decisions.

Our group has been developing gene expression approaches for radiation biodosimetry [1-3]. The gene expression response to ionizing radiation is known to vary dynamically as a function of time after exposure [4-6], and different radiation qualities may trigger different signaling pathways with different effects on modification of gene expression. Thus, it may be possible to develop gene expression signatures capable of discriminating between neutron and gamma-ray exposures.

Cell cycle progression is a major biological function that is affected by radiation. Regulation of cell cycle delay impacts radiosensitivity and cell fate in response to DNA

**Table 1.** Significantly differentially expressed genes in mouse blood after X-ray or neutron treatment relative to untreated controls.

Dose	Time (days)	Differentially Expressed Genes (#)	Over Expressed (%)	Under Expressed (%)
1 Gy X-ray	1	744	49	51
4 Gy X-ray	1	3427	39	61
0.25 Gy Neutron	1	1	0	100
1 Gy Neutron	1	1879	46	54
1 Gy X-ray	7	549	30	70
4 Gy X-ray	7	1528	69	31
0.25 Gy Neutron	7	663	3	97
1 Gy Neutron	7	5699	10	90

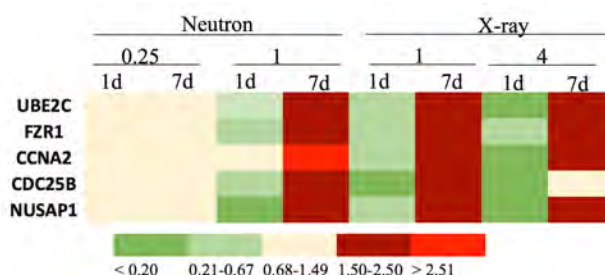


**Figure 1.** Heatmap illustrating relative expression of cell cycle genes that are temporally regulated in response to neutron and X-ray irradiation. The mean (n=6) fold change in gene expression is color coded according to the scale bar at the bottom of the figure. Measurements were made by microarray analysis.

damage. In the current study, we investigated the effects of X-ray and neutron irradiation on the expression of cell cycle-regulated genes in mouse blood.

## Results

Mice were either sham-irradiated or exposed to 0.25 or 1 Gy of neutrons using the RARAF IND-spectrum neutron source [7], or to 1 or 4 Gy of X-rays. Mice were sacrificed at 1 or 7 days after irradiation and global gene expression was measured in their blood using Agilent Mouse Whole Genome Microarrays. Significantly differentially expressed genes ( $p < 0.001$ , false discovery rate (FDR)  $< 5\%$ ) at each exposure dose and sacrifice time (Table 1) were identified using BRB-Array Tools [8]. Concentrating on the response to the higher dose exposures (4 Gy X-ray and 1 Gy neutron), the differentially expressed genes were functionally classified into gene ontology categories using the Database for Annotation, Visualization, and Integrated Discovery (DAVID) [9, 10]. Finally, microarray results were confirmed by measuring expression of selected differentially expressed genes by quantitative real-time PCR (qRT-PCR).

DAVID analysis revealed a number of biological processes that were over-represented among up- or down-regulated genes in the blood of irradiated mice compared with controls. Some processes were significant at only one time point, while others were common to both 1 and 7 days post-irradiation. All processes common to both times consistently involved either under- or over-expressed genes, with the exception of biological processes related to cell cycle regulation, which displayed a more complex temporal pattern. Following exposure to either 1 Gy neutron or 4 Gy X-ray, cell cycle processes were significantly over-represented among down-regulated

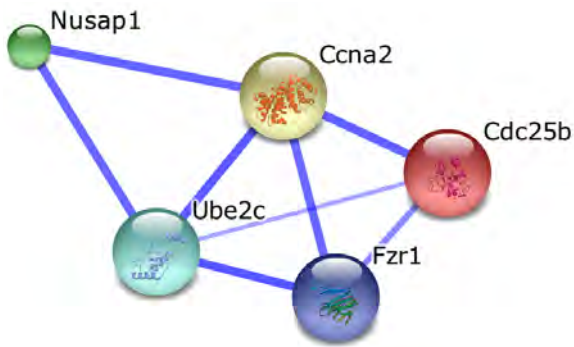


**Figure 2.** STRING network analysis [16] illustrates the functional relationship between cell-cycle proteins coded for by genes regulated by  $\gamma$ -rays or neutrons. Line thickness reflects the confidence score of the relationships.

genes on day 1 post-irradiation, and among up-regulated genes on day 7 post-irradiation.

Mice exposed to neutron radiation (1 Gy, 1d) showed 86 differentially under-expressed cell cycle genes, whereas, on day 7, 22 cell cycle genes were up-regulated. When mice were exposed to X-ray irradiation, 53 cell cycle genes were under-expressed on day 1, after 4 Gy radiation, whereas, on day 7, 51 cell cycle genes were over-expressed. Comparing the gene lists from neutron and X-ray exposure on day 1, 33 genes were common to both radiation types, which corresponded to 38% and 62% of the total number of downregulated genes after neutron or X-ray radiation, respectively. On the other hand, on day 7, neutron (1 Gy) and X-ray (4 Gy) shared 8 overexpressed genes, which corresponded to 36% and 16% of the total number of over-expressed cell cycle genes, respectively.

Next, we looked to see if any individual cell cycle-related genes were underexpressed on day 1 and overexpressed on day 7, and identified a small number of genes (*Ube2c*, *Fzr1*, *Ccna2*, *cdc25B*, and *Nusap1*), which showed this expression pattern (Fig. 1). These genes also showed the same expression pattern after 1 Gy of X-ray exposure. We confirmed that, as expected, there was very little variation in the expression of these genes between days 1 and 7 in the blood from the unexposed control mice.

The proteins encoded by all the genes identified as having this expression pattern are known to play important roles in the regulation of mitosis. Specifically, the UBE2C and FZR1 (also known as CDH1) proteins are components of the anaphase promoting complex/cyclosome (APC/C), an important determinant of cell cycle progression and genome integrity [11, 12], whereas CCNA2 (cyclin A2) is a substrate of the APC/C [13]. CDC25B [14] and NUSAP1 (nucleolar and spindle associated protein 1) [15] participate in centrosomal microtubule nucleation and spindle pole formation, respectively. Network analysis was conducted using STRING (Search Tool for the Retrieval of Interacting

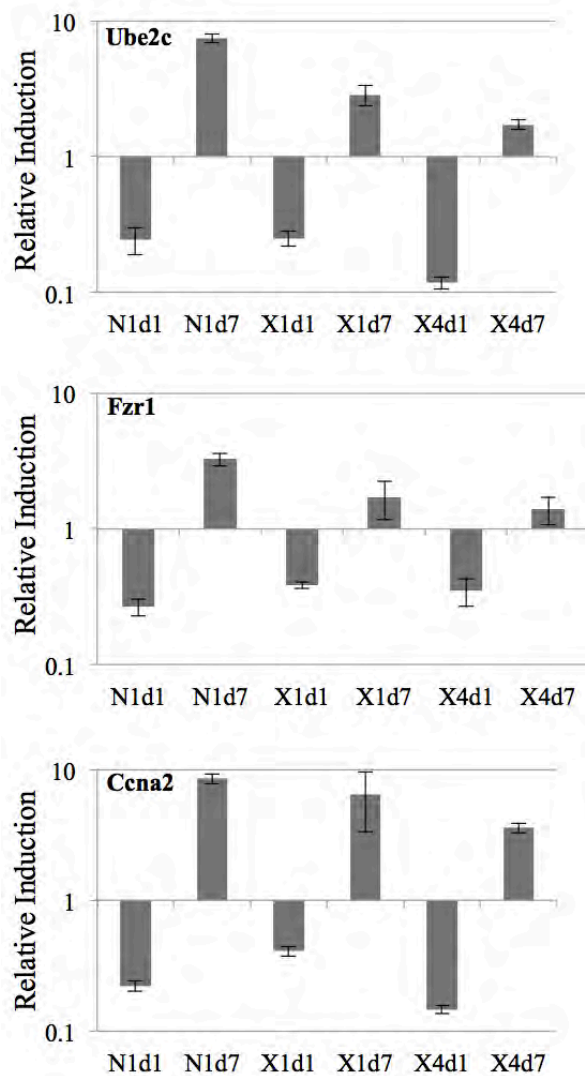


**Figure 3.** Gene expression measured by qRT-PCR. Expression of three genes (*Ube2c*, *Fzr1*, and *Ccna2*) that were shown by microarray analysis to be temporally regulated is depicted. Data represent the mean  $\pm$  S.E.M. ( $n=6$ ). N1d1: 1 Gy neutron, day 1; N1d7: 1 Gy neutron, day 7; X1d1: 1 Gy X-rays, day 1; X1d7: 1 Gy X-rays, day 7; X4d1: 4 Gy X-rays, day 1; X4d7: 4 Gy X-rays, day 7.

Genes/Proteins) [16] to model the functional interconnection of the identified genes (Fig. 2).

We confirmed the expression pattern of three of these genes (*Ube2c*, *Fzr1*, and *Ccna2*) by qRT-PCR. As shown in Fig. 3, the magnitude of expression change of these genes was in good agreement with the findings of the global gene expression analysis.

In summary, our results show that many genes involved in cell cycle regulation respond to both neutron and X-ray irradiation. However, a few cell cycle genes show a reversal of expression between one and seven days after exposure that is common across the two radiation qualities. The genes sharing this complex response pattern are functionally interconnected and play important roles in mitosis.

**References**

1. Amundson SA and Fornace AJJ (2001) Gene expression profiles for monitoring radiation exposure. *Radiat Prot Dosimetry* **97**: 11-16.
2. Paul S and Amundson SA (2008) Development of gene expression signatures for practical radiation biodosimetry. *Int J Radiat Oncol Biol Phys* **71**: 1236-1244.
3. Paul S, Barker CA, Turner HC, McLane A, Wolden SL and Amundson SA (2011) Prediction of in vivo radiation dose status in radiotherapy patients using ex vivo and in vivo gene expression signatures. *Radiat Res* **175**: 257-265.
4. Ghandhi SA, Sinha A, Markatou M and Amundson SA (2011) Time-series clustering of gene expression in irradiated and bystander fibroblasts: an application of FBPA clustering. *BMC Genomics* **12**: 2.
5. Kim KH, Yoo HY, Joo KM, Jung Y, Jin J, Kim Y, Yoon SJ, Choi SH, Seol HJ, Park WY and Nam DH (2011) Time-course analysis of DNA damage response-related genes after in vitro radiation in H460 and H1229 lung cancer cell lines. *Exp Mol Med* **43**: 419-426.
6. Paul S, Ghandhi SA, Weber W, Doyle-Eisele M, Melo D, Guilmette R and Amundson SA (2014) Gene expression response of mice after a single dose of <sup>137</sup>CS as an internal emitter. *Radiat Res* **182**: 380-389.
7. Xu Y, Randers-Pehrson G, Turner HC, Marino SA, Geard CR, Brenner DJ and Garty G (2015) Accelerator-Based Biological Irradiation Facility Simulating Neutron Exposure from an Improvised Nuclear Device. *Radiat Res* **184**: 404-410.
8. Simon R, Lam A, Li M-C, Ngan M, Menenzes S and Zhao Y (2007) Analysis of gene expression data using BRB-Array Tools. *Cancer Informatics* **2**: 11-17.
9. Huang DW, Sherman BT and Lempicki RA (2009) Bioinformatics enrichment tools: paths toward the comprehensive functional analysis of large gene lists. *Nucleic Acids Res* **37**: 1-13..
10. Huang DW, Sherman BT and Lempicki RA (2009) Systematic and integrative analysis of large gene lists using DAVID bioinformatics resources. *Nat Protoc* **4**: 44-57.
11. Yu H, King RW, Peters JM and Kirschner MW (1996) Identification of a novel ubiquitin-conjugating enzyme involved in mitotic cyclin degradation. *Curr Biol* **6**: 455-466.
12. Engelbert D, Schnerch D, Baumgarten A and Wäsch R (2008) The ubiquitin ligase APC(Cdh1) is required to maintain genome integrity in primary human cells. *Oncogene* **27**: 907-917.
13. Wolthuis R, Clay-Farrace L, van Zon W, Yekezare M, Koop L, Ogink J, Medema R and Pines J (2008) Cdc20 and Cks direct the spindle checkpoint-independent destruction of cyclin A. *Mol Cell* **30**: 290-302.
14. Chou HY, Wang TH, Lee SC, Hsu PH, Tsai MD, Chang CL and Jeng YM (2011) Phosphorylation of NuSAP by Cdk1 regulates its interaction with microtubules in mitosis. *Cell Cycle* **10**: 4083-4089.
15. Gabrielli BG, De Souza CP, Tonks ID, Clark JM, Hayward NK and Ellem KA (1996) Cytoplasmic accumulation of cdc25B phosphatase in mitosis triggers centrosomal microtubule nucleation in HeLa cells. *J Cell Sci* **109**: 1081-1093.
16. Szklarczyk D, Franceschini A, Wyder S, Forslund K, Heller D, Huerta-Cepas J, Simonovic M, Roth A, Santos A, Tsafou KP, Kuhn M, Bork P, Jensen LJ and von Mering C (2015) STRING v10: protein-protein interaction networks, integrated over the tree of life. *Nucleic Acids Res* **43**: D447-52. ■



Gerhard Randers-Pehrson, David Brenner



Sally Amundson, Guy Garty



Charles Geard, Steve Marino

# Development of a Variable Dose-rate External $^{137}\text{Cs}$ Irradiator (VADER)

Yanping Xu, Gerhard Randers-Pehrson, Guy Garty, and David J. Brenner

## Overview

In many radiation exposure scenarios, including human exposures to fallout resulting from the detonation of improvised nuclear devices (IND), ingestion of Cesium-137, a radioisotope with nominal atomic weight 137 and a half-life of about 30.5 years, is often a major source of radiation dose [1-3]. Internally deposited radionuclides also have a biological half-life, determined by both the physical half-life and the rate at which they are cleared from the body, resulting in complex exposures at dose rates that change over time. Experiments simulating such internal exposures are very expensive and cumbersome, and produce radioactive excreta and biofluids, which require dedicated “hot” equipment for analysis and are expensive to dispose of.

We are working on a new project to make an alternate approach using continuously retracting low-activity  $^{137}\text{Cs}$  sources that can mimic any time-dose profile from an internal  $^{137}\text{Cs}$  exposure. Because of the high-energy of the  $^{137}\text{Cs}$  gamma-rays, the physical dose distribution will be the same for the internal vs. external exposures. Thus, the VADER is designed to simulate the time-dependent internal-emitter  $^{137}\text{Cs}$  exposures, increasing the practicality and cost-effectiveness of research aimed at understanding internal-emitter  $^{137}\text{Cs}$  radiobiology. Used in its static mode, the VADER can also provide extremely low constant dose rates.

The planned irradiator is based on recycling old  $^{137}\text{Cs}$  brachytherapy seeds. These seeds were much used starting in the 1980s to treat cervical cancer using low dose rates [4], but many of these  $^{137}\text{Cs}$  seeds are no longer in use and are in long-term storage, making them readily available. At Columbia University we have 30 such sources, each in the ~20 mCi range.

## Design

A preliminary design is shown in Figure 1. A cage has been specially designed to house up to 18 mice for exposure in the VADER. It has optional dividers and dimensions of 50 cm x 50 cm x 12 cm, and is placed between two source assemblies each containing ten 20 mCi  $^{137}\text{Cs}$  seeds positioned in a circular pattern, one above and one below the mouse cage. This configuration can provide a dose rate of between 0.05 and 1.5 Gy/day depending on the vertical position of the sources.

During irradiation, the source assemblies (Fig. 1) are slowly retracted under computer control away from the mouse cage. As the sources are retracted over time-scales of days to weeks, the mice are exposed to a decreasing

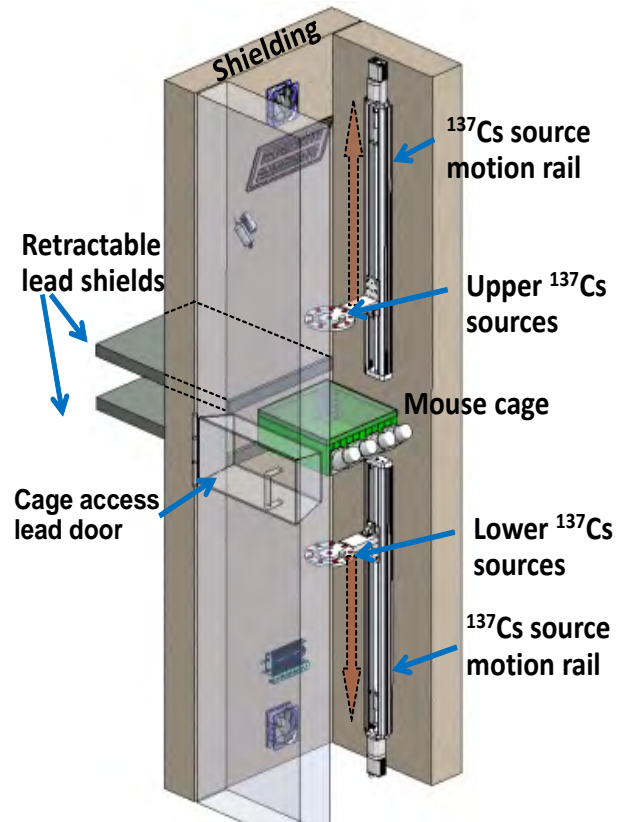


Figure 1. Open-view schematic of the VADER irradiator design.

dose rate that can mimic the dose-rate / time pattern shown in Figure 2, or any other desired dose-rate / time pattern, such as the much slower  $^{137}\text{Cs}$  retention kinetics in man [5], or at a constant low dose rate.

For these long-term irradiations, the mice are free to move around, eat and drink *ad libitum*. Within the irradiator, temperature, humidity, airflow and lighting are fully controlled to the required animal care standards. Mouse handling is possible at any time by inserting retractable lead shields (Fig. 1), opening the interlocked lead cage access door, and extracting the cage. The cage will be cleaned and resupplied with food and water as appropriate.

## Irradiation Experiment

In an example experiment using the VADER system, mice are transported to RARAF, where the VADER system is located. There, the mice are housed in a satellite animal facility for three days to allow acclimation and recovery from any stress due to transportation. On day 3 after arrival, up to 18 mice are placed in the specially

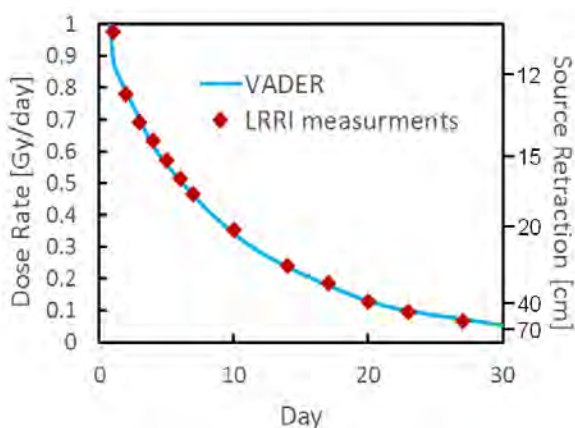


**Figure 2.** Dose rates measured at the Lovelace Respiratory Research Institute (LRRR) in  $^{137}\text{Cs}$ -injected mice (red symbols) vs. a dose-rate profile for implementation in the VADER (blue line).

designed mouse cage containing water and food supplies in dispensers. The cage is placed between two  $^{137}\text{Cs}$  source assemblies in a shielded housing with shielding walls. Temperature of 21 °C, humidity between 40 and 60%, and 10 volumes air exchange per hour are maintained by a portable air conditioning system. The mice are kept on a 12-hour light cycle and are under constant observation using a webcam. Every 48 hours, the mouse cage is removed from the irradiator for closer observation of the mice, and for bedding, food and water change.

### Irradiation Dosimetry

The irradiator and shielding were designed based on a Monte-Carlo transport simulation of the entire system, which allowed us to generate a design with a predicted spatially uniform dose distribution across the mouse cage at source-cage separations of 10 cm and greater. Spatial dose homogeneity at the location of the mouse cage will be verified using Gafchromic film, with absolute dosimetry based on our NIST-traceable ion chamber. Our calculations have also shown that possible dose variations

due to mutual shielding (e.g. by the mice huddling together) are small. Nevertheless we can also verify individual dosimetry on a mouse-by-mouse basis by subcutaneously injecting into each an encapsulated high-sensitivity “pin-worm”  $\text{LiF:Mg,Cu,P}$  miniature TLD rod (diameter 0.6 mm, length 6 mm). These TLDs (Rexon, Beechwood, OH) are designed for insertion into needles / catheters for *in vivo* application, and provide a linear dose response up to 10 Gy with better than 2% reproducibility [6]. Following sacrifice, the TLD will be removed and read, giving the cumulative skin dose received by that mouse.

### References

1. Simon SL, Bouville A, Beck HL. The geographic distribution of radionuclide deposition across the continental US from atmospheric nuclear testing. *J Environ Radioact.* 2004;74:91-105.
2. Homeland Security Council. National Planning Scenarios (Final Version 21.3) Washington DC, 2006. Available from: <https://www.llis.dhs.gov/content/national-planning-scenarios-final-version-213-0>.
3. Yasunari TJ, Stohl A, Hayano RS, Burkhardt JF, Eckhardt S, Yasunari T. Cesium-137 deposition and contamination of Japanese soils due to the Fukushima nuclear accident. *Proceedings of the National Academy of Sciences.* 2011;108:19530-4 PMID: PMC3241755.
4. Bateman TJ, Davy TJ, Skeggs DB. Five years hospital experience with the Amersham caesium 137 manual afterloading system. *Br J Radiol.* 1983;56:401-7.
5. Leggett RW. Biokinetic models for radiocaesium and its progeny. *J Radiol Prot.* 2013;33:123-40.
6. Kliuga P, Rossi HH, Johnson G. A multi-element proportional counter for radiation protection measurements. *Health Phys.* 1989;57:631-6. ■



(l to r): David Welch, Brian Ponnaiya, Guy Garty, Andrew Harkin.

# Progress in Validation of an Anatomically Accurate Mouse Phantom using Radiographic Film Dosimetry and MCNP Simulations

*David Welch, Gerhard Randers-Pehrson, and David J. Brenner*

Radiation biology experiments often utilize mice as test animals because the well-known genetic similarities within a strain provide an excellent model system for analysis. Accurate radiation dosimetry is crucial to correctly interpret the results of such experiments. However, determining the precise dose delivered to each region within test animals is difficult to accomplish, due to their intricate anatomy and the associated complex physics phenomena. Density inhomogeneity within a mouse, associated with lung and bone regions for example, complicates organ dose and dosimetry assessment [1, 2]. We recently reported on the construction of the first anatomically accurate mouse phantoms composed of regions of tissue-, bone-, and lung-equivalent materials for use in radiation dosimetry studies [3]. We continue to work with these unique phantoms to validate their utility in the assessment of dosimetry throughout the complex geometry of a mouse under various irradiation conditions.

## Updated Mouse Phantom

Our initial set of mouse phantoms were constructed based on a standard geometry atlas known as the Digimouse [4]. The Digimouse model was a useful guide for constructing our initial phantoms because it has widespread use by other research groups. The Digimouse model also came as a neatly segmented computer model, which was easily adapted for fabrication as a physical model. However, the Digimouse model is based on a mouse that was no longer living, and was thus subsequently posed in an unnatural position to achieve consistent positioning throughout the various imaging modalities employed for model creation.

For our updated mouse phantoms we chose to model them after a mouse in a natural living position. We obtained a full body CT scan of an adult wild type mouse



**Figure 1.** We imaged a mouse using micro CT and produced a three-dimensional reconstruction using 3D Doctor. The reconstruction was produced by segmenting the CT into regions of bone (white), lung (yellow) and tissue (red). This model was subsequently sliced along a desired plane and fabricated using our published methods.

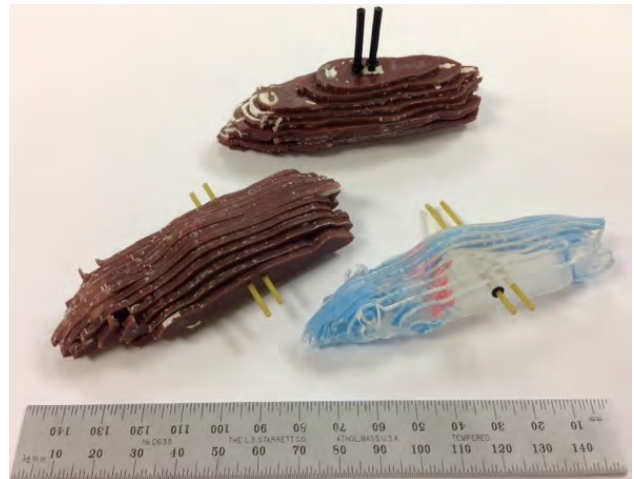


**Figure 2.** The two new mouse phantoms are shown at the top (coronal slices) and the left (sagittal slices). Also pictured is a version of the sagittal mouse phantom made using transparent acrylic in place of tissue equivalent material, blue wax in place of bone equivalent material, and pink wax in place of lung equivalent material, which shows the complex interior features within these phantoms.

using the Quantum FX micro CT Imaging System. The high resolution CT scan was then imported into 3D Doctor, a 3D image processing and measurement tool for imaging applications. With 3D Doctor we were able to segment the entire CT scan into regions of bone, lung, and tissue; a 3D view of the entire segmented mouse is shown in Figure 1. The segmented data could then be exported to MATLAB and processed to create mouse phantoms using the same methods we described for our previous models. Figure 2 shows the two new phantoms based on this new more natural mouse position, one with slices in the coronal plane, the other with slices in the sagittal plan. We obtained CT scans of these newly produced mouse phantoms that all indicate excellent agreement between the structures in the original mouse scan and our mouse phantoms. Figure 3 shows each of the mouse phantoms deconstructed so that the high detail in the interior lung and bone geometry can be more easily seen.

## SARRP Testing of the Mouse Phantoms

The Small Animal Radiation Research Platform (SARRP, Xstrahl) combines CT imaging with precision radiation delivery to enable targeting of anatomical features with x-ray beams. The SARRP located at the Columbia University Center for Radiological Research is commonly used for mouse studies, and thus it is a good system to validate our mouse phantoms.



**Figure 3.** The mouse phantoms are shown in a deconstructed state to better illustrate the interior bone and lung features.

In order to measure dose delivered to different points in our phantoms, we can place pieces of radiographic film between slices in a phantom. The film we use, Gafchromic EBT3, is approximately 280  $\mu\text{m}$  thick and can be cut to different sizes as needed. The film exhibits a color change proportional to the dose delivered and can be analyzed by scanning the film into a computer. A set of calibration films is necessary to generate a fitting function so that any dose can be determined from the color change

produced in the exposed film. A picture of a mouse phantom in the SARRP is shown in Figure 4. The figure also includes a piece of film positioned in the middle of the coronal sliced phantom.

### MCNP

Monte Carlo for Neutral Particles (MCNP) software is a powerful tool used to model radiation transport. The code, developed by Los Alamos National Laboratory, allows a user to define all aspects of a transport problem including materials, geometry, particle properties, and a huge range of other factors. Our goal in using MCNP is to replicate the exact irradiation performed on a mouse phantom using the SARRP. We plan to compare the results for dose distribution obtained using Gafchromic film with the MCNP results to validate our mouse phantoms as reliable tools to assess complicated irradiation experiments.

The first step to matching our MCNP simulations with the experimental configuration was to start with a simple geometry. Therefore, we chose to model the setup used for film calibrations. Film calibrations are performed by placing a piece of EBT3 Gafchromic film in between two pieces of 5 mm thick tissue equivalent plastic. The film is irradiated perpendicular to the film and plastic sandwich. This simple geometry is easy to replicate in MCNP. A scaled image of the normalized dose distribution produced from an MCNP simulation is shown in Figure 5. Figure 5 also shows a scanned image of an exposed film. Comparing the dose distribution between the measured values in the film and the simulated values produced with MCNP is best accomplished by plotting the dose along a line traversing the exposed region. A graph showing the dose profiles obtained in this way from each data set is shown in Figure 5 to compare results from the two methods.

The graph in Figure 5 demonstrates that our simulation is producing results that are close to the

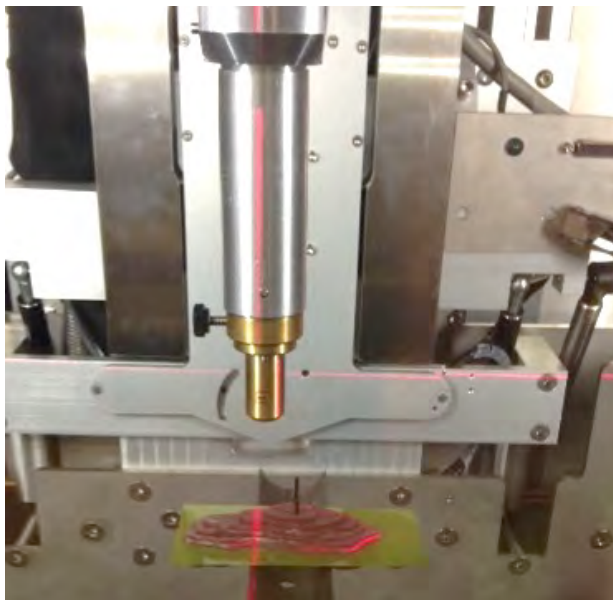


**Figure 4.** A coronal slice mouse phantom in the SARRP. A cone beam computed tomography image is first generated and a computer program allows the user to select a point in the 3D image to target. The moveable couch, which supports the mouse phantom, and the x-ray source are mechanically positioned to accurately direct the beam. The collimator, extending from the top and ending at the brass piece in the center of the photo, directs an x-ray beam to the targeted region of the phantom. The SARRP is equipped with collimators to expose an area of 10x10 mm, 5x5 mm, 3x3 mm, 2x9 mm, 1 mm diameter circle, or 0.5 mm diameter circle at a point 350 mm away from the source.

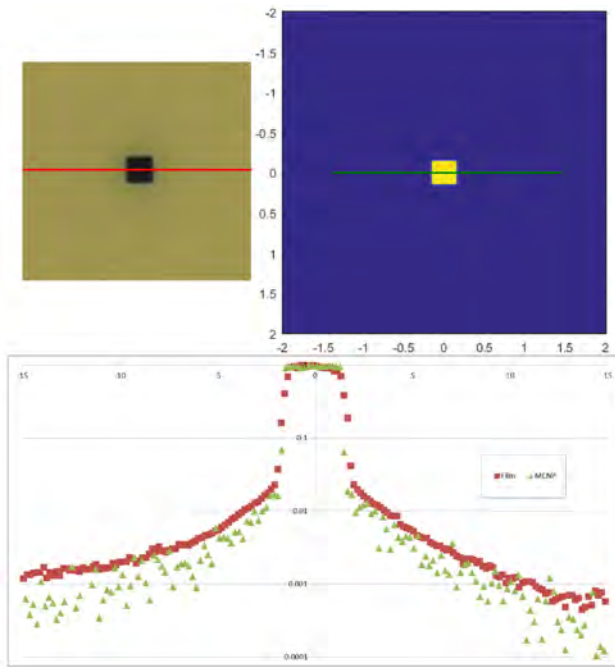


**Figure 5.** A piece of radiographic film that has been exposed to a radiation dose with the 3x3 mm collimator on the SARRP is shown on the upper left. On the upper right is a simulated dose map produced using MCNP. A profile of the values along the red (film) and green (MCNP) lines is shown in the graph below with the dose values normalized and plotted in the corresponding color on a logarithmic scale. We are currently working to improve the MCNP model to achieve better agreement between these plots.

experimentally measured values of the film. However, we aim to improve our model to get an even better fit before proceeding. The current iteration of the model doesn't include much of the collimator geometry present on the machine. We believe that inclusion of these collimator features will increase scattering in the MCNP model and,

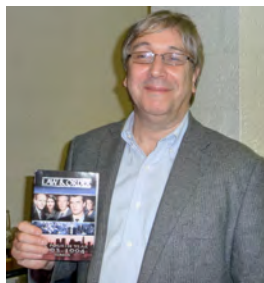
therefore, bring up the dose in the regions outside of the targeted region to achieve better agreement with the measured values.

**Future Work**

We are currently working to demonstrate good agreement between MCNP simulations and film response in the simple exposure configuration explained in this report. The next step in this project will be to simulate the entire mouse phantom in MCNP and to examine performance versus doses measured using film. This model will be significantly more complicated due to the complex geometry and various materials used throughout the phantom. The overall goal of this work is to eventually validate our mouse phantoms as good models for examining dose distributions during targeted irradiations of mice.

**References**

1. Chow, James CL, et al. "Dosimetric variation due to the photon beam energy in the small-animal irradiation: A Monte Carlo study." *Medical physics* 37.10 (2010): 5322-5329.
2. Bazalova, Magdalena, and Edward E. Graves. "The importance of tissue segmentation for dose calculations for kilovoltage radiation therapy." *Medical physics* 38.6 (2011): 3039-3049.
3. Welch, D., et al. "Construction of mouse phantoms from segmented CT scan data for radiation dosimetry studies." *Physics in medicine and biology* 60.9 (2015): 3589.
4. Dogdas, Belma, et al. "Digimouse: a 3D whole body mouse atlas from CT and cryosection data." *Physics in medicine and biology* 52.3 (2007): 577. ■



**Top** (l to r): Tom Hei, Veronica Haynes, Martin Hauer-Jensen; David Brenner; Sally Amundson, Guy Garty. **Bottom** (l to r): Dannis Jinhua Wu, Hongning Zhu, Qin Zhang; Aesis Luna, Mashkura Chowdhury.

# Factors in the Reliability of $\gamma$ -H2AX Scoring by Quantitative Fluorescence

Guy Garty, Helen C. Turner, Maria Taveras, and David J. Brenner

## The $\gamma$ -H2AX assay

The  $\gamma$ -H2AX assay is a measure of DNA double-strand breaks (DSB) induced by ionizing radiation. It quantifies through immune staining, the phosphorylated H2AX histone, which localizes to DSBs [3], and has a highly linear relationship with dose [1, 2].

Under the standard manual procedure, the yield of phosphorylated H2AX is quantified by counting foci at high magnification [4]. Several automation systems based on counting foci have been described in the literature [5, 6] but they require acquisition of Z-stacks and high-resolution imaging. Although very sensitive at low doses, the focus-counting technique is less appropriate for higher doses, due to overlap of foci, resulting in reduced focus counting efficiency at doses of 2 Gy or more [7]. The applications of interest in our Center revolve around higher doses in the 2-6 Gy range, both for radiological triage [2] and for investigations of DNA repair capacity across populations [8]. In both cases, we are trying to achieve the maximal throughput, and therefore would like to eliminate the requirement for Z-stack acquisition and use the lowest magnification possible.

We therefore use an alternate technique for quantifying H2AX phosphorylation [2]. Two fluorescent images are taken (one of the DAPI-stained nucleus and

one of the  $\gamma$ -H2AX-bound fluorescent antibody). Nuclei are identified from the DAPI-stained image and the fluorescent intensity in the nucleoplasm is integrated and scored. This allows the use of much lower magnification, resulting in both higher throughput (fewer images) and greatly increased depth of field. Using this technique we have seen a linear response up to at least 8 Gy with sensitivity around 0.3 Gy. Similar assays have been developed in our lab for other proteins [8, 9].

As an example, Fig. 1 shows the captured images (at various magnifications) of cells irradiated with 4 Gy, using the custom imaging system we have built [10]. The upper row shows a full frame image (1760x1776) demonstrating typical cell yields in each field of view. The bottom row shows an additional 10x expansion, demonstrating image quality for individual cells. As described previously [2], the analysis software performs a background subtraction based on the fluorescence intensity in the immediate area of the cell.

## Choice of objective

The choice of objective for an experiment is dictated by a balance of the required resolution with the need for a large field of view to obtain the best possible statistics from a minimal number of images - the number of cells scored per frame will, on average, quadruple when the

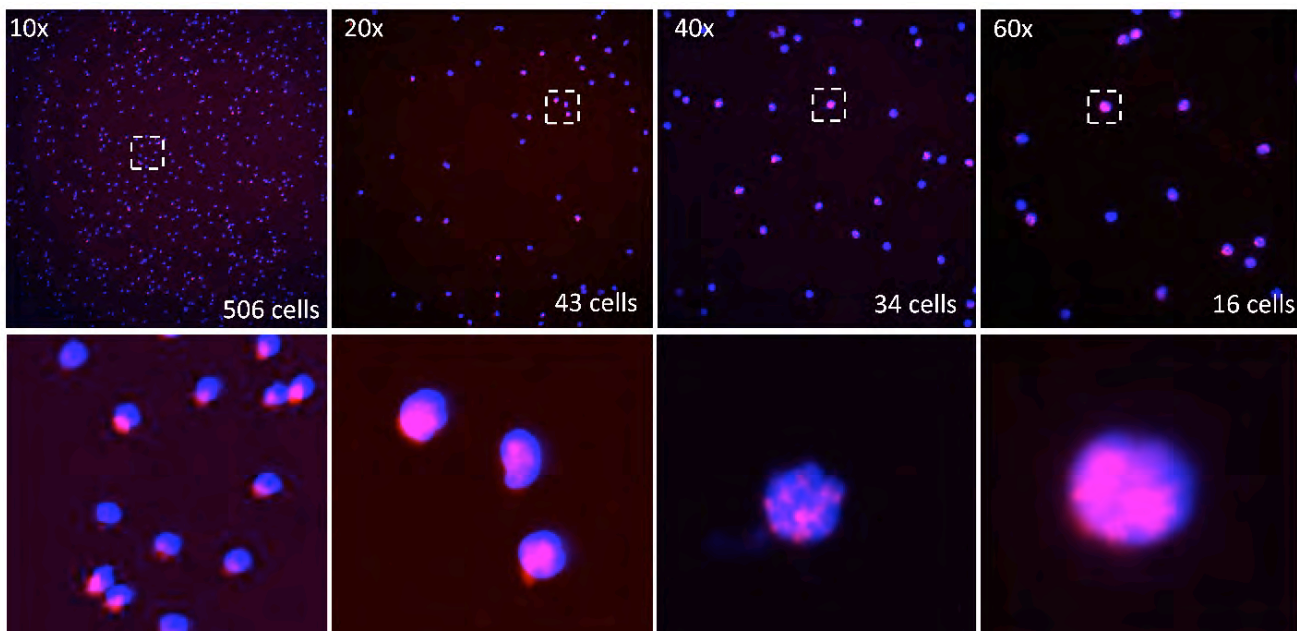


**Figure 1:**  $\gamma$ -H2AX foci imaged at different magnifications. The top row shows a full frame image (1776x1760). The number of cells scored from each image is indicated. The bottom row shows a 10x magnification of the region indicated in the dashed frame in the images in the top row. The red channel corresponds to the AF-555-tagged  $\gamma$ -H2AX antibody and the blue channel to the DAPI counterstain.

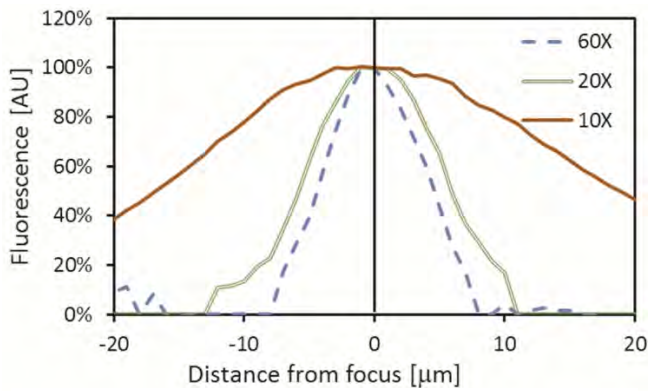


**Figure 2:**  $\gamma$ -H2AX yields as a function of distance from focus for different lenses.

magnification is halved.

A second consideration is the Numerical Aperture (NA) of the objective, which determines both the depth of field and the amount of light passing through the lens.

We have experimented with imaging using 60x oil, 40x air, 20x air and 10x air objectives and observed good correlative results with all magnifications. Although the resolution of the 10x image does not allow detection of individual foci, the image quality is sufficient to discriminate between valid (round) and apoptotic cells, and to perform a quantitative fluorescence measurement. As the 10x lens is more prone to misalignments (see below), the 20x air objective, with its relatively large field of view ( $0.6 \times 0.6 \text{ mm}^2$ ), is preferred. With the 20x air objective, the number of cells required for analysis can be obtained with fewer image fields than required with the higher power objectives.

**Focusing**

Numerical aperture and magnification also determine the depth of field, which is the precision with which the system needs to be focused. The concern here is that an out of focus image would result in a lower fluorescence yield. However, as long as all fluorescence light is collected, the measured fluorescence values will not change significantly even when the image is taken somewhat out of focus [11]. Using our imaging system

and analysis routines, this is indeed the case as the fluorescence is summed within a nuclear boundary determined by the nuclear image (taken at the same focal plane, using the same optics). As an example, Fig. 2 shows the average brightness of fluorescently labeled cells as a function of distance from optimal focus at different magnifications. While the fluorescent values drop rapidly when a low depth of field 60x lens is used, a 10x lens will allow quantitative fluorescence measurements within about  $\pm 5 \mu\text{m}$  of the best focus.

**Alignment**

$\gamma$ -H2AX analysis by quantitative fluorescence requires aligning the nuclear areas determined in one image with the antibody recorded on a separate image. In the previous iteration of the RABiT imaging system, these two images were acquired by independent (but identical) cameras, separated by a dichroic mirror [12]. This placed strict requirements on the physical alignment of the cameras. The move to a single camera system [10], removed the possibility of physical misalignments.

Other sources of misalignment, which are harder to remove, are chromatic aberrations and pixel shift in the emission filters.

In the first case, unless achromatic optics are used, different wavelengths will be imaged differently through the optics. Fortunately, most modern objectives and tube lenses are corrected to provide achromatic imaging properties across the visible spectrum.

Pixel shift in the emission filters [13] is caused in the manufacturing process where the two surfaces of the filter are not exactly parallel, forming a small displacement of the light, which can be on the order of a few pixels on the camera. Using multiple filters with different displacements in different directions will result in few-pixel misalignments in the images. As can be seen, in Fig. 1, at low magnification (e.g. 10x and to a lesser extent 20x) this results in much of the antibody fluorescence being imaged outside the nuclear boundaries.

There are three approaches to solve this issue,

1. To realign the images during analysis, e.g. by

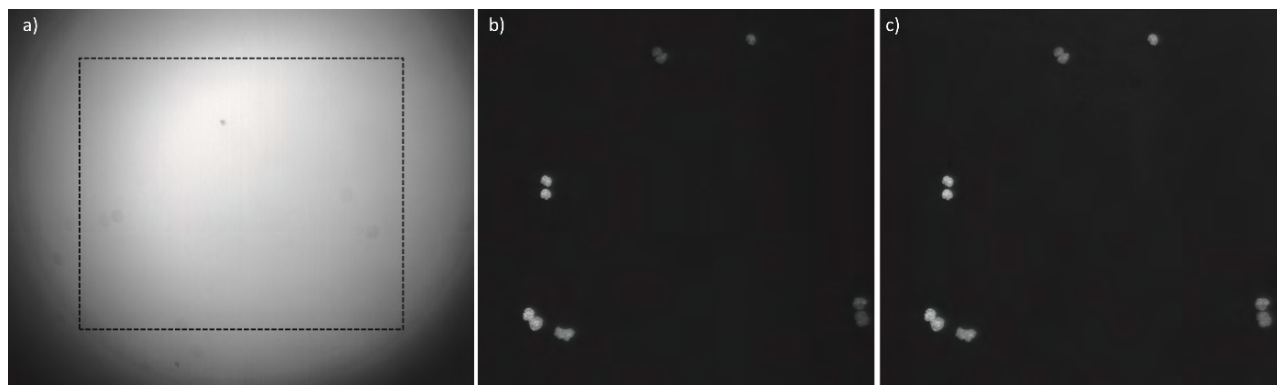


**Figure 3:** a) Full frame image of a uniform fluorescence test slide – the dashed line denotes the 1776x1760 frame used in the images in panels b) and c). b) Image of a field of nuclei (only top right quadrant of the image is shown) without gain correction. c) The same image with gain correction. Note that cells in image periphery (top and right) are much brighter than in Fig. 3b.

shifting the antibody image a few pixels with respect to the nuclear image.

2. To use filters with matched pixel shifts.
3. To use “zero-pixel-shift” filters, which have parallel surfaces (within a few arc seconds), eliminating the problem completely.

The latter is, of course, the easiest as “zero-pixel-shift” filters are commercially available, although they are more expensive than standard filters.

#### Flatness of field

The sCMOS camera used provides high resolution through the use of a large (1” diagonal) sensor. As we are using 1” optics in the beam path, it was extremely difficult to provide uniform light collection over such a large area. Figure 3a shows a full sensor image of a uniform brightness test slide. It is evident that brightness varies significantly across the field resulting in big uncertainties in quantitative fluorescence assays like  $\gamma$ -H2AX.

Two approaches were investigated to overcome this issue. Initially, the sensor was cropped to 1776 x 1770 pixels (dashed line in Fig. 3a). Figure 3b shows that this is still not sufficient as nuclei in the corners of the image are very dim and may not be reliably detected. To overcome this problem a gain correction was added to the analysis. This is similar to the approach described by Model [11] whereas an image of a flat field was taken and the images to be scored were divided by it. As seen in Fig. 3c, this works well to equalize cell brightness across the image.

#### Photobleaching

Photobleaching of the sample is a major concern in manual imaging, where a single region on the sample may be illuminated with UV (ultraviolet) light for a prolonged time during focusing and scoring. In our system we do not use UV illumination (the DAPI excitation LED has a wavelength of 405 nm) and, with the possible exception of the first frame, do not illuminate any region of the sample for more than a few seconds as fields of view are imaged once for each channel with the illumination turned on immediately before image acquisition. Consequently,

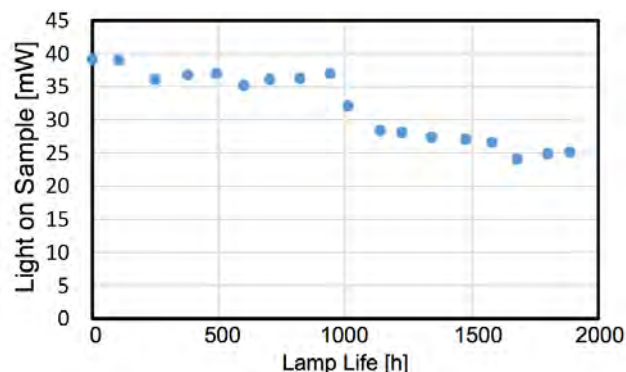


**Figure 4:** Intensity of excitation light on a microscope slide as a function of hours of operation of the lamp. (Using an EXFO 120PC Hg lamp and DAPI cube)

we have not seen any significant photobleaching of either DAPI or the antibody-conjugated fluorophore, even when illuminating the same field of view for multiple minutes.

#### Reproducibility

The actual fluorescence values obtained using this type of measurement depend linearly on the illumination brightness which, depending on the illuminator used, may vary by 50% or more over the life of the lamp (Fig. 4). In order to compensate for this, the lamp intensity needs to be monitored and either adjusted to a constant value or corrections made to the obtained fluorescence yields.

Additionally, fluorescence calibration beads are available with well-defined fluorescence values (expressed as molecules of equivalent fluorochrome - MEF). These beads can be used to convert the values obtained in the quantitative fluorescence measurement to absolute values that can be compared across instruments and over long time scales, compensating for any slow drift in the quality of the imaging optics (e.g. potential degradation of the emission filters).

#### References

1. Redon, C.E., et al., The Use of gamma-H2AX as a Biodosimeter for Total-Body Radiation Exposure in Non-Human Primates. PLoS ONE, 2010. 5(11): p. e15544.
2. Turner, H.C., et al., Adapting the  $\gamma$ -H2AX assay for Automated Processing in Human Lymphocytes. 1. Technological Aspects. Radiation Research, 2011. 175(3): p. 282-290.
3. Rothkamm, K. and Löbrich, M., Evidence for a lack of DNA double-strand break repair in human cells exposed to very low x-ray doses. Proc Natl Acad Sci U S A, 2003. 100(9): p. 5057-62.
4. Mariotti, L.G., et al., Use of the  $\gamma$ -H2AX Assay to Investigate DNA Repair Dynamics Following Multiple Radiation Exposures. PLoS ONE, 2013. 8(11): p. e79541.
5. Hou, Y.N., et al., Development of an automated gamma-H2AX immunocytochemistry assay. Radiat Res, 2009. 171(3): p. 360-7.
6. Valente, M., et al., Automated gamma-H2AX focus scoring method for human lymphocytes after ionizing radiation exposure. Radiation Measurements, 2011. 46(9): p. 871-876.
7. Böcker, W. and Iliakis, G., Computational Methods for Analysis of Foci: Validation for Radiation-Induced  $\gamma$ -H2AX Foci in Human Cells. Radiation Research, 2006. 165(1): p. 113-124.
8. Sharma, P.M., et al., High throughput measurement of  $\gamma$ -H2AX DSB repair kinetics in a healthy human population PLOS One 2015. 10(3): p. e0121083.
9. Turner, H.C., et al., The RABiT: high-throughput technology for assessing global DSB repair.

- Radiation and Environmental Biophysics, 2014. 53(2): p. 265-272.
10. Garty, G., et al., An Automated Imaging System for Radiation Biodosimetry. *Microscopy Research and Technique*, 2015. 78(7): p. 587-598.
  11. Model, M., Intensity Calibration and Flat-Field Correction for Fluorescence Microscopes, in *Current Protocols in Cytometry*. 2014, John Wiley & Sons, Inc. p. 10.14.1-10.14.10.
  12. Garty, G., et al., The RABiT: A Rapid Automated Biodosimetry Tool For Radiological Triage II. *Technological Developments International Journal of Radiation Biology*, 2011. 87(8): p. 776-790.
  13. Erdogan, T., Optical Filters for Wavelength Selection in Fluorescence Instrumentation, in *Current Protocols in Cytometry*. 2001, John Wiley & Sons, Inc. ■

## *In Vivo* Response Patterns in Mice Exposed to the Internal Emitters Cesium-137 and Strontium-90

*Helen C. Turner, Igor Shuryak, Shanaz A. Ghandhi, Maryam Goudarzi<sup>a</sup>, Waylon Weber<sup>b</sup>, Melanie Doyle-Eisele<sup>b</sup>, Raymond Guilmette<sup>b</sup>, Dunstana Melo<sup>b</sup>, Albert J. Fornace<sup>a</sup>, Sally A. Amundson, and David J. Brenner*

In the event of a dirty bomb scenario or an industrial nuclear accident, a significant dose of volatile, long-lived and water-soluble radionuclides such as <sup>137</sup>Cs and <sup>90</sup>Sr may be dispersed into the atmosphere as components of fallout and inhaled or ingested by hundreds or thousands of people. In general, biodosimetry techniques have focused on assessment of radiation doses resulting from external exposures to ionizing irradiation, and have not accounted for those from radioisotopes incorporated into the body through inhalation or ingestion. As a result, most research in the biodosimetry field has focused on acute-whole body photon irradiation, while the effects of internal emitters have received little attention. Exposures from internal emitters can involve different radiation qualities, different tissue exposure patterns, and changing dose rates.

The biochemical and physical properties of the <sup>137</sup>Cs and <sup>90</sup>Sr radionuclides contribute to their unique temporal pattern and biological behavior [1-3]. With similar chemical and physical properties as potassium, <sup>137</sup>CsCl is rapidly absorbed from the gastrointestinal tract or lungs and permeates the entire body, providing relatively uniform protracted beta-particle and gamma irradiation [2, 4], whereas <sup>90</sup>Sr chemically resembles calcium and is readily incorporated into bones and teeth.

As part of the Columbia CMCR program, we have developed mouse models for: a) chronic relatively uniform whole-body irradiation using intraperitoneally-injected, systemically distributed <sup>137</sup>CsCl as a radiation source, and b) chronic non-uniform low-LET radiation resulting from intraperitoneally-injected liquid soluble <sup>90</sup>SrCl<sub>2</sub>. In this study, we used three different biodosimetry approaches to assess prolonged exposure to

ingested radionuclides: fully-automated cytogenetics (Project 1), functional genomics (Project 2), and metabolomics (Project 3). Central to the study design was that blood samples from the same mice were shared between all three projects.

### IRRADIATION AND DOSIMETRY

Based on known biokinetics for <sup>137</sup>CsCl and <sup>90</sup>SrCl<sub>2</sub> [5-8], a single injection activity was calculated for each isotope. The experiments were designed to cover a dose range important for radiological triage (2 to 10 Gy). For <sup>137</sup>CsCl injection, the activity (8.0 ± 0.3 MBq) was calculated to produce accumulated total-body absorbed doses of up to 10 Gy over 30 days of protracted exposure, and for <sup>90</sup>SrCl<sub>2</sub> (200 ± 0.3 kBq), skeletal absorbed doses ranging from 0 to 5 Gy over the same time period. The radioisotope injections were performed at the Lovelace Respiratory Research Institute. C57BL/6 mice were divided into five radiation dose and control groups, eight animals per group.

The committed absorbed doses of the two internal emitters as a function of time post exposure were calculated based on their retention parameters in the mice on the study and their derived dose coefficients for each

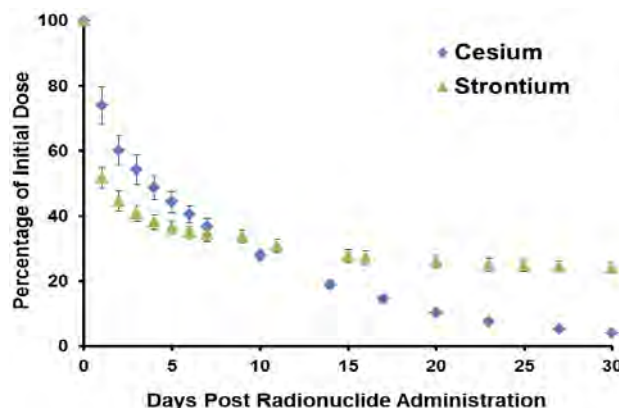


Figure 1. Retention profiles for <sup>137</sup>CsCl and <sup>90</sup>SrCl<sub>2</sub>.

<sup>a</sup>Lombardi Comprehensive Cancer Center, Georgetown University, Washington, DC

<sup>b</sup>Lovelace Respiratory Research Institute, Albuquerque, NM

**Table 1.** Total body absorbed doses (Mean  $\pm$  SD) and dose rates (average across time) through the 30-day study period.

Cs-137			Sr-90		
DAY	Dose (Gy)	Dose Rate (mGy/min)	DAY	Dose (Gy)	Dose Rate (mGy/min)
2	2.0 $\pm$ 0.1	0.67	4	1.2 $\pm$ 0.1	0.21
3	2.7 $\pm$ 0.4	0.52	7	1.8 $\pm$ 0.1	0.14
5	4.1 $\pm$ 0.4	0.5	9	2.1 $\pm$ 0.3	0.11
20	9.5 $\pm$ 0.4	0.25	25	4.8 $\pm$ 0.4	0.11
30	9.9 $\pm$ 1.2	0.03	30	5.3 $\pm$ 0.7	0.07

specific sacrifice time. Figure 1 shows the whole-body counting data normalized to the amount of  $^{137}\text{Cs}$  and  $^{90}\text{Sr}$  present in each animal on Day 0 following isotope injection. The biokinetic and dosimetric modeling showed that within the first week, more than 60% of the initial activity of both isotopes had been excreted. By Day 30, only 4% of the  $^{137}\text{Cs}$  activity still remained in the animals, whereas 24% of the  $^{90}\text{Sr}$  was retained in the skeleton.

Table 1 shows the changing dose rates for the exposure from internal  $^{137}\text{Cs}$  and  $^{90}\text{Sr}$  at specific time points over the 30-day study. In the  $^{90}\text{Sr}$  study, the resulting total accumulated doses to bone were on average about half the total body doses received by the mice in the  $^{137}\text{Cs}$  study at the same times after isotope injection. Mouse urine and blood samples were collected at the time of sacrifice for the measurement of biodosimetric endpoints.

## OVERVIEW OF THE STUDY RESULTS

### Cytogenetics

To evaluate the ionizing radiation-induced DNA damage effects in peripheral mouse blood lymphocytes, Project 1 used the established biodosimetry biomarker  $\gamma\text{-H2AX}$  [9-11] to measure the induction and repair of nuclear DNA double strand breaks (DSBs) in peripheral blood lymphocytes after protracted exposure to the radionuclides [12]. Gamma H2AX foci were detected by indirect immunostaining and quantified by fluorescence intensity relative to the unirradiated control cells.

Figure 2, shows the median total  $\gamma\text{-H2AX}$  fluorescence yields measured at the specific time points following the injection of the radionuclides at time zero.

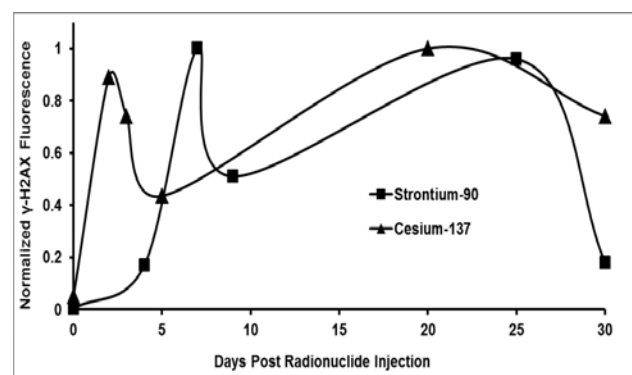


**Figure 2.** In vivo median response pattern of  $\gamma\text{-H2AX}$  yields in peripheral blood mouse lymphocytes after long-term internal exposures to  $^{137}\text{Cs}$  and  $^{90}\text{Sr}$ . The points are joined by a spline curve fitted in Excel.

The  $\gamma\text{-H2AX}$  kinetic profile for  $^{137}\text{Cs}$  exposure indicated that the  $\gamma\text{-H2AX}$  yields peak by Day 2 (mean total body committed absorbed dose = 1.95 Gy) followed by a rapid decline in  $\gamma\text{-H2AX}$  frequency by Day 5 (4.14 Gy), after which time there is a gradual increase in the  $\gamma\text{-H2AX}$  frequency up to 30 Days. As the rate of accumulation of the  $^{137}\text{Cs}$  decreased, the apparent lack of dose response for the formation of  $\gamma\text{-H2AX}$  suggests that the rate of  $\gamma\text{-H2AX}$  disappearance is not a simple function of dose rate. The  $\gamma\text{-H2AX}$  kinetic profile for  $^{90}\text{SrCl}_2$  showed that total  $\gamma\text{-H2AX}$  fluorescence levels continue to increase up to Day 7 (mean total body committed absorbed dose = 1.8 Gy), after which time there is an apparent 50 % drop in  $\gamma\text{-H2AX}$  levels. At some point between Day 9 and Day 25 the  $\gamma\text{-H2AX}$  protein levels started to increase again leading to a drop off in yields by Day 30.

Analysis of the  $^{90}\text{Sr}$  and  $^{137}\text{Cs}$  data using a mathematical model suggested that the temporal kinetics of  $\gamma\text{-H2AX}$  foci after radionuclide administration were consistent with two distinct peaks: the first occurring during the first week, and the second occurring about 3 weeks later. Our mechanistic interpretation for the two-peak temporal pattern of  $\gamma\text{-H2AX}$  fluorescence assumes two populations of cells. The  $\gamma\text{-H2AX}$  signal is initially observed in differentiated mature lymphocytes, whereas the second, delayed peak represents DNA damage in newly formed lymphocytes generated from irradiated progenitors. The fact that the onset of the first  $^{137}\text{Cs}$  peak was earlier than the first  $^{90}\text{Sr}$  peak is perhaps due to the fact that  $^{137}\text{Cs}$ , and the DNA damage it induced, was distributed more homogeneously throughout the body. This could in turn mean that the timing of  $\gamma\text{-H2AX}$  appearance was mostly determined by cell turnover/apoptosis rates, rather than by the amount of DNA damage.

A key finding in this work is that the  $\gamma\text{-H2AX}$  assay provides a strong signal for several weeks after the start of an internal emitter exposure. This is in clear contrast to  $\gamma\text{-H2AX}$  signals after acute exposures, when the signal is typically undetectable after ~24 h. The  $\gamma\text{-H2AX}$  signals for both isotopes at late times are very much larger than would be predicted from the acute-exposure data, but can be understood as resulting from the complex interplay between changing dose, dose rate, and the biokinetics of the death and production of new lymphocytes. Given the different biokinetics of  $^{137}\text{Cs}$  and  $^{90}\text{Sr}$ , a simple biophysical model was able to explain the observed results. Further targeted studies are ongoing to refine and validate these models, which can in principle be applied to the human experience, given knowledge of the isotope biokinetics in humans [13].

### Functional Genomics

Project 2 measured global gene expression in the same  $^{137}\text{Cs}$  [14] and  $^{90}\text{Sr}$  [15] exposed mice. For the transcriptomics studies, RNA was extracted from blood collected by cardiac puncture, and globin transcripts were reduced as previously described [16]. Global gene

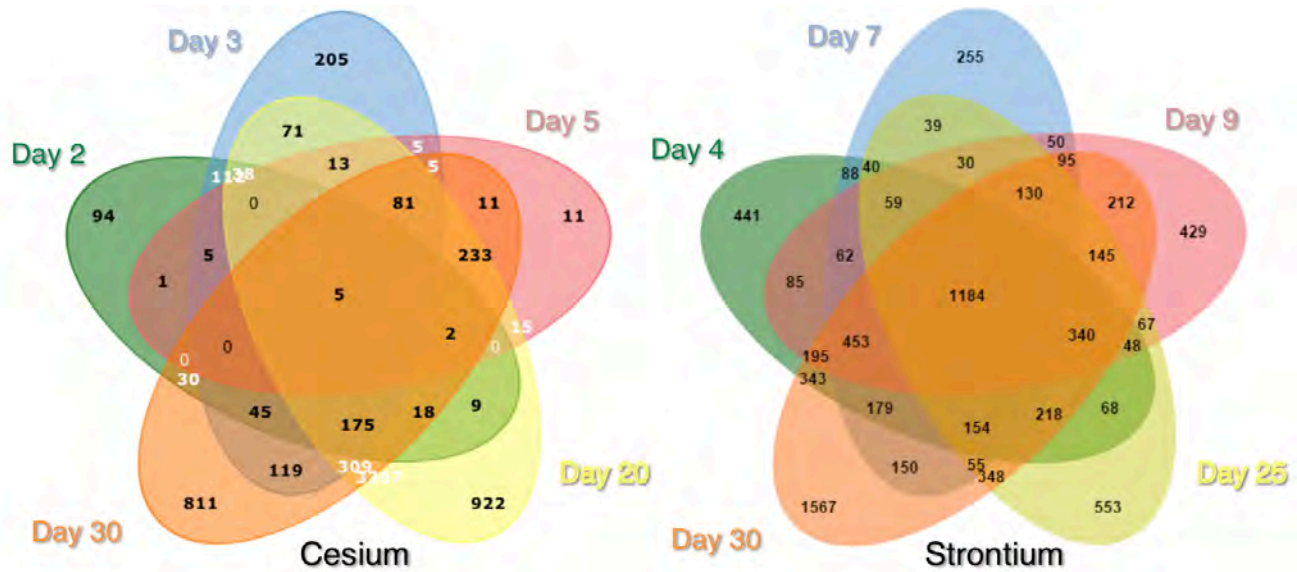


**Figure 3.** Comparison of the numbers of differentially expressed genes at the different sacrifice times in the <sup>137</sup>Cs study (left panel) and the <sup>90</sup>Sr study (right panel). Strikingly, a large number of genes were significantly differentially expressed at all times tested after <sup>90</sup>Sr administration in contrast to only 5 genes in the <sup>137</sup>Cs study.

expression was measured using Agilent whole genome mouse arrays, and analyzed using BRB Array-Tools to identify genes significantly differentially expressed ( $p < 0.001$ ;  $FDR < 0.05$ ) compared to time-matched controls.

The two different isotopes yielded broadly different patterns of gene expression changes. After <sup>90</sup>Sr administration, similar numbers of differentially expressed genes were found at all time points. Many of these differentially expressed genes showed sustained responses across multiple times, with 1184 genes differentially expressed at all the times tested (Figure 3), most of these being down regulated. A different general response was seen following the <sup>137</sup>Cs exposure, with only a few genes down regulated early on, and increasing numbers down regulated throughout the experiment. In contrast with the <sup>90</sup>Sr exposure, only 5 genes were significantly regulated at all time points after <sup>137</sup>Cs administration (Figure 3). Most of these 5 genes were under expressed at all time points, and showed a pattern similar to that seen in the genes under expressed at all times in the <sup>90</sup>Sr study; an early rapid decline without

much alteration in response to either the increasing dose or the decreasing dose rate with increasing time since injection (Fig.4A). It is interesting that the magnitude of response was also similar in both studies, despite the nearly two-fold difference in dose, further suggesting that these responses may be largely independent of both dose and dose rate.

Very few up-regulated genes showed persistent responses across all times in both studies. One example was Mt2, which increased at an essentially identical rate over the first week or so of both studies, then declined more rapidly in the cesium study, reaching essentially background levels by day 30 (Fig. 4B). Expression of Mt2 appeared to reach higher levels in the <sup>90</sup>Sr-treated mice and decline more slowly, despite the lower doses accrued. Other metallothioneins including Mt1 and Mt4 showed similar patterns of expression in the two studies. It is possible that the chemical properties of Sr cause it to elicit a greater response from these metal-binding proteins than does Cs.

In the most striking gene expression pattern seen after <sup>137</sup>Cs injection, numerous genes were over-expressed at days 2-3, and then under-expressed by days 20-30. Although the times and accrued doses differed somewhat in the experiments with the two different isotopes, the “inversion” phenomenon found in the cesium study, where a large number of genes switched from over to under expressed around five days after <sup>137</sup>Cs administration, was not evident in the <sup>90</sup>Sr study.

This work has shown that many genes are regulated in response to the bone-seeking internal emitter <sup>90</sup>Sr, with patterns that seem to differ from gene expression responses to <sup>137</sup>Cs administered as an internal emitter. Further work will be required to understand the mechanisms driving these differences, and to more fully

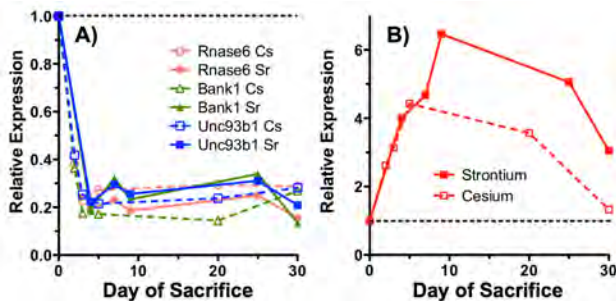


**Figure 4.** Average relative expression levels by microarray in the <sup>137</sup>Cs (open symbols) and <sup>90</sup>Sr (filled symbols) studies of (A) three genes with significantly lower expression at all times, and B) Mt2. The dotted lines indicate levels in time-matched controls.

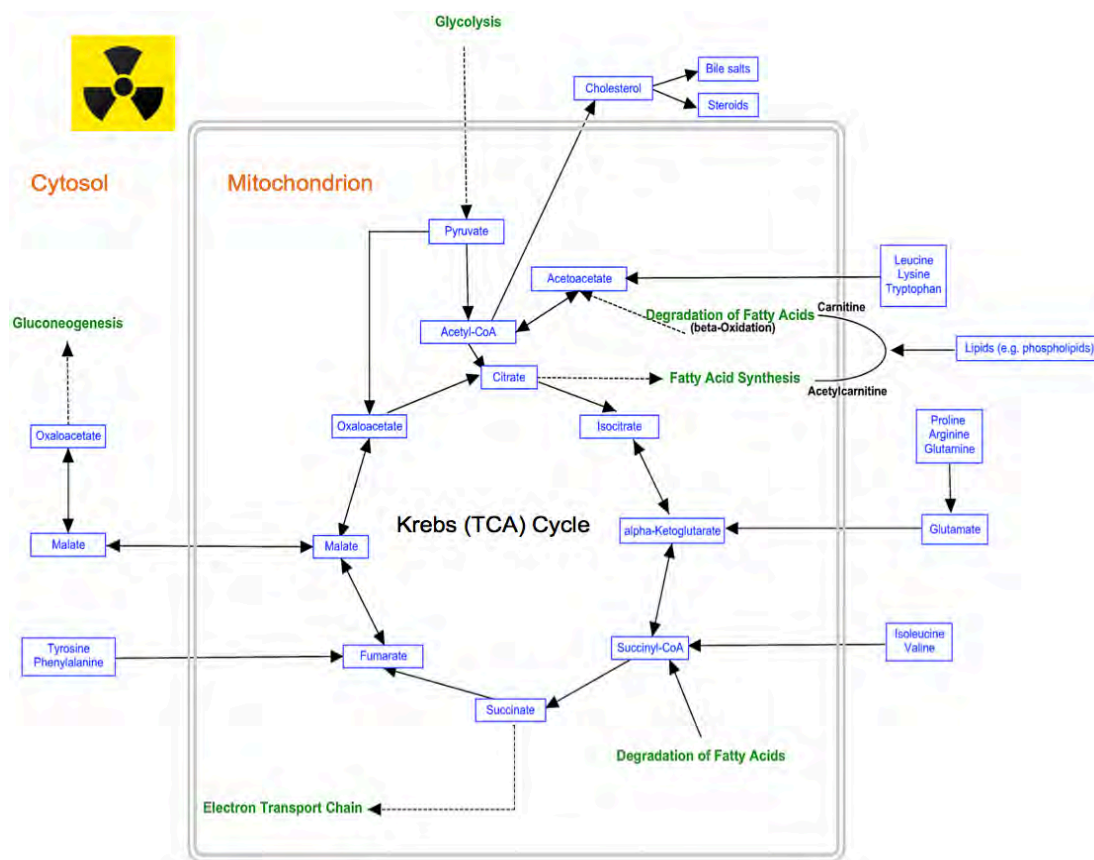


**Figure 5.** Exposure to internal emitters induced perturbations in energy metabolism including intermediates of the Krebs cycle, lipid metabolism, and amino acid metabolism. All metabolites in blue text were present at significantly different levels after internal emitter exposure. Key affected processes are indicated in green text. However, the different physicochemical properties, dose rate, and tissue clearance of  $^{137}\text{Cs}$  and  $^{90}\text{Sr}$  resulted in different exposure-induced magnitude and direction (increase/decrease) of perturbations of the intermediates in these pathways. For instance,  $^{90}\text{Sr}$  induced a persistent decrease in the metabolites shown in this figure, which lasted throughout the 30-day study, while  $^{137}\text{Cs}$  exposure induced a reversible and mixed response in these same intermediates.

assess the potential impact that internal emitters may have on biodosimetry using gene expression profiles.

### Metabolomics

Project 3 profiled urinary and serum metabolomes in the same mice for up to 30 days during internal exposure to  $^{137}\text{Cs}$  [17, 18] and  $^{90}\text{Sr}$  [19, 20]. In-vivo metabolic phenotyping revealed significant shifts in metabolism post-exposure. Comprehensive analysis of serum and urine from the exposed mice indicated that while exposure to both  $^{137}\text{Cs}$  and  $^{90}\text{Sr}$  induced changes primarily in energy metabolism pathways (Figure 5); the isotope and the dose rate modulated these changes. For instance, internal exposure to  $^{90}\text{Sr}$  caused a gross and persistent decrease in the serum levels of many metabolites including PCs, LPCs, PEs, LPEs, SMs, palmitic acid, and linoleic acid. In contrast, exposure to  $^{137}\text{Cs}$  caused a more transient change in the levels of such metabolites, with the levels returning to pre-exposure levels by the end of the 30-day experiment. Cholesterol and bile acid synthesis were also similarly perturbed after exposure to both radionuclides. Increases in lipid inflammatory mediators such as arachidonic acids were also found in both exposures. Several intermediates of the TCA cycle, such as alpha-ketoglutarate, fumarate, malate, and citrate,

displayed lower urinary excretion levels in exposed mice compared to the control mice. Amino acid metabolism (e.g. tryptophan, phenylalanine, and leucine) was also significantly affected in both exposure cases.

All the observed changes following internal exposure to the two radionuclides are centered around energy metabolism and the TCA cycle. This perturbation in energy metabolism can point to a functional deficiency in mitochondria, which serve as the hub of cellular energy production. Mitochondrial function and morphology are known to be sensitive to environmental stressors such as radiation. Our data suggests the involvement of mitochondrial pathways, such as TCA, and closely associated pathways, such as lipid and amino acid metabolism, in response to  $^{137}\text{Cs}$  and  $^{90}\text{Sr}$  exposure.

### SUMMARY AND FUTURE DIRECTIONS

Project 1 studied the kinetics of the  $\gamma\text{-H2AX}$  assay in the peripheral blood lymphocytes during  $^{137}\text{Cs}$  and  $^{90}\text{Sr}$  internal exposure. From a practical perspective, the observation that the  $\gamma\text{-H2AX}$  assay provides a strong signal for at least 4 weeks after initial exposure, even at a time when the dose rate has become very low, is clearly of some significance for internal emitter biodosimetry. The  $\gamma\text{-H2AX}$  data from the  $^{137}\text{Cs}$  study suggest that peak

lymphocyte death occurs following a cumulative <sup>137</sup>Cs total body committed absorbed dose of about 4 Gy, achieved 5 days after isotope administration. The gene expression response pattern measured in the same blood samples, reported fewer differentially expressed genes compared to the earlier and later time points at the accrued dose of 4.1 Gy (Day 5), suggesting a general transition point around this time since the beginning of <sup>137</sup>Cs exposure. The same pattern was also seen for many significantly enriched gene ontology categories. This widespread switch over of gene expression patterns is a novel observation, which we plan to explore further in subsequent studies. Urine and serum profiles also showed clear changes in the metabolome and lipidome as a result of internal isotope exposure, with significant changes in the urinary profile in as little as 2 days, with clear dose / time dependent responses.

The complex responses seen in multiple biodosimetric endpoints may also provide opportunities for distinguishing internal emitter exposures from acute and low-dose rate external exposures. Such studies will help us begin to understand the impact that fallout may have on radiation biodosimetry and the mechanisms involved.

### References

- Whicker FW. Radionuclide transport processes in terrestrial ecosystems. *Radiation Research* 1983;**94**(1):135-50
- Stather JW. Risk of radiation-induced cancer at low doses and low dose rates. *The Medical journal of Australia* 2000;**172**(7):352
- Bertho JM, Louiba S, Faure MC, et al. Biodistribution of (137)Cs in a mouse model of chronic contamination by ingestion and effects on the hematopoietic system. *Radiation and Environmental Biophysics* 2010;**49**(2):239-48
- Baskaya H, Dogru M, Kucukonder A. Determination of the (137)Cs and (90)Sr radioisotope activity concentrations found in digestive organs of sheep fed with different feeds. *Journal of Environmental Radioactivity* 2014;**134**:61-5
- Fujita M, Iwamoto J, Kondo M. Comparative metabolism of cesium and potassium in mammals--interspecies correlation between body weight and equilibrium level. *Health Physics* 1966;**12**(9):1237-47
- Stara JF, Nelson NS, Della Rosa RJ, Bustad LK. Comparative metabolism of radionuclides in mammals: a review. *Health Physics* 1971;**20**(2):113-37
- Stara JF, Thomas RG. The Tissue Distribution and Excretion of Cesium-137 Following Inhalation--Preliminary Data for Rats. Lf-4. Fission product inhalation project [technical progress report]. Lovelace Foundation for Medical Education and Research 1963;**84**:1-21
- Varga LP, Sztanyik LB, Ronai E, et al. Mobilization of radioactive strontium from mouse and rat using dicarboxylic acid derivatives of cryptand (2.2). *International Journal of Radiation Biology* 1994;**66**(4):399-405
- Rogakou EP, Pilch DR, Orr AH, Ivanova VS, Bonner WM. DNA double-stranded breaks induce histone H2AX phosphorylation on serine 139. *The Journal of Biological Chemistry* 1998;**273**(10):5858-68
- Rothkamm K, Horn S. gamma-H2AX as protein biomarker for radiation exposure. *Annali dell'Istituto Superiore di Sanita* 2009;**45**(3):265-71
- Turner HC, Shuryak I, Taveras M, et al. Effect of Dose Rate on Residual gamma-H2AX Levels and Frequency of Micronuclei in X-Irradiated Mouse Lymphocytes. *Radiation Research* 2015;**183**(3):315-24
- Turner HC, Shuryak I, Weber W, et al. gamma-H2AX Kinetic Profile in Mouse Lymphocytes Exposed to the Internal Emitters Cesium-137 and Strontium-90. *PloS One* 2015;**10**(11)
- Harrison J, Day P. Radiation doses and risks from internal emitters. *Journal of Radiological Protection : Official Journal of the Society for Radiological Protection* 2008;**28**(2):137-59
- Paul S, Ghandhi SA, Weber W, et al. Gene expression response of mice after a single dose of (137)Cs as an internal emitter. *Radiation Research* 2014;**182**(4):380-9
- Ghandhi SA, Weber W, Melo D, et al. Effect of <sup>90</sup>Sr internal emitter on gene expression in mouse blood. *BMC Genomics* 2015; **16**: 586
- Paul S, Amundson SA. Development of gene expression signatures for practical radiation biodosimetry. *International Journal of Radiation Oncology, Biology, Physics* 2008;**71**(4):1236-44
- Goudarzi M, Weber WM, Mak TD, et al. Metabolomic and lipidomic analysis of serum from mice exposed to an internal emitter, Cesium-137, using a shotgun LC-MS approach. *Journal of Proteome Research* 2014; **14**: 374-384
- Goudarzi M, Weber W, Mak TD, et al. Development of urinary biomarkers for internal exposure by cesium-137 using a metabolomics approach in mice. *Radiation Research* 2014;**181**(1):54-64
- Goudarzi M, Weber WM, Mak TD, et al. A Comprehensive Metabolomic Investigation in Urine of Mice Exposed to Strontium-90. *Radiation Research* 2015;**183**(6):665-74
- Goudarzi M, Weber WM, Chung J, et al. Serum Dyslipidemia Is Induced by Internal Exposure to Strontium-90 in Mice, Lipidomic Profiling Using a Data-Independent Liquid Chromatography-Mass Spectrometry Approach. *Journal of Proteome Research* 2015;**14**(9):4039-49 ■

# The Decade of the RABiT (2005-2015)

Guy Garty, Helen C. Turner, Y. Lawrence Yao<sup>a</sup>, and David J. Brenner

In 2005, the US government identified the development of improved methods for radiation biodosimetry as a high priority need in an environment of heightened concern over possible nuclear or radiological terrorist attacks [1]. To address this need, the Columbia Center for High Throughput Minimally Invasive Radiation Biodosimetry (CHTMIRB) was funded by the National Institute of Allergy and Infectious Diseases (NIAID) of the National Institutes of Health. CHTMIRB began development of the Rapid Automated Biodosimetry Tool (RABiT), which was designed to be a completely automated, ultra-high throughput robotically-based biodosimetry workstation [2-7].

Although different aspects of cytogenetically-based bioassays (from chromosome preparations [8], to scoring [9] and sample tracking [10]) had previously been automated, the RABiT was to be the first end-to-end system where the only human contact with samples would be at the sample collection step [11] (and of course interpretation of the resultant dose prediction by a qualified medical professional).

In order to efficiently develop the RABiT system, the Center for Radiological Research (CRR) teamed up with the laboratories of Professors Yao and Simaan at the

Department of Mechanical Engineering at Columbia University, where the Robotics systems for the RABiT were developed and tested. Program management support was given by Prof. Zenhausern's group (which had moved from Motorola to Arizona State University a few years earlier). This group was also able to provide a product development perspective.

## The original Assays

The RABiT was originally designed to automate two mature, biodosimetry assays (Fig. 1): (a) The  $\gamma$ -H2AX assay [12, 13], which quantifies DNA strand breaks by immunolabelling phosphorylated histone H2AX and (b) the micronucleus assay [14-17], which scores persistent chromosomal aberrations as post-mitotic micronuclei. As the  $\gamma$ -H2AX assay is relatively rapid (requiring only a few hours to provide a dose estimate, as compared to 72h for the micronucleus assay), it is the preferred assay. Unfortunately, its persistence is low, with the signal fading over 24-48h (whereas the micronucleus assay has a half-life of about a year). The RABiT was therefore designed to allow a fast switchover, with the  $\gamma$ -H2AX assay used for samples arriving within 48h post exposure and the micronucleus assay to be used at later times.

These two assays drove development of the automation platform, with continued feedback between the Mechanical Engineering team and the CRR team as the assays were fine-tuned to facilitate automation in multiwell plates, and the robotics were developed to perform the assays in an optimal manner.

## Automation

Development of the RABiT was divided into two phases with a simpler phase I system initially developed for lower throughput (~6000 samples per day) [3] and a Phase II system with improved performance and throughput reaching 30,000 samples per day [4].

The design layout of the RABiT is shown in Fig. 2 and consisted of several processing stations located around a central Selectively Compliant Articulated Robot Arm (SCARA).

In the field, blood samples (30  $\mu$ l) were collected by finger stick into heparinized capillary tubes, and placed into the holders containing separation medium and sealing material [11]. The blood-filled capillaries were shipped in these capillary holders (32 capillaries each), which, upon delivery to the RABiT, were placed onto the input stage (see Fig. 2b). The SCARA robot would then load the four centrifuge buckets (containing 3 holders each, for a total of 384 capillaries) into a centrifuge, which separated the lymphocyte band from the red blood cells. The SCARA robot would then transfer the buckets to the harvest

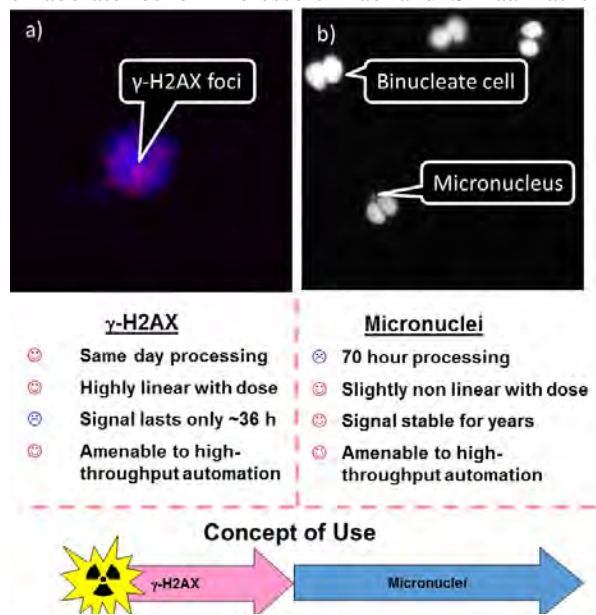


**Figure 1.** The original RABiT assays. (a)  $\gamma$ -H2AX foci (red) and DAPI (blue) counterstain in a 4 Gy irradiated lymphocyte. (b) Micronucleus in binucleate cell (also in 4 Gy irradiated lymphocytes).

<sup>a</sup>Department of Mechanical Engineering, Columbia University, New York, NY

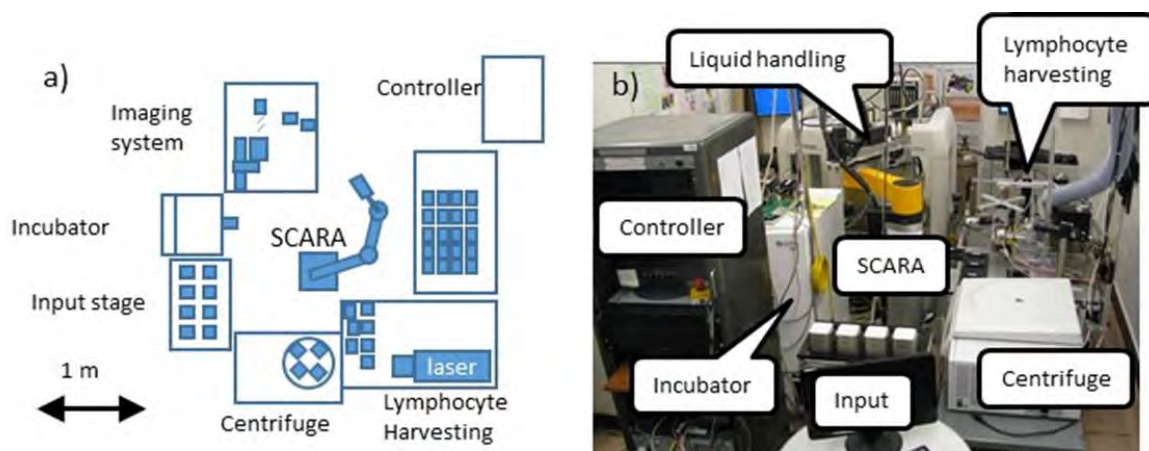


**Figure 2.** (a) Layout of the Phase I RABiT and (b) photo of the Phase II RABiT.

station where the lymphocytes were transferred to four filter bottom 96-well plates.

Each multiwell plate, containing 96 samples, was then transferred to a liquid handling system, which could dispense reagents into the plate or drain reagents through the filter bottoms. This system, in conjunction with a robotic incubator was programmed to perform the  $\gamma$ -H2AX [12] and micronucleus assays. The filter bottoms, containing fluorescently labeled cells, were removed from the multiwell plates using a custom robot, and imaged using a dedicated imaging system, developed to support the RABiT. This novel automated imaging system [6] made use of multiple simultaneous light paths, one step automated focusing, and light steering to accelerate grabbing multiple adjacent fields of view. Image analysis software was written to allow both on- and off-line analysis for all assays.

In 2009, we finalized and tested the Phase I system prototype, with a throughput of up to 6000 samples/per day. After a successful demonstration for our program officer, in August, 2009, development shifted to the construction of a modified system that could achieve a much higher throughput of 30,000 samples per day. Following an analysis of the bottlenecks in the Phase I system, it was determined that the cell harvest station was the main limitation on throughput, as it was there that samples were handled individually rather than in parallel.

The tasks performed in this workstation were to read the barcode on the capillary (and associate it with the barcode and well number on a multiwell plate), locate the lymphocyte band, cut the capillary below the lymphocyte band (using a UV laser), discard the red blood cells, dispense the lymphocytes into the multiwell plate, and discard the capillary.

In the Phase I implementation, the harvest module used the SCARA robot to move each capillary between the different processing steps, resulting in about 11 seconds being needed to process each capillary. This also had the effect of tying up the SCARA robot, limiting its ability to load and unload the centrifuge and to transfer

multiwell plates between the harvest station, liquid handling system and incubator.

To overcome this, the harvest station was parallelized [4] to process four capillaries at once, using dedicated robotics, reaching a processing time of 2.2 sec/capillary and freeing up the SCARA robot for other tasks.

An additional change to the RABiT, required for achieving high throughput, which was not made due to financial constraints, was an increase in the incubator capacity, to allow storage of more samples during the culturing step of the micronucleus assay.

**The second funding cycle (2010-2015)**

In 2010, the CHTMIRB was funded by NIAID for a second 5-year cycle. At this point, robotics development took a back seat to the development of novel assays that could be implemented on the RABiT and testing of the existing assays under complex exposure scenarios. In parallel the RABiT technology was also transitioned to funding by The Biomedical Advanced Research and Development Authority (BARDA) for further development. Under BARDA funding, the assays and image analysis software were rigorously validated [18] in preparation for an FDA submission.

**New Cytogenetics Assays**

In the second funding cycle, two additional assays, based on partial chromosome painting, were developed for incorporation into the RABiT (Fig. 3). First, the

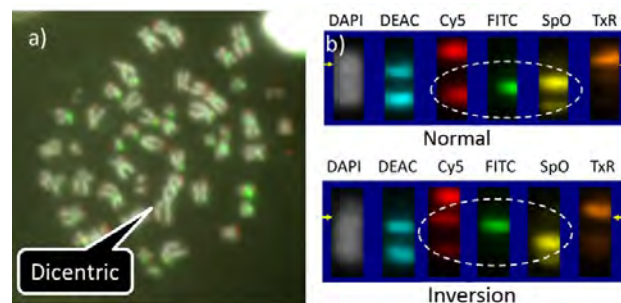


**Figure 3.** Chromosome based assays developed for the RABiT. a) Dicentrics and b) mBAND. Images reproduced, with permission, from [25] ©2015 Wiley Periodicals Inc.

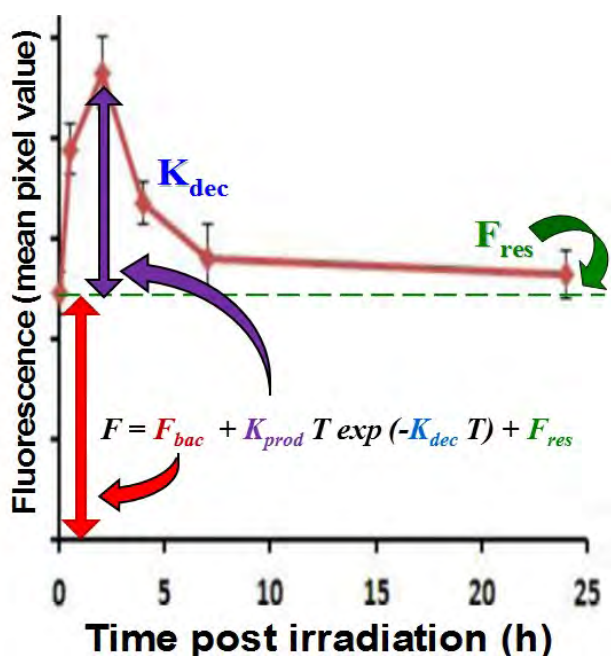


**Figure 4.** Repair kinetics assay.  $\gamma$ -H2AX yields are measured at various times following a 4-Gy irradiation.

dicentric assay [19, 20], which is the gold standard for radiation biodosimetry, was automated. In this assay, dicentric chromosomes are scored by incorporating centromeric probes and identifying chromosomes with two, vs one centromeric spot. The second was the mBAND assay [21-23], which can distinguish high-LET exposures (neutrons and ingested alpha emitters). Here intra-chromosomal rearrangements are scored by “barcoding” the chromosome using partial paints, and scoring those chromosomes that have a different band order from the expected one. In order to support these new assays the imaging system was equipped with a high numerical aperture 60x oil immersion lens and a high sensitivity, high resolution scientific CMOS camera [24]. The multiple optics paths for imaging were eliminated as it was deemed infeasible to expand this feature to support six stains [25].

An assay for quantifying DNA repair kinetics [26, 27] was also developed by modifying the  $\gamma$ -H2AX RABiT assay. In the modified assay an irradiated sample is split and analyzed at multiple time points post irradiation, generating a curve as seen in Fig 4. A model fit provides parameters that can potentially be used to predict an individual’s susceptibility to late sequelae.

### RABiT II – looking forward beyond 2015

When this program started in 2005, commercial robotically-based platforms for high content and cellular screening were rare. Hence the motivation to build the RABiT prototype specifically tailored for cell based bioassays. In the intervening years, commercial fully-automated cell screening platforms have become quite ubiquitous. There are many advantages to transitioning the RABiT platform from the custom designed and



**Figure 5.** The RABiT’s liquid handling system being disassembled and removed from Columbia University’s Department of Mechanical Engineering.

homebuilt prototype to a commercial “off the shelf” system [28], the major advantage being that of deployment. A recent estimate of the number of such machines in university, industry, and clinical testing laboratories in the New York City metropolitan area was 20, with 400 such machines nationwide.

A second major advantage is that of reliability. A commercial system with such wide deployment undergoes more rigorous quality control than a university-built system during development, manufacture and most importantly maintenance. It also has a broader base of trained users and maintenance personnel ensuring operation in time of crisis.

Our future goals are to transition the RABiT assay protocols for operation on commercial systems [28, 29]. Recently we have published a modified Micronucleus assay for 96-well plates using whole blood. This assay is fully automatable on a commercial high throughput screening platform [14].

In December 2015 the Columbia University RABiT system was decommissioned.

### Acknowledgements

Development of the robotic systems involved in the RABiT was performed at the department of Mechanical Engineering at Columbia University’s Fu Foundation School of Engineering and Applied Science, in the respective labs of Profs. Y. Lawrence Yao and Nabil Simaan (Currently at Vanderbilt University) by Alessio Salerno, Youhua Chen, Jian Zhang, Anubha Bhatla, Hongliang Wang and Dakai Bian.

Assay development was performed at the Center for Radiological Research by Helen C. Turner, Antonella Bertucci, Aparajita Dutta, Adayabalam S. Balajee, Mikhail Repin, Stan Lue, Maria Taveras, Oleksandra V. Lyulko, Preety Sharma, Igor Shuryak, Jay R. Perrier, Julia Schaefer, Jing Nie and Barbara Szolc.

**References**

1. Pellmar, T.C. and Rockwell, S., *Priority list of research areas for radiological nuclear threat countermeasures*. Radiation Research, 2005. **163**: p. 115-123.
2. Salerno, A., et al. *Design Considerations for a Minimally Invasive High-Throughput Automation System for Radiation Biodosimetry*. in *IEEE International Conference on Automation Science and Engineering, CASE 2007* 2007. Scottsdale, AZ.
3. Garty, G., et al., *The RABIT: a rapid automated biodosimetry tool for radiological triage*. Health Phys, 2010. **98**(2): p. 209-17.
4. Garty, G., et al., *The RABiT: A Rapid Automated Biodosimetry Tool For Radiological Triage II. Technological Developments* International Journal of Radiation Biology, 2011. **87**(8): p. 776-790.
5. Chen, Y., et al., *Design and Preliminary Validation of a Rapid Automated Biodosimetry Tool for High Throughput Radiological Triage*. Proc ASME Des Eng Tech Conf, 2009. **3**: p. 61-67.
6. Chen, Y., et al., *Development of a Robotically-based Automated Biodosimetry Tool for High-throughput Radiological Triage*. International Journal of Biomechatronics and Biomedical Robotics, 2010. **1**(2): p. 115-125.
7. Chen, Y., et al., *Automated recognition of robotic manipulation failures in high-throughput biodosimetry tool*. Expert Systems with Applications, 2012. **39**(10): p. 9602-9611.
8. Hayata, I., et al., *Robot system for preparing lymphocyte chromosome*. J. Radiation Research, 1992. **33**(Supplement): p. 231-241.
9. Schunck, C., et al., *New developments in automated cytogenetic imaging: unattended scoring of dicentric chromosomes, micronuclei, single cell gel electrophoresis, and fluorescence signals*. Cytogenetic and Genome Research, 2004. **104**(1-4): p. 383-389.
10. Martin, P.R., et al., *Sample tracking in an automated cytogenetic biodosimetry laboratory for radiation mass casualties*. Radiation Measurements, 2007. **42**(6-7): p. 1119-1124.
11. Garty, G., Karam, P.A., and Brenner, D.J., *Infrastructure to Support Ultra High Throughput Biodosimetry Screening after a Radiological Event*. International Journal of Radiation Biology, 2011. **87**(8): p. 754-765.
12. Turner, H.C., et al., *Adapting the  $\gamma$ -H2AX assay for Automated Processing in Human Lymphocytes. I. Technological Aspects*. Radiation Research, 2011. **175**(3): p. 282-290.
13. Nakamura, A., et al., *Techniques for gamma-H2AX detection*. Methods Enzymol, 2006. **409**: p. 236-50.
14. Lue, S.W., et al., *Development of a High-Throughput and Miniaturized Cytokinesis-Block Micronucleus Assay for Use as a Biological Dosimetry Population Triage Tool*. Radiation Research, 2015. **184**(2): p. 134-142.
15. Lyulko, O.V., et al., *Fast image analysis for the micronucleus assay in a fully automated high-throughput biodosimetry system*. Radiat Res, 2014. **181**(2): p. 146-61.
16. Fenech, M., et al., *HUMN project: detailed description of the scoring criteria for the cytokinesis-block micronucleus assay using isolated human lymphocyte cultures*. Mutation Research, 2003. **534**(1-2): p. 65-75.
17. IAEA, *Cytogenetic analysis for radiation dose assessment: A manual*. Technical reports series (International Atomic Energy Agency) No. 405. 2001, Vienna: International Atomic Energy Agency.
18. Garty, G., et al., *Implementing quality-control at the Center for High Throughput Minimally Invasive Biodosimetry*. CRR Annual Report, 2011: p. 79-82.
19. Wilkins, R.C., et al., *Biological Dosimetry by the Triage Dicentric Chromosome Assay – Further validation of International Networking*. Radiation measurements, 2011. **46**(9): p. 923-928.
20. Garty, G., Repin, M., and Brenner, D.J., *Automated Scoring of Dicentric Chromosomes*. CRR Annual Report, 2014: p. 81-82.
21. Mitchell, C.R., et al., *Stable intrachromosomal biomarkers of past exposure to densely ionizing radiation in several chromosomes of exposed individuals*. Radiation Research, 2004. **162**(3): p. 257-263.
22. Chudoba, I., et al., *mBAND: a high resolution multicolor banding technique for the detection of complex intrachromosomal aberrations*. Cytogenet Genome Res, 2004. **104**(1-4): p. 390-3.
23. Bigelow, A.W., et al., *Development of an Automated High-throughput System for Detection of Intrachromosomal Rearrangements*. CRR Annual Report, 2014: p. 83-85.
24. Fowler, B., et al. *A 5.5Mpixel 100 frames/sec wide dynamic range low noise CMOS image sensor for scientific applications*. 2010.
25. Garty, G., et al., *An Automated Imaging System for Radiation Biodosimetry*. Microscopy Research and Technique, 2015. **78**(7): p. 587-598.
26. Sharma, P.M., et al., *High throughput measurement of  $\gamma$ -H2AX DSB repair kinetics in a healthy human population* PLOS One 2015. **10**(3): p. e0121083.
27. Turner, H.C., et al., *The RABiT: high-throughput technology for assessing global DSB repair*. Radiation and Environmental Biophysics, 2014. **53**(2): p. 265-272.

28. Repin, M., et al., *Next generation platforms for high-throughput biodosimetry*. Radiation Protection Dosimetry, 2014. **159**(1-4): p. 105-110.

29. Repin, M., et al., *High-throughput biodosimetry: The use of biotech robots for automated preparation of cytogenetic samples*. CRR Annual Report, 2014: p. 80-81. ■

## Automated High-Throughput Preparation and Analysis of Blood Samples in Biodosimetry using Commercial Biotech Robotic Systems

*Mikhail Repin, Sergey Pampou<sup>a</sup>, and David J. Brenner*

Cytogenetic methods are extensively used in radiation biology for estimating the absorbed radiation dose in humans [1]. In the case of radiological accidents, several thousands of people are likely to require screening for radiation exposure. Therefore, development of large-scale sample processing techniques is critical for the timely diagnosis and treatment of exposed people. Processing of a large number of samples according to standard protocols is not only time consuming but also expensive because large volumes of reagents are used. To circumvent these technical difficulties, improved preparative methods are needed to increase the speed of large scale sample processing for cytogenetic analyses. We developed a method for high-throughput culturing and fixation of human peripheral blood lymphocyte samples [2, 3]. Previously, the  $\gamma$ -H2AX assay was automated in our Center for High Throughput Minimally Invasive Radiation Biodosimetry using the RABiT system specifically developed for biodosimetry purposes [4]. A versatile and efficient imaging system was also developed as a part of the RABiT system [5].



**Fig. 1.** Cell::explorer robot (Perkin Elmer) at the Columbia Genome Center.



**Fig. 2.** Automated IN Cell Analyzer 2000 high-throughput imaging system (GE Healthcare) at the Columbia Genome Center.

We continued our work on assay optimization and automation for biodosimetry purposes, focusing on the use of available cost-effective commercial biotech robotic systems for sample preparation (Fig. 1) and high-throughput imaging systems (Fig. 2). This has become possible due to the introduction of the next generation biodosimetry platforms, which work with tubes in racks and plates with ANSI/SLAS microplate format [3].

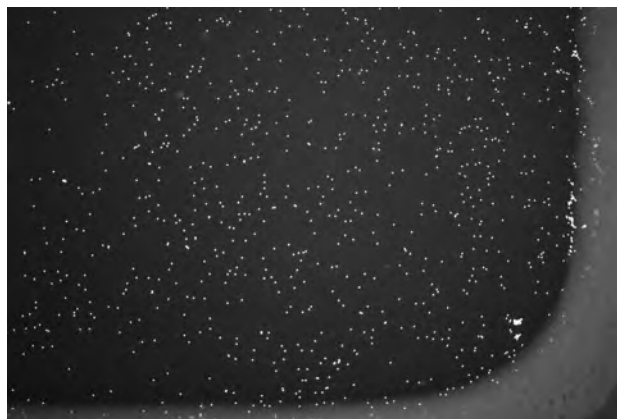


**Fig. 3.** Distribution of DAPI-stained nuclei of human lymphocytes on the surface of an image plate after culturing, fixation and staining of cells on the cell::explorer robot.

<sup>a</sup>Department of Systems Biology, Columbia University, New York, NY

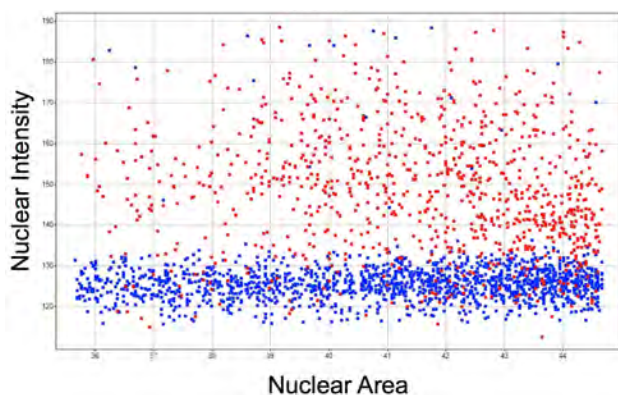


**Fig. 4.** Distribution of fluorescence intensity of  $\gamma$ -H2AX signal in control (blue dots) and irradiated (red dots) human lymphocytes. Signal intensity is not dependent on nucleus size.

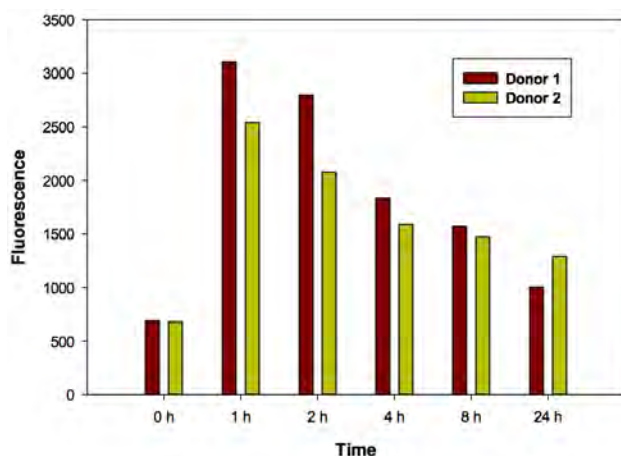


**Fig. 5.** Fluorescence intensity of  $\gamma$ -H2AX signal on irradiated human blood samples (4  $\mu$ l, 2 donors) fixed after different times in culture. Cells were cultured, fixed and stained on the cell::explorer robot (Perkin Elmer, USA) and images were captured on the automated IN Cell Analyzer 2000 (GE Healthcare) using a 20X objective lens.

In this report, we show the use of commercial automated systems for the  $\gamma$ -H2AX assay. The even distribution of nuclei (Fig. 3) was achieved by optimizing conditions of fixation and preparation of cells by the

cell::explorer robot from only 4  $\mu$ l of human peripheral blood. Immuno-staining using directly-labeled  $\gamma$ -H2A antibodies was also performed with the cell::explorer robot. Irradiated cells showed increased levels of fluorescence intensity in comparison with non-irradiated cells independent of cell nucleus size (Fig. 4).

Data analysis of the integrated fluorescence intensity of  $\gamma$ -H2AX signal for blood samples (2 donors) fixed after different times in culture post irradiation shows the well-known dependence of  $\gamma$ -H2AX signal intensity on DNA repair time, with a strong increase in signal during the first hour after irradiation ( $\gamma$ -H2AX induction phase) and a later exponential decrease phase (Fig. 5).

In summary, we have demonstrated that universal biotech robotic systems can be successfully used in biodosimetry for high-throughput preparation of blood samples and corresponding high-throughput image capturing in microplate formats.

### References

1. IAEA, International Atomic Energy Agency. Cytogenetic dosimetry: applications in preparedness for and response to radiation emergencies. IAEA Emergency Preparedness and Response Series. IAEA (2011). Emergency Preparedness and Response. 2011, Vienna: IAEA. 229.
2. Lue, S.W., et al., Development of a High-Throughput and Miniaturized Cytokinesis-Block Micronucleus Assay for Use as a Biological Dosimetry Population Triage Tool. *Radiat Res*, 2015. 184(2): p. 134-42.
3. Repin, M., et al., Next generation platforms for high-throughput biodosimetry. *Radiat Prot Dosimetry*, 2014. 159(1-4): p. 105-10.
4. Turner, H.C., et al., The RABiT: high-throughput technology for assessing global DSB repair. *Radiat Environ Biophys*, 2014. 53(2): p. 265-72.
5. Garty, G., et al., An automated imaging system for radiation biodosimetry. *Microsc Res Tech*, 2015. 78(7): p. 587-98. ■



L to R: Shanaz Ghandhi, David Welch, Manuela Buonanno, Aesis Luna

# Lung Irradiation of Non-Human Primates Induces Persistent Gene Expression Changes in Peripheral Blood

Shanaz A. Ghandhi, Jean Gardin<sup>a</sup>, J. Mark Cline<sup>a</sup>, and Sally A. Amundson

The Non-Human Primate (NHP) is a useful model for the study of radiation countermeasures and radiation response, especially the Acute Radiation Syndrome (ARS), and the *in vivo* effects of radiation on immune function [1]. In the study reported here, 8 NHPs received a single x-ray dose of 10 Gy to the anterior-posterior midplane of the thorax (covering most of both lungs) at Wake Forest School of Medicine. Peripheral blood samples were drawn into PAXgene tubes prior to irradiation and on days 2, 5 and 30 after irradiation, and shipped to the CRR. We isolated RNA from the stabilized whole blood using the PAXgene Blood RNA method (PreAnalytix), and then depleted Globin transcripts using the Ambion GLOBINclear-Human kit (Life Technologies) following the protocols suggested by the manufacturers. We then processed the RNA samples for hybridization to Agilent Whole Human Genome 4X44K arrays, following the Agilent recommended protocol. We analyzed the data using BRB Array Tools and performed class comparisons using a p-value cut-off of 0.005 and false discovery rate <10%.

Results from the array analysis showed that 1187 genes were significantly differentially expressed over the course of the study, when compared with pre-exposure levels. Class comparisons were paired with pre-exposure controls by animal and 545, 273 and 603 genes were significantly differentially expressed at the mRNA level on days 2, 5 and 30, respectively. A summary of the direction of change of the differentially expressed genes is shown in Figure 1A.

Figure 1B shows the overlap of genes that were affected by irradiation at the different time points in the study. Twenty-five genes were differentially expressed at all three of the time points studied. All of these genes showed a consistent direction of change, either up or down regulated, throughout the study.

We then looked for biological processes that were significantly affected among these 25 consistently changed genes, using DAVID Gene Ontology analysis [2]. Two processes, plasma membrane signaling (Bonferroni-corrected p-value  $9 \times 10^{-4}$ ) and immune response (Bonferroni-corrected p-value  $4 \times 10^{-2}$ ) were found to be significantly enriched among these genes. The expression of genes from both categories is illustrated in Figure 2 for the three times in the study.

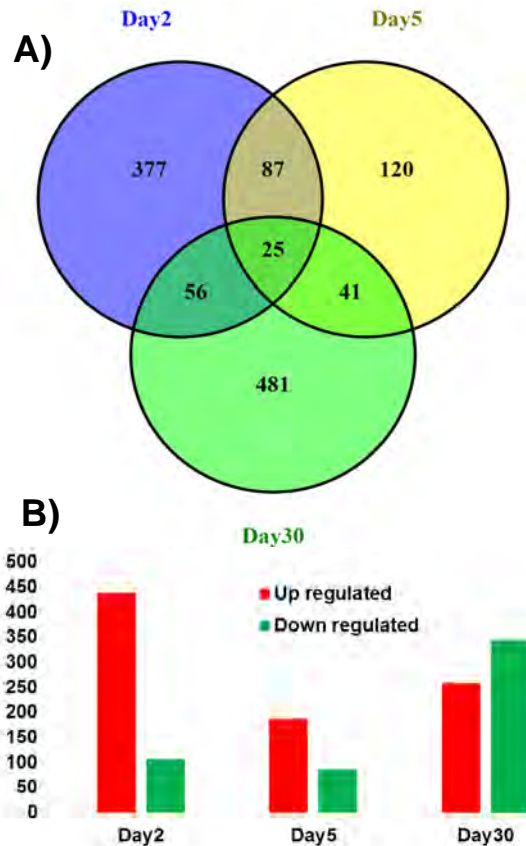


**Figure 1.** Summary of differentially expressed genes across the study. A) Number of differentially expressed genes at each day by direction of change. B) Venn diagram showing the numbers of differentially expressed genes common to the different time points.

There were genes in common to the two processes, such as *AQP9* (Aquaporin 9) and *FAIM3* (Fas apoptotic inhibitory molecule 3), suggesting the potential for interaction and crosstalk between these two biological processes. The other genes that are affected by partial body irradiation to the lung, especially those contributing to immune response, such as *IL1R1* (Interleukin 1 receptor, type 1) and *TLR6* (Toll-like receptor 6), suggest that there may be a continuous inflammatory response that occurs over the course of the 30-day study. This would be consistent with a previous study on GI-ARS and H-ARS in NHP (69 male Rhesus monkeys) exposed to doses of radiation between 10 and 14 Gy, in which large decreases were observed in blood cell counts for neutrophils, lymphocytes, and platelets for at least 16 days after total body irradiation [3].

<sup>a</sup>Department of Pathology, Wake Forest School of Medicine, Winston-Salem, NC

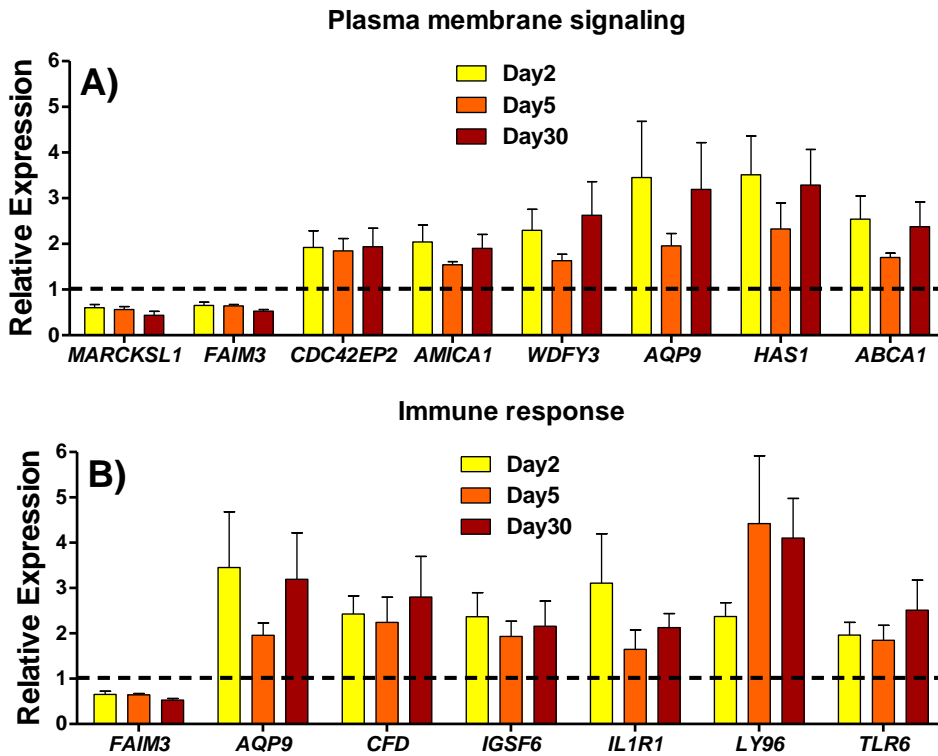


**Figure 2.** Relative expression of genes belonging to two biological process categories that were significantly over-represented among consistently differentially expressed genes in NHP after lung irradiation, A) Plasma membrane signaling and B) Immune response genes. Results are the average and SEM of 5 independent replicates.

In the present study, we examined gene expression in peripheral blood up to 30 days after irradiation. Interestingly, we found that the largest number of genes were affected at the latest time point in our study (Figure 1), which suggests that partial-body irradiation to the lung can have long-term effects on blood cell function and the immune response in NHP.

**References**

- Williams JP, Brown SL, Georges GE, Hauer-Jensen M, Hill RP, Huser AK, Kirsch DG, Macvittie TJ, Mason KA, Medhora MM *et al*: **Animal models for**

**medical countermeasures to radiation exposure.** *Radiat Res* 2010, **173**(4):557-578.

- Huang da W, Sherman BT, Lempicki RA: **Systematic and integrative analysis of large gene lists using DAVID bioinformatics resources.** *Nat Protoc* 2009, **4**(1):44-57.
- MacVittie TJ, Farese AM, Bennett A, Gelfond D, Shea-Donohue T, Tudor G, Booth C, McFarland E, Jackson W, 3rd: **The acute gastrointestinal subsyndrome of the acute radiation syndrome: a rhesus macaque model.** *Health Phys* 2012, **103**(4):411-426. ■



Speakers in “Physics and Biology of a Mars Mission”, a symposium at the 61<sup>st</sup> Annual Radiation Research Society Meeting. (l to r): Cary Zeitlin, Lori Ploutz-Snyder, Mike Weil, and Jeffrey Jones with Session Chair Tom Hei.

# Effects of DNA Repair Deficiency on the Transcriptional Radiation Response in Mouse Blood

Nils Rudqvist, Evagelia C. Laiakis<sup>a</sup>, Mashkura Chowdhury, Sunirmal Paul<sup>b</sup>, M.A. Sureshkumar, Albert J. Fornace<sup>a</sup>, and Sally A. Amundson

## Introduction

There is a perceived need to develop tools for high-throughput biodosimetry [1]. This was clearly demonstrated in the 1987 radiation incident in Goiânia when a medical radiation source from an abandoned hospital was scavenged and breached: about 130,000 individuals were screened within the first days, but only 20 required medical attention [2]. In the case of an improvised nuclear device in a major city, potentially millions of people would have to be screened to assign exposed individuals to appropriate treatment.

Gene expression represents an emerging approach to biodosimetry that could provide an estimate of absorbed dose and indicate potential radiation-induced injury. In 2008, Paul and Amundson [3] used whole genome gene expression profiling of ex vivo irradiated human blood to build a 74-gene predictor signature able to distinguish between 0, 0.5, 2, 5, and 8 Gy radiation exposure.

Through epidemiological studies on populations exposed to irradiation, it has emerged that about 2-4 percent of the population may be considered sensitive to radiation. Such radiosensitivity may impact both the general gene expression radiation response and the sensitivity and specificity of the biodosimetric gene expression signatures currently being developed. Individual variations in DNA repair capacity may contribute to radiosensitivity. We report here an initial investigation into the impact of the major DNA repair

pathways on the gene expression response to radiation and on gene expression biodosimetry, using wild-type mice (WT) and genetically engineered mouse models deficient in pathways known to impact radiation signaling and double-strand break repair (*Atm*<sup>-/-</sup>), and non-homologous end joining (*Prkdc*<sup>scid</sup>).

## Gene expression responses of Wild-Type, *ATM*<sup>-/-</sup>, and *PRKDC*<sup>Scid</sup> phenotypes to radiation

Wild-type, *ATM*<sup>-/-</sup>, and *PRKDC*<sup>Scid</sup> (SCID) mice were exposed to equitoxic whole body absorbed doses (8, 4, and 3 Gy, respectively) of <sup>137</sup>Cs  $\gamma$ -rays. Twenty-four hours after exposure, the mice were sacrificed, and RNA was extracted from whole blood using the PAXgene method. Whole genome gene expression was measured using Agilent Whole Mouse Genome Microarrays (4x44K v2), following a typical Agilent workflow. The data were analyzed using BRB-Array Tools [4]. As seen in Figure 1, WT mice responded with both a larger number of statistically significant ( $p < 0.001$ ; fold-change  $> 1.5$ ) genes (454 genes; Benjamini-Hochberg FDR  $\leq 0.037$ ) and with higher fold changes of regulation compared with both *ATM*<sup>-/-</sup> (188 genes; FDR  $\leq 0.089$ ) and SCID (217 genes; FDR  $\leq 0.077$ ). Down-regulation was more common than up-regulation for all three phenotypes, but most prominent in SCID, then *ATM*<sup>-/-</sup>, and least prominent in WT mice. The gene expression response in WT involved typical p53-regulated genes such as *Bbc3* (up 3.4-fold), *Cdkn1a* (up 19-fold), *Gadd45a* (down 3.7-fold), and

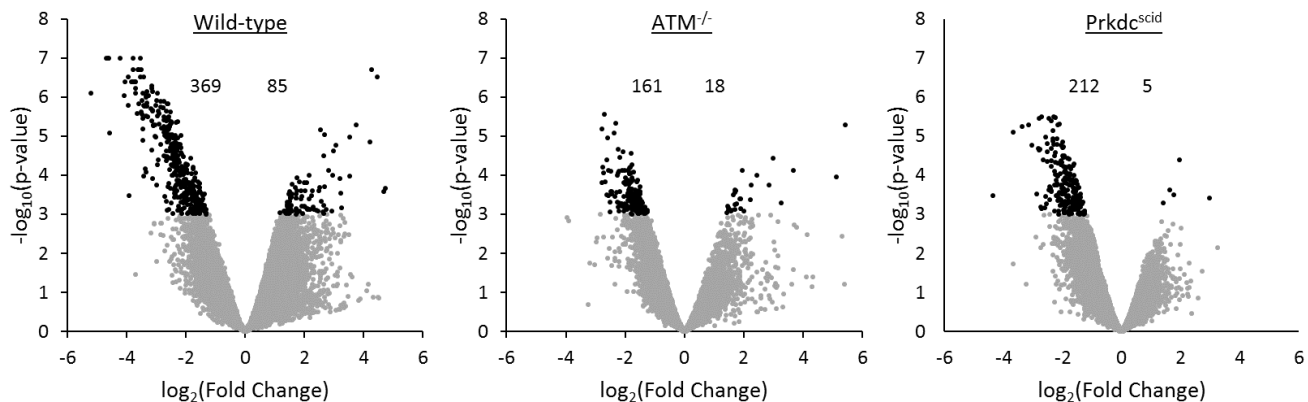


**Figure 1. Volcano plots showing expression and statistical significance of genes.** Black dots represent genes passing the statistical cut-off:  $p\text{-value} < 0.01$  ( $-\log_{10}[p\text{-value}] > 3$ ) and fold change  $> 1.5$  ( $-\log_2[\text{fold change}] > 0.58$ ). Grey dots represent genes not passing the statistical cut-off. Numbers indicate down- and up-regulated genes for each phenotype, respectively.

<sup>a</sup>Department of Biochemistry and Molecular & Cellular Biology, Georgetown University, Washington DC

<sup>b</sup>Rutgers University, Newark, NJ

<sup>c</sup>University of Texas Health Science Center, San Antonio, TX

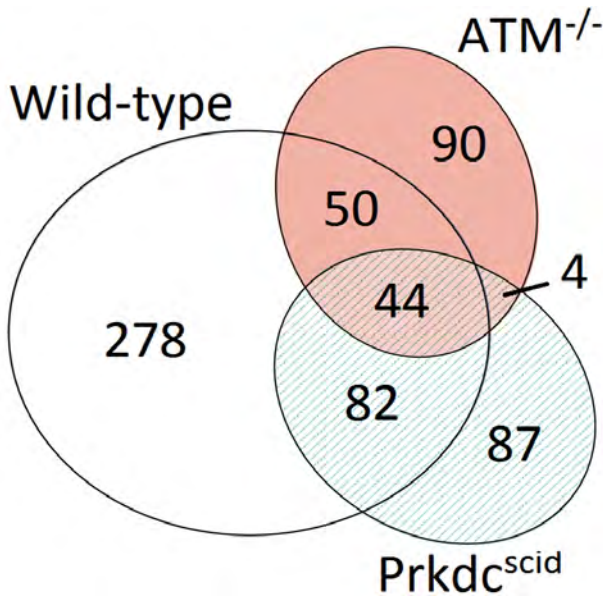


**Figure 2. Venn diagram showing the distribution of statistically significant genes.** Genes regulated in two or more phenotypes always showed the same direction of regulation. The numbers in each section represent number of statistically significant regulated genes ( $p$ -value < 0.01, fold change > 1.5), also represented by area

*Mdm2* (up 3.0-fold), consistent with responses seen previously at doses as high as 8 Gy [5]. The response in  $ATM^{-/-}$  and SCID departed from the typical pattern, however, (although *Cdkn1a* was upregulated 7.9-fold in SCID) and involved fewer genes.

The numbers of radiation-responsive genes shared between different genotypes are shown in Figure 2. With 278 genes regulated exclusively in WT mice, this phenotype demonstrated the highest proportion of phenotype-specific regulated genes (61%). Corresponding

numbers for  $ATM^{-/-}$  and SCID were 90 and 87 exclusive genes, respectively, although the proportion of phenotype-specific genes was slightly higher in  $ATM^{-/-}$  (48%) compared with SCID (40%). Interestingly, only four genes (*Rbbp4*, *Myo1d*, *NAP093099-001*, *Metap2*) were regulated in both  $ATM^{-/-}$  and SCID, but not WT. Of these four genes, all but *NAP093099-001* showed a larger magnitude of downregulation in SCID compared with  $ATM^{-/-}$ , most notably *Myo1d*, which decreased 10-fold in SCID and 3-fold in  $ATM^{-/-}$ .

**Gene ontology analysis**

The DAVID bioinformatics resource tool (<http://david.abcc.ncifcrf.gov/>) [6, 7] was used to find overrepresented Gene Ontology (GO) terms among the responding genes. Similar proportions of the responsive genes in each genotype had GO annotations and were used in the analysis (WT: 40% annotated genes,  $ATM^{-/-}$ : 41%, and SCID: 34%). A Benjamini-Hochberg FDR < 0.1 was used to determine statistically significant GO terms. In all, 37, 16, and 10 GO terms were statistically significantly overrepresented in the gene expression responses of the WT,  $ATM^{-/-}$ , and SCID phenotypes, respectively. As similar proportions of the responsive gene lists were included in the GO analysis for all the genotypes, the reduction in the number of statistically significant GO terms for  $ATM^{-/-}$  and SCID suggests a loss of radiation response functions in these phenotypes compared to WT.

Eight GO terms (related to cellular, protein, and macromolecule metabolism) were enriched among radiation responsive genes in all three phenotypes (Figure 3). GO terms exclusively regulated in WT were related to cell death, homeostasis, stress response, DNA damage, and cell cycle, implying a strong impact of both ATM and

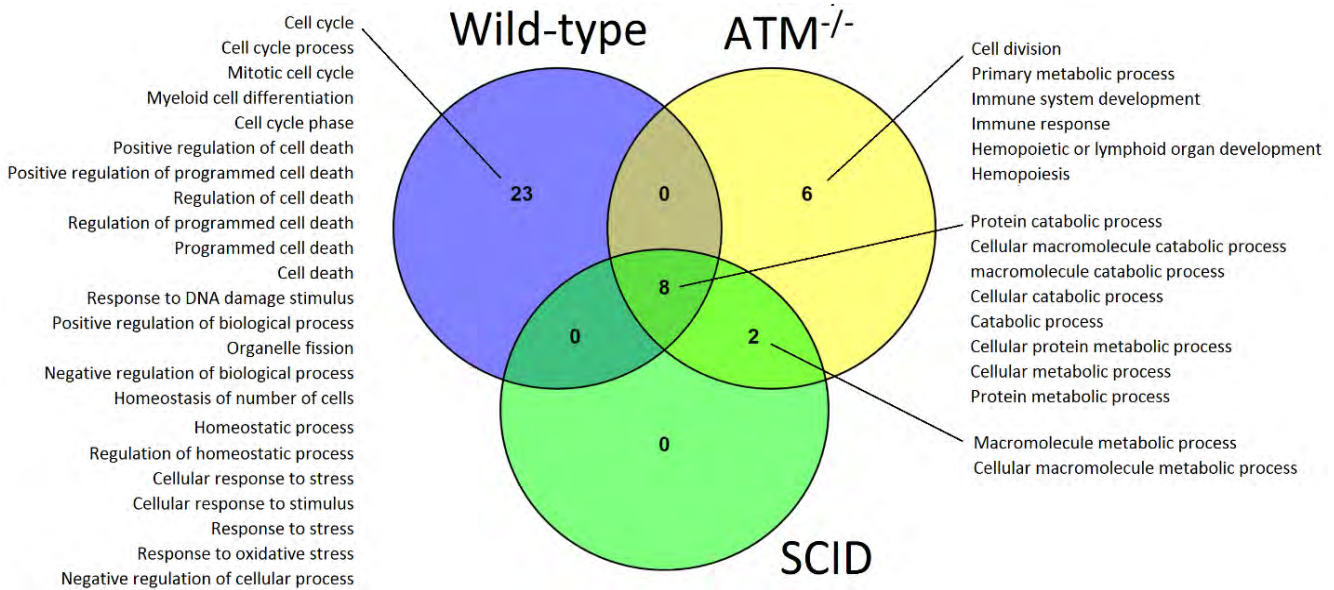


**Figure 3. Overrepresented Gene Ontology terms.** The DAVID bioinformatics resource tool (<http://david.abcc.ncifcrf.gov/>) was used to find overrepresented Gene Ontology (GO) terms [6, 7] among the genes significantly differentially expressed after radiation exposure in the three genotypes. GO terms with a Benjamini-Hochberg FDR < 0.1 were considered to be statistically significant. Only terms at GO level 2, 3, and 4 were included in the analysis.

**Table 1.** Performance of 102-gene binary classifiers built using the WT data as a training set and tested on the ATM<sup>-/-</sup> and SCID data.

Method*	ATM <sup>-/-</sup>		SCID		Overall	Overall
	Sens	Spec	Sens	Spec	Sens	Spec
<b>1) Compound Covariate Predictor</b>	67%	100%	100%	80%	82%	90%
<b>2) Linear Discriminant Analysis</b>	67%	100%	100%	80%	82%	90%
<b>3) 1-Nearest Neighbor</b>	50%	100%	60%	100%	55%	100%
<b>4) 3-Nearest Neighbors</b>	50%	100%	100%	80%	73%	90%
<b>5) Nearest Centroid</b>	67%	100%	100%	80%	82%	90%
<b>6) Support Vector Machines</b>	50%	100%	60%	100%	55%	100%
<b>7) Bayesian Compound Covariate Predictor</b>	50%	100%	100%	80%	73%	90%

\*The class prediction tool of BRB-ArrayTools was used to determine sensitivity (Sens) and specificity (Spec) for each of the algorithms.

SCID on these central radiation response pathways. Six GO terms (related to the immune system, metabolism, hemopoiesis, and cell division) were significant only in the ATM<sup>-/-</sup> response. In SCID mice, only general GO terms related to metabolism were significantly enriched among responsive genes, and none of these were exclusive to SCID, although two GO terms were common to SCID and ATM<sup>-/-</sup>. Broadly, fewer and more general GO terms were regulated in ATM<sup>-/-</sup> and SCID compared with WT, suggesting a dramatic reduction in the radiation-specific biological response in these two phenotypes.

### Commonly regulated genes

A total of 44 genes, all of which were downregulated, responded to radiation in all three phenotypes. Generally, the response of these genes was strongest in WT mice that also received the highest absorbed dose (8 Gy). SCID mice (3 Gy) generally demonstrated slightly stronger downregulation than ATM<sup>-/-</sup> (4 Gy), supporting the idea that gene expression may reflect individual sensitivity, and not just absorbed dose. Additionally, using DAVID to perform a GO analysis of these 44 genes, the GO term protein catabolism had a Benjamini-Hochberg FDR < 0.1.

### Predicting radiation exposure in DNA repair impaired phenotypes

We next used class prediction methods in BRB-Array Tools (Compound Covariate Predictor, Linear Discriminant Analysis, 1-Nearest Neighbor, 3-Nearest Neighbors, Nearest Centroid, Support Vector Machines, and Bayesian Compound Covariate Predictor) to test whether impairment of DNA repair impacted the ability of a gene panel to predict radiation exposure. WT mice were used as a training set to build binary classification algorithms which were then tested for their ability to classify ATM<sup>-/-</sup> and SCID mice as irradiated or not. The sensitivity and specificity of each algorithm were calculated for the ATM<sup>-/-</sup> and SCID phenotypes. Additionally, an overall sensitivity and specificity were

calculated for operation on the combined ATM<sup>-/-</sup> and SCID datasets (Table 1). Generally, the gene panel predictors showed better sensitivity than specificity for ATM<sup>-/-</sup>, and the opposite for SCID. The three best-performing algorithms, Compound Covariate Predictor, Linear Discriminant Analysis, and Nearest Centroid, had an overall sensitivity of 82% and overall specificity of 90%.

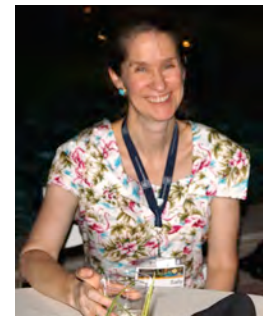
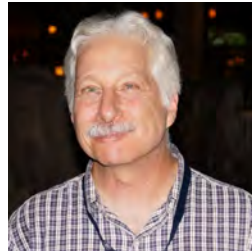
### Conclusion

In this study, we used wild-type (WT) mice and genetically engineered mouse models deficient in two different DNA repair pathways, Atm<sup>-/-</sup> (double-strand break repair) Prkdc<sup>scid</sup> (non-homologous end joining) in an initial investigation into the impact of DNA repair deficiency on the gene expression response to radiation in the context of biodosimetry. The results indicate that ablation of DNA repair pathways has a substantial impact on gene expression and inferred downstream biological functions at 24 h after exposure to equitoxic LD<sub>50/30</sub> absorbed dose levels. Analysis of this dataset suggests that DNA repair deficiency may impair the performance of dosimetric signatures developed using only individuals of average sensitivity. This suggests that sensitive subpopulations need to be considered and included at the gene selection level in order to produce biodosimetric classifiers that are robust to variations in DNA repair capacity and radiation sensitivity.

### References

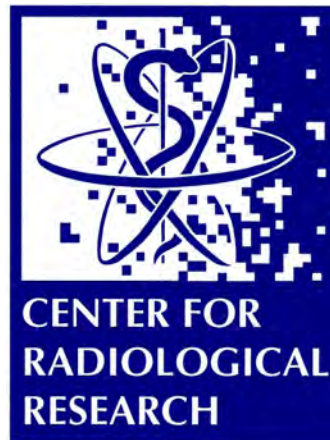
1. Pellmar, T.C. and S. Rockwell, *Priority list of research areas for radiological nuclear threat countermeasures*. Radiation research, 2005. **163**(1): p. 115-123.
2. Agency, I.A.E., *The Radiological accident in Goiânia*. 1988, International Atomic Energy Agency: Vienna.
3. Paul, S. and S.A. Amundson, *Development of gene expression signatures for practical radiation*

- biodosimetry*. *Int J Radiat Oncol Biol Phys*, 2008. **71**(4): p. 1236-1244.
4. Benjamini, Y. and Y. Hochberg, *Controlling the False Discovery Rate - a Practical and Powerful Approach to Multiple Testing*. *Journal of the Royal Statistical Society Series B-Methodological*, 1995. **57**(1): p. 289-300.
  5. Amundson, S.A., *Functional genomics in radiation biology: a gateway to cellular systems-level studies*. *Radiat Environ Biophys*, 2008. **47**(1): p. 25-31.
  6. Huang, D.W., B.T. Sherman, and R.A. Lempicki, *Systematic and integrative analysis of large gene lists using DAVID bioinformatics resources*. *Nat Protoc*, 2009. **4**(1): p. 44-57.
  7. Huang, D.W., B.T. Sherman, and R.A. Lempicki, *Bioinformatics enrichment tools: paths toward the comprehensive functional analysis of large gene lists*. *Nucleic Acids Res*, 2009. **37**(1): p. 1-13. ■



**Top row** (l to r): Shanaz Ghandhi, Helen Turner; Howard Lieberman; Nils Rudqvist. **Second Row** (l to r): Guy Garty, Eric Hall; Jingsong Yuan, Helen Turner; Sally Amundson. **Third row** (l to r): Charles Geard, David Brenner; David Brenner, Norm Kleiman, Aesis Luna. **Bottom row** (l to r): Guy Garty, Tom Hei, Andrew Harkin (photobomber), Margaret Zhu.

# THE RADIOLOGICAL RESEARCH ACCELERATOR FACILITY (RARAF)



# THE RADIOLOGICAL RESEARCH ACCELERATOR FACILITY

An NIH-Supported Resource Center

[WWW.RARAF.ORG](http://WWW.RARAF.ORG)

Director: David J. Brenner, Ph.D., D.Sc.

Associate Director: Gerhard Randers-Pehrson, Ph.D.

## RESEARCH USING RARAF

The “bystander” effect - the response of cells that are not directly irradiated but are in close contact with, nearby, or only in the presence of irradiated cells, has been the focus for many of the biological studies at RARAF over the past two decades. Both the Microbeam and the Track Segment Facilities continue to be utilized in various investigations of this response to radiation exposure. This year the number of biological experiments investigating the mechanism(s) by which the effect is transmitted has declined somewhat, with newer

experiments starting to use the Microbeam Facility to examine damage to sub-cellular structures (e.g., mitochondria, telomeres, and specific chromosomes) and other radiation effects. Research into bystander effects *in vivo* continued this past year with irradiations of the ears of mice.

## Experiments

Listed in Table 1 are the experiments performed using the RARAF Singletron between January 1 and December 31, 2015, and the number of shifts each was run in this period. Fractional shifts are assigned when experimental

**Table 1.** Experiments Run at RARAF January 1 - December 31, 2015

Exp No.	Experimenter	Institution	Exp. Type	Title of Experiment	Shifts Run
110	Tom K. Hei	CRR	Biology	Identification of molecular signals of alpha particle-induced bystander mutagenesis	48.5
113	Alexandra Miller	AFRRI	Biology	Role of alpha particle radiation in depleted uranium-induced cellular effects	3
146	Michael Bardash	QEL	Physics	Development of a solid state microdosimeter	1
163	Lubomir Smilenov, Anna Saran	CRR/ENEA	Biology	Mouse ear irradiation of connexin deficient mice	2
164	Lubomir Smilenov	CRR	Biology	Mouse irradiation using IND spectrum neutrons	2
165	Helen Turner	CRR	Biology	Mouse/blood irradiation using IND spectrum neutrons	1
172	Susan Bailey	Colorado State University	Biology	Targeted telomeric damage and the persistent DNA damage response	2
173	Ekaterina Dadachova	Albert Einstein College of Medicine	Biology	Comparison of fungal cell susceptibility to external alpha particle beam radiation versus alpha particles delivered by <sup>213</sup> Bi-labeled antibody	3.5
174	Gordana Vunjak-Novakovic	Columbia University	Biology	Micro proton induced x-ray emission of bone/cartilage grown on artificial scaffolds	2
175	Constantinos Broustas	CRR	Biology	Mouse/blood irradiation using IND spectrum neutrons	1
176	Art Pallone	Norwich University	Physics	Development of CCD sensors for ion beam measurements and dosimetry	1
177	Kathryn Held, Hongning Zhou	Harvard Medical School/CRR	Biology	Induction of superoxides in bystander cells	1
178	Alejandro Carabe-Fernandez	University of Pennsylvania	Physics	Microdosimetric and radiobiological characterization of new Si-based microdosimeters using particle microbeams	2
179	John Ng	Cornell University	Biology	Effect of LET on immunotoxicity	2.5

time is shared among several users (e.g., track segment experiments) or when experiments run for significantly more or less than an 8-hour shift. Use of the accelerator for experiments was 37% of the regularly scheduled time (40 hours per week). Fourteen different experiments were run during this period. Four experiments were undertaken by members of the CRR, supported by grants from the National Institutes of Health (NIH), including the National Cancer Institute (NCI), the National Institute of Allergies and Infectious Diseases (NIAID) and the National Institute of Biomedical Imaging and Bioengineering (NIBIB). Eight experiments were performed by external users, supported by grants and awards from the Department of Energy (DoE), the Department of Defense (DoD), the NIH, the National Aeronautics and Space Administration (NASA), the National Science Foundation (NSF), the National Cancer Institute (NCI), and internal funding from the Georgetown University Department of Radiation Medicine. Two experiments were collaborations between RARAF/CRR staff and outside users. Brief descriptions of these experiments follow.

A group led by Tom Hei of the CRR continued experiments investigating the effects of cytoplasmic irradiation and the radiation-induced bystander effect (Exp. 110). Using the Microbeam Facility, Jinhua Wu investigated mechanisms by which cytoplasmic stimuli modulate mitochondrial dynamics and functions in human small airway epithelial cells (SAECs). Their recent studies have shown that mitochondrial fragmentation induced by targeted cytoplasmic irradiation of human SAE cells is mediated by up-regulation of dynamin-regulated protein 1 (DRP1), a mitochondrial fission protein. To further explore the role of mitochondria in modulating the biological activities of high-LET radiation, autophagy in SAECs was examined. Autophagy was observed as early as 30 minutes after cytoplasmic irradiation with 10 alpha particles and peaked at 4 hours based on LC3B punctae formation. Sequestration of free radicals by DMSO abolished the induction of LC3B punctae formation, suggesting that activation of autophagy is free radical-dependent. Autophagy led to an increase of  $\gamma$ -H2AX foci that was dramatically reduced by chloroquine (CQ) or 3-methyladenine (3-MA), which are known inhibitors for autophagy. The DRP1 inhibitor mdivi-1 also significantly reduced autophagy, indicating that it plays a key role in activation of autophagy. DRP1 knockout HCT116 cells showed little or no autophagy after cytoplasmic irradiation, further confirming its role in autophagy induction. DRP1-dependent up-regulation of autophagy-initiating protein beclin-1 was also observed. Finally, a sustained activation of ERK was detected, suggesting potential involvement of the non-canonical MEK/ERK pathway in regulating autophagy in cytoplasmic irradiated cells.

Alexandra Miller of the Armed Forces Radiobiological Research Institute (AFFRI) continued

studies using the Track Segment Facility to evaluate depleted uranium (DU) radiation-induced carcinogenesis and other late effects using *in vitro* models and to test safe and efficacious medical countermeasures (Exp. 113). One objective of this study has been to determine if phenylbutyrate (PB), a histone deacetylase inhibitor and epigenetic effector, can mitigate neoplastic cell transformation induced by different qualities of radiation, and if so, to identify which adverse epigenetic mechanisms are involved and potentially reversed by PB. This also would be of interest for Space missions and alpha particle exposures from accidental releases. Track segment irradiations with  $^4\text{He}$  ions were performed on human small airway epithelial cells (SAECs) and growth rate, transformation, and genomic instability were quantified. Irradiation of SAECs overcame contact inhibition and caused an increase in transformation frequency and induction of gene amplification, i.e., genomic instability. Treatment with PB following irradiation resulted in a significant suppression of transformation frequency and gene amplification. Studies are ongoing evaluating the impact of PB treatment on changes in DNA methylation caused by irradiation with  $^4\text{He}$  ions.

In a second part of the study, rodent bone marrow stromal cells were irradiated and co-cultured with unirradiated hematopoietic progenitor cells (FDC-P1). The FDC-P1 cells were monitored for their ability to grow in agar to assess neoplastic transformation. The data have demonstrated that co-culturing irradiated bone marrow stromal cells with FDC-P1 cells causes an increase in neoplastic transformation of FDC-P1 cells that involves the process of cell-cell communication. Additional mechanistic studies have shown that antioxidant processes are also involved in the non-targeted effect in FDC-P1 cells. Further studies with this model are ongoing, and are evaluating the involvement of non-targeted effects in the response to multiple exposures at low doses (5 cGy).

Tests of a solid-state microdosimeter were made by Michael Bardash of QEL, Inc. He has designed and constructed an electronic device with an active area of a few  $\mu\text{m}^2$  and a thickness of less than one  $\mu\text{m}$ , on the order of the dimensions of a cell nucleus. The Track Segment Facility was used to irradiate the device with 4 He ions, which, because of their high LET, would deposit enough energy in the very thin device to make a measurable signal. While results were inconclusive, Michael will be returning in 2016 to continue the experiments with improved devices.

We have expanded the mouse ear irradiation protocols this year with a collaboration with Anna Saran of the Laboratory of Radiation Biology and Biomedicine at ENEA, Rome, using mice that are deficient in connexin 43, which she has developed. Using a mouse ear model, we have shown bystander effects induced by microbeam irradiation in an intact living mammal (Figure 1;

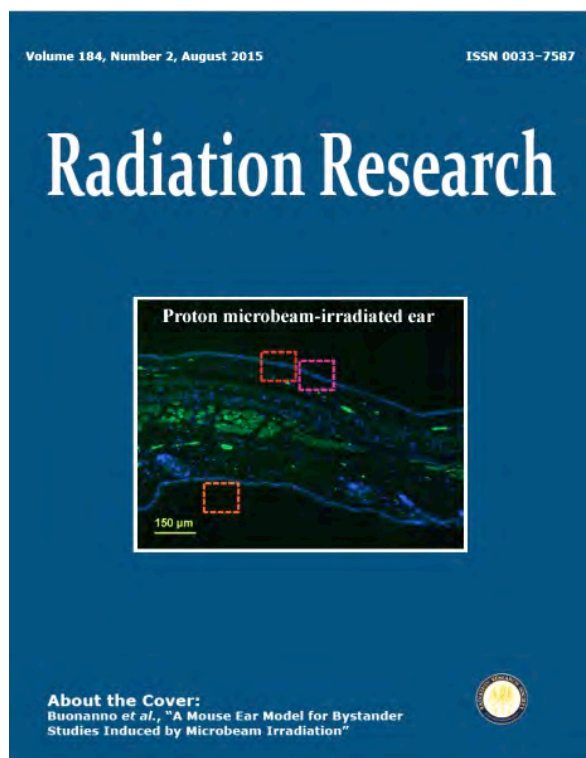


**Figure 1.** Publication of *in vivo* microbeam studies on the mouse ear featured on the cover of *Radiation Research*. Reproduced here with permission from the journal.

Buonanno, M., et. al. A Mouse Ear Model for Bystander Studies Induced by Microbeam Irradiation, *Radiat Res.* 2015 Aug;184(2):219-25.) Recent findings suggest gap junctions, which are communicating channels between adjacent cells, may be involved in the *in vivo* bystander effect and that certain proteins in gap junctions called "connexins" are required. Specifically, connexin 43 (cx43) was identified as critical to the radiation induced bystander effects: knocking out cx43 blocks the bystander effect *in vitro*. However, knocking out cx43 is embryonically lethal in mice. Dr. Saran has established a mouse model in which one of the two cx43 alleles is defective, leading to substantial reduction in gap junction function. Unlike the connexin 43 knockout mice, these mice are viable and fertile. The cx43<sup>+/-</sup> mice and their wild type counterpart were shipped from Rome and delivered to RARAF. We followed our mouse ear microbeam irradiation protocol, in which only selected cells of the ear are irradiated with a 30-micron diameter proton microbeam to create clear regions of irradiated and non-irradiated tissue. Thirty minutes after the exposure, both irradiated and non-irradiated ear tissues were examined for evidence of specific radiation-induced biomarkers of DNA damage (i.e.  $\gamma$ H2AX foci formation). As expected, irradiation of a small number of cells of the mouse ear elicited a bystander response in both wild type mice and cx43<sup>+/-</sup> mice, however in the latter, the extent of the response was significantly less.

Lubomir Smilenov, Helen Turner, and Constantinos Broustas made use of our improvised nuclear device

(IND)-spectrum neutron irradiation system to study the effects of the IND-spectrum irradiation of mice and blood samples. This work is supported by the Columbia Center for High-throughput Minimally-invasive Radiation Biodosimetry as a NIAID-funded Center for Medical Countermeasures against Radiation. Mice were irradiated with up to 2 Gy of neutrons, with comparison mice given up to 4 Gy of x-rays using the Westinghouse orthovoltage x-ray system at RARAF. Some mice were also given 1 Gy of neutrons and then a secondary dose of x-ray to simulate a mixed field. The mice were sacrificed 1 to 7 days after the exposure, and blood was collected and either scored for micronuclei and  $\gamma$ H2AX foci, or processed for global RNA expression measurements. The animals were also held in metabolic cages for collection of urine and feces, which were processed for metabolomics. Human donor blood samples were also exposed to up to 2 Gy of IND-spectrum neutrons and 4 Gy of x-rays and assessed for the same endpoints as the mouse blood.

Susan Bailey from Colorado State University works on the effects of telomere length and damage on the health and viability of cells. She makes use of the RARAF microbeam to target and irradiate telomeres in the cells. The work performed this year focused on telomere degradation following targeted nuclear irradiation. The experiment also was used by the RARAF staff as a baseline test for the imaging of telomeres using the labels of interest to Dr. Bailey with the new super resolution microscope, as that facility will become available early next year.

Ekaterina Dadachova at the Albert Einstein College of Medicine, working with Igor Shuryak of the CRR, has been developing radioimmunotherapy (RIT) for treatment of *Cryptococcus neoformans* infections using <sup>213</sup>Bi-labeled antibodies specific to the cryptococcal capsule. She is performing a comparison of fungal cell susceptibility to external  $\alpha$ -particle beam radiation versus  $\alpha$  particles delivered by the bismuth-labeled antibodies (Exp. 173). Fungi grown to stationary phase in defined minimal medium were suspended in solution. As has been done in past experiments, the solution was formed into a thin layer with a known uniform thickness under a cover slip. The fungi were irradiated with doses of 1 to 80 Gy of 125 keV/ $\mu$ m <sup>4</sup>He ions. Results so far indicate that: a) *C. neoformans* is more sensitive to external beam  $\alpha$  particles than to external  $\gamma$  rays; b)  $\alpha$  particles delivered by the capsule-binding antibodies may be more cytotoxic to the *C. neoformans* cells than external beam  $\alpha$  particles. This work has expanded in the past year to include proteomic, transcriptomic and metabolomic research into the radioresistance seen in these fungi.

Gordana Vunjak-Novakovic uses our charged particle microbeam facilities for PIXE analysis of cartilage-bone interfaces looking at chemical compositions of the two materials as they interface and progress through the life cycle. The change of concentration of calcium in both

materials through the development of arthritis is of high interest in arthritis care and prevention. This past year, the neutron microbeam line has been modified to allow for this work to be performed at that endstation. This allows higher beam currents on target for more rapid data acquisition. Samples from both sacrificed animals and laboratory constructs on artificial scaffolds are being employed in these studies. The design of the artificial scaffolds could lead to the ability to grow in the lab bone and cartilage replacements from a patient's own stem cells for joint reconstruction and repair.

Art Pallone, working with Alan Bigelow, made use of our microbeam to test CCD sensors as potential alpha particle detectors for ion beam optics and parameterization. Using a pixelated detector, with suitably sized pixels and energy resolution, it is possible to determine the size and particle energy of a charged particle beam. Dr. Pallone is interested in the potential to use simple web cam CCDs as radiation sensors for low cost teaching opportunities and experimental platforms.

Kathryn Held, working with Hongning Zhou of the CRR, used the microbeam facility for gathering preliminary data on the induction of superoxides in bystander cells at early times following irradiation (5-20 minutes). These experiments were successful and we hope Dr. Held will return in 2016 for additional experiments.

Dr. Carabe-Fernandez of the University of Pennsylvania is developing silicon 3D radiation microsensor arrays, capable of quantifying deposited energies within micron-sized targets. Compared to traditional tissue equivalent proportional counters (TEPCs), these detectors do not require a gas supply, operate at low voltages, are light and easily portable, and have a fast response. The goal of this project is to use the targeting ability of the microbeam to characterize individual microsensors within the microdosimeter array. Different microdosimeters of different dimensions (diameter, depth and pitch) representing different cell types will be exposed, and the derived relative biological effectiveness (RBE) from mechanistic biophysical models (e.g. Microdosimetric Kinetic Model (MKM) and Local Effect Model (LEM)) will be calculated. The experimental RBE obtained from clonogenic assays of individual cells exposed to the microbeam will also be obtained and compared to that obtained from the microsensors. This will allow the investigators to: 1) characterize the microdosimetric properties of each individual microsensor as well as study crosstalk between the sensors in an array; 2) validate the microsensors as viable instruments to calculate RBE; and 3) determine new features required to develop current microsensor technology to a new generation that allows more precise RBE measurements.

John Ng began preliminary work on the effects of charged particles at different LETs (10 – 50 keV/ $\mu\text{m}$ ) on immunotoxicity in cancer cell lines. This exploratory work builds off his experience in clinical cancer



**Figure 2.** Superconducting solenoid installation. A) Dr. Harken and Mr. Farrell positioning the bottom field restricting plate. B) Delicately lifting the solenoid down to the second mezzanine level at RARAF. C) Drs. Randers-Pehrson and Bigelow positioning the solenoid on the restricting plate and table. D) Alignment of the solenoid to the bottom restricting plate. E) Final testing assembly of the solenoid with both restricting plates, cooling lines, monitoring sensors, current lines, and vacuum support connected.

treatments using targeted particle therapy as one of the main irradiation protocols. The aim is to determine effects of targeted radiotherapy that can be combined with immunotherapy to increase the efficacy of treatment of many types of cancers. The results are promising and John anticipates continuing this project in 2016.

#### DEVELOPMENT OF FACILITIES

Development continued on a number of extensions of our irradiation facilities and capabilities for imaging and irradiating biological specimens:

- Focused particle microbeams
- Focused x-ray microbeam
- Neutron microbeam
- IND-spectrum neutron source

- Advanced imaging systems
- Targeting and manipulation of cells
- New cell analysis tools
- Small animal systems

### Focused particle microbeams

The electrostatically focused microbeam was consistently operated with a 1-2  $\mu\text{m}$  diameter beam and a 0.5  $\mu\text{m}$  diameter beam when called for by an experiment. We have continued the protocol of performing a test run of the microbeam system on the evening preceding an irradiation day. These test runs have become a vital point of development for new techniques and training of operators for the microbeam system.

The Super-Microbeam development continued with the design and purchase of the super conducting solenoid magnet from Cryomagnetics, Inc. We took possession of the solenoid this year and performed verification and field-testing of the magnet (Figure 2). The construction of the Stimulated Emission Depletion (STED) super resolution microscope extension continued with the integration of the laser introduction pathway for the STED depletion laser co-alignment. The interface of the STED development with the multi-photon microscope was begun with a low power alignment laser. The 2W continuous wave (CW) high power laser was purchased and will be installed for imaging in early 2016.

The permanent magnet microbeam (PMM) was used as a secondary charged particle microbeam endstation for the development of our Flow and Shoot (FAST) microfluidic irradiation system, the capillary electrophoresis (CE) system, and the automated cell picking system. The PMM has all of the irradiation capabilities of the electrostatic microbeam except the sub-micron beam spot size. The PMM is also free from the electrical breakdown potential from failures of the vacuum window, making it an ideal initial testbed for all our new technologies.

### Focused x-ray microbeam

The x-ray microbeam uses characteristic Ti  $K\alpha$  x rays (4.5 keV) generated by proton-induced x-ray emission (PIXE). PIXE produces a nearly monochromatic x-ray source (extremely low bremsstrahlung) of the characteristic target x-ray energy. This allows these x-rays to be focused using a Fresnel zone plate to a spot size of 5  $\mu\text{m}$  from a proton beam size of  $\sim 50$   $\mu\text{m}$  in diameter.

The x-ray microbeam is stationed on a dedicated horizontal beamline at RARAF with the x-ray beam focused up in the vertical direction with the same microscope and stage geometry of the charged particle microbeam systems, allowing for easy intercomparison between the microbeam types. While minimally used this year, the x-ray microbeam remains available for users.

### Neutron microbeam

The neutron microbeam at RARAF is the world's first microbeam that can irradiate single cells with neutrons.

Incident protons near the reaction threshold (1.881 MeV) of the  ${}^7\text{Li}(p,n){}^7\text{Be}$  reaction generate neutrons that are severely forward coned in the laboratory frame of reference. By placing the target cells close to the lithium target it is possible to limit this cone to a single cell target. The Neutron microbeam uses a proton beam at 1.886 MeV focused to 8  $\mu\text{m}$  on the lithium target. This results in a neutron spot size at the cell targets of 20  $\mu\text{m}$  diameter with neutron energies ranging from 10-50 keV and a dose rate of 27 mGy/min.

The neutron microbeam is located in the accelerator bay at RARAF on a dedicated horizontal beam line. The proton beam is focused using a single quadrupole quadruplet with the spot size measured using an ionization counter and a knife-edge occlusion measurement. The center of the proton beam, visualized using a thin scintillator, is the center of the neutron beam. The proton beam measurements are made with a thin Havar metal window, which is exchanged with the lithium target for diagnostics.

The neutron spot size is measured using CR-39 track-etched plastic coated with a thin layer of lithium carbonate heavily enriched with  ${}^6\text{Li}$ . The neutrons interact with the  ${}^6\text{Li}$  through the  ${}^6\text{Li}(p,\alpha){}^3\text{H}$  reaction, producing energetic  $\alpha$  and  ${}^3\text{H}$  recoils that are easily observable as pits in the etched CR-39 using a microscope.

### IND-spectrum neutron source

The improvised nuclear device (IND)-spectrum irradiator was completed in 2014 and was used extensively this past year to irradiate both whole blood and small animals.

This fast neutron irradiation source was designed to generate the neutron spectrum seen from the "Little Boy" atomic bomb at Hiroshima at 1.5 km from ground zero, as representing an energy spectrum and distance of relevance to detonation of an IND. This field is generated through the reactions  ${}^9\text{Be}(d,n){}^{10}\text{B}$  and  ${}^9\text{Be}(p,n){}^9\text{B}$  using a mixed beam of monoatomic, diatomic and triatomic protons and deuterons. The RARAF Singletron uses a gas mixture of hydrogen to deuterium of 1:2, which feeds into the RF plasma ion source. This irradiator is on the  $0^\circ$  beam line, as any bending of the beam to get to a target would separate the six different beams and prevent the spectrum generation.

The neutron spectrum was verified using two proton recoil detection systems. A 2" diameter 2" thick liquid scintillator for energies  $>1$  MeV and a 1.5" diameter spherical gas proportional counter with 3 atmospheres of hydrogen gas for  $<1$  MeV. Using MCNPX-PoliMi Monte Carlo simulations to calculate the exact response functions of the detectors, it is possible to reconstruct the spectrum from the readout of the detectors in the neutron field.

The dose rate has been calibrated to deliver 0.25 Gy of neutrons in 10 minutes (with a gamma-ray contribution of

an additional 1%). This dose rate allows the delivery of 1 Gy in less than 1 hour.

### Advanced imaging systems

We continue to develop new techniques to obtain two- and three-dimensional images of cells, reduce UV exposure and improve resolution.

#### *Real-time imaging*

Short-term biological effects that happen within seconds to the first few minutes after irradiation set the stage for later effects. Real-time imaging and observation of the short-term effects will give insight to experimenters into their endpoints. Techniques have been developed using our EMCCD camera and our fast switching SOLA LED light source to acquire images with several frames per second to observe the short-term effects of irradiation on a timescale of minutes to hours following irradiation.

#### *Multi-photon microscope with the UV microspot*

The multi-photon microscope was developed several years ago and integrated with the charged particle microbeam irradiator. This microscope, through the long wavelength incident laser, allows in depth imaging of 3D tissues and small animals, such as *C. elegans* and zebrafish embryos. This is achieved using the sectioning capability of the multi-photon effect where the photon density increases to generate constructive interference producing a 3D voxel of photons with half the wavelength and twice the energy, which can locally excite fluorophores and/or other fluorescent effects (e.g. auto fluorescence and second-harmonic generation). This 3D voxel is then scanned through a single layer and stepped through the sample using the nanoprecision z-stage, generating a stack of 3D slices of the sample that are reconstructed into 3D images.

If the intensity of the laser is increased, there can be a 3-photon interference at the area of constructive interference, resulting in a voxel with 1/3 of the wavelength (and three times the energy), generating a voxel of UV light that is used as the UV microspot. The UV microspot can induce localized damage within a 3D target.

#### *STED*

We are developing a Stimulated Emission Depletion (STED) super resolution microscope system with optical resolution of 75 nm in combination with our super microbeam to achieve compatible imaging resolution and beam spot size. The STED system at RARAF builds off the multi-photon microscope using it as the primary excitation laser. A second CW laser is added in parallel with the multi-photon laser. Using polarization optics, the second laser projects a donut shaped point spread function around the excitation spot of the multi-photon system. With proper selection of the second laser wavelength and sufficient intensity, the second laser will deplete the fluorescent states around the excitation spot allowing

emission of fluorescence only from the center of the donut, which will be reduced to nanometer sizes.

The use of STED imaging on live cells using a water immersion lens was shown to be possible using the STED super resolution microscope at Dr. Liao's Lab in the Mechanical Engineering Department. This system, while not optimized for water immersion optics, gave a resolution of <100 nm.

The STED development continues on the microbeam endstation. The second laser introduction pathway has been completed and the initial co-alignment of the STED laser beam with the multi-photon laser has been performed. We have purchased the 2W CW laser for the STED imaging system. It will be installed in early 2016, at which time imaging tests will commence.

### Targeting and manipulation of cells

We have the capability to fabricate microfluidic devices in hard plastics, such as acrylic, and soft plastics, such as polydimethylsiloxane (PDMS). The micro-milling machine installed at RARAF has software to produce parts designed using the Solid Works computer-aided design (CAD) program. This system has been used to manufacture the single-cell dispenser and the microfluidic chips for the cell sorter and microFACS systems (described below). Several new microfluidic systems are being developed to target, manipulate, and analyze cells.

#### *FAST*

The Flow And ShooT (FAST) microfluidic irradiation system has continued in development. This system flows non-adherent cells, such as lymphocytes, through a microfluidic channel over the microbeam window, where the Point and Shoot magnetic deflector tracks, targets and irradiates the cells as they pass the beam location.

We have modified the design of the FAST chip to allow more reliable and convenient incorporation into the microbeam endstation. Previously, we had tested various all-PDMS or PDMS adhered to thin plastic foil designs and found them to be unreliable. In particular, it was difficult to reliably connect them to other devices (such as a syringe pump or a cell dispenser) while providing clearance for an objective lens and particle detector above and the beamline below.

The new design (Figure 3) involves two silicon pieces that have been selectively etched to leave regions of 1000 nm thick silicon nitride supported in a silicon frame (similar to the silicon nitride exit windows already used for microbeam irradiations). A layer of adhesive, approximately 50 microns thick, is patterned on top of one of the silicon pieces to create a flow channel across the window. The other silicon piece is flipped over to attach to the first chip and act as a lid to the channel. Proper alignment of the windows in each of the two silicon pieces with the defined flow region patterned out of the adhesive creates an ultrathin channel for imaging

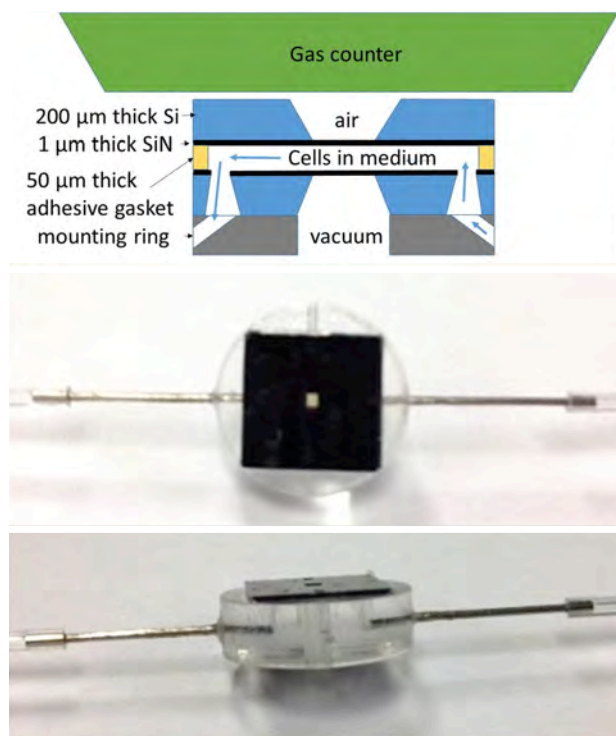


**Figure 3.** New design for the FAST microfluidic irradiation system shown in schematic (top), top view (middle) and side view (bottom).

and irradiation. This design allows for the bottom silicon piece to act as the microbeam exit window for maximum accuracy of the point and shoot irradiations. Furthermore, the thin microfluidic environment has fluidic access ports that integrate into a custom designed snout to eliminate fluidic connections on the top of the chip. The channel and the SiN layers are thin enough for particles to pass completely through the chip and into the gas ionization counter mounted on the microscope objective. This new design has been successfully tested with a wide range of flow rates and has shown good performance with the existing Flow and Shoot irradiation setup.

#### Cell picker

We have incorporated a semi-automated cell picker into the Permanent Magnet Microbeam endstation. Joystick control of the picker has been integrated into the microbeam software, allowing the user to select an individual cell and remove it from the microbeam dish post irradiation.

#### Cell dispenser

Development of the automated cell dispenser has continued with a focus on combining the sensing ability, the dispensing mechanism, and controlled fluid flow into a single device. Much of the work up to this point has been in developing each of these separately but many challenges were faced in combining these abilities into a single device. The current iteration of the dispensing chip combines the superior sensing properties of gold electrodes on a glass surface with a polymethyl

methacrylate (PMMA) structure that can be machined to stably hold a high-pressure solenoid valve. A layer of double-sided adhesive is patterned and placed between the glass layer and the PMMA layer to define the fluid flow channel while also holding the assembly together.

A key design change in the past year has been in turning the dispensing direction so that it is perpendicular to the horizontal fluid path. The new design dispenses a droplet through the glass slide in a vertical direction using a hole drilled through it, which makes accurate droplet placement easier. The detection mechanism, involving sensing impedance differences across a set of three electrodes, remains the same as in previous versions and is still used to trigger a dispensing event. Work continues with testing for consistent droplet volume and accurate droplet dispensing location. With the improved design we are able to begin testing our ability to reliably dispense a single cell.

#### MicroFACS

The microfluidic Fluorescence-Activated Cell Sorting (microFACS) system has continued development to combine flow cytometry and sorting with our other microfluidic irradiation and dispensing technologies.

The microFACS system uses Dean vortex drift flow focusing to entrain the samples into a sheath flow focused column for flow cytometry detection in the main channel. The sample is illuminated with a laser through fiber optic coupling with the fluorescent output also detected through fiber optic coupling. The combination of fiber optics and microfluidics will allow for the microFACS to be coupled to the other microfluidic systems in close proximity to the microbeam endstations.

Computerized data acquisition and scoring were integrated into the microFACS during 2015. While still being optimized, this has allowed better quantification of the quality of the data being generated in the microFACS system, and represents a significant advance toward accurate scoring of samples. The design of the flow system to generate lower speeds to match the FAST irradiator and other systems also continued. The channel sizes and length of curved sections for Dean vortex drift flow focusing were adjusted as results of output speed and scoring quality tests dictated.

#### AMOEBAs

An automated system for precise regulation and control of environmental conditions for biological samples before, during, and after microbeam irradiations, our Automated Microbeam Observation Environment for Biological Analysis (AMOEBAs) system will establish, maintain and change conditions (e.g. temperature, pH, pCO<sub>2</sub>, drug concentrations) in the culture as our microbeam users require. This system will provide feedback for automated fluid-flow control systems for all of the needed parameters through a distributed electronics control packaged.

The AMOEBA is being designed in two comparable systems: the standard AMOEBA for dish based microbeam experiments and the  $\mu$ AMOEBA for microfluidics based irradiation experiments. Initial testing has verified that we can control temperature ( $37 \pm 1$  °C) and pH over long periods with minimal feedback circuitry. We have begun using these basic controls for monitoring cell kinetics involving DNA repair, cell-cycle progression and chromosomal domain dynamics.

### New cell analysis tools

#### CE-LIF

We have finished construction and begun testing of our Capillary Electrophoresis – Laser Induced Fluorescence (CE-LIF) system (Figure 4) to provide our users with the capability of measuring reactive oxygen species within individual cells immediately after irradiation. The nanoliter input volumes make this system ideal for single-cell, small-scale biochemical analyses.

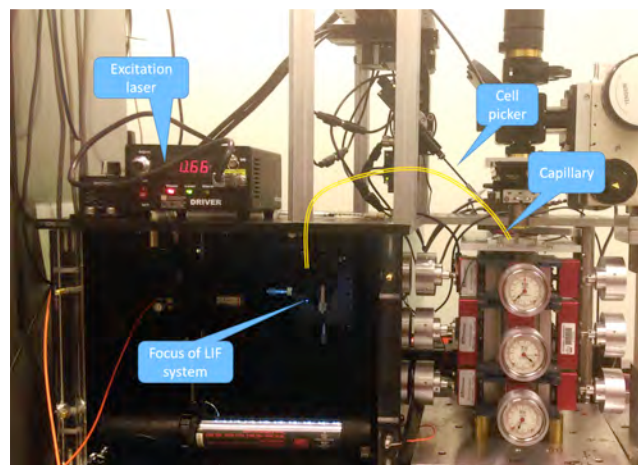


**Figure 4.** The current CE-LIF system at RARAF.

The CE-LIF system at RARAF (Figure 4): The grounded end of a 50  $\mu$ m bore capillary is brought to the cell using the semi-automated cell picker. Once a cell is aspirated into the capillary, 20-30kV is applied between the grounded end of the capillary and the Laser Induced Fluorescence (LIF) system, enclosed in a light tight insulating box. This results in two superimposed flow modalities experienced by the analytes: (1) Electrophoretic flow, responsible for separating the analytes by charge and Stokes radius; (2) Electroosmotic flow, which drives the buffer and analytes (regardless of polarity) toward the detector. The electroosmotic flow is much stronger than the electrophoretic flow, ensuring that all analytes will reach the detector. In the LIF system, the analytes are hydrodynamically focused into the path of a laser, with the light collected perpendicularly and detected by a high-sensitivity spectrometer. We have recently acquired a deep cooled Bayspec spectrometer, providing highly sensitive detection of fluorescent molecules.

#### Small animal systems

Investigations of radiation-induced bystander effects have been conducted in cell cultures and 3-D systems *in*

*vitro*. The next logical step was to develop and implement microbeam irradiation protocols to study effects in living organisms. We have developed a mouse ear model for *in vivo* bystander studies. With an average thickness of 250-300  $\mu$ m, this model can be used to investigate radiation-induced bystander effects with a 3-MeV proton microbeam having a range of 134  $\mu$ m.

Using gentle suction, the ear of an anesthetized mouse is flattened onto the underside of a flat plate of a custom-made holder. The flattened mouse ear is then placed over the microbeam port and cells along a line on the ear are irradiated with the proton microbeam. At chosen times after irradiation, mice are sacrificed and a punch of the ear is collected. Tissues are then fixed, paraffin-embedded and cut in 5- $\mu$ m sections perpendicularly to the direction of the line of irradiation. The sections are then analyzed for biological endpoints (i.e., formation of repair protein foci, apoptosis) as a function of the distance from the irradiated line.

### SINGLETRON UTILIZATION AND OPERATION

Table 2 summarizes accelerator usage for the past year. The nominal Singletron availability is one 8-hour shift per weekday (~248 days per year), however the accelerator is frequently run well into the evening, often on weekends, and occasionally 24 hours a day for experiments or development. Total use for experiments and development this year was 57.5% of the regularly available day shifts.

Accelerator use for radiobiology and associated dosimetry was about 125% that for last year and right at the average for the last 5 years. About 66% of the use for all experiments was for charged particle microbeam irradiations, 22% for track segment irradiations, and 12% for neutron irradiations. Approximately 26% of the experiment time was for studies proposed by external users, and 74% was for internal users.

On-line facility development and testing was about 20.5% of the available time, primarily for development and testing of multiple microfluidic and analysis tools using the PMM endstation. This was about 20% less than

**Table 2.** Accelerator Use, January 1 - December 31, 2015  
Normally Scheduled Shifts

Radiobiology and associated dosimetry	35.5%
Radiological physics and chemistry	2.5%
On-line facility development and testing	19.5%
Safety system	2.5%
Accelerator-related repairs/maintenance	0%
Other repairs and maintenance	2.5%
Off-line facility development	54%

the average over the last five years and slightly less than last year due to an emphasis on development not requiring accelerator use and previously developed systems coming into online use.

The accelerator was not opened during the calendar year of 2015. The accelerator was last opened in October of 2014 when the ion source was changed. We anticipate this will need to be performed again in early 2016 and will be timed to coincide with the reconfiguration of the microbeam.

## TRAINING

### REU

Since 2004 we have participated in the Research Experiences for Undergraduates (REU) project in collaboration with the Columbia University Physics Department. This is a very selective program that attracts highly talented participants. For 9-10 weeks during the summer each student attends lectures by members of different research groups at Nevis Laboratories, works on a research project, and presents oral and written reports on his or her progress at the end of the program. Among other activities, the students receive a seminar about and take a tour of RARAF.

The 2015 REU participant at RARAF was Leah Turner from Lehigh University. Leah worked with David Welch to fabricate a new generation of anatomically accurate mouse phantoms for use in radiation dosimetry studies (Figure 5). Along with the construction of the phantoms, Leah also helped with preliminary studies to analyze the performance of the phantoms using the Small Animal Radiation Research Platform.

### Group Training

In addition to training individuals at RARAF, staff members also participate in training courses presented at other facilities as a means of introducing microbeam concepts and experiments to a broader audience. As for the past two years, Gerhard Randers-Pehrson lectured on “High/low LET microbeams” at the NASA Space



**Figure 5.** Anatomically correct mouse phantom made by our REU student Leah Turner.

Radiation Summer School, Brookhaven National Laboratory, Upton, NY, on June 11, 2015.

### Microbeam Training Course

In 2015, we postponed our Microbeam Training Course for one year in anticipation of the microbeam renovation that began for the replacement of the electrostatic microbeam with the superconducting solenoid Super Microbeam. We will resume the Microbeam Training Course in May of 2016

## DISSEMINATION

### Web site

The RARAF website design that was created in 2013 provides clear and effective presentation while improving access to content. Functional menus (including a home page rotating-picture menu) were designed to make navigation through the content easy and interesting, with a hierarchical structure from general information, suitable for a general or non-science audience, to more-detailed technical content.

The site contains information on microbeams in general, as well as detailed technical information on our various microbeams; *in-vitro* and *in-vivo* endpoints that we use; details of available on-line and off-line imaging capabilities; microfluidic systems we are developing; other charged particle and neutron irradiation facilities available at RARAF; our on-line training course materials; publications lists; information on RARAF contacts and directions to the facility. The site is periodically updated to include new radiation facilities, cell handling and analysis capabilities, publications and other information.

### Virtual training course

We have developed an on-line virtual microbeam training course, based on the three-day microbeam training courses. This on-line course was designed to give interested physicists and biologists who could not attend in person a thorough introduction to microbeam technology.

The goal of the online course, as for the face-to-face course, is to facilitate a better understanding of how microbeams work, what experiments can be performed using a microbeam, why these experiments are of biological interest, and how to design / perform these experiments.

The on-line material consists of audio podcasts and the same handouts that the face-to-face students received. The audio of each podcast is synched with the accompanying PowerPoint slides (viewable on a video iPod, tablet, PC or Mac, or smart phone), as well as a PDF version of the slides. High-resolution video (720p, with audio) was also used to document demonstrations of all aspects of a microbeam experiment, from making microbeam dishes to irradiating cells and performing online analyses. After extensive editing, this resulted in

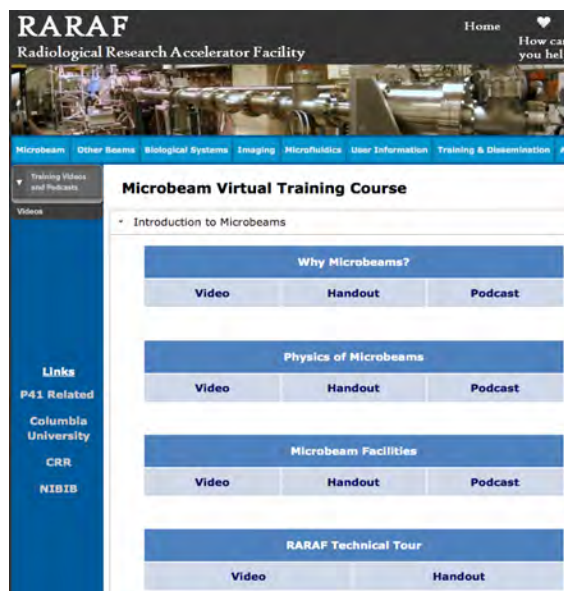


**Figure 6.** RARAF webpage for the virtual microbeam training course.

about 4½ hours of video footage. Additional material is added to the on-line course for new course presentations or lecturers. The on-line training course (Figure 6) can be accessed through the RARAF website ([www.RARAF.org](http://www.RARAF.org)) and YouTube channel (<http://www.youtube.com/user/RARAFcourses>). The videos can be viewed on any Internet-enabled device supporting YouTube format.

### Tours

In addition to training students, tours of the Facility provide a general introduction to the research performed at RARAF and the irradiation facilities that are available. This year we gave tours to more than 30 scientists, students, and members of the public.



**Figure 7.** Dr. Harken presenting at the Science-on-Hudson public lecture series at the Columbia Nevis Campus. He presented “RARAF: Radiation on the Small Scale Working on Some Big Questions”

As an example, twelve high school seniors who had been offered priority admission to Columbia as physics majors, some of whom were Columbia I. I. Rabi Scholarship winners, toured RARAF in April along with John Parsons from the Physics Department at Nevis Labs.

### Public Presentation

Dr. Harken presented “RARAF: Radiation on the Small Scale Working on some Big Questions” at the new Science-on-Hudson Series of public presentations at the Columbia University Nevis Campus (Figure 7). Science-on-Hudson is a series of public lectures for the Westchester community to come and learn about the work being performed at the Nevis Campus, of which RARAF is a part.

### PERSONNEL

The Director of RARAF is Dr. David Brenner, the Director of the Center for Radiological Research (CRR). The accelerator facility is operated by Dr. Gerhard Randers-Pehrson, the Associate Director of RARAF.

Dr. Charles Geard, a Professor Emeritus, continues to visit RARAF frequently and lend his considerable expertise.

Dr. Brian Ponnaiya, an Associate Research Scientist, is the biology advisor for RARAF. He collaborates with many of the external users and coordinates with the CRR, where he spends about half his time.

Dr. Alan Bigelow, an Associate Research Scientist, developed the multiphoton microscopy system, which includes the UV microspot irradiation facility, and worked on the development of the Raman spectroscopy and AMOEBA systems.

Dr. Guy Garty, an Associate Professor, developed the Flow and Shoot (FAST) system and is developing the CE-LIF system. He spends about half his time working on the CRR National Institute of Allergy and Infectious Diseases (NIAID) project, for which he is the project manager.

Dr. Andrew Harken, an Associate Research Scientist, is responsible for the x-ray microbeam. He is also working on the imaging of cells without stain using a highly sensitive EMCCD camera, the STED system for extremely high-resolution spectroscopy, and the microFACS system.

Dr. Yanping Xu, an Associate Research Scientist, is developing the neutron microbeam. He is also developing the accelerator-generated IND-spectrum neutron source.

Dr. Manuela Buonanno, a Postdoctoral Research Scientist in radiation biology, collaborates with many of our external users and performs the assays for the mouse ear microbeam irradiations.

Dr. David Welch, a Postdoctoral Research Scientist, is responsible for the development of new microfluidic tools and interfaces for microfluidic irradiation tools. His



**RARAF Staff:** (front row, l-r) Yanping Xu, Guy Garty, Matt England, Dennis Farrell, David Brenner, (back row, l-r) David Welch, Gerhard Randers-Pehrson, Andrew Harken, Manuela Buonanno, Brian Ponnaiya.

expertise in microfluidics has been of considerable assistance in the development of our microfluidics applications.

Mr. Matt England is a Ph.D. candidate at the University of Surrey in the U.K. and has joined the RARAF staff this year as the development of the AMOEBA system for microbeam platforms is his Ph.D. dissertation work. He is supervised locally by Drs Bigelow, Garty, and Harken.

Mr. Dennis Farrell has joined the RARAF staff on a part time basis. He is performing microbeam irradiations, serving as the Radiation Safety Officer and providing management support for the RARAF staff.

**RECENT PUBLICATIONS OF WORK PERFORMED AT RARAF**

Buonanno M, Randers-Pehrson G, Smilenov LB, Kleiman NJ, Young E, Ponnaiya B and Brenner DJ (2015) A Mouse Ear Model for Bystander Studies Induced by Microbeam Irradiation. *Radiat Res* **184**: 219-225.

Garty G, Ehsan MU, Buonanno M, Yang Z, Sweedler JV and Brenner DJ (2015) Microbeam-coupled capillary electrophoresis. *Radiat Prot Dosimetry* **166**: 188-191.

Sun H, Olsen T, Zhu J, Tao J, Ponnaiya B, Amundson SA, Brenner DJ and Lin Q (2015) A Bead-Based

Microfluidic Approach to Integrated Single-Cell Gene Expression Analysis by Quantitative RT-PCR. *RSC Adv* **5**: 4886-4893.

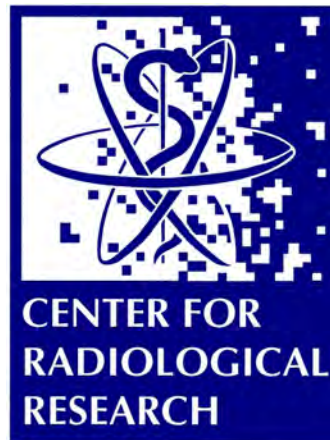
Sun H, Olsen T, Zhu J, Tao J, Ponnaiya B, Amundson SA, Brenner DJ and Lin Q (2015) A microfluidic approach to parallelized transcriptional profiling of single cells. *Microfluid Nanofluid* **19**: 1429-1440.

Xu Y, Randers-Pehrson G, Turner HC, Marino SA, Geard CR, Brenner DJ and Garty G (2015) Accelerator-Based Biological Irradiation Facility Simulating Neutron Exposure from an Improvised Nuclear Device. *Radiat Res* **184**: 404-410.

Xu Y, Randers-Pehrson G, Marino SA, Garty G, Harken A and Brenner DJ (2015) Broad Energy Range Neutron Spectroscopy using a Liquid Scintillator and a Proportional Counter: Application to a Neutron Spectrum Similar to that from an Improvised Nuclear Device. *Nucl Instrum Methods Phys Res A* **794**: 234-239.

Xu Y, Zhang B, Messerli M, Randers-Pehrson G, Hei TK and Brenner DJ (2015) Metabolic oxygen consumption measurement with a single-cell biosensor after particle microbeam irradiation. *Radiat Environ Biophys* **54**: 137-144. ■

# PUBLICATIONS



## Publications

- Beitler JJ, Bentzen SM and Hall EJ (2015) In reply to Boon et al. *Int J Radiat Oncol Biol Phys* **91**: 456-457.
- Brenner DJ (2015) Should we worry about inherited radiation risks? *Lancet Oncol* **16**: 1275-1276.
- Brenner DJ, Chao NJ, Greenberger JS, Guha C, McBride WH, Swartz HM and Williams JP (2015) Are We Ready for a Radiological Terrorist Attack Yet? Report From the Centers for Medical Countermeasures Against Radiation Network. *Int J Radiat Oncol Biol Phys* **92**: 504-505.
- Buonanno M, Randers-Pehrson G, Smilenov LB, Kleiman NJ, Young E, Ponnayia B and Brenner DJ (2015) A Mouse Ear Model for Bystander Studies Induced by Microbeam Irradiation. *Radiat Res* **184**: 219-225.
- Dong C, He M, Tu W, Konishi T, Liu W, Xie Y, Dang B, Li W, Uchihori Y, Hei TK and Shao C (2015) The differential role of human macrophage in triggering secondary bystander effects after either gamma-ray or carbon beam irradiation. *Cancer Lett* **363**: 92-100.
- Garty G, Ehsan MU, Buonanno M, Yang Z, Sweedler JV and Brenner DJ (2015) Microbeam-coupled capillary electrophoresis. *Radiat Prot Dosimetry* **166**: 188-191.
- Garty G, Bigelow AW, Repin M, Turner HC, Bian D, Balajee AS, Lyulko OV, Taveras M, Yao YL and Brenner DJ (2015) An automated imaging system for radiation biodosimetry. *Microsc Res Tech* **78**: 587-598.
- Ghandhi SA, Smilenov LB, Elliston CD, Chowdhury M and Amundson SA (2015) Radiation dose-rate effects on gene expression for human biodosimetry. *BMC Med Genomics* **8**: 22.
- Ghandhi SA, Weber W, Melo D, Doyle-Eisele M, Chowdhury M, Guilmette R and Amundson SA (2015) Effect of 90Sr internal emitter on gene expression in mouse blood. *BMC Genomics* **16**: 586.
- Gong X, Ivanov VN and Hei TK (2015) 2,3,5,6-Tetramethylpyrazine (TMP) down-regulated arsenic-induced heme oxygenase-1 and ARS2 expression by inhibiting Nrf2, NF- $\kappa$ B, AP-1 and MAPK pathways in human proximal tubular cells. *Arch Toxicol*
- Goudarzi M, Weber WM, Chung J, Doyle-Eisele M, Melo DR, Mak TD, Strawn SJ, Brenner DJ, Guilmette R and Fornace AJ (2015) Serum Dyslipidemia Is Induced by Internal Exposure to Strontium-90 in Mice, Lipidomic Profiling Using a Data-Independent Liquid Chromatography-Mass Spectrometry Approach. *J Proteome Res* **14**: 4039-4049.
- Goudarzi M, Weber WM, Mak TD, Chung J, Doyle-Eisele M, Melo DR, Brenner DJ, Guilmette RA and Fornace AJ (2015) Metabolomic and lipidomic analysis of serum from mice exposed to an internal emitter, cesium-137, using a shotgun LC-MS(E) approach. *J Proteome Res* **14**: 374-384.
- Goudarzi M, Weber WM, Mak TD, Chung J, Doyle-Eisele M, Melo DR, Strawn SJ, Brenner DJ, Guilmette RA and Fornace AJ (2015) A Comprehensive Metabolomic Investigation in Urine of Mice Exposed to Strontium-90. *Radiat Res* **183**: 665-674.
- Halm BM, Franke AA, Lai JF, Li X, Custer LJ, Pagano I, Cooney RV, Turner HC and Brenner DJ (2015) Pilot study for the establishment of biomarkers for radiation damage after computed tomography in children. *Hawaii J Med Public Health* **74**: 112-119.
- Hei TK (2015) From the desk of the Editor-in-Chief. *Life Sci Space Res (Amst)* **4**: A1.
- Hei TK (2015) From the desk of the Editor-in-Chief. *Life Sci Space Res (Amst)* **6**: A1.
- Herr L, Shuryak I, Friedrich T, Scholz M, Durante M and Brenner DJ (2015) New Insight into Quantitative Modeling of DNA Double-Strand Break Rejoining. *Radiat Res* **184**: 280-295.
- Ivanov VN and Hei TK (2015) Regulation of viability, differentiation and death of human melanoma cells carrying neural stem cell biomarkers: a possibility for neural trans-differentiation. *Apoptosis* **20**: 996-1015. PMC4449821.
- Liu J, Fang H, Chi Z, Wu Z, Wei D, Mo D, Niu K, Balajee AS, Hei TK, Nie L and Zhao Y (2015) XPD localizes in mitochondria and protects the mitochondrial genome from oxidative DNA damage. *Nucleic Acids Res* **43**: 5476-5488.
- Liu L, Huang J, Wang K, Li L, Li Y, Yuan J and Wei S (2015) Identification of hallmarks of lung adenocarcinoma prognosis using whole genome sequencing. *Oncotarget* **6**: 38016-38028.
- Liu Y, Kobayashi A, Fu Q, Yang G, Konishi T, Uchihori Y, Hei TK and Wang Y (2015) Rescue of Targeted Nonstem-Like Cells from Bystander Stem-Like Cells in Human Fibrosarcoma HT1080. *Radiat Res* **184**: 334-340.
- Liu Y, Kobayashi A, Maeda T, Fu Q, Oikawa M, Yang G, Konishi T, Uchihori Y, Hei TK and Wang Y (2015) Target irradiation induced bystander effects between stem-like and non stem-like cancer cells. *Mutat Res* **773**: 43-47.
- Lue SW, Repin M, Mahnke R and Brenner DJ (2015) Development of a High-Throughput and Miniaturized Cytokinesis-Block Micronucleus Assay for Use as a Biological Dosimetry Population Triage Tool. *Radiat Res* **184**: 134-142.
- Ng J and Shuryak I (2015) Minimizing second cancer risk following radiotherapy: current perspectives. *Cancer Manag Res* **7**: 1-11.
- Panigrahi SK, Hopkins KM and Lieberman HB (2015) Regulation of NEIL1 protein abundance by RAD9 is important for efficient base excision repair. *Nucleic Acids Res* **43**: 4531-4546.

- Paul S, Smilenov LB, Elliston CD and Amundson SA (2015) Radiation Dose-Rate Effects on Gene Expression in a Mouse Biodosimetry Model. *Radiat Res* **184**: 24-32.
- Radvoyevitch T, Sachs RK, Gale RP, Molenaar RJ, Brenner DJ, Hill BT, Kalaycio ME, Carraway HE, Mukherjee S, Sekeres MA and Maciejewski JP (2015) Defining AML and MDS second cancer risk dynamics after diagnoses of first cancers treated or not with radiation. *Leukemia*, in press.
- Sharma PM, Ponnaiya B, Taveras M, Shuryak I, Turner H and Brenner DJ (2015) High throughput measurement of gammaH2AX DSB repair kinetics in a healthy human population. *PLoS One* **10**: e0121083.
- Shuryak I, Bryan RA, Broitman J, Marino SA, Morgenstern A, Apostolidis C and Dadachova E (2015) Effects of radiation type and delivery mode on a radioresistant eukaryote *Cryptococcus neoformans*. *Nucl Med Biol* **42**: 515-523.
- Shuryak I, Carlson DJ, Brown JM and Brenner DJ (2015) High-dose and fractionation effects in stereotactic radiation therapy: Analysis of tumor control data from 2965 patients. *Radiother Oncol* **115**: 327-334.
- Shuryak I and Dadachova E (2015) New Approaches for Modeling Radiopharmaceutical Pharmacokinetics Using Continuous Distributions of Rates. *J Nucl Med* **56**: 1622-1628.
- Sun H, Olsen T, Zhu J, Tao J, Ponnaiya B, Amundson SA, Brenner DJ and Lin Q (2015) A Bead-Based Microfluidic Approach to Integrated Single-Cell Gene Expression Analysis by Quantitative RT-PCR. *RSC Adv* **5**: 4886-4893.
- Sun H, Olsen T, Zhu J, Tao J, Ponnaiya B, Amundson SA, Brenner DJ and Lin Q (2015) A microfluidic approach to parallelized transcriptional profiling of single cells. *Microfluid Nanofluid* **19**: 1429-1440.
- Sweasy JB, Lieberman HB, Volkert M and George D (2015) Evelyn Witkin and the coordinated response to DNA damage. *DNA Repair (Amst)* **35**: 154-155.
- Turner HC, Shuryak I, Taveras M, Bertucci A, Perrier JR, Chen C, Elliston CD, Johnson GW, Smilenov LB, Amundson SA and Brenner DJ (2015) Effect of Dose Rate on Residual gamma-H2AX Levels and Frequency of Micronuclei in X-Irradiated Mouse Lymphocytes. *Radiat Res* **183**: 315-324.
- Turner HC, Shuryak I, Weber W, Doyle-Eisele M, Melo D, Guilmette R, Amundson SA and Brenner DJ (2015)  $\gamma$ -H2AX Kinetic Profile in Mouse Lymphocytes Exposed to the Internal Emitters Cesium-137 and Strontium-90. *PLoS One* **10**: e0143815.
- Wang MM, Wang YC, Wang XN, Liu Y, Zhang H, Zhang JW, Huang Q, Chen SP, Hei TK, Wu LJ and Xu A (2015) Mutagenicity of ZnO nanoparticles in mammalian cells: Role of physicochemical transformations under the aging process. *Nanotoxicology* **9**: 972-982.
- Wang TJ, Wu CC, Chai Y, Lam RK, Hamada N, Kakinuma S, Uchihori Y, Yu PK and Hei TK (2015) Induction of Non-Targeted Stress Responses in Mammary Tissues by Heavy Ions. *PLoS One* **10**: e0136307.
- Wang X, Huang P, Liu Y, Du H, Wang X, Wang M, Wang Y, Hei TK, Wu L and Xu A (2015) Role of nitric oxide in the genotoxic response to chronic microcystin-LR exposure in human-hamster hybrid cells. *J Environ Sci (China)* **29**: 210-218.
- Wang Y, Zhang X, Wang M, Cao Y, Wang X, Liu Y, Wang J, Wang J, Wu L, Hei TK, Luan Y and Xu A (2015) Mutagenic Effects of Perfluorooctanesulfonic Acid in gpt Delta Transgenic System Are Mediated by Hydrogen Peroxide. *Environ Sci Technol* **49**: 6294-6303.
- Welch D, Harken AD, Randers-Pehrson G and Brenner DJ (2015) Construction of mouse phantoms from segmented CT scan data for radiation dosimetry studies. *Phys Med Biol* **60**: 3589-3598.
- Xu G, Chapman JR, Brandsma I, Yuan J, Mistrik M, Bouwman P, Bartkova J, Gogola E, Warmerdam D, Barazas M, Jaspers JE, Watanabe K, Pieterse M, Kersbergen A, Sol W, Celie PH, Schouten PC, van den Broek B, Salman A, Nieuwland M, de Rink I, de Ronde J, Jalink K, Boulton SJ, Chen J, van Gent DC, Bartek J, Jonkers J, Borst P and Rottenberg S (2015) REV7 counteracts DNA double-strand break resection and affects PARP inhibition. *Nature* **521**: 541-544.
- Xu Y, Randers-Pehrson G, Marino SA, Garty G, Harken A and Brenner DJ (2015) Broad energy range neutron spectroscopy using a liquid scintillator and a proportional counter: Application to a neutron spectrum similar to that from an improvised nuclear device. *Nucl Instrum Methods Phys Res A* **794**: 234-239.
- Xu Y, Randers-Pehrson G, Turner HC, Marino SA, Geard CR, Brenner DJ and Garty G (2015) Accelerator-Based Biological Irradiation Facility Simulating Neutron Exposure from an Improvised Nuclear Device. *Radiat Res* **184**: 404-410.
- Xu Y, Zhang B, Messerli M, Randers-Pehrson G, Hei TK and Brenner DJ (2015) Metabolic oxygen consumption measurement with a single-cell biosensor after particle microbeam irradiation. *Radiat Environ Biophys* **54**: 137-144.
- Xue G, Ren Z, Grabham PW, Chen Y, Zhu J, Du Y, Pan D, Li X and Hu B (2015) Reprogramming mediated radio-resistance of 3D-grown cancer cells. *J Radiat Res* **56**: 656-662. ■



*Former Center Director Eric Hall (l) congratulates current Director David Brenner (r) after his Weldon Prize lecture in Oxford.*